



**Measurement of $B\bar{B}$ Angular Correlations
based on Secondary Vertex Reconstruction
in Proton-Proton Collisions at $\sqrt{s} = 7$ TeV**

A dissertation submitted to
ETH ZURICH
for the degree of
DOCTOR OF SCIENCES

presented by
LUKAS DAVID WEHRLI
Dipl. Phys. ETH
born on March 4, 1982
citizen of Küttigen (AG)

accepted on the recommendation of
Prof. Dr. Günther Dissertori (examiner),
Prof. Dr. Christophorus Grab (co-examiner) and
Prof. Dr. Thomas Kurt Gehrman (co-examiner)

2011

Abstract

In proton-proton collisions at the CERN Large Hadron Collider (LHC), pairs of beauty quarks are abundantly produced through strong interaction. Studies of the b quark production and the angular correlations between b and \bar{b} quarks reveal substantial information on the dynamics of the hard scattering subprocesses within perturbative Quantum Chromodynamics (QCD). Beauty quarks are relevant for physics studies with top quarks and for low mass Higgs searches and $b\bar{b}$ production is a main background for many new physics searches.

A measurement of the angular correlations between beauty and anti-beauty hadrons ($B\bar{B}$) produced in proton-proton collisions at a center-of-mass energy of 7 TeV is presented. The region of small angular separation between the two hadrons is probed for the first time. The B hadrons are identified by the presence of displaced secondary vertices from their decays and the angle is measured between the directions from the reconstructed primary-interaction vertex to the secondary vertex positions. To reconstruct $B\bar{B}$ pairs even at small opening angle, a method based on an iterative secondary vertex finder is introduced.

The differential $B\bar{B}$ production cross section is measured as a function of the opening angle using data collected with the Compact Muon Solenoid (CMS) detector during 2010 and corresponding to an integrated luminosity of 3.1 pb^{-1} . The measurement is performed for different event energy scales, characterized by the leading jet transverse momentum. The data exhibit a substantial enhancement of the cross section in the collinear region. The relative amount of $B\bar{B}$ pairs produced with small opening angles, compared to the pairs with back-to-back topology, increases with the event energy scale. The measurements are compared to theoretical predictions based on perturbative QCD calculations. It is observed that in particular in the collinear region the measured data is not described well by any of the Monte Carlo predictions.

Zusammenfassung

In Proton-Proton Kollisionen am Large Hadron Collider (LHC) am CERN werden Paare von Beauty Quarks durch die starke Wechselwirkung sehr zahlreich erzeugt. Studien zur Produktion von b Quarks und zur Verteilung der Öffnungswinkel zwischen b und \bar{b} Quarks können umfangreiche Erkenntnisse über die Dynamik des harten Streuprozesses innerhalb der störungstheoretischen Quantenchromodynamik (QCD) liefern. Beauty Quarks spielen eine wesentliche Rolle in Physikstudien mit top Quarks und für die Suche nach dem Higgs Boson, falls es relativ leicht ist. Weiter sind $b\bar{b}$ Paare ein Hauptuntergrund für viele Studien, welche nach neuer Physik jenseits des Standardmodells suchen.

In dieser Doktorarbeit wird eine Messung der Winkelverteilung zwischen beauty und anti-beauty Hadronen ($B\bar{B}$), welche in Proton-Proton Kollisionen mit einer Schwerpunktsenergie von 7 TeV erzeugt wurden, vorgestellt. Zum ersten Mal können auch kleine Öffnungswinkel gemessen werden. Um die B Hadronen zu identifizieren, werden ihre sekundären Zerfallsvertices rekonstruiert. Die Öffnungswinkel werden zwischen den Richtungen vom rekonstruierten primären Kollisionsvertex zu den beiden sekundären Vertices gemessen. Um auch B Hadronpaare mit kleinem Öffnungswinkel richtig rekonstruieren zu können, wird eine Methode vorgestellt, die auf einem iterativen Rekonstruktionsalgorithmus für sekundäre Vertices basiert.

Der differentielle $B\bar{B}$ Wirkungsquerschnitt wird als Funktion des Öffnungswinkels gemessen. Dazu werden Daten verwendet, welche mit dem Compact Muon Solenoid (CMS) Detektor im Laufe des Jahres 2010 gemessen wurden. Sie entsprechen einer integrierten Luminosität von 3.1 pb^{-1} . Die Messung wird für verschiedene Energieskalen durchgeführt. Die Energieskala wird durch den Transversalimpuls des energiereichsten Jets charakterisiert. Der höchste Wirkungsquerschnitt wird bei kleinen Winkeln gemessen. Die relative Zahl von gemessenen Ereignissen mit kleinem Winkel im Vergleich zu Ereignissen mit einem grossen Winkel (nahe 180°) steigt mit der Energie. Die Messungen werden mit zahlreichen auf der störungstheoretischen QCD basierenden theoretischen Vorhersagen verglichen. Es zeigt sich, dass vor allem für kleine Winkel keine der Monte Carlo Vorhersagen die Daten sehr gut beschreibt.

Contents

1	Introduction	9
2	Beauty Physics	15
2.1	Quantum Chromodynamics	15
2.1.1	Renormalization and Running Coupling	16
2.2	Hadron-Hadron Collisions	17
2.2.1	Event Kinematics	18
2.2.2	Factorization	18
2.2.3	Parton Density Functions	20
2.2.4	Hadronization	21
2.2.5	Beauty Production in Proton-Proton Collisions	24
2.2.6	B Hadrons	25
2.2.7	Underlying Event	26
2.3	Monte Carlo Event Generators	27
2.3.1	PYTHIA	29
2.3.2	MadGraph/MadEvent	29
2.3.3	MC@NLO	29
2.3.4	CASCADE	30
2.3.5	Herwig	30
3	The LHC and the CMS Experiment	31
3.1	Large Hadron Collider	32
3.2	Compact Muon Solenoid Detector	35
3.3	Geometry / Coordinate System	37
3.4	A Generic LHC Detector	38
3.5	The CMS Tracker	42
3.5.1	Pixel Detector	42
3.5.2	Silicon Strip Tracker	46
3.6	The CMS Electromagnetic Calorimeter	49
3.7	The CMS Hadronic Calorimeter	51
3.8	The CMS Solenoid Magnet	54
3.9	The CMS Muon System	54
3.10	The CMS Trigger System	57
3.11	Computing in CMS	60

4	Analysis Overview	63
4.1	Trigger	63
4.2	Data Samples	64
4.3	Event Simulation	66
4.4	Event Selection	67
4.5	Monte Carlo Event Generators	69
5	B-tagging	71
5.1	Input for B-tagging	71
5.1.1	Jets	71
5.1.2	Tracks	73
5.1.3	Primary Vertex	73
5.1.4	Leptons	73
5.2	Impact Parameter and Impact Parameter Significance	74
5.3	B-tagging Algorithms used in CMS	75
5.4	Small Opening Angles between Two B Hadrons	77
6	Track and Vertex Reconstruction	79
6.1	Track Reconstruction	79
6.2	Adaptive Vertex Fitter	82
6.3	Adaptive Vertex Reconstructor	85
6.4	Secondary Vertex Definitions	86
6.5	Simple Secondary Vertex Algorithm	87
6.6	Two B Hadrons in a Single Jet	88
6.7	Inclusive Vertex Finder	94
6.7.1	Track Clustering	94
6.7.2	Vertex Fitting	96
6.7.3	Vertex Merging and Track Arbitration	96
6.7.4	Vertices for Correlation Measurement	97
6.7.5	Performance	97
6.8	B Candidate Identification	108
6.9	Resolution of the ΔR Reconstruction	113
7	Efficiency and Purity Correction	117
7.1	Kinematics of Events with Two B Hadrons	117
7.2	Efficiency and Purity Determination	121
8	Measured Properties of Reconstructed B Candidates	131
9	Systematic Uncertainties	135
9.1	Shape Dependent Systematic Uncertainties	135
9.1.1	Algorithmic Effects (data mixing)	135
9.1.2	B Hadron Kinematics	137
9.1.3	Jet Energy Scale	137
9.1.4	Phase Space Correction	137

9.1.5	Bin Migration from Resolution	142
9.1.6	Monte Carlo Statistics Uncertainty	142
9.1.7	Total Systematic Uncertainties	142
9.2	Systematic Uncertainties Affecting the Absolute Normalization	143
9.2.1	Uncertainties for Both Methods	143
9.2.2	Uncertainties for IVF Efficiency Correction	143
9.2.3	Uncertainties for B-Jet Matching Method	144
9.2.4	Total Systematic Uncertainties	144
10	Results	147
10.1	Differential Cross Section Distributions in ΔR and $\Delta\phi$	147
10.2	Detailed Comparison with Theoretical Predictions	154
11	Conclusions and Outlook	157
A	Numerical Values for Efficiency and Purity Correction	159
B	Reconstructed B Candidate Properties: Additional Plots	161
C	Systematic Uncertainties and Results: Additional Information	167
C.1	Systematic Uncertainties	167
C.2	Results	170

Chapter 1

Introduction

The desire to investigate the matter surrounding us and to understand which are the forces holding it together has always preoccupied human beings. The concept that matter is built of discrete units that cannot be divided into smaller pieces was first documented in ancient India and Greece more than two thousand years ago. The idea was based on abstract philosophical reasoning rather than experimental facts. The Greek philosopher Democritus called such a hypothetical indivisible brick *átomos*, which means *uncuttable*.

From a scientific point of view the atomic theory is much younger. The first empirical evidences that matter consists of atoms were found in the 18th century. Antoine Lavoisier discovered in 1789 that in chemical processes the mass of the reactants is the same as the mass of the products (law of conservation of mass) and in 1803 John Dalton found that elements react only in ratios of integer numbers (law of multiple proportions). Dmitri Mendeleev, a Russian chemist and inventor, found around 1869 that the elements exhibit an apparent periodicity of properties, if they are arranged according to their atomic weight. In 1827 Robert Brown observed through his microscope that dust grains floating in water move chaotically. This phenomenon, the “Brownian motion”, was first explained mathematically in 1905 by Albert Einstein. The reason for the chaotic movement of the dust particles are collisions with the surrounding water particles.

The picture of atoms being indivisible was proven wrong in 1897, when J.J. Thompson discovered the electron. In 1910 Ernest Rutherford performed his famous experiment with alpha rays bombarding a gold foil and concluded that the positive charge of an atom, together with most of its mass, is concentrated in a nucleus at the center of the atom. Later it was found that the nucleus consists of protons and neutrons. The neutron was first detected in 1932 by James Chadwick.

During the 20th century a large number of other particles have been discovered, mostly in cosmic rays. In 1933 C. D. Anderson found the first antimatter particle, the anti-electron. The new particle was named positron. The electron neutrino was predicted 1930 by Wolfgang Pauli to explain the energy loss in the beta decay and experimentally discovered in 1956 by Clyde L. Cowan and Frederick Reines. In 1937 the muon, a particle very similar to an elec-

tron, but 200 times heavier, was detected in cosmic rays. In 1947 the pion was discovered and in the years after many more particles followed. Most of the new particles were unstable and decayed into lighter fragments. Before these discoveries, all matter was thought to be built of three types of particles: protons, neutrons and electrons. After many other particles had been found, the situation looked more complex. In addition, scattering experiments revealed a non-uniform charge distribution inside the proton, and there was experimental evidence that the neutron contained charged subcomponents. Physicists realized in the middle of the 1960's that their understanding of the world was insufficient. It was time for new, innovative and groundbreaking ideas, which finally lead to the development of the *Standard Model of particle physics*.

The Standard Model (SM) describes both the elementary subatomic particles and the interactions between them. In the SM matter consists of two types of elementary particles, where elementary means indivisible: *quarks* and *leptons*. From the particles mentioned above the electron, the positron, the muon and the neutrino belong to the leptons. There exist three families of leptons that are, apart from the mass, almost identical. The first family is built from the electron e and the electron neutrino ν_e (plus their antiparticles). The second and third family consist of the muon (μ) and the tau (τ) particles, respectively, plus their corresponding neutrinos (ν_μ, ν_τ).

The rest of the particles that have been named above, including the neutron and the proton, are not elementary particles. They are built of quarks. As for leptons, three families of two quarks exist (plus their antiparticles). One quark per family is positively charged ($2/3$ of the absolute electron charge) and the other one has negative charge ($1/3$ of the electron charge). The positive quarks are the up, charm and top quarks and the negative ones are called down, strange and bottom. The top and bottom quarks are also called truth and beauty quark, respectively. It has been found that quarks can appear in combination of either one quark and one antiquark (*mesons*) or three (anti-) quarks (*baryons*). The pion is the lightest meson and the proton and neutron are the lightest baryons. All particles built of quarks are called *hadrons*.

The SM describes three interactions between quarks and leptons: the electromagnetic, the weak and the strong interaction. The weak interaction acts on all quarks and leptons. It is responsible for the radioactive beta decay of subatomic particles. The exchange particles of the weak force are the W and Z bosons. The electromagnetic force acts on charged particles (not on neutrinos). The force carrier is the photon (γ) and the quantum field theory of the electromagnetic interaction is the *Quantum Electrodynamics* (QED). The SM unifies the weak and the electromagnetic interaction into an electroweak interaction. The strong interaction acts only on quarks and on gluons. The gluon is the force carrier of this third interaction, and it literally glues together the quarks in the hadrons and it also holds the nucleus together. The quantum field theory of the strong interaction is the *Quantum Chromodynamics* (QCD).

The success of the SM comes from the fact that it is a very predictive theory: seven of the elementary particles were first predicted before they have been discovered experimentally.

Those are the charm, the bottom and the top quark, the tau neutrino, the gluon and the W/Z bosons. The predicted properties of these particles were experimentally confirmed with good precision.

There is one SM particle that has not been discovered so far: the Higgs Boson. It has been predicted in 1964 almost simultaneously by three groups of theorists: By Peter Higgs, by François Englert and Robert Brout and by Gerald Guralnik, Carl R. Hagen and Tom Kibble. It is believed to be responsible for particles having intrinsic mass. It explains the difference between the massless photon and the massive W and Z bosons through the process of spontaneous symmetry breaking. The mass of the Higgs boson is a free parameter of the SM.

In spite of the effectiveness at describing a wide variety of phenomena within its domain, the SM cannot be considered a complete theory, because it incorporates only three out of the four fundamental forces, omitting gravity, and because it leaves many important questions unanswered. Why are three generations of quarks and leptons realized in nature? Might there be more? What is the nature of the *dark matter* that is predicted to make up 23 % of the mass-energy density of the universe? Why is our universe made of matter, and what happened to the missing antimatter?

In order to answer these questions, many theories extending the SM have been developed. Supersymmetry (SUSY) predicts “superpartners” for all known particles to solve some of the problems of the SM and provide a candidate for dark matter. Other exotic models predict more hypothetical particles or extra dimensions of space. Many of the theories predict effects that should be verifiable at the TeV energy scale.

In this exciting time of unanswered questions and exotic models a very powerful tool has been built by the European Organization for Nuclear Research (CERN) to bring light into the dark. The Large Hadron Collider (LHC) started operation in 2008. The first proton-proton collisions at a center-of-mass energy of 7 TeV have been recorded in March 2010 and a new chapter of the hunt for the elusive Higgs Boson has started. Due to the need of a large amount of good quality data the discovery of the Higgs particle may take some time. Apart from this discovery and testing other models, which predict physics beyond the Standard Model, one short term goal of the LHC physics program is to confirm the SM at the new energy scale. In order to commission the detector facilities of the four LHC experiments, many already known physics quantities need to be re-measured at higher energy scales. The design center-of-mass energy of the LHC is $\sqrt{s} = 14$ TeV. The current plan is to collect a large amount of data at 7 TeV, and then to restart taking data at 14 TeV after a one year shutdown period in 2013.

When the work for this thesis started, the startup of the LHC was expected soon. A good topic for a thesis was a measurement that needs a small amount of data. The field of beauty physics is promising, because pairs of beauty quarks are abundantly produced through strong interaction in proton-proton collisions. The cross section for $b\bar{b}$ production is measured to be at the order of $100 \mu\text{b}$ at $\sqrt{s} = 7$ TeV [1–3]. Studying b production provides substantial information about the dynamics of the underlying hard scattering subprocesses within per-

turbative QCD (pQCD). In lowest order QCD, momentum conservation requires the b and \bar{b} to be emitted back-to-back. In higher order subprocesses with additional partons (notably gluons) emitted, different topologies of the final state b quarks are observed. Consequently, measurements of angular and momentum correlations between b and \bar{b} provide a sensitive test of the pQCD leading-order (LO) and next-to-leading order (NLO) cross sections and their evolution with the event energy scales. As $b\bar{b}$ production is expected to be a main background for many new physics searches, and as b quarks play a crucial role in some physics studies (top physics, low mass Higgs searches), it is of great importance to correctly identify b quarks and to know as much as possible about their properties.

In this thesis, the angular correlations between pairs of beauty hadrons, hereafter referred to as B hadrons, are studied using data collected with the Compact Muon Solenoid (CMS) detector during 2010. The CMS detector is well suited for studying $b\bar{b}$ production because of its good muon detecting capabilities and the precise tracking detectors. B hadrons have a relatively long lifetime compared to lighter hadrons produced in proton-proton collisions. Hence, they decay significantly displaced from the primary “collision” vertex. The long lifetime is exploited to identify the B hadrons by reconstructing their decay vertex from the tracks of charged decay products. The angular correlations are then measured between the flight directions of the two B hadrons, where the flight direction is defined to be the direction from the primary collision vertex to the secondary B hadron decay vertex. The kinematic properties of the B hadrons can also be reconstructed using jets or muons from semileptonic decays. The advantage of using B hadron flight directions instead of directions of b -jets for a correlation measurement is that the region of very small opening angles is probed. Two decay vertices can be reconstructed even if two B hadrons are too collinear to produce two distinct jets. A good angular resolution for the vertexing is required, especially if both B hadrons decay within a single reconstructed jet. An iterative inclusive secondary vertex finder that is independent of any jet direction has been developed for this purpose. In the study presented here, the angles between the B hadrons are not extrapolated back to the angles between the b and \bar{b} quarks. This would introduce additional uncertainty due to the modeling of the b fragmentation and hadronization. Previously, studies of azimuthal $b\bar{b}$ correlations have been performed in $p\bar{p}$ collisions at lower center-of-mass energy [4, 5].

This thesis is organized as follows: In the next chapter an overview on theoretical aspects of beauty physics is given. This includes a review of the main principles of QCD relevant for hadron-hadron collisions and an introduction to beauty physics at LHC. The chapter is closed with a short overview about the Monte Carlo Event Generators used in this study. In chapter 3, the experimental facilities, the LHC accelerator and the CMS detector are described. Chapter 4 contains an analysis overview. In chapter 5 standard techniques applied for b -tagging are explained and the algorithms implemented in the CMS software framework are described. Chapter 6 is devoted to track and vertex reconstruction. The inclusive vertex finder algorithm developed for this thesis is described in detail and its performance and the resolution for the angular measurement are studied. In the next chapter, efficiency and purity corrections are discussed. In chapter 8 some properties of the B candidates used for the correlation analysis are shown. Chapter 9 covers the systematic uncertainties relevant for the

analysis and in chapter 10 the results are shown. The conclusions are given in chapter 11.

If not indicated differently, *natural units* are used in this thesis ($c = \hbar = 1$). Energy, momentum and mass are given in eV.

Chapter 2

Beauty Physics

The study of heavy quark production is a very interesting scientific field. In proton-proton collisions at the LHC center-of-mass energies (7 – 14 TeV) heavy quarks are abundantly produced. The LHC will be described in more detail in the next chapter. Studies of heavy quark production may provide substantial information about the dynamics of the underlying hard scattering subprocesses within pQCD and insight into the hadronization properties of heavy quarks at new energy scales. They may reveal new information on the heavy quark content of protons. Heavy quarks include the charm and the beauty quarks. The up, down and strange quarks are much lighter and the top quark does not hadronize because its lifetime is significantly shorter than the timescale for strong interactions. In this study the focus will be on physics including beauty quarks (B physics).

At the LHC beauty quarks and antiquarks are predominantly produced in pairs through strong interaction. For many new physics searches $b\bar{b}$ production is one of the main backgrounds and therefore identifying b quarks and precise measurements of their properties are crucial. In addition, b quarks play an important role in top physics since the top quark decays almost exclusively to a W boson and a b quark.

In this chapter a short overview on some important aspects of QCD will be given. These include the applicability of pQCD, renormalization, and the running of the strong coupling constant. Subsequently, hadron-hadron collisions are discussed. The use of the concept of factorization for cross section calculations is explained. Parton density and fragmentation functions are introduced. Afterwards, beauty production and some properties of B hadrons are discussed. The last section introduces the concept of Monte Carlo Event generators and presents a few examples of such generators.

2.1 Quantum Chromodynamics

In the SM of particle physics the forces between quarks and leptons are described by *gauge theories*. The field theory of the strong interactions is QCD [6–9]. A very comprehensive overview on QCD is given in [10]. Readers interested in Quantum Field Theories in general

are encouraged to read [11]. There are a few differences between QCD and Quantum Electrodynamics (QED), which is the theory of the electromagnetic interaction. A fundamental difference is that the strong interaction is characterized by a non-abelian SU(3) gauge symmetry, while the U(1) symmetry of QED is abelian. The charge of the strong interaction is called *color*. It comes in three flavors (red, green and blue). From the fundamental spin $\frac{1}{2}$ fields of the SM of particle physics only the *quarks* carry color, while the *leptons* do not. Color is exchanged by eight bicolored gluons. Since gluons themselves carry color charge, they can interact with other gluons (see figure 2.1). There is no such self-interaction in QED, since the photon does not carry an electric charge. The gluon self-interaction has some consequences for the behavior of the effective strong coupling strength. The force between two quarks that are separated from each other does not diminish with their distance, it rather increases. This is called color confinement and it is the reason why free quarks are never observed. Quarks always form hadrons.



Figure 2.1: Gluon self-interaction: triple-gluon vertex (left) and four-gluon vertex (right).

2.1.1 Renormalization and Running Coupling

In QCD, as in all renormalizable theories, all the ultraviolet divergencies arising in loop diagrams are cancelled. An arbitrary renormalization scale μ_R has to be defined. Note that typically for cross section prediction μ_R is set equal to a physical scale Q of the process at hand. However, physical quantities cannot depend on the choice of μ_R and this is used to derive the following *Renormalization Group Equation* (RGE) [10]:

$$Q^2 \frac{\partial \alpha_s(Q^2)}{\partial Q^2} = \beta(\alpha_s(Q^2)) = -\alpha_s^2 (\beta_0 + \beta_1 \alpha_1 + \dots). \quad (2.1)$$

The coefficient β_0 is computed to be

$$\beta_0 = \frac{33 - 2n_f}{12\pi}, \quad (2.2)$$

where n_f is the number of light quark flavors (light compared to the scale Q). For $n_f = 6$, β_0 is positive and β negative. In QED β is positive. This is the reason why the coupling behavior is different in QCD than in QED: α_s is large for small Q (confinement) and as the value Q is increased the coupling decreases. For large values of Q , hadrons appear to be composed of gluons and quarks (partons) that are (because of the running of the coupling) only weakly interacting with each other. This phenomenon is called asymptotic freedom.

Perturbative techniques are applicable to compute color interactions only if α_s is sufficiently small. The energy scale Λ_{QCD} at which non-perturbative effects become important is experimentally found to be at the order of 200 MeV (which is a bit above the pion mass). At

leading-order the solution of the equation (2.1) is

$$\alpha_s(Q^2) \equiv \frac{g_s^2(Q^2)}{4\pi} = \frac{1}{\beta_0 \ln(Q^2/\Lambda_{\text{QCD}}^2)}. \quad (2.3)$$

This equation describes the evolution of α_s , but experimental data must be used to measure the normalization. The value for α_s is usually given at the Z boson mass m_Z . The value reported by the Particle Data Group (PDG) [12,13] is

$$\alpha_s(m_Z) = 0.1184 \pm 0.0007. \quad (2.4)$$

The running of the coupling α_s is shown in figure 2.2.

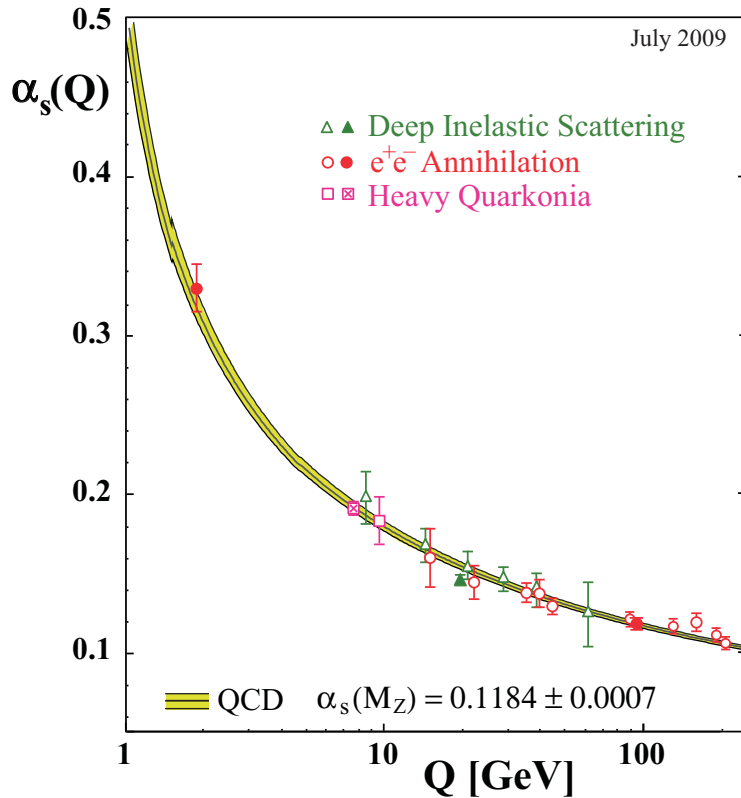


Figure 2.2: Summary of measurements of the strong coupling α_s as function of the energy scale Q . The curves are QCD predictions for the combined world average value of $\alpha_s(M_Z)$ [13].

2.2 Hadron-Hadron Collisions

Perturbative QCD can be used to calculate cross sections only for processes with a large momentum transfer. Hadron-hadron scattering events are divided in two classes. Soft interactions with low momentum transfer are sensitive to long-distance effects and they are

(due to the coupling being large) not computable using pQCD, while pQCD is applicable for hard interactions with high momentum transfer. In this section we concentrate on hard interactions. In the case of heavy flavor production the mass of the heavy quark guarantees to have a relatively large scale.

2.2.1 Event Kinematics

Since hadrons contain quarks and gluons, hadron-hadron scattering is more complex than lepton-lepton scattering. In very high-energy reactions, quarks and gluons interact very weakly (asymptotic freedom). For collisions between hadrons this means that only one parton inside the proton takes part in the hard scattering (*quark parton model*). The validity of the parton model is proven in field theory. For a more intuitive approach we consider a hadron with mass M that is probed by a vector boson with momentum Q . In the parton model picture the hadron consists of partons sitting in clouds of other partons that are continuously emitted and absorbed. Since the hadron remains intact and high momentum transfers between partons are suppressed, the partons have lifetimes of the order of $1/M$. If Q is large compared to M the lifetime of the partons is long compared to the vector boson interaction time $1/Q$. Thus the vector boson sees a static picture of the proton and the parton that is hit is approximately free (it has no time to interact with other partons).

For a collision between two hadrons h_1 and h_2 with four-momenta P_1 and P_2 the center-of-mass energy is given by

$$s = (P_1 + P_2)^2. \quad (2.5)$$

In the quark parton model the scattering is assumed to happen between one constituent (parton) per proton with momentum $p_i = x_i P_i$ ($i = 1, 2$) and the partons are assumed to be massless. The virtuality of the process is then defined as

$$Q^2 = \hat{s} = x_1 x_2 s. \quad (2.6)$$

For production of heavy particles with mass M the scale is given by the mass ($Q \approx M$). Given the center-of-mass energy s , the momentum fraction is calculated for centrally produced objects

$$x_1 = x_2 = \frac{M}{\sqrt{s}}. \quad (2.7)$$

2.2.2 Factorization

Even for hard scattering processes the long-distance behavior (which is not computable in pQCD) must be taken into account, e.g. when calculating cross sections of processes with hadrons in the initial or final state. Factorization theorems [14] allow to derive predictions for these cross sections by separating (factorizing) short-distance from long-distance behavior in a systematic way. Taking the production of B hadrons in proton-proton collisions as an example: Only the hard scattering process, during which b quarks are produced from gluons or quarks present in the incoming protons is described by pQCD. For the modeling of the gluons and quarks in the proton so called parton density functions (PDFs) are introduced in section 2.2.3. The hadronization, which is the transition from outgoing quarks into colorless

hadrons, is described in section 2.2.4. The partonic cross sections for beauty production in proton-proton collisions are discussed in section 2.2.5. Besides the renormalization scale μ_R the factorization procedure requires the introduction of a second, arbitrary factorization scale μ_F . The two scales μ_R and μ_F are independent. However, they are often chosen to be equal ($\mu_R = \mu_F = Q$) for numerical calculations.

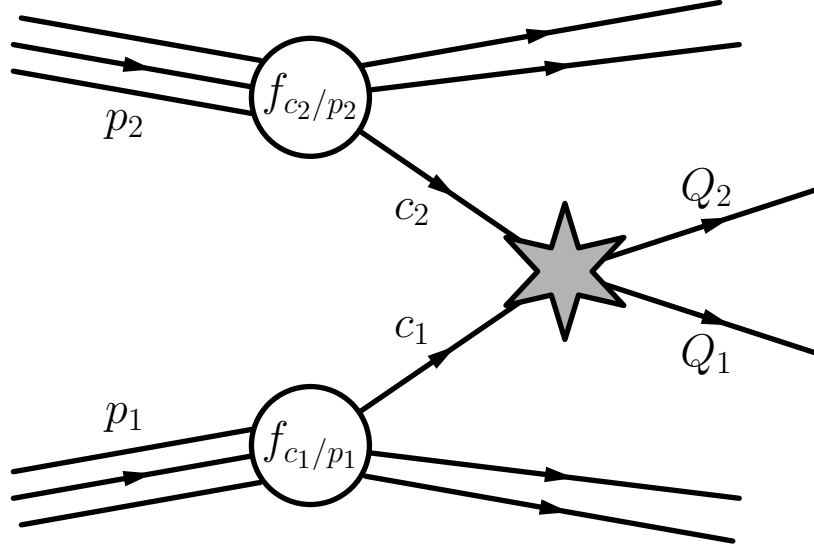


Figure 2.3: Schematic view of hard collision process $p_1 p_2 \rightarrow Q_1 Q_2$.

The cross section is then computed by convoluting the tree-level scattering or annihilation of individual partons with the appropriate PDFs and the fragmentation function for the transition into hadrons. As an example the cross section of producing two quarks Q_1 and Q_2 in a proton-proton collision is given below. In this calculation there is no hadronization of the final state quarks. For the two quarks being b and \bar{b} the inclusive $b\bar{b}$ cross section is calculated. The cross section formula for collisions of protons p_1 and p_2 to produce quarks Q_1 and Q_2 (see figure 2.3) can be written as

$$d\sigma(p_1 p_2 \rightarrow Q_1 Q_2) = \int_0^1 dx_1 \int_0^1 dx_2 \sum_{c_1, c_2} \left[f_{c_1/p_1}(x_1, \mu_F^2) f_{c_2/p_2}(x_2, \mu_F^2) \cdot d\hat{\sigma}^{(c_1 c_2 \rightarrow Q_1 Q_2)}(Q^2, \mu_F^2, \mu_R^2) \right], \quad (2.8)$$

where $d\hat{\sigma}^{(c_1 c_2 \rightarrow Q_1 Q_2)}$ is the cross section for the hard subprocess $c_1 c_2 \rightarrow Q_1 Q_2$ and $f_{c_i/p_i}(x_i, \mu_F^2)$ is the PDF for proton p_i to contain the parton c_i with momentum fraction x_i at scale μ_F ($i = 1, 2$). The c_i are quarks, antiquarks or gluons and the sum runs over all processes that contribute to the production of Q_1 and Q_2 . In the example of $b\bar{b}$ production there are contributions from $q\bar{q} \rightarrow b\bar{b}$ and $gg \rightarrow b\bar{b}$. The two-to-two scatterings included in this formula give the leading-order contributions to the hard subprocess. If higher order processes (two-to-three, etc.) are taken into account, $\hat{\sigma}$ is written as a perturbative expansion ($\hat{\sigma} = C_{LO}\alpha_s^n + C_{NLO}\alpha_s^{n+1} + \dots$). The higher order contributions contain singularities if

two incoming or outgoing partons become collinear. These singularities are absorbed into the PDFs and fragmentation functions (see sections 2.2.3 and 2.2.4) which leads to a μ_F^2 dependency of these functions.

2.2.3 Parton Density Functions

To describe the quark and gluon content of hadrons PDFs are used. These describe the probability density of partons inside a hadron as a function of the fraction x of the mother hadron momentum they carry and on the factorization scale μ_F^2 .

To understand how the PDFs depend on x (for fixed μ_F) the parton content of the proton must be known. The proton consists of three bound *valence* quarks that determine its quantum numbers. The distribution would then be expected to be smeared around $\frac{1}{3}$. But this is not what is found experimentally. The reason are virtual quark-antiquark pairs called *sea* quarks. These form when a gluon contained in the hadron's color field splits. The sea quarks lead to higher values of the PDFs for small x .

When calculating processes in pQCD infrared (IR) divergencies can arise. An IR divergence is a situation in which an integral diverges because of contributions of objects with small (almost zero) energy. To be more precise IR divergencies can come from real gluon radiation with the gluon being very soft (soft divergences) or nearly collinear to the parton it was emitted from (collinear divergences). The contributions from non resolvable gluon radiation are absorbed into the PDFs by redefining the PDFs at a given factorization scale μ_F . Experimentally non resolvable means that the effect of these gluons cannot be measured in the detector. The dependence on the scale can intuitively be explained by the sea quarks: if the energy of the probing vector boson is increased the PDF at high x is decreased because of gluon radiation (the momentum is shared by more partons) and the PDF at low x is increased because, for example, of pair production ($g \rightarrow q\bar{q}$). This is illustrated in figure 2.4. The fact that the PDFs depend on both, x and the scale, is called scaling violation.

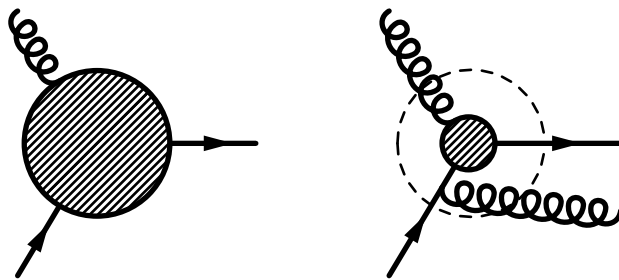


Figure 2.4: If Q^2 of the probing vector boson is increased (from left to right plot) the resolution is improved and finer structures are observed.

Unfortunately, the PDFs cannot be computed by pQCD but must be obtained using experimental data. However, physical measurable quantities as cross sections cannot depend on the factorization scale. This is used to derive an equation to describe the scale dependency of

PDFs, the so called DGLAP equation [15–17]. Given a scale μ_0 and the values of the quark and gluon PDFs at that scale, they are used to predict the PDFs at any other scale μ_F . At leading-order the DGLAP equations for quarks and gluons are [10]

$$\begin{aligned} \mu_F^2 \frac{\partial q_i(x, \mu_F^2)}{\partial \mu_F^2} &= \int_x^1 \frac{dz}{z} \frac{\alpha_s}{2\pi} \left[P_{q_i q_j}(z, \alpha_s) q_j \left(\frac{x}{z}, \mu_F^2 \right) + P_{q_i \bar{q}_j}(z, \alpha_s) \bar{q}_j \left(\frac{x}{z}, \mu_F^2 \right) \right. \\ &\quad \left. + P_{q_i g}(z, \alpha_s) g \left(\frac{x}{z}, \mu_F^2 \right) \right] \quad (2.9) \\ \mu_F^2 \frac{\partial g(x, \mu_F^2)}{\partial \mu_F^2} &= \int_x^1 \frac{dz}{z} \frac{\alpha_s}{2\pi} \left[P_{gg}(z, \alpha_s) g \left(\frac{x}{z}, \mu_F^2 \right) + \sum_{f=q, \bar{q}} P_{gf}(z, \alpha_s) f \left(\frac{x}{z}, \mu_F^2 \right) \right] \end{aligned}$$

The functions $P_{xy}(z, \alpha_s(\mu_F^2))$ are known as Altarelli-Parisi splitting functions. They are expressed as power series in α_s . Some diagrams contributing to the leading order splitting functions are shown in figure 2.5.

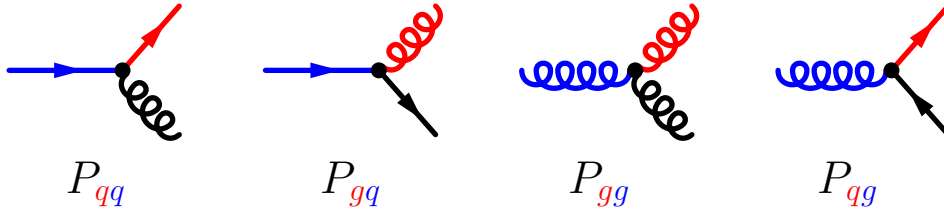


Figure 2.5: Some diagrams contributing to the leading-order Altarelli-Parisi splitting functions. Each function $P_{xy}(z)$ gives the probability for parton splitting.

Even if PDFs cannot be computed in first place, pQCD makes useful predictions, since the PDFs are independent of the hard scattering process and the DGLAP equations can be used to compute PDFs at any scale if they are known at a reference scale. PDFs are measured at one scale and evolved to a higher scale using equations 2.9. Experimental data taken at higher energy scales are used to optimize the extrapolation. In the case of the LHC the PDFs are mostly taken from measurements at the Hadron-Elektron-Ring-Anlage (HERA) detectors H1 and Zeus. At HERA, the PDFs are measured in electron-proton collisions at 300 GeV center-of-mass energy. The fact that the same PDFs are suited for hadron-hadron collisions (the presence of an incoming hadron does not change the structure of the other hadron) shows the importance of the factorization theorem. Many sets of PDFs are available. An example for the quark and gluon PDFs measured at HERA [18] for $Q^2 = 10 \text{ GeV}$ is shown in figure 2.6.

2.2.4 Hadronization

In pQCD quark and gluon final states are calculated, while in an experiment the colorless hadrons are observed. The transition between the two states is called hadronization and is a non-perturbative effect. Again, a factorization ansatz is used to separate the perturbatively calculable short distance cross section from the long distance behavior, which is expressed by a fragmentation function $D_a^h(z; \mu_R, \mu_F)$. It gives the probability that a parton a produces a

H1 and ZEUS

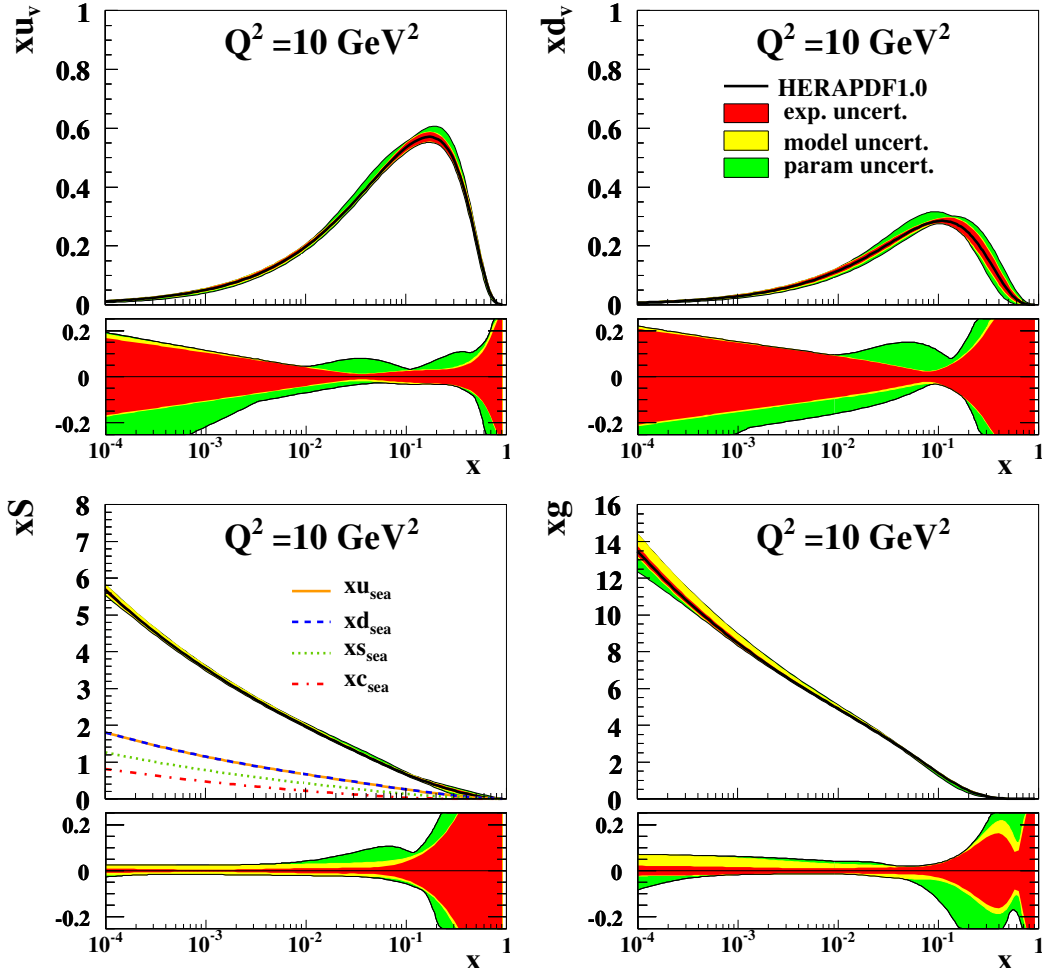


Figure 2.6: PDFs from HERAPDF1.0, xu_v , xd_v , $xS = 2x(\bar{U} + \bar{D})$ and xg at $Q^2 = 10 \text{ GeV}^2$. For the sea quark distribution the u , d , s , c part is illustrated. Fractional uncertainty bands are shown below each PDF, separately for experimental, model and parametrization uncertainty [18].

hadron h that carries a fraction z of the momentum of a . The fragmentation functions are treated similarly to the PDFs. In particular note that D_a^h is universal and does not depend on the hard process.

For heavy quark fragmentation the Peterson parametrization is used [19]. The fragmentation function for a heavy quark Q is given by

$$D_Q^h(z) \propto z^{-1} \left(1 - \frac{1}{z} - \frac{\epsilon_Q}{1-z}\right)^{-2}, \quad (2.10)$$

where $\epsilon_Q \approx \frac{m_q^2}{m_Q^2}$ is a free parameter (ϵ_b is measured to be of the order of 0.005).

The hadron-hadron collision can be seen as sequence of five steps: the first step is initial state radiation, leading up to the hard scattering of two partons. The next step is the hard scattering itself, where a fixed number of primary partons are produced. In the third step, these partons are evolved from the hard scale down to a soft cut-off scale Q_0 (typically $\mathcal{O}(1 \text{ GeV})$) by gluon emission (“shower”). The fourth step is the transition from colored partons (final state quarks and gluons) to color-singlet hadrons. As mentioned before, this is a non-perturbative effect that cannot be calculated in pQCD. As a last step, any unstable particles decay into stable hadrons, leptons and photons. Branching ratios are obtained from particle decay tables [12]. All steps apart from the first two are included in the fragmentation function. It gives the probability that the parton a produces, in the evolution down to the cut-off scale, any parton x that forms a hadron X , with X decaying into a hadron of type h (plus other particles). While pQCD is used for the evolution and tables from previous measurements are used for the hadron decays, the intermediate step needs to be modeled.

There exist different models that describe the transition from partons to hadrons. The common idea is that it is, due to the strength of the strong force at low momentum transfer, energetically favorable to populate the vacuum with virtual $q\bar{q}$ pairs. The energy stored in the gluon field is then used to convert these pairs into real particles. These real particles arrange themselves together with the partons present from the interaction into color-singlet hadrons. The *string model* [20,21] and the *cluster model* [22] are described in the following. Both are based on a probabilistic and iterative procedure and provide rules to determine the quark flavors, the primary hadrons that are produced and their momenta.

As described in [20] and [10], the simplest system to study the fragmentation is a $q\bar{q}$ pair as produced for example in e^+e^- annihilation. The energy stored in the color dipole field between the quark and the antiquark increases linearly with the separation between the two. This linear confinement is the starting point of the string model. The physical picture is that of a color flux tube with uniform energy density per unit length being stretched between the q and \bar{q} . The energy per unit length is measured to be $\kappa \approx 1 \text{ GeV/fm}$. The transverse size of a string is small compared to its typical length and therefore its dynamics are described by a massless relativistic string with no transverse degrees of freedom. As the q and \bar{q} move apart, the energy increases and the string may break by production of a new $q'\bar{q}'$ pair. Now there are two color-singlet systems $q\bar{q}'$ and $q'\bar{q}$. For pairs with high invariant mass further breaks

may occur. Gluons cause kinks along the string. In the Lund string model this continues until only on-mass-shell hadrons remain. Assuming that the $q'\bar{q}'$ pair is produced at a point, the separation of the q' and \bar{q}' that is needed for the pair building is reached by quantum mechanical tunneling. The tunneling implies a suppression of heavy quark production, such that charm and bottom quarks are not expected to be produced in soft fragmentation, but only in perturbative parton shower branchings $g \rightarrow q\bar{q}$. The production of baryons is not well understood. In the simplest approach, diquarks are used with a generalization of the meson production mechanism [23, 24]. A more complex scenario is the popcorn model, where quark antiquark pairs are produced one after the other [25].

In the cluster model, the gluons remaining after the parton shower at the cut-off scale Q_0 are split into light $q\bar{q}$ pairs. Neighboring $q\bar{q}'$ pairs form color singlets. These are assumed to form clusters, which mostly decay isotropically to pairs of hadrons, chosen according to the density of states with appropriate quantum numbers. The cluster model has few parameters and a natural mechanism for suppressing heavy particle production. However, it may have some problems for massive clusters.

The situation is more complex in collisions with hadrons involved than in lepton-lepton collisions. The reason is that hadrons are composed of quarks. In high-energy reactions only one parton per proton takes part in the hard scattering. It is kicked out of the proton and leaves its cloud of partons behind. This *remnant*, which is a colored object, continues to fly in target direction. Since the partons in the remnant have nothing to be reabsorbed, they shower and hadronize and form a jet in target direction. The parton that was hit out of the proton fragments and produces a second jet. There is a color field between the hit parton and the remnant, which leads to emission of low energy hadrons flying in the plane between the two jets.

Fortunately the effect of hadronization on pQCD predictions appears to be small, such that accurate predictions for properties of events with hadronic final states can be calculated.

2.2.5 Beauty Production in Proton-Proton Collisions

Heavy quark production is convenient to handle both experimentally and theoretically. Since hadrons containing c or b quarks have a long lifetime their decay vertex can be reconstructed in modern tracking detectors. Their large mass introduces a hard scale. Therefore, pQCD is applicable and cross sections can be calculated.

At LO $b\bar{b}$ pairs are produced either via gluon fusion or via annihilation of light quarks (see figure 2.7). Both types of diagrams are commonly referred to as Flavor Creation (FCR). In proton-proton collisions at LHC gluon fusion is the dominant process, since protons do not contain valence antiquarks and since the momentum fractions x_1, x_2 of the partons from the two protons are expected to be very small, and the gluon PDF dominates at small x . For a $b\bar{b}$ pair produced centrally at $\sqrt{s} = 7 \text{ TeV}$ we can estimate $x = x_1 = x_2$ using equation (2.7) to be $x \approx \frac{2m_b}{s} \approx 0.0014$. For LO $b\bar{b}$ production, the b and \bar{b} are produced back-to-back in the azimuthal plane because of momentum conservation, and they are produced symmetric

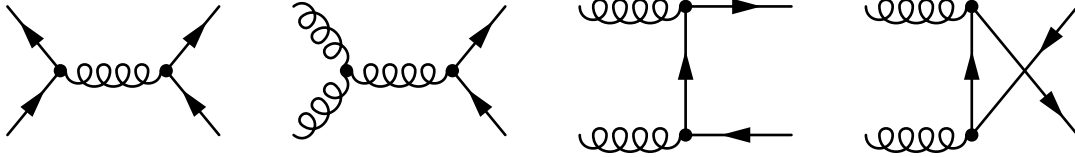


Figure 2.7: Leading order Flavor Creation diagrams: $q\bar{q}$ annihilation (left) and gluon fusion (others).

in transverse momentum (p_T).

The total partonic cross sections for $q\bar{q}$ annihilation and gluon fusion are calculated in [26]. The high energy limits ($\hat{s} \rightarrow \infty$, where \hat{s} is the center-of-mass energy in the partonic system) are

$$\hat{\sigma}(q\bar{q} \rightarrow Q\bar{Q}) \rightarrow \frac{1}{\hat{s}} \quad (2.11)$$

$$\hat{\sigma}(gg \rightarrow Q\bar{Q}) \rightarrow \frac{1}{\hat{s}} \left(\frac{1}{\beta} \log \left(\frac{1+\beta}{1-\beta} \right) - 2 \right) \quad (2.12)$$

where $\beta \equiv \sqrt{1 - \frac{4m^2}{\hat{s}}}$ is the heavy quark velocity in the center of mass frame.

At NLO there are real and virtual emission FCR diagrams. Ultraviolet divergencies are removed by the renormalization procedure, infrared and collinear divergencies cancel between real radiation and virtual corrections or are absorbed in the PDFs. Complete NLO calculations were done in [27, 28].

In CDF and D0 at Tevatron the leading-log FCR $b\bar{b}$ pair production has been found to be a factor of four below the data, while the factor NLO FCR divided by LO FCR contribution is found to be roughly two [29]. There are two classes of $b\bar{b}$ production diagrams that first enter at NLO and that are therefore expected to give meaningful results.

One class of diagrams are the so called Flavor Excitation (FEX) diagrams, where one b or \bar{b} that is already present in the initial state is scattered out of the initial into the final state by a gluon or light (anti-) quark. FEX contributions are sensitive to the number of b and \bar{b} in the proton (i.e. to the PDFs). FEX $b\bar{b}$ pairs are produced asymmetric in p_T and with a flat opening angle distribution. The other class are the Gluon Splitting (GSP) diagrams. For these a final state gluon splits into a $b\bar{b}$ pair, while neither b nor \bar{b} is taking part in the hard scattering process. Pairs from GSP are produced with small opening angles and asymmetric in p_T . Examples of GSP and FEX diagrams are shown in figure 2.8.

2.2.6 B Hadrons

Hadrons containing a b or \bar{b} are referred to as B hadrons. Depending on whether a hadron contains b or \bar{b} and on the flavor of the other quark different B hadrons are distinguished.

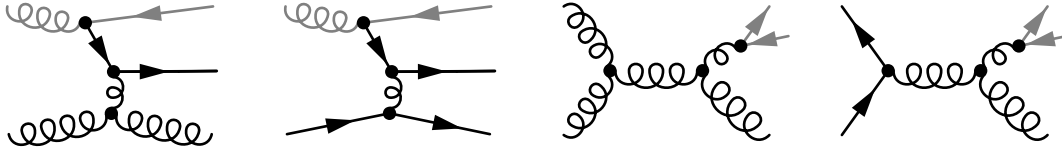


Figure 2.8: Flavor Excitation and Gluon Splitting diagrams: The hard scattering process is shown in black. For Flavor Excitation, one initial-state b or \bar{b} is taking part in the hard scattering. In Gluon Splitting diagrams a final state gluon splits into a $b\bar{b}$ pair.

Some B hadrons and their properties are given in table 2.1 [12].

	quark content	mass (MeV)	lifetime τ (ps)	decay length $c\tau$ (μm)
B^\pm	$u\bar{b}, \bar{u}b$	5279.17 ± 0.29	1.638 ± 0.011	491.1
B^0	$d\bar{b}$	5279.50 ± 0.30	1.525 ± 0.009	457.2
B_s^0	$s\bar{b}$	5366.3 ± 0.6	1.472 ± 0.026	441
B_c^\pm	$c\bar{b}, \bar{c}b$	6277 ± 6	0.453 ± 0.041	135.8
Λ_b^0	udb	5602.2 ± 1.6	1.391 ± 0.038	417

Table 2.1: Properties of B hadrons: quark content, mass, mean life time τ and decay length $c\tau$.

While b quarks are mainly produced through strong interaction at LHC, B hadrons usually decay weakly. The b decays into a c or an u quark, while the other constituents of the B hadron act as spectators. Information on the strength of the flavor changing weak decays is contained in the Cabibbo-Kobayashi-Maskawa (CKM) matrix. The charged current interactions couple to the up- and down-type quarks with couplings given by

$$V = \begin{pmatrix} V_{ud} & V_{us} & V_{ub} \\ V_{cd} & V_{cs} & V_{cb} \\ V_{td} & V_{ts} & V_{tb} \end{pmatrix} \quad (2.13)$$

The CKM matrix is unitary and it is parametrized by three mixing angles and a CP violating phase. The two elements relevant for b quark decays are $|V_{ub}| = (3.89 \pm 0.44) \cdot 10^{-3}$ and $|V_{cb}| = (40.6 \pm 1.3) \cdot 10^{-3}$ [12]. The relatively long life time of the B hadrons is explained by the fact that both CKM elements are small compared to other matrix elements. Since V_{cb} is more than a factor 10 larger than V_{ub} the b quark decays almost exclusively to a c quark ($b \rightarrow c + W^-$). Hadrons containing a c quark or a \bar{c} antiquark are called D hadrons.

2.2.7 Underlying Event

So far, parton-parton scattering with a large momentum transfer has been discussed. In hadron-hadron scatterings there can be additional hadronic activity that can not be attributed to the hadronization of partons involved in the hard scattering or to related initial

and final state radiation. This activity is called *underlying event*. It is attributed to the hadronization of partonic constituents that have undergone multiple parton interactions and to the interaction between the two beam remnants. The underlying event activity in proton-proton collisions at $\sqrt{s} = 7$ TeV has been measured and published by CMS [30].

2.3 Monte Carlo Event Generators

Monte Carlo (MC) event generators are software packages that numerically implement cross section calculations based on pQCD and produce events with fully hadronic final states. They have become an indispensable part of modern high energy physics experiments because they are used to translate theoretical predictions into observables that are comparable to experimental data. Their use is of vital importance in every phase from planning and designing an experiment to analyzing its data. Also for developing and tuning reconstruction software and for estimating selection efficiencies MC event generators are crucial.

Two types of MC event generators are distinguished: Fixed-order and all-order MCs [10]. The two categories have a different approach to approximate the cross section and the way they describe the event is also different.

The fixed-order MCs compute the matrix element exact at a fixed-order in perturbation theory. At tree level a set of phase space cuts is necessary to eliminate collinear and soft singularities. The squared matrix element is used as probability density function for parton configurations. There are MCs that produce events with weights (events produced in the allowed phase space and the weight assigned to an event is the matrix element squared) and others that produce unweighted events (event selection such that events are distributed in phase space as the matrix element squared). Matrix element calculations at higher orders is challenging because calculations become increasingly difficult, in particular for loop diagrams. Fixed-order MCs produce partonic final states. In order to produce hadronic final states the events are passed to an all-order MC for showering and hadronization.

All-order MCs impose the factorization of the perturbative and non-perturbative parts of an event. This allows the decomposition into four steps [31]. First a hard subprocess is generated according to the leading-order matrix element. Typically the user can specify a set of subprocesses to be included. The second step is called parton shower: an arbitrary number of branchings of one parton into two or more are combined to yield multijet events (with no explicit upper limit on the number of partons). The parton shower approximates logarithmic corrections to all orders in α_s . In hadronic collisions, the parton showering occurs both in the initial and in the final state. High-virtuality partons are evolved using the DGLAP equations down to a scale where perturbation theory is not valid anymore. Initial state partons are selected from the PDFs and follow a backward evolution to bring the virtuality back down to values compatible with confinement of partons in bound states (hadrons). In this backward evolution gluons and quarks are absorbed (looking in forward time direction they are emitted by quark radiation and gluon splitting). These quarks and gluons increase the final state multiplicity (they are present in the beam remnants). The parton shower

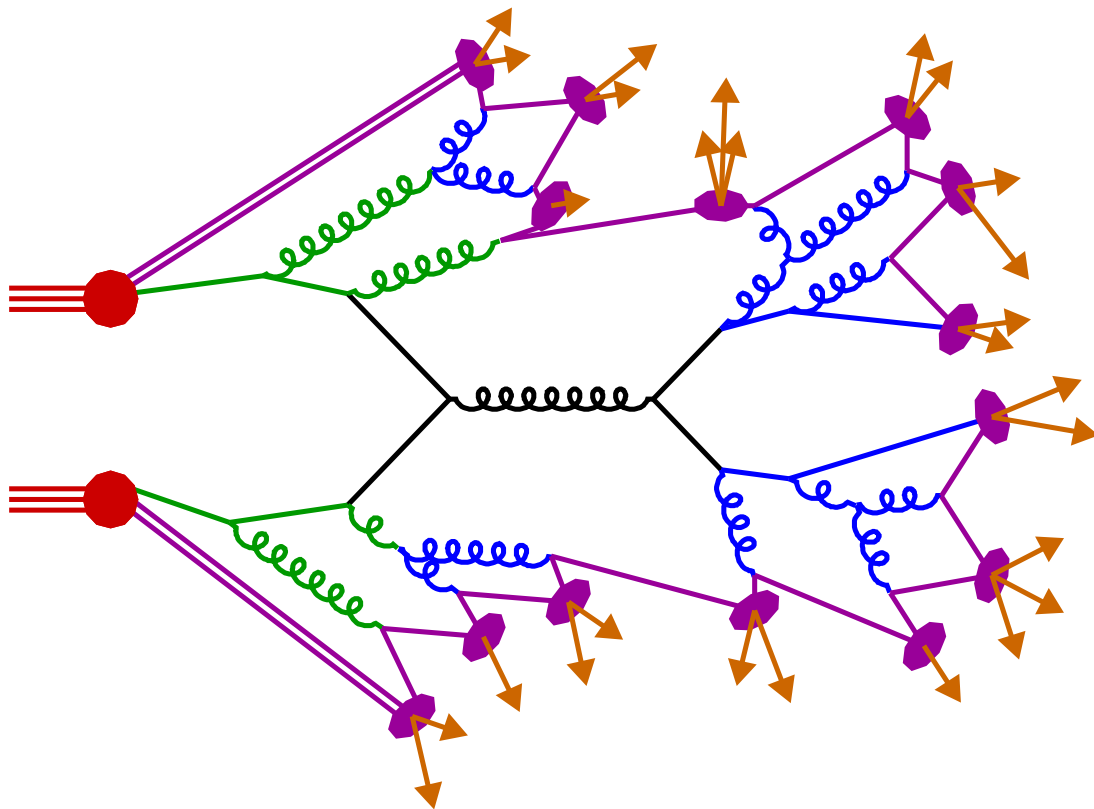


Figure 2.9: MC event generation in several steps: First the hard event scattering is calculated (black). Second there are initial (green) and final (blue) state parton showers. For modeling the hadron content PDFs are used (red). The cluster/string formation is drawn in purple. Finally the unstable hadrons are decayed into stable particles (brown).

model implemented in event generators is a leading-logarithmic (LL) approximation (with some next-to-leading-logarithmic corrections). It is accurate in the limit of soft and collinear emissions while it is a bad approximation for widely separated hard QCD jets. The third step is to use a hadronization model. This is the first non-perturbative step. For the soft underlying event models similar to the hadronization models are used. Finally the unstable primary hadrons are decayed using previously derived decay tables [12]. Figure 2.9 shows schematically the different steps of an all-order MC event generator.

In the analysis presented in this thesis the PYTHIA 6.422 [21], MC@NLO 3.4 [32–34], Herwig 6.510 [35], MadGraph/MadEvent 4 [36, 37] and CASCADE [38] MC programs are used for developing the event selection, optimizing the secondary vertex reconstruction tools and for comparison between theoretical predictions and data measured in the CMS experiment.

2.3.1 Pythia

PYTHIA is an all-order multipurpose event generator program. The matrix element for a $2 \rightarrow 2 + X$ process is computed at LO. PYTHIA contains about 300 hard processes with mostly one or two final state objects. Parton showers will then add more activity, i.e. more jets in the final state. For modeling the hadronization, PYTHIA includes the (independently developed) JETSET program which uses string fragmentation in form of the Lund model. For the longitudinal fragmentation function the Lund symmetric function is taken for light flavors, while the Peterson function, see equation (2.10), is taken for charm and beauty flavors (with parameters $\epsilon_c = 0.05$ and $\epsilon_b = 0.005$, determined from data). Different sets of PDFs are used to describe the quark and gluon content of protons. For the study presented in this thesis the CTEQ6L1 PDFs [39] are applied. For underlying event modeling a parameter set called tune D6T [40] is used. The b quark mass is set to $m_b = 4.8 \text{ GeV}$.

2.3.2 MadGraph/MadEvent

MadEvent is a multipurpose event generator based on MadGraph [41]. It provides the possibility to simulate $2 \rightarrow 2, 3$ subprocesses at tree-level, providing a hybrid solution between $2 \rightarrow 2$ at LO and the NLO simulations. MadGraph can identify all contributing diagrams for a user-defined process (given by specifying initial and final state particles), generate amplitudes and pass them to MadEvent. Unweighted parton-level events are produced in standard output format that are fed into an all-order MC program for showering and hadronization. In order to avoid double counting of emissions when combining matrix element generators with parton showering a matching scheme must be used. For the analysis presented here the showering is performed with PYTHIA and the " k_T -MLM" [42] jet matching scheme was used. As for PYTHIA the CTEQ6L1 PDFs are chosen [39], the mass of the b quark is set to $m_b = 4.75 \text{ GeV}$.

2.3.3 MC@NLO

MC@NLO is a MC event generator that matches NLO QCD massive matrix element calculations with the parton shower simulations as implemented in Herwig. For modeling the soft underlying event the external package JIMMY is used [43]. In MC@NLO a set of weighted

events is produced for a specified hard process (e.g. $h_1 h_2 \rightarrow b\bar{b} + X$, where h_1 and h_2 are the incoming hadrons). Some events can have negative weights. The event file is passed to Herwig for showering and hadronization. For the analysis in this thesis the CTEQ6M PDF set [39] and standard MC@NLO settings are used (with $m_b = 4.75$ GeV).

2.3.4 CASCADE

CASCADE is an event generator that is based on LO matrix elements using high-energy factorization [44], convoluted with unintegrated parton distributions. Unweighted, full hadron-level events are produced in three steps [38]: for the hard scattering off-shell matrix elements are used. The initial state radiation is generated according to a backward evolution approach using the CCFM equation. For final state radiation the parton shower routine of PYTHIA is used and for the hadronization the Lund string model is applied as in PYTHIA (JETSET). For the events produced for studying $b\bar{b}$ angular correlations the CCFM set A [45] of unintegrated PDFs were used. The processes included in the calculations are $g^*g^* \rightarrow b\bar{b}$ and $g^*q \rightarrow gq \rightarrow b\bar{b}X$ ¹. The matrix element for the first of those processes already includes a large fraction of the process $g^*g \rightarrow gg \rightarrow b\bar{b}X$ [44, 46]. Therefore, the last process is not included to avoid double counting.

2.3.5 Herwig

Herwig is an all-order general-purpose MC event generator. It uses the parton shower approximation for initial and final state radiation and a cluster model for hadronization. The cluster model is based on non-perturbative gluon splitting. For the underlying hadronic event a similar cluster model is used. Standalone Herwig has not been used in this thesis, but the events produced with MC@NLO have been passed to Herwig for showering and hadronization.

¹ g^* is an off-shell gluon.

Chapter 3

The LHC and the CMS Experiment

The European Organization for Nuclear Research (CERN) is the world's largest center for particle physics research. It is located near Geneva at the border between Switzerland and France. CERN was founded in 1954 and has 20 member states. In order to learn more about the basic constituents of matter, particles are accelerated to very high energies and brought to collision. The collisions are observed using different kinds of detectors.

From 1989 until 2000 the Large Electron-Positron Collider (LEP) was in operation. A 26.7 km long ring tunnel had been excavated for this circular collider. Detailed studies of the electroweak interaction were made at center-of-mass energies from 91 GeV up to 209 GeV. The masses of the W and Z bosons (which were discovered in 1983 at the *Super Proton Synchrotron* (SPS) collider at CERN) were precisely measured, and it was proven that exactly three light neutrino flavors exist.

Back in the early 1980s—years before LEP started operation—scientists first imagined re-using the LEP tunnel for a more powerful machine, colliding two beams of protons to reach highest possible collision energies. The project officially started in 1984 and the new machine was named Large Hadron Collider. Ten years later the CERN council approved the construction of the LHC and in 1996 the first two experiments, CMS and ATLAS were officially approved. Both of them aim to discover the elusive Higgs boson and help answering other open questions in high energy physics. In the following years two more experiments, ALICE and LHCb, were approved. After LEP stopped operation in the year 2000, it was dismantled, and the construction and assembling of the LHC and its experiments started.

In this chapter a short overview of the LHC and its experiments is given. Some design parameters of the LHC [47] are discussed and a short summary about the data taking at the LHC is given. The CMS detector with its sub-detectors suited for measuring energies and momenta of the particles produced in LHC collisions is described. The CMS trigger system is explained, and the chapter finishes with some explanation on computing in CMS.

3.1 Large Hadron Collider

The collider tunnel is located at a depth between 50 and 175 m under ground. Its diameter is 3 m and contains two pipes enclosed within thousands of superconducting magnets cooled by liquid helium ($T = 1.9$ K). The LHC injector chain is drawn in figure 3.1. The protons accelerated in the SPS are inserted into the main ring at an energy of 450 GeV and then accelerated to have an energy of up to 7 TeV. The design value of the center-of-mass energy is $\sqrt{s} = 14$ TeV. A proton needs about 90 μs to circle the collider once. The number of protons per bunch is up to $1.15 \cdot 10^{11}$ and the maximum number of bunches is 2808. The energy stored per beam is around 360 MJ. This corresponds to the kinetic energy of a 200 m long train with a speed of 155 km/h. Interactions between the two beams will take place at intervals of at least $t_{BC} = 25$ ns. One important parameter of a collider is the luminosity \mathcal{L} . It is approximately

$$\mathcal{L} = fn \frac{N_1 N_2}{A}, \quad (3.1)$$

where f is the revolution frequency, n the number of bunches, N_i the number of protons in bunch i and A the cross section given by $A = 4\pi\sigma_x\sigma_y$. The design value for the transverse beam size at the interaction point is $\sigma_x = \sigma_y = 16.7 \mu\text{m}$ for the LHC. The peak luminosity at the LHC will therefore be $1 \cdot 10^{34} \text{ cm}^{-2}\text{s}^{-1}$. The total proton-proton cross section is predicted to be about 100 mb^1 . Given the luminosity, the cross section and the bunch spacing, the maximum number of reactions per bunch crossing is estimated to be $\sigma\mathcal{L}t_{BC} \approx 25$.

There are different types of magnets used to deflect and squeeze the proton beams. To bring the proton beams on their circular orbit 1232 dipole magnets are used. Each has a length of 14.3 m and a maximum field of 8.33 Tesla. The bending radius is 2.8 km (total length of all magnets divided by 2π). The magnetic field in dipole magnets is approximately homogenous. Charged particles are bent because of the Lorentz force $\vec{F} = q(\vec{v} \times \vec{B})$, where q is the charge and \vec{v} the velocity of the particle and \vec{B} the magnetic field. In LHC magnets both beam pipes run through the same magnet modules. Since both pipes contain particles with the same charge sign, the fields have to point in opposite directions. The maximum proton energy or momentum (which is approximately the same because the proton mass $m_p \approx 1$ GeV is much smaller than the proton momentum, that is $\mathcal{O}(\text{TeV})$) is estimated using the magnet parameters given above. If \vec{v} is perpendicular to \vec{B} and v and B are absolute values, the centripetal force ($F = mv^2/R$) is used to find an equation for the momentum p of the particle,

$$\begin{aligned} qvB = \frac{mv^2}{R} &\Rightarrow p = mv = qRB \\ &\Rightarrow p \text{ (in GeV/c)} \approx 0.3 \cdot B \text{ (in Tesla)} \cdot R \text{ (in meter)} \approx E_p, \end{aligned} \quad (3.2)$$

where in the last equation the charge of one proton is inserted for q . Using the bending radius and the field given above the maximum proton energy is indeed computed to be around 7 TeV.

¹One barn (1 b) is equal to 10^{-24} cm^2 .

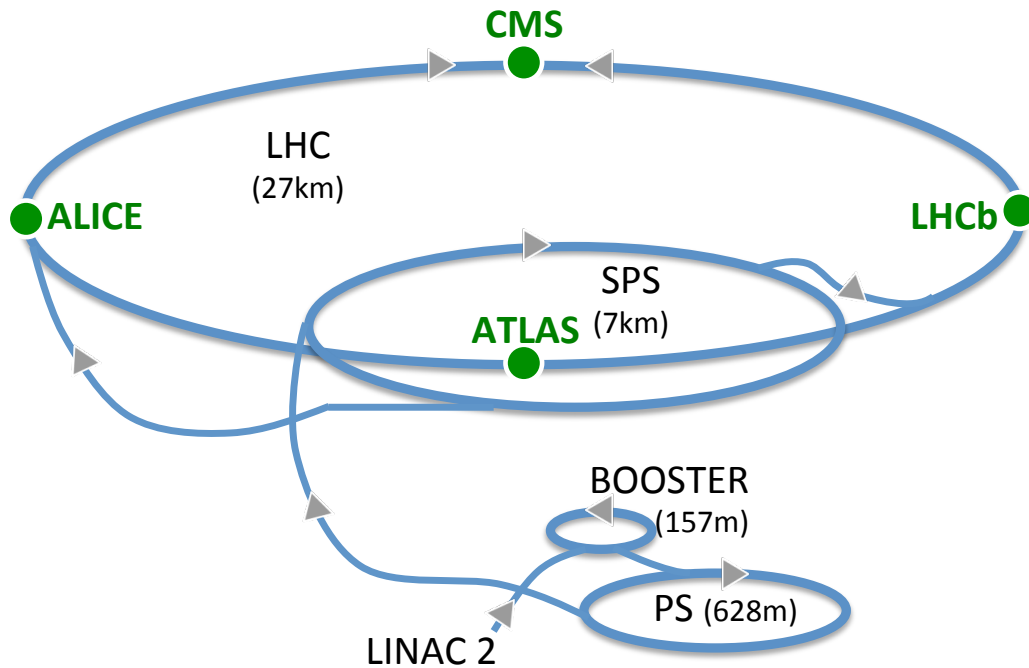


Figure 3.1: LHC injector chain: Linac 2 - Proton Synchrotron Booster (1.4 GeV) - Proton Synchrotron (PS, 25 GeV) - Super Proton Synchrotron (SPS, 450 GeV) - LHC (7 TeV). The distances given in the diagram are the circumferences of the circular accelerators. In this legend the center-of-mass energies of the different injectors are indicated in brackets.

Different multipole magnets are used to squeeze the beam. Series of quadrupole magnets focus the beam in the transverse plane and sextupole magnets are focussing in flight direction. There are also octupole and decapole magnets for further squeezing and dealing with higher modes.

To accelerate the protons, eight superconducting radio frequency (RF) cavities are installed per beam. RF cavities use a standing wave, whose frequency is set such that the particle bunches are accelerated when passing the cavities. Each of the RF cavities is capable of delivering an accelerating field of 5 MV/m at a frequency of 400 MHz. The LHC radio frequency has to be a multiple of the operating frequency of the SPS (200 MHz), to allow rapid transfer of proton bunches. The cavities are operated at a temperature of 4.5 K.

LHC can also be used to collide heavy ions (for example lead ${}^{208}_{82}\text{Pb}$) with a collision energy of 1.150 PeV (the collision energy per nucleon is 2.759 TeV) and a peak luminosity of $1 \cdot 10^{27} \text{ cm}^{-2}\text{s}^{-1}$. The plan is to have up to 592 bunches with $7 \cdot 10^7$ ions.

The two beams collide in four points, where the main experiments are located:

- **ALICE** (A Large Ion Collider Experiment [48]): This heavy-ion detector will exploit the unique physics potential of nucleus-nucleus interactions at high-energy densities, where the formation of a new phase of matter, the quark-gluon plasma, is expected. This plasma probably existed just after the Big Bang, when the universe was still extremely hot and quarks were free and not bound with gluons. The detector is built asymmetrically with a central barrel and a single arm forward muon spectrometer. It is located in St. Genis-Pouilly (France), has a weight of 10000 t and is 26 m long, 16 m high and 16 m wide.
- **ATLAS** (A large Toroidal LHC ApparatuS [49, 50]): This experiment is designed to observe phenomena that involve highly massive particles which were not observable using earlier lower-energy accelerators and might shed light on new theories of particle physics beyond the SM. ATLAS is composed of six sub-detector systems to measure momentum and energy of particles. In order to measure the momentum of muons, a huge magnet system is bending their paths. ATLAS is the largest volume particle detector ever built, it weights 7000 t and it is 46 m long, 25 m high and 25 m wide. The experiment is located in Meyrin (Switzerland) where a huge underground cavern had to be excavated.
- **CMS** (Compact Muon Solenoid [51–53]): The goals of this experiment are the same ones as those of the ATLAS experiment: exploring physics at the TeV scale, discovering the Higgs boson and looking for evidence of physics beyond the Standard Model (supersymmetry, extra dimensions, dark matter). The CMS detector is built around a huge solenoid magnet, generating a magnetic field of up to 3.8 T. The field is confined by a heavy steel yoke. The CMS detector was built on the surface and lowered into the cavern in Cessy (France) in 15 sections. The detector dimensions are 22 m \times 15 m \times 15 m and its weight is 12500 t. The detector is symmetric and it consists of a barrel and two endcaps. It will be described in more detail later in section 3.2.
- **LHCb** (Large Hadron Collider beauty [54]): This is a b physics experiment, particularly aimed at measuring the parameters of CP violation in the interactions of B hadrons. Finding the reason for CP violation helps understanding why we live in an Universe composed of matter, but no antimatter. LHCb is built asymmetrically and consists of a series of sub-detectors that measure momentum and energy of particles in the forward direction. To tag b quarks, LHCb has developed a sophisticated system of movable tracking detectors close to the proton beam. The experiment is 21 m long, 10 m high and 13 m wide and its weight is 5600 t. It is located in Ferney-Voltaire (France).

After a long phase of planning and preparation, the world's most powerful particle accelerator started operation in 2008. On September 10, the first beam was circulated in the ring. Unfortunately, there was an incident, caused by a faulty electrical connection between two magnets that lead to a helium leak in one of the LHC sectors. This incident resulted in a one year long period needed for repairs and magnet tests. On November 23 2009, the first collisions with center-of-mass energy of 900 GeV were recorded. After that, the beam energy has been increased and on March 30 2010 two beams with a center-of-mass energy of 7 TeV have been colliding for the first time. Since then a large statistic sample of collision data at

$\sqrt{s} = 7$ TeV has been recorded and analyzed by the experiments. The number of protons per bunch and the number of bunches (and therefore the luminosity) has been increased steadily. After a technical stop in winter 2010, the machine has been successfully restarted to take data at even higher luminosities in 2011.

The historical development of colliders with increasing center-of-mass energies is shown in figure 3.2 (*Livingston plot*). It is found that the dependence of the center-of-mass energies on the starting year was close to a straight line in the logarithmic plot. For new machines as the LHC there is kind of a saturation effect. Currently there is one other powerful hadron collider in operation, the Tevatron accelerator at Fermilab (Batavia, Illinois), where collisions between protons and antiprotons at a center-of-mass energy of 1.96 TeV are studied. The Tevatron luminosity is $3 \cdot 10^{32} \text{cm}^{-2} \text{s}^{-1}$ (a factor of 30 smaller than the LHC design luminosity). At the Tevatron the top quark has been discovered in 1995 by the CDF and D0 collaborations [55,56]. In September 2011 the Tevatron will be shut down.

3.2 Compact Muon Solenoid Detector

Approximately 3000 scientists and engineers from 183 institutes in 38 countries form the CMS collaboration (June 2008). The CMS experiment is located in an underground cavern at Cessy in France, but the different parts of the detector have been built all over the world. They have been shipped to CERN, lowered into the cavern 100 m underground and assembled. The CMS detector is cylindrical, 21.6 m long and 15 m diameter and weigh approximately 12500 tonnes. Figure 3.3 gives an overview of the CMS detector. The name *Compact Muon Solenoid* stresses three main features of the detector: its relatively small size (compared e.g. to ATLAS), its powerful solenoid magnet giving a 3.8 T strong magnetic field, and its muon chambers, which make the detector optimal for muon tracking. Leptons will play an important role in many of the new physics searches at the LHC energy scale. Vector bosons can decay into pairs of leptons or quarks. Since there is an enormous background due to QCD processes (strong interaction), the leptonic decay channels are experimentally favored and thus, ability for accurate lepton detection will be important for all LHC experiments.

CMS was ready to record LHC collision data from the very beginning. In figure 3.4 one of the first $\sqrt{s} = 7$ TeV collision events is shown. It was recorded by CMS on March 30 2010.

Many of the interesting events produced at LHC will contain leptons in the final state. Having good muon and electron detectors allows to study the same process in different channels. The capability of detecting muons and measuring charge and momentum for muons with very low transverse momentum and for TeV muons is challenging. In addition the muon system must provide fast information for triggering purposes.

Multiple W and Z boson production is possible at the LHC up to high energies. The discovery of the postulated Higgs boson is a primary goal of the CMS detector. If the Higgs boson is heavy enough, it can decay into ZZ or WW and events with four charged or two charged and two neutral leptons comprise golden signatures of the Higgs particle. For a low mass

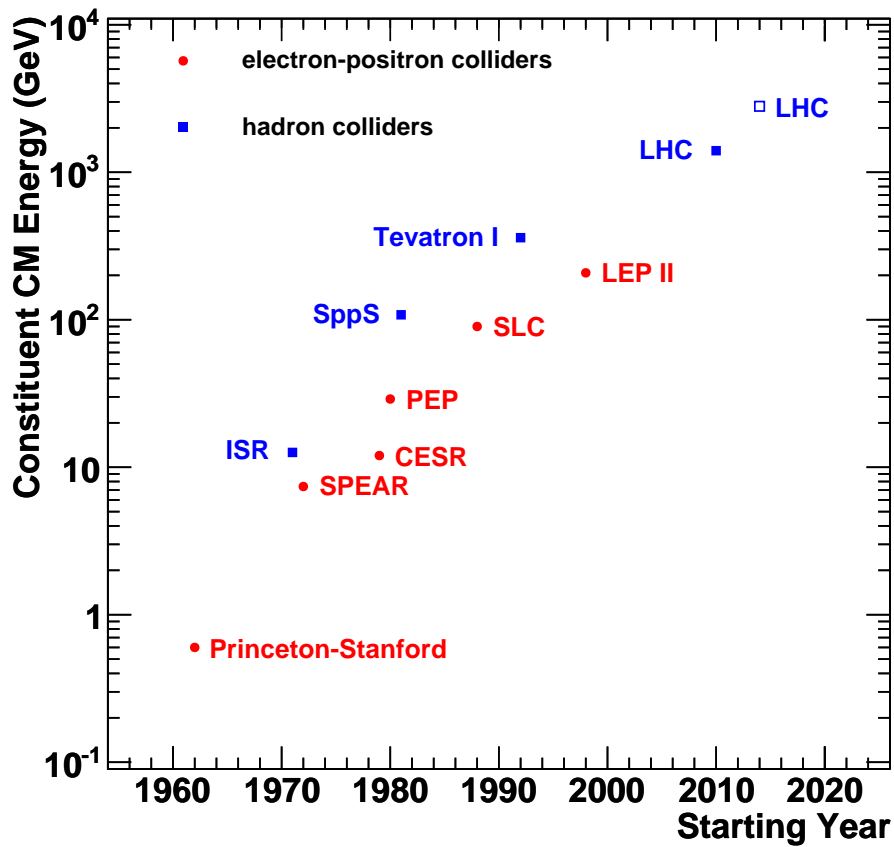


Figure 3.2: Available center-of-mass energies of accelerator facilities as function of the starting year. For hadron colliders the available center-of-mass energy has been divided by a factor of 5 to approximate the effect of hadrons not being fundamental particles. For the LHC there is one entry for the run at 7 TeV that started 2010 and one for 14 TeV that is planned to start in 2014.

Higgs boson in the range between 115 and 130 GeV, the decay $H \rightarrow \gamma\gamma$ is the most promising discovery channel. A good energy resolution of the electromagnetic calorimeter is crucial for Higgs searches in this channel.

Before giving more details about how the CMS detector is supposed to measure energy and momentum of photons, electrons, muons and other particles, the CMS coordinate system is introduced in section 3.3 and a short description of a *generic detector* is given in section 3.4, where generic means a modern (multi-purpose) particle physics detector such as ATLAS or CMS, suited for LHC. This will make it easier to point out special properties when describing the CMS sub-detectors in more detail.

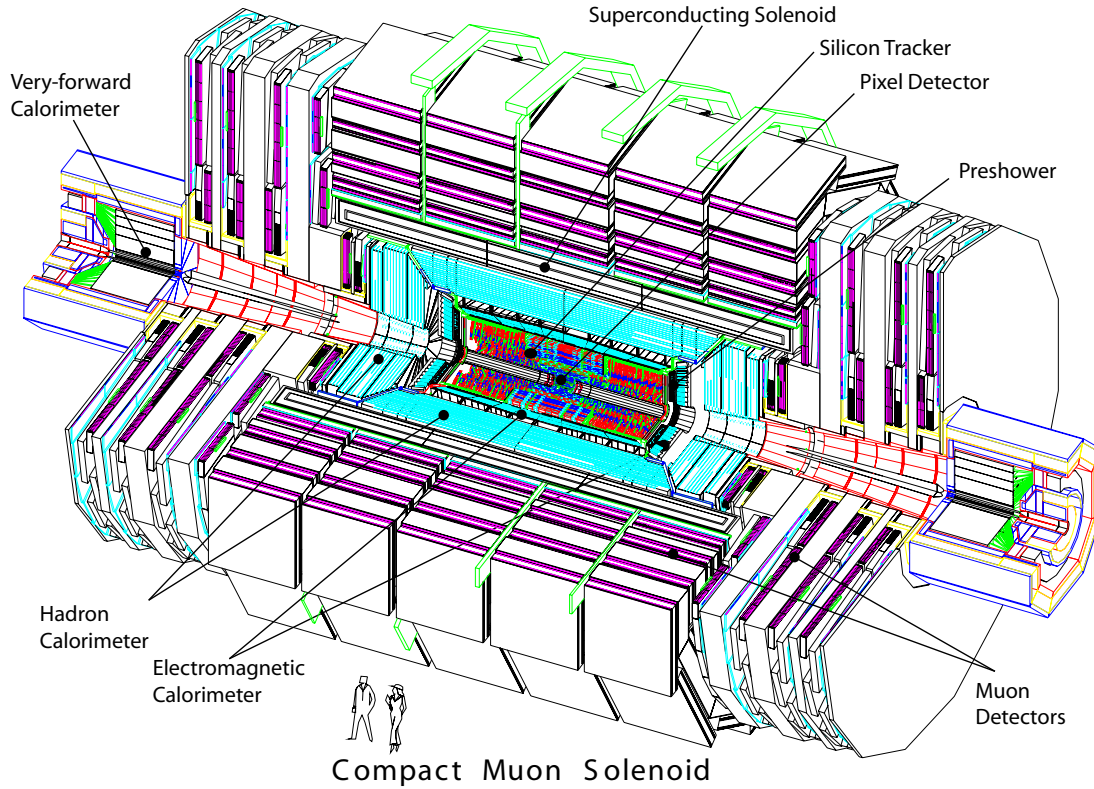


Figure 3.3: Schematic view of the CMS detector [51].

3.3 Geometry / Coordinate System

The CMS detector is located in the north of the LHC ring center. The coordinate system is as follows: The origin is the collision point. The x axis is pointing south towards the LHC center. The y axis is pointing upwards and the z axis is along the beam direction such that the coordinate system is a right-handed system (i.e. the z axis is pointing west). Spherical coordinates (r, ϕ, θ) are advantageous. The polar angle θ is measured with respect to the z axis ($\theta = 0$ is the $+z$ direction and $\theta = \pi$ is the $-z$ axis). The azimuthal angle ϕ is measured in the xy plane such that $\phi = 0$ is the $+x$ direction, $\phi = \pi/2$ is the $+y$ axis and $-\pi < \phi < \pi$. In some CMS event displays cylindrical coordinates (ρ, ϕ, z) are used.

The pseudorapidity $\eta = -\ln(\tan(\frac{\theta}{2}))$ is defined such that the sign is the same as the sign of the z coordinate. The rapidity y of a particle is defined as $y = \frac{1}{2} \ln \frac{E+p}{E-p}$. For measuring angles between two points the difference in azimuthal angle $\Delta\phi = \phi_2 - \phi_1$, the difference in pseudorapidity $\Delta\eta = \eta_2 - \eta_1$ and also the combined angle $\Delta R = \sqrt{(\Delta\eta)^2 + (\Delta\phi)^2}$ are used.

The magnetic field is pointing in $+z$ direction. The momentum transverse to the beam direction (*transverse momentum*) is given by $p_T = \sqrt{p_x^2 + p_y^2}$. *Missing transverse momentum*

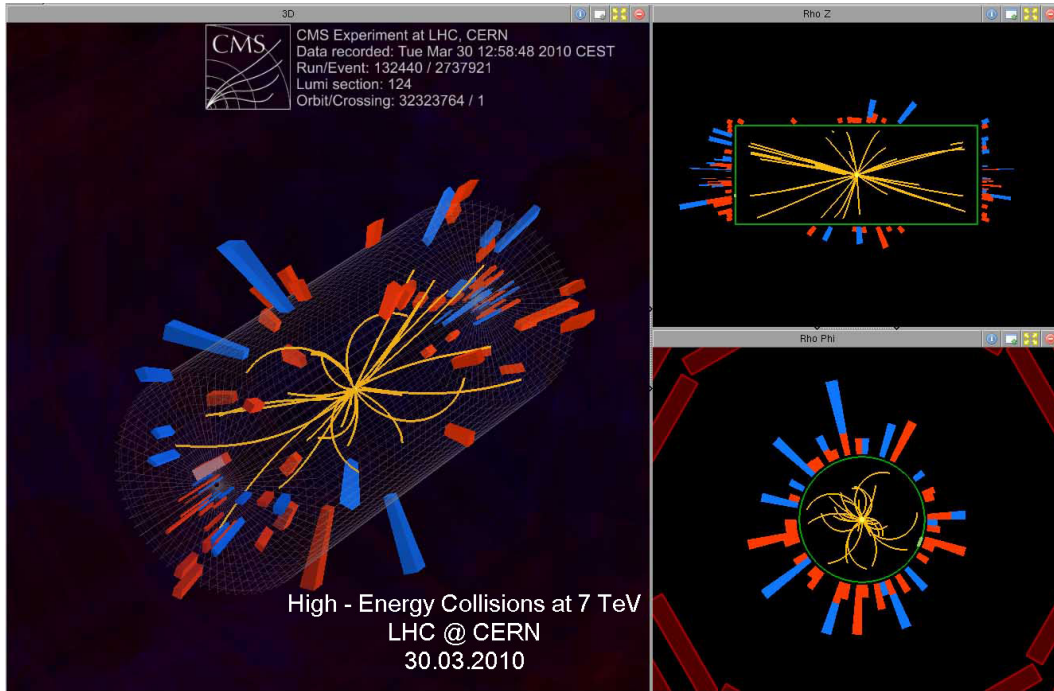


Figure 3.4: One of the first collisions at $\sqrt{s} = 7$ TeV recorded with the CMS detector. Shown are the 3D view (left), the ρz view (top right) and the $\rho\phi$ view (bottom right) of the same event. The orange lines correspond to tracks measured in the tracking devices and the red (blue) bars are energy deposits in the electromagnetic (hadronic) calorimeter.

is a sign for particles which escape the detector without leaving a trace (e.g. neutrinos or hypothetical weakly interacting particles). The missing transverse momentum is defined as the apparent imbalance of the component of the total momentum in the plane perpendicular to the beam direction. Its magnitude is referred to as *missing transverse energy* (MET).

3.4 A Generic LHC Detector

The high luminosity at the LHC requires radiation hard, finely segmented and fast detectors. The detector will have to deal with pile up of up to 25 events per bunch crossing. It is estimated that a detector needs to cover the rapidity range $|y| < 5$ (in order to detect most of the produced particles) [57]. Since decay products of heavy particles are in general produced at low rapidity the main focus of the detectors will be in the central region (rapidity range $|y| < 2.5$). Around 2250 pions with an average transverse momentum of about 0.8 GeV cross the detector per bunch crossing [57].

In order to allow for a full reconstruction of an event, all SM particles need to be identified and the detector should thus be as hermetic as possible. Quarks produced in hard interactions will hadronize and the result will be *jets* of hadrons that need to be detected. Hadrons containing heavy quarks (b, c) are relatively long living, and they are detected by recon-

structing their decay *vertices*. Photons and electrons passing through material will produce electromagnetic *showers*. Muons are detected through the *ionization* of material they pass. Neutrinos do only weakly interact with other particles and therefore most neutrinos leave the detector without interaction. For hermetic detectors neutrinos are detected through *missing transverse momentum* or *energy* (because the initial state contains almost no transverse momentum).

Because of the protons coming from both sides, a cylindrical detector shape consisting of a *barrel* and two *endcap* detectors is favored. In order to measure different properties of particles (e.g. momentum, charge, energy) detectors are in general built of several subsystems that are arranged in layers around the beam pipe. The innermost layer is usually dedicated to vertex reconstruction. Around this vertexing layer a tracking subsystem is arranged to measure the charge, position and momentum of all charged particles. A solenoid is needed to provide a magnetic field to bend particle trajectories for measuring their momenta. The energy of the produced particles is measured in calorimeters. They are located outside the tracking detectors, because the particles are absorbed in the calorimeters. There are usually two types, an electromagnetic calorimeter (ECAL) that measures energy of electrons and photons, and a hadronic calorimeter (HCAL) to measure energy of hadrons. Since electron and photon absorption needs much less space than hadron absorption the ECAL is in most detectors located closer to the beam pipe. For muons the rate of interaction with matter is significantly lower than for other particles. Specialized muon systems are located outside the calorimeters.

Vertex System: The lifetimes of particles containing b and c quarks are $(c\tau)_b \approx 475 \mu\text{m}$ and $(c\tau)_c \approx (123, 312) \mu\text{m}$ (D^0, D^\pm). In order to reconstruct decay vertices of B and D hadrons, the vertex system must be located close to the beam pipe, where the number of particles per unit area is large and radiation damage is a problem. Both, CMS and ATLAS comprise a silicon pixel detector. Silicon detectors work by doping small silicon regions (strips or pixels) to turn them into diodes. The diodes are reverse biased leading to an electric field in the depletion zone. Charged particles passing the silicon cause ionization currents, which are measured to obtain information on particles crossing the detector. The resolution needed to reconstruct secondary vertices, the distance of the pixels to the beam pipe and the space needed for the readout electronics determine the size of the pixels. When reading out not only the position of a charge deposit, but also the amount of charge deposited, the spatial resolution can be increased by comparing charge deposits in neighboring pixels. The pixel system is also used to find track patterns.

Tracker: Charged particles leave tracks in a detector because of excitation and ionization of the detector material. The information is used to identify the particle and measure its position, direction and momentum. Different types of tracking detectors exist, e.g. multi-wire or drift chambers [58], and silicon detectors. In gaseous tracking detectors with a drift velocity of about $5 \text{ cm}/\mu\text{s}$ particles travel only 0.12 cm during one bunch crossing (25 ns). These detectors are therefore likely to integrate over several bunch crossings, which makes tracking very difficult. Both, ATLAS and CMS have chosen silicon strip detectors. The outer tracker of ATLAS is a combined straw tracker and transition radiation detector [49]. The

resolution of silicon tracking detectors depends on the strip size, the number of tracking layers, the magnetic field and the choice of digital or analog readout. At lower momentum scale, scattering in the tracker material also decreases the measurement accuracy. The amount of material used in the tracker should be minimized in order to decrease the effect of multiple scattering. Since the particle is bent in the azimuthal plane the measurement of the z coordinate is less demanding and the strips are oriented along (or close to) the beam direction. The occupancy in the tracker increases due to loopers, particles that have low transverse momentum. Because of the strong magnetic field they are bent on loops and make multiple hits in each tracker layer. About every second charged particle produced in inelastic scattering has a momentum below 0.8 GeV and does therefore never reach the calorimeters [57].

ECAL: Calorimeters initiate interactions of the incoming particles and absorb the resulting energy. The interactions result in geometrically growing showers of particles. The particles are absorbed while measuring their energy. At high energies, incoming photons interact with the calorimeter primarily via pair production ($\gamma \rightarrow e^+e^-$). Incoming electrons or positrons tend to emit photons (bremsstrahlung). These two processes continue until the remaining particles have lower energy. Electrons and positrons at lower energies then lose energy via scattering and finally are absorbed by atoms. The shower depth X is calculate to be

$$X = X_0 \frac{\ln(E_0/E_c)}{\ln 2}, \quad (3.3)$$

where E_0 is the energy of the incoming particle, X_0 is the radiation length (depends on the material used) and E_c is the critical energy (which is the energy at which probability for bremsstrahlung becomes comparable to the probability for scattering or ionization). The characteristic radius of the shower is called Molière radius. It is the radius of a cone containing 90% of the shower energy. The size of a detector unit is chosen such that it is comparable to the Molière radius. The energy deposit dE/dt in the calorimeter material as a function of depth rises steeply at small depth due to geometric shower growth. Since the remaining energy is shared among more and more particles the particle energies decrease, particles are absorbed and dE/dt decreases. It is found that the shower is fully contained in a depth of about $20 X_0$ [57]. The number of showering particles is up to about 100.

Electrons are produced e.g. in the decay of the Z and W bosons. The ECAL energy resolution should be good enough to not increase the natural width of the Z resonance and therefore be smaller than 1.2% [57]. Poor resolution can come from non-uniformity of the medium used in the ECAL, and from a stochastic contribution ($dE/E \propto \sqrt{E_c/E}$). Hadrons do not lose much energy in the ECAL, and the transverse size of hadron showers is much wider than for electrons and photons. Particle identification is improved when reading out segments of different depths independently. Resolving showers from two photons from a high-energy pion decay is challenging. To better reject pions, detectors with finer segmentation are needed. They need to be located earlier in the shower and are called preshower detectors.

HCAL: In the HCAL, the energies of strongly interacting quarks and gluons are measured by absorbing the jets of hadrons produced. Charged hadrons produce partially electromagnetic showers. But hadrons do also interact strongly with a nucleus to produce several lower-energy

hadrons (mostly pions). This continues until all particles are stopped and absorbed in the material. The shower is parametrized using a nuclear interaction length λ_0 , which is in general much longer than the radiation length X_0 . A resolution at the order of the natural width of the W boson decaying into quarks is not attainable. Asking 99% shower containment requires a total depth of $10\lambda_0$ [57]. The tower size can again be set to be similar to the transverse shower size, which is at the order of λ_0 . For the HCAL it is very important to be hermetic (in rapidity range $|y| < 5$). A large amount of missing transverse energy (MET) is then a sign of a neutrino that escaped undetected, and the MET provides a measurement of the neutrino transverse energy. Missing energy forms also a crucial signature of new particles. The dose for the forward calorimeter is large and it needs to be built in some distance to the interaction point.

Solenoid magnet: The tracker needs to be located in a strong magnetic field, which is uniform in beam direction. The position of the solenoid is outside the tracking detector (ATLAS) or outside the calorimeters (CMS).

Muon system: Since muons are charged particles with a long lifetime of $2.2\ \mu\text{s}$, their momenta and positions are first measured in the tracking system. While (almost) all other particles are absorbed in the calorimeters, muons leave only ionization energy in ECAL and HCAL and are (ideally) the only particles apart from neutrinos escaping the calorimeters and entering the muon detectors. The muon parameters are measured combining both tracker and muon detector information. Measuring muons from vector boson decays with high accuracy is fundamental for LHC experiments, because the lepton channels for many heavy objects are clean and have low backgrounds. Other sources of muons are pion/kaon and heavy flavor decays. Muons from pions and kaons can be recognized by the kink in the track (at the decay point of the hadron). The rate of muons from heavy quark decays is (at LHC design luminosity) around 0.6 MHz [57], which is too large with respect to acceptable trigger rates. Providing a trigger to reduce the rate of muons coming from heavy flavor decays, while keeping muons from vector boson decays, is a key requirement of the muon system. One other key requirement on the muon system is to provide a good measurement of the muon momentum up to high muon energies. For high momentum muons, bremsstrahlung and pair production become comparable to ionization. Measuring the muon trajectory will then be more demanding. One way to obtain a good trajectory measurement is to perform several measurements and to isolate the different measurements by interposing material. Another way is to operate in a large magnetic field that will separate the low energy showering particles from the muons. Different types of detectors can be used for muon identification and measuring muon parameters, e.g. drift tubes, cathode strip chambers and scintillation counters. Gas detectors (drift tubes, cathode strip chambers) are most commonly used for muon tracking and a nice description can be found in [58]. Scintillation counters are used before/after absorber material for muon identification or triggering. They are, compared to other muon detectors, faster and less sensitive to backgrounds, but more expensive to be built. Different choices are made for the muon systems of ATLAS and CMS.

3.5 The CMS Tracker

For particle identification and the reconstruction of secondary vertices from heavy quark or τ lepton decays an excellent tracking system with an impact parameter resolution on the order of $100\ \mu\text{m}$ is needed (the impact parameter is the perpendicular distance between the track and the interaction point). The CMS tracking system [59,60] is designed to reconstruct particles with high momentum resolution and efficiency of more than 98 % for $|\eta| < 2.5$.

The CMS collaboration decided to use an all-silicon solution for the tracker. There are silicon pixels in the high, and silicon microstrips in the medium and low occupancy regions. The tracker is divided in two sub-detectors, a silicon pixel detector and a silicon microstrips detector.

3.5.1 Pixel Detector

The impact parameter resolution is mainly determined by the resolution of the innermost detector layers. When the LHC runs at full luminosity detectors close to the beam pipe will be traversed by order of 100 million particles per cm^2 and per second. In order to have good impact parameter resolution and to keep the occupancy at a manageable level, a silicon pixel detector is chosen as vertex detector. Because of its importance for tracking and vertexing and hence for the study presented herein, the pixel detector is described in more detail than the other sub-detectors.

Pixel geometry

Many arguments have to be considered when designing the pixel in terms of size and shape. The optimal pixel size is estimated considering the Lorentz drift. The pixel detector is operating in a strong magnetic field, therefore the Lorentz force acts on electrons (and holes) produced in the silicon. They will not drift along the electric field lines and this leads to a spread of the charge distribution, see figure 3.5. If pixels are small enough, the charge will be shared among several pixels. The analog pulse height information can then be used to compute the center-of-gravity of the charge and to improve the spatial resolution. The sensors are read out on the n side. This choice is motivated by the large Lorentz angle of 32° for electrons in the 4 T magnetic field, which leads to a Lorentz drift of almost $200\ \mu\text{m}$ for a $300\ \mu\text{m}$ thick sensor. The pixel size was chosen to be $100\ \mu\text{m}$ in the $\rho\phi$ plane. Since for a detector built to reconstruct secondary decay vertices both coordinates are important, a square shape of the pixels seems to be adequate. The minimum pixel area needed for readout circuitry was believed to be roughly $0.015\ \text{mm}^2$, hence the pixel size along the z direction was set to be $150\ \mu\text{m}$.

Detector layout

The CMS pixel detector consists of a cylindrical central detector with three barrel layers at radii 4.4 cm, 7.3 cm and 10.2 cm from the beamline. The total length of the barrel is 53.3 cm ($z = \pm 266.6\ \text{mm}$), so the innermost layer covers the pseudorapidity range up to $|\eta| = 2.5$, while the second (third) layer covers only $|\eta| < 2.0$ ($|\eta| < 1.7$). To cover the whole rapidity range $|\eta| \leq 2.5$ with all layers the barrel would need to be up to 125 cm long. Such a long

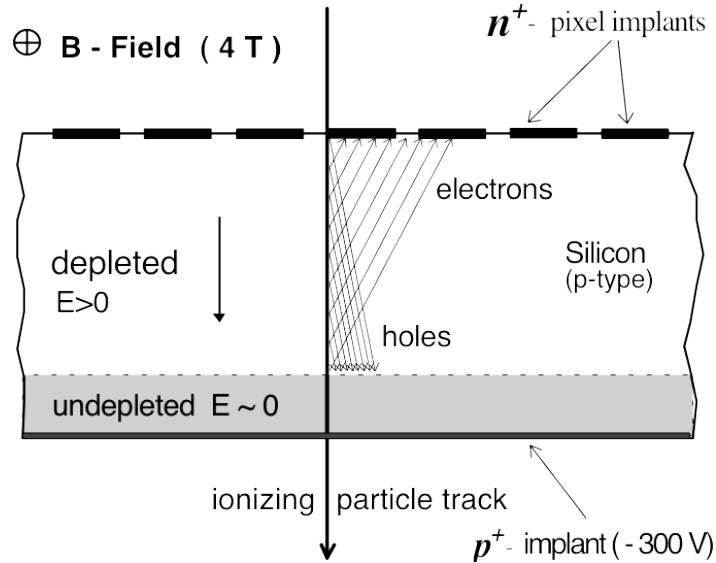


Figure 3.5: The Lorentz drift caused by the magnetic field leads to charge sharing among several pixels [59]: Because of the silicon diodes being reverse biased there is an electric field in the depletion zone perpendicular to the pixel surface. Electrons and holes produced by charged particles passing the detector are deflected by the magnetic field, and the charge is shared among several pixels.

barrel is disfavored because the tracks would leave long clusters due to small incoming angle in the high rapidity range. Instead there are two forward detectors (one at either end of the barrel), each containing two disks. The endcap disks cover radii from 6 cm to 15 cm. Their position is at $z = \pm 34.5$ cm and ± 46.5 cm. Using endcap disks instead of a long barrel leads to the same coverage $|\eta| < 2.5$ using less detector material. One disadvantage is that the material of the bulkhead of the barrel lies within the tracker volume. A schematic view of the detector is shown in figure 3.6 and the layout and η coverage in figure 3.7.

Radiation hardness

Since the pixel detector is very close to the beam pipe, radiation hardness is a crucial prerequisite. For the LHC running at full luminosity, the lifetimes of the three layers are estimated to be 2, 5 and 10 years (see [57], chapter 2). This means that the second layer would need to be replaced at least once in a 10 year running period of the LHC and the innermost layer every two years. Initially the plan was to use the two inner layers for low luminosity phase of LHC, and then remove the damaged innermost layer and insert the third layer for the high luminosity phase. This plan was abandoned and the full three layer detector was installed in 2008.

Modules

The three layers of the central pixel detector are made up of rectangular modular units. They are arranged to form ladders. A ladder consists of 8 modules. The gap between two modules is 0.4 mm. The four endcap disks consist of 24 blades arranged in a turbine geometry. The blades are rotated by 20° away from the $r\phi$ plane. The reason for this rotation is to introduce

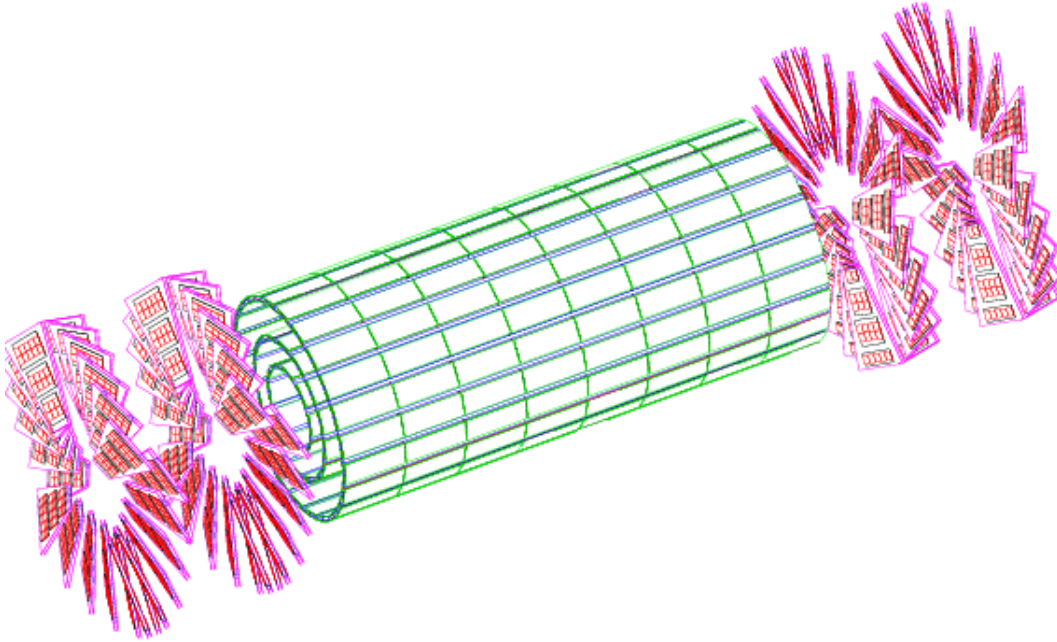


Figure 3.6: Schematic view of the CMS pixel detector: Three barrel layers (at 4.4 cm, 7.3 cm and 10.2 cm) and two endcap disks (covering radii from 6 to 15 cm) [51].

an angle between electric and magnetic field and do allow for a Lorentz drift. An overview of the barrel and endcap detectors is shown in table 3.1.

Detector	Layers/ Disks	Ladders/ Blades	Modules	Chips	Pixels (10^6)	Area (m^2)
Barrel	3	96	768	11520	48	0.78
Endcap	4	96	672	4320	18	0.14
Total			1440	15840	66	0.92

Table 3.1: Overview of the numbers of modules, chips and pixels in the three different pixel barrel layers and in the four endcap disks.

In total there are about 66 million pixels. A full readout of all channels in all bunch crossings is impossible, only a small number of bunch crossings with interesting hard events will be read out. The CMS trigger latency is $3.2 \mu s$. During this time all hit information must be stored.

The design of a barrel module is shown in figure 3.8. A full module consists of a thin, segmented sensor with 16 highly integrated readout chips (ROCs) connected to them using the bump bonding technique. The sensor is $285 \mu m$ thick, 66.6 mm long, 18.6 mm wide and it consists of n-on-n devices. Endcap blades have 7 sensors with between 2 and 10 readout chips. They are placed on both sides of the blade.

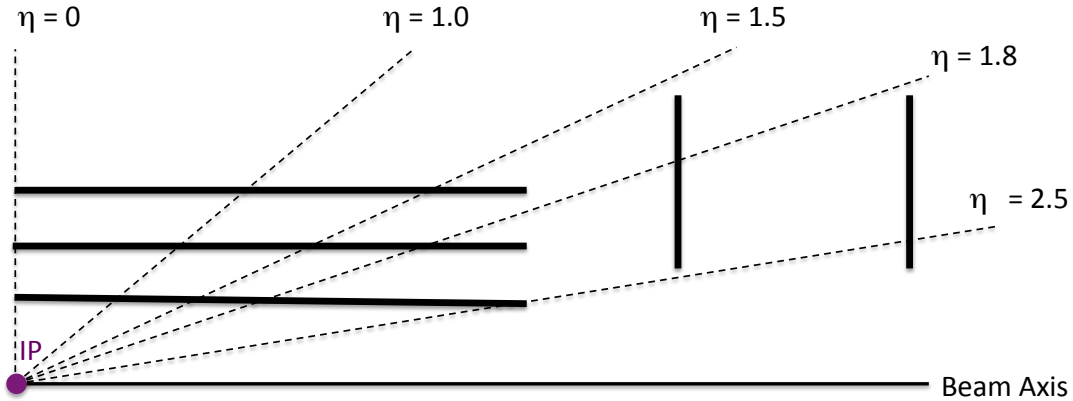


Figure 3.7: Pixel detector layout: Straight lines coming from the interaction point (IP) cross at least two layers and/or disks in the full pseudorapidity range $|\eta| < 2.5$.

The ROC (IBM-PSI46) consists of 52 times 80 pixels. The power consumption of a pixel is about $28 \mu\text{W}$. Each sensor pixel is connected via a solder bump to a pixel unit on the ROC (see figure 3.9). For barrel modules the ROCs are glued on $250 \mu\text{m}$ Si-Nitride basestrips. The baseplate is 65 mm long and 26 mm wide. The High Density Interconnect (HDI) Board (flexible, low mass PCB), is glued on the sensor and wirebonded to the ROCs. A readout controller chip, the Token Bit Manager (TBM) is glued and wirebonded on top of the HDI. The power cable is soldered to the HDI. To connect the module and the endprint a kapton cable is glued and wirebonded to the HDI. The weight of a module is approximately 2.2 g and the cables weigh about 1.3 g. The power consumption of a full barrel module is about 2 W.

Pixel chip

The CMS pixel chip main tasks are to register signals of particles crossing the detector, store the signals (time, position, charge), wait for trigger information and send out data for bunch crossings selected by the trigger. It is organized in 26 double columns of 80 pixels ($52 \cdot 80 = 4160$ pixels per chip). There are 12 8-bit time stamp buffers and 32 data buffers at the periphery of each double column. Both buffers are circular.

A sensor pixel is connected via solder bump to each pixel unit on the ROC. Hit data are stored in the edge of the chip to wait for trigger information. Each chip has four counters: a bunch crossing counter (8 bits), a bunch crossing counter with trigger delay (8 bits, delay selectable), a trigger counter (4 bits) and a token counter (4 bits). The contents of those counters are available in each double column periphery.

If the charge in at least one pixel of a double column exceeds a programmable threshold, the pixel addresses and analog signals of all hit pixels in this double column are stored in the data buffer (autonomously and asynchronously in each double column). The hits are validated by an external level 1 trigger and hits that are not triggered are cleared. The TBM controls the

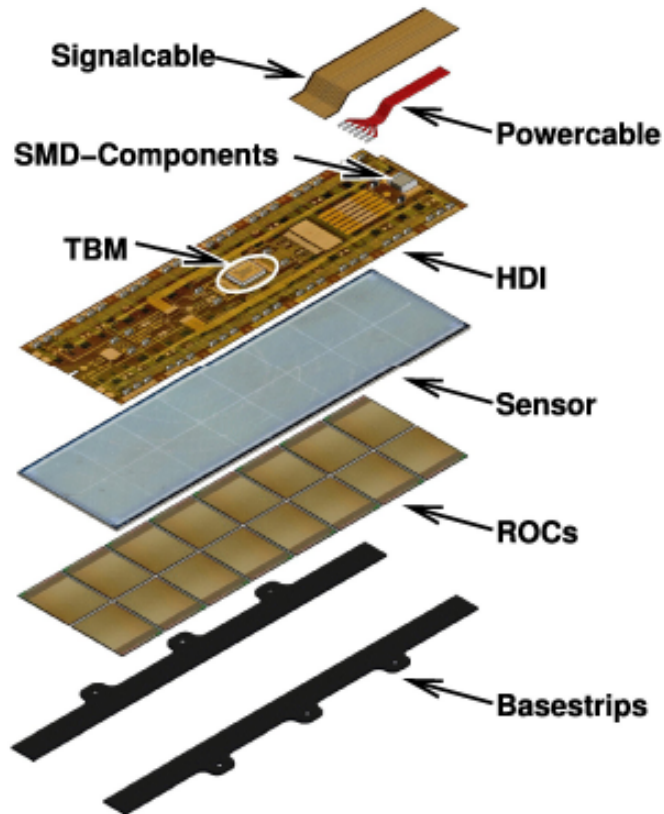


Figure 3.8: Design of a pixel barrel module [53]: The HDI is glued on the sensor plate, which is bump bonded to the ROCs. The ROCs are glued on basestrips. Power and signal cables are connected to the HDI. The TBM is placed in the middle of the HDI.

readout. The different ROCs on a module send their data serially.

Assembling and installation

The CMS barrel pixel detector was designed, assembled and tested at PSI in collaboration with Swiss and Austrian universities². The forward pixel detector was built by US groups³ at Fermilab. It was commissioned and tested at CERN. Both detectors were installed and commissioned in July 2008.

3.5.2 Silicon Strip Tracker

Back in the early 1990s there have been two technologies with potential for being used in an LHC tracker: silicon strip sensors and microstrip gas chambers (MSGCs). Silicon sensors are well suited for high occupancy and high resolution experiments due to their fast response.

²ETH Zürich, University of Zürich, University of Basel, HEPHY Vienna

³Northwestern, Rutgers, FNAL, Purdue, John Hopkins, Mississippi, Davis, Nebraska, Iowa, Kansas State, Cornell, Milan.

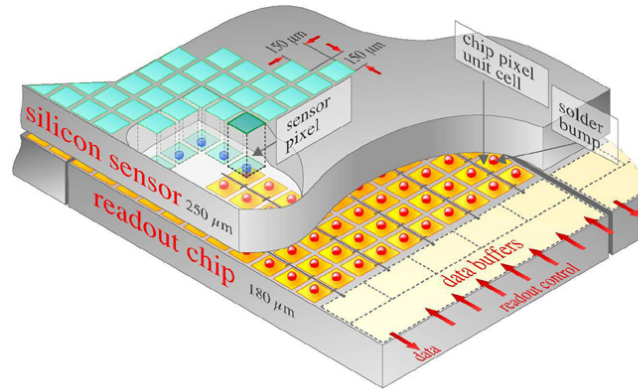


Figure 3.9: Design of the Read Out Chip [59].

The MSGC were thought to be less expensive. In 1998, when the CMS Technical Design Report was written, four inner silicon strip sensors and six outer MSGC layers were planned for the barrel detector complemented by endcap disks to extend the coverage to $|\eta| < 2.5$. Later it was realized that concentrating all available effort to one kind of detector was advantageous and thus the decision to build an all-silicon strip tracker was taken.

In total the CMS tracker implements 25000 silicon strip sensors covering an area of 210 m^2 . With its diameter of 2.4 m, a length of 5.4 m, and a volume of 24.4 m^3 it is the largest silicon strip tracker ever built. The operating temperature is -10°C and the cooling fluid temperature is around -25°C . Unlike in the pixel detector all channels are read out.

One of the key requirements for an LHC detector is to be able to accurately measure high p_T isolated leptons coming from vector boson decays. While the ECAL provides a precise measurement of the energy of high p_T electrons the tracker must be able to provide a precise measurement of high p_T muon momenta. The precision should be $\Delta p_T/p_T \approx 0.15 p_T$ (p_T in TeV/c) over the full pseudorapidity range. The coordinate measurements must be of sufficient precision and robustness such that track reconstruction is performed using a relatively small number of measurements per track.

Strip geometry

Efficient and robust track reconstruction at high transverse momenta requires a low cell occupancy. The segmentation of the detector is chosen in a way that typical channel occupancies are about 1% everywhere in the detector. In absence of a magnetic field the track density decreases as $1/r^2$. Due to the presence of a strong magnetic field low p_T tracks are curled up in the detector volume. Because of the large number of tracks with transverse momenta below 1 GeV the occupancy in the inner region is higher if the magnetic field is on. Cell sizes in the range of $20\text{--}100 \text{ mm}^2$ meet the occupancy requirement. The strips are between 10 cm and 20 cm long. The pitches range from 80 to $205 \mu\text{m}$. In the outer regions (radius above 60 cm), higher noise due to longer strips is compensated by larger signal height using $500 \mu\text{m}$ thick sensors (instead of $300 \mu\text{m}$). For the measurement along z direction a resolution of 1 mm

is sufficient. To provide this resolution, a stereo arrangement with an angle of 100 mrad is chosen.

Detector layout

As for the pixel detector, the tracker is divided into a barrel and an endcap part. The barrel is divided in a tracker inner barrel (TIB) with four layers from 20 cm to 60 cm radius and a tracker outer barrel (TOB) with six layers above 60 cm. The inner two layers of both TIB and TOB incorporate stereo layers. TIB and TOB have different lengths chosen in a way the outermost layer covers a range up to $\theta = 45^\circ$. Hence the TIB is shorter than the TOB and three tracker inner disks (TID) are used to complement the nine tracker endcap (TEC) disks ranging from 20 cm to 110 cm in radius. A schematic view of the tracker layout is shown in figure 3.10.

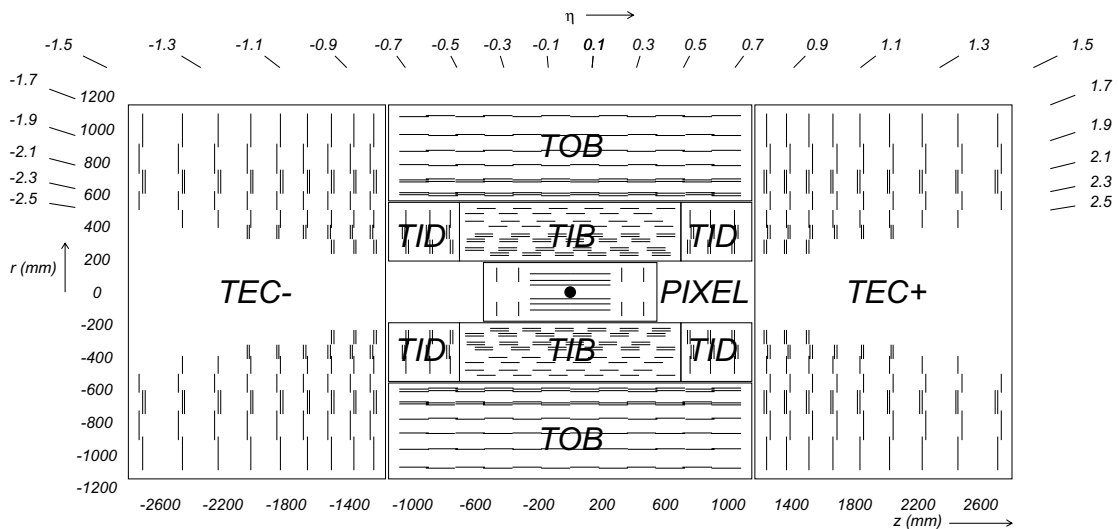


Figure 3.10: The layout of the CMS tracker [53]: There are three layers and two endcap disks of pixel detectors. The strip detector has four inner barrel layers (the two inner ones double-sided), two inner endcaps (each composed of three small disks), six outer barrel layers (two double-sided) and two endcaps (mounted in 7 rings on $2 \cdot 9$ disks). The layout ensures a pseudorapidity coverage of $|\eta| \leq 2.5$.

Installation and commissioning

Many institutes in Europe and the United States have been collaborating in the tracker project. The tracker has been installed in the CMS experiment by the end of 2007. After connection to all services and commissioning in stand-alone mode and together with the other sub-detectors large amounts of cosmic ray track data have been collected. In September 2008 the tracker system (including the pixel detectors) has been fully operational with more than 98% of all detector channels working.

3.6 The CMS Electromagnetic Calorimeter

The CMS ECAL is a homogeneous calorimeter made of lead tungstate (PbWO_4) crystals. Those high density crystals are fast and radiation hard. As the inner sub-detectors, it consists of a barrel (61200 crystals) and two endcap detectors (7324 crystals). There is a preshower detector installed in front of the endcap crystals. The photodetectors used in the barrel are avalanche photodiodes (APDs), and the ones in the endcap are vacuum photodiodes (VPTs). The design photon resolution is 0.5% above 100 GeV.

Crystals

Some properties of lead tungstate are summarized in table 3.2. About 80% of the light is emitted in 25 ns (bunch crossing time). At 18°C about 4.5 photoelectrons per MeV are collected in the photodetectors. The scintillation light has a maximum at 420 – 430 nm (blue-green). The crystals are polished in order to reach better internal reflection and hence better light collection on the photodetectors. Because of the pyramidal shape of the barrel crystals, the light collection is non-uniform. Better uniformity along the crystal length is achieved by depolishing one lateral face. The nominal operating temperature is $(18 \pm 0.05)^\circ\text{C}$. It has to be kept constant because the number of scintillation photons in lead tungstate and the amplification of the APDs both vary with temperature. The crystals and the electronics are cooled with water.

Density	8.28	g/cm^3
Radiation length	0.89	cm
Molière radius	2.2	cm

Table 3.2: Properties of lead tungstate relevant for the CMS ECAL.

Detector Layout

The pseudorapidity range covered by the barrel calorimeter (EB) is $|\eta| < 1.479$. The crystals are mounted with a small angle of 3° with respect to the vector from the nominal interaction point. This is to avoid particle trajectories along the crystal boundaries. The crystal length is 230 mm which corresponds to $25.8 X_0$. The volume of the barrel is 8.14 m^3 and it weights 67.4 t. Pairs of crystals are combined into submodules. Due to different shapes of the crystals there exist 17 different types of submodules. Submodules are assembled into modules of 400 – 500 crystals. A supermodule is made of four modules (1700 crystals) and covers 20° in ϕ . Eighteen supermodules form half a barrel. The ECAL endcaps (EE) cover the pseudorapidity range $1.479 < |\eta| < 3.0$. The distance between endcaps and nominal interaction point is 315.4 cm. The endcap crystals are all identically shaped and combined to supercrystals of 25 crystals. The supercrystals are arranged in a rectangular grid, pointing 1300 mm beyond the interaction point. Every crystal has a length of 220 mm and front/rear surfaces are quadratic with a side length of 28.62 mm/30 mm. The EE volume is 2.90 m^3 and it weights 24.0 t. There is a laser based light-monitoring system installed. It will allow the monitoring of the crystal transparency with good precision (0.1%). The layout of the ECAL detector is shown in figure 3.11.

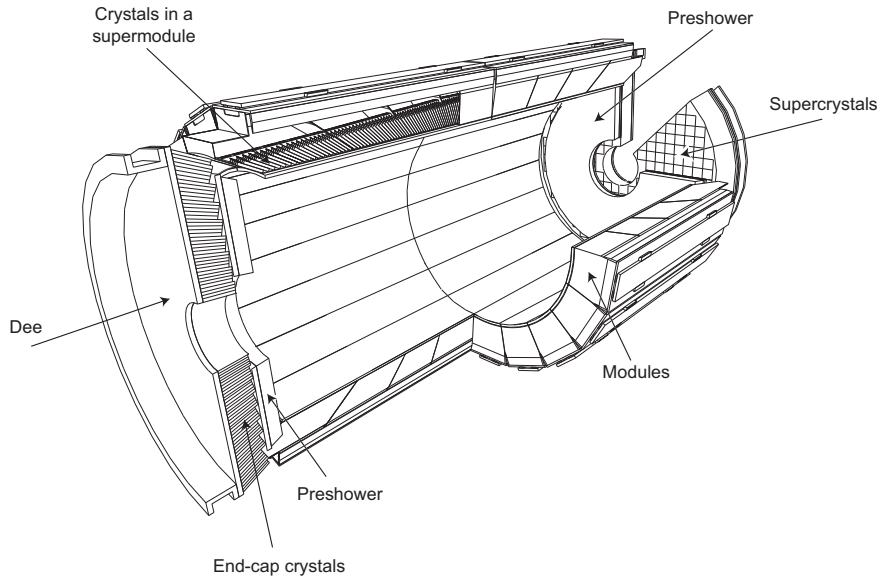


Figure 3.11: Schematic layout of the ECAL detector [53].

Photodetectors

Photodetectors suited for an LHC experiment should meet the following requirements: they should be radiation hard, insensitive to particles crossing them, and they must be operable in a strong magnetic field. Since the light yield of lead tungstate is low (about 5% of CsI or BGO), amplification is needed. For the barrel, APDs are chosen. They have an active area of 25 mm^2 and are operated at a gain of 50. One pair of them is mounted per crystal and the readout is parallel. The APDs were tested in order to ensure 10 years of operation with over 99% working fraction. In the endcap, VPTs specially developed for CMS are used. VPTs are photomultipliers with a single gain stage (10.2 at zero magnetic field). One VPT with an active area of 280 mm^2 is glued to each crystal. The response in a (strong) magnetic field is slightly reduced. The effect depends on the angle between VPT axis and magnetic field. For the CMS field and an angle of 15° the response is $> 90\%$ of that in zero field.

Preshower

The preshower detector helps to identify photons coming from neutral pion decays. The CMS preshower detector is a sampling calorimeter with lead radiators that initiate showers from incoming photons and electrons, and silicon strip sensors to measure the shower energies. It covers the pseudorapidity region $1.653 < |\eta| < 2.6$, and the total thickness is 20 cm. 32 strips with a pitch of 1.9 mm form a sensor with an active area of $61 \times 61 \text{ mm}^2$.

Energy Resolution

The energy resolution is parametrized with the following equation:

$$\left(\frac{\sigma}{E}\right)^2 = \left(\frac{S}{\sqrt{E}}\right)^2 + \left(\frac{N}{E}\right)^2 + C^2, \quad (3.4)$$

where S is a stochastic term, N a noise term, C the constant term and the unit for the energy E is GeV.

Installation and commissioning

In 2004 a fully equipped barrel supermodule was tested at CERN with electrons having momenta between 20 and 250 GeV. The energy resolution parameters were found to be $S = 0.028 \sqrt{\text{GeV}}$, $N = 0.12 \text{ GeV}$ and $C = 0.3\%$ [53]. The full detector was installed and commissioned in 2008.

3.7 The CMS Hadronic Calorimeter

The CMS HCAL is a sampling calorimeter, where the material producing the particle shower is distinct from the material measuring the deposited energy. The two materials are alternating. In the CMS HCAL, brass is used as absorber material and sheets of scintillator as active material. The active material is Kuraray SCSN81, which is chosen because of its long-term stability and moderate radiation hardness. There are 17 layers of plastic scintillators in total. The scintillator is divided into tiles. These are read out with wavelength shifting fibers, which are connected to clear fibers. They carry the light to the outer radius of the HCAL, where photodetectors are installed at the back of the calorimeter, see figure 3.12. The strong magnetic field limited the number of suitable photodetectors severely. A hybrid photodiode (HPD) with a gain of 1000 – 2000 was developed for the CMS HCAL.

Absorber

Since the HCAL is located inside the magnet solenoid, the absorber needs to be made from non-magnetic material. It must have good mechanical properties and shall not be too expensive. These requirements lead to the choice to take C26000 cartridge brass. Some properties of this brass are listed in table 3.3.

chemical composition	70 % Cu 30 % Zn
density	8.53 g/cm ³
radiation length	1.49 cm
interaction length	16.42 cm

Table 3.3: Properties of the C26000/cartridge brass used as absorber material in the CMS HCAL [53].

Detector Layout

The central HCAL is located inside the solenoid. This choice increases the bending path of the muons. In addition, it allowed for a robust magnet design. On the other hand, the space for absorber material is constrained by the size of the solenoid. In order to maximize the absorbing power, the brass plates are relatively thick (between 5.05 and 5.65 cm) and the scintillators relatively thin (about 3.7 mm).

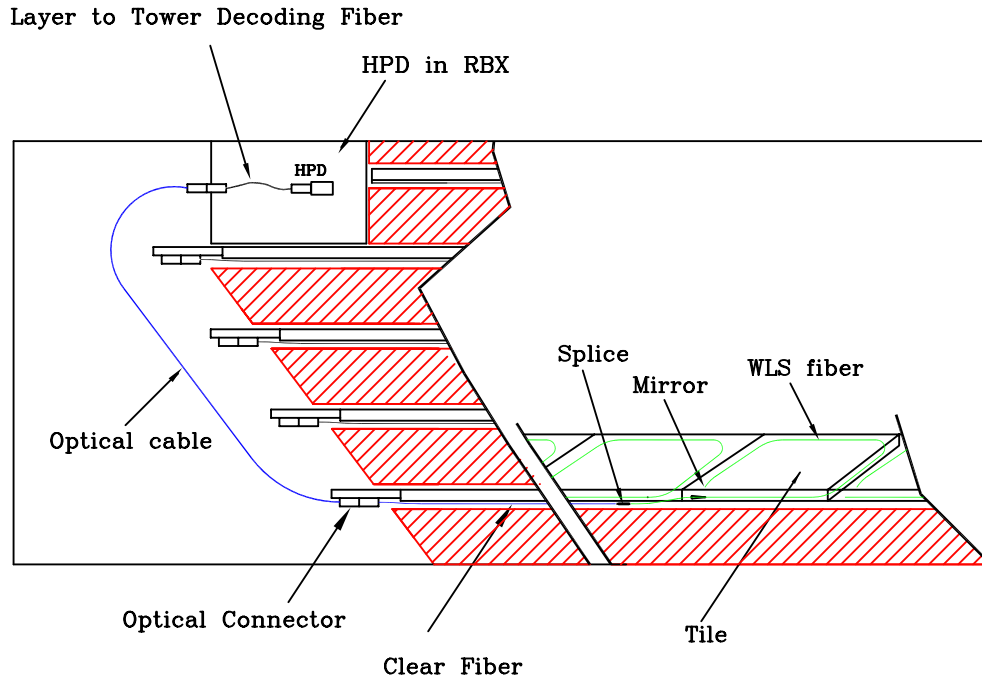


Figure 3.12: A schematic view of the HCAL readout [53]. In total there are 9528 readout channels.

The HCAL layout is shown in figure 3.13. Tower numbers are indicated and the relative thickness compared to the magnet solenoid is shown.

The central HCAL consists of a barrel (HB) covering the $|\eta| < 1.3$ range and an endcap (HE) covering $1.3 < |\eta| < 3$. The HB is divided in two half barrels (HB+ and HB-). Each consists of 36 azimuthal wedges constructed of flat brass absorber plates. The plates are oriented along the z axis. Each wedge is divided into four ϕ sectors. The total absorber thickness at 90° is 5.82 interaction lengths λ_I and it increases with $1/\sin\theta$. The ECAL in front of HB adds about $1.1 \lambda_I$. The hadron endcaps (HE) are attached to the muon endcap yoke. The brass plates in the HE are 7.9 cm thick and there are 9 mm gaps for the scintillators. The total length of the hadronic and electromagnetic endcap calorimeters is about $10 \lambda_I$. The photodetectors are placed on the outer side of towers 14 (HB) and 18 (HE).

The very forward calorimeter, the HF, is covering the pseudorapidity range $3.0 < |\eta| < 5.0$. It is located outside the magnetic field, with the front face at a distance of 11.2 m from the interaction point. On average, 760 GeV per proton-proton interaction is deposited into the two forward calorimeters. This is almost a factor of 8 more than for the rest of the detector. In the HF, Cerenkov radiating quartz fibers are used as active material because they are radiation hard. The HF is cylindrical and consists of 5 mm thick grooved steel plates. The quartz fibers for the readout are inserted into these grooves (running parallel to the beam pipe). There are two longitudinal segments: half of the fibers run through the whole 165 cm deep

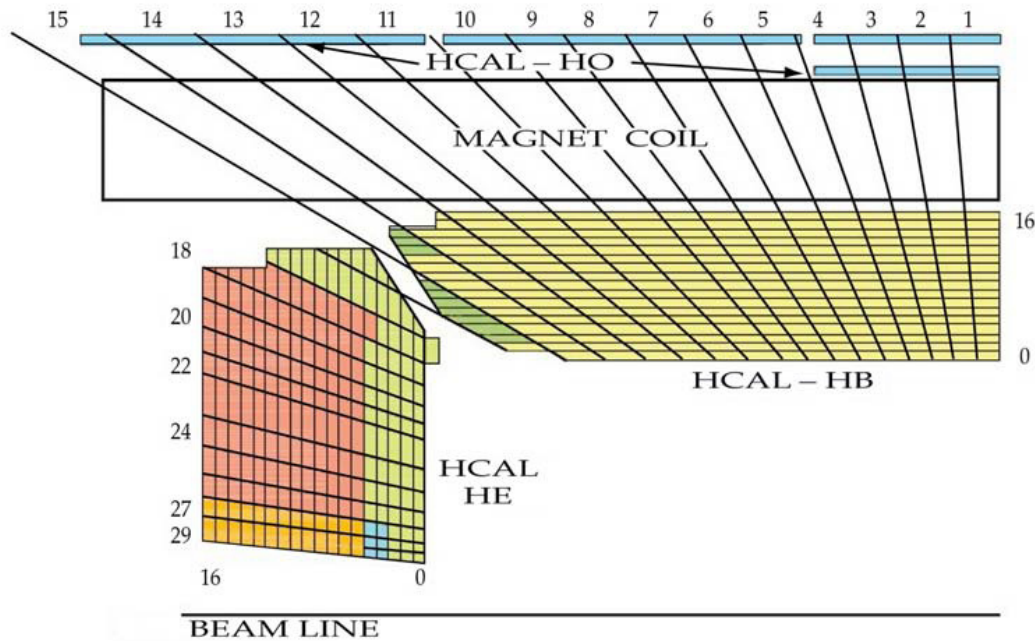


Figure 3.13: A schematic view of the HCAL layout [53]. The plastic scintillator is divided into 16η sectors for the HB and 14 for HE. The longitudinal segmentation of the readout of every tower is shown with different colors (between one and three channels). The HO is organized in five rings. The central ring has two layers of scintillators on each side of a 19.5 cm thick piece of iron, the other rings have one (at a radial distance of about 4 m).

absorber, the others start at a depth of 22 cm from the front of the detector. The two sets are read out separately to be able to distinguish between showers initiated by electrons/photons and hadronic showers.

The fourth part of the HCAL is an outer calorimeter, HO, which is installed outside the solenoid and uses its material as additional absorber of $1.4/\sin\theta\lambda_I$. Its purpose is to identify late starting showers and to measure shower energy deposited after the central HCAL for $|\eta| < 1.3$.

Installation and commissioning

For the energy calibration of HCAL, test beams and radioactive source measurements have been used [61]. The absolute energy scale was established measuring the response to 50 GeV pions. The tower-to-tower calibration was done in the CMS surface hall in 2005 and 2006 using radioactive sources. In summer 2006 the HCAL was lowered into the CMS cavern.

3.8 The CMS Solenoid Magnet

The CMS solenoid reaches a magnetic field of 3.8 T when passing a current of 19.4 kA through the coil of niobium-titanium superconductor. The coil is indirectly cooled by saturated helium at 4.5 K. It has a bore of 5.9 m diameter and is 12.5 m long, large enough to contain the CMS tracker and the full calorimetry. The energy stored in the magnet is 2.6 GJ at full current. The ratio between stored energy and cold mass is 11.6 kJ/kg, very high compared to other solenoids, see figure 3.14. The striking feature of the 220 t cold mass is the four layer winding made from a NbTi conductor. The cold mass is about 30 cm thick. For the flux return there are 5 iron wheels and two endcaps, consisting of three disks each. The lightest wheel weights 400 t and the central wheel, which includes also the coil and the cryostat, weights 1920 t. The total weight is 10000 t.

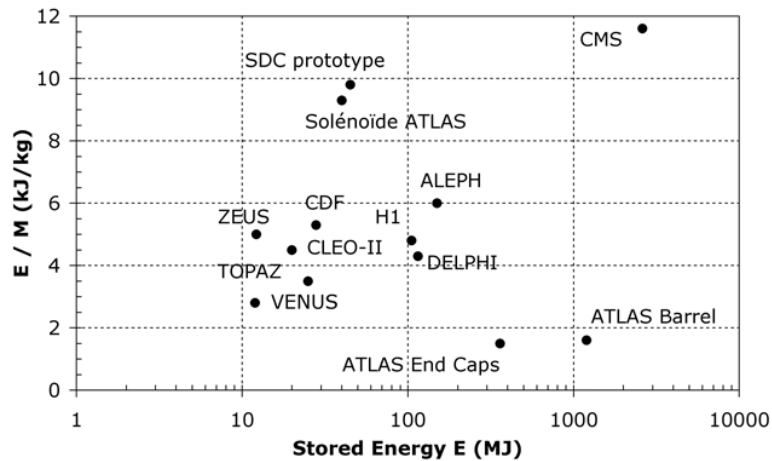


Figure 3.14: Ratio of energy stored in a magnet divided by the cold mass, as a function of the energy for different magnets [53].

Installation and commissioning

The CMS solenoid has been designed and built by an international team. It has been assembled and tested at CERN during the autumn of 2006 in a surface hall. Two years later it has been recommissioned underground.

3.9 The CMS Muon System

The CMS muon system is located outside the solenoid. The total material of the inner detectors and the solenoid corresponds to about 11 interaction and 110 radiation lengths, see figure 3.15. Therefore the rate of hadron or electron punch-through is reduced below the rate of muons and whatever comes out of the inner detectors is considered a muon. Three different types of gaseous particle detectors are used for muon identification: drift tubes, cathode strip chambers and resistive plate chambers. The muon detectors are arranged in concentric

cylinders around the beam line in the barrel region, and in disks perpendicular to the beam line in the endcaps. They are interspersed among the layers of the flux return plates which serve as additional absorber material, see figure 3.15.

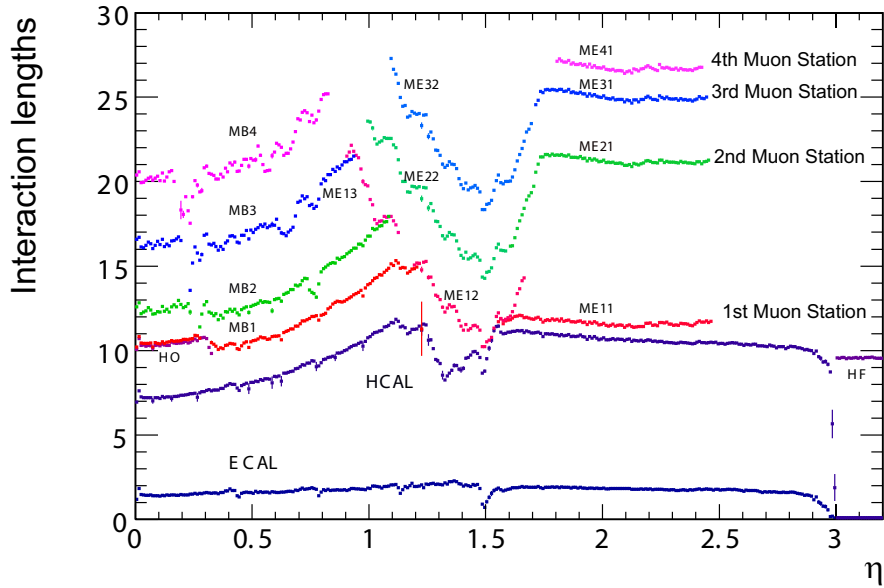


Figure 3.15: Material thickness in units of interaction lengths at different radii as function of pseudorapidity [53].

Detector Layout

In the barrel region the muon rate is low compared to the rate in the endcap region. Rectangular drift tubes (DTs) cover the pseudorapidity region $|\eta| < 1.2$. The DTs are organized in four stations with 8 chambers to measure the muon coordinate in the $r\phi$ plane. Three of the stations contain also four chambers to measure the z coordinate. In the endcap region, where the muon rate is higher, cathode strip chambers (CSCs) are used. There are four stations of CSCs between the flux return plates of each endcap to cover $0.9 < |\eta| < 2.4$. They provide a precise measurement in the $r\phi$ plane with the cathode strips running radially outwards. The DT and CSC systems are used for triggering. Because the timing resolution is eventually not good enough for correct bunch crossing identification, there is a complementary trigger system consisting of resistive plate chambers (RPCs), both in the barrel and in the endcap regions. They provide an independent and fast trigger with good p_T and time resolution. In the barrel, there are in total 6 layers of RPCs, and in the endcap three layers. In order to improve the muon momentum resolution, an optical system is installed for aligning the muon detectors with respect to each other and to the inner tracking system. Figure 3.17 shows the layout of the CMS muon system. In total there are 250 DTs installed in the barrel and 540 CSCs in the endcaps.

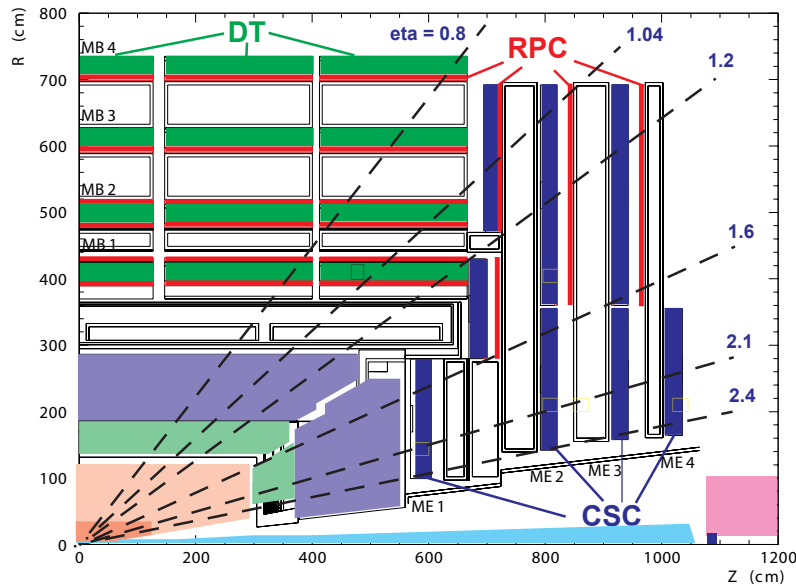


Figure 3.16: Layout of the CMS muon system for initial low luminosity running [51].

Drift tubes

The choice of DTs for the barrel muon system is motivated by the low magnetic field (the field is mostly contained in the steel yoke) and the relatively small rate. The positively charged anode wire is 2.4 m long and 50 μm thick. The drift cell is 1.3 cm high and 4.2 cm wide. This means that the maximum drift distance is 2.1 cm, corresponding to a maximum drift time of 380 ns in a gas mixture of 85 % of Ar and 15 % of CO_2 . Aluminum field electrodes, placed at the top and bottom and the aluminum cathodes, are located on both sides of the cell. The drift cells operate with a gas gain of 10^5 . A superlayer (SL) is made out of 4 layers of drift cells. Each layer is shifted by half a cell with respect to the previous layer. The SL is the smallest independent unit. Three (or two) SL make a DT chamber, separated by a thin aluminum honeycomb plate. The outer two SL have their wires along the beam direction to provide a measurement in the $r\phi$ plane. The inner SL measures the z position along the beam (the wire is orthogonal to the beam direction). This inner SL is not present in the fourth station.

Cathode strip chambers

The CSCs are multi-wire proportional chambers. They are trapezoidal and cover either $\Delta\phi = 10^\circ$ or $\Delta\phi = 20^\circ$, and are made of 7 panels. Anode wires run azimuthally in the 6 gas gaps between the panels to measure the muons radial coordinate. Cathode strips of constant $\Delta\phi$ run radially. The largest chambers are about $3.4 \times 1.5 \text{ m}^2$ in size. The number of anode wire readout channels is about 180'000 and there are about 220'000 cathode strip readout channels.

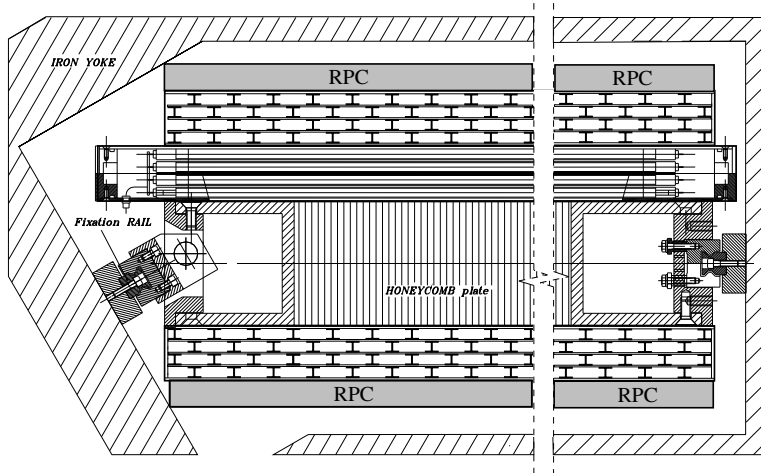


Figure 3.17: Drift tube chamber layout ($r\phi$ view): two SL with wires along beam direction and one with orthogonal wires [53].

Resistive plate chamber systems

RPCs are gaseous parallel-plate avalanche detectors. The Bakelite plates are 2 mm thick and highly resistive (order of $10^{10} \Omega/\text{cm}$). The gap is about 2 mm. Charged particles moving through the gap induce an electrical signal on a plane of insulated strips behind the plate. The RPCs are well suited for tagging the time of an ionizing event with an accuracy much better than 25 ns. One RPC module has two gaps with readout strips in between. The total signal is the sum of the two signals of the single gaps, therefore the single gaps can operate at lower gain. The 480 barrel chambers are rectangular, 2455 mm long (with a few exceptions) and between 1500 mm and 2500 mm wide. In the endcap the chambers have trapezoidal shape and they cover 20° or 10° in ϕ (same as the CSCs).

Installation and commissioning

The CMS muon detectors have been pre-assembled on the surface. The rate of cosmic muons was high enough for high statistics tests during a relatively short period of time. In summer 2006, a test of the magnet has been performed. Since the detector needed to be closed, this was also an opportunity to test the muon system again with cosmic particles. In the following, the muon wheels have been lowered into the cavern and in 2008 the full CMS detector was operable.

3.10 The CMS Trigger System

At the LHC design center-of-mass energy of 14 TeV the total cross section is predicted to be around 100 mb, the total inelastic cross section around 70 mb. This leads, at full luminosity $\mathcal{L} = 10^{32} \text{ cm}^{-2}\text{s}^{-1}$, to an interaction rate of $7 \cdot 10^8 \text{ Hz}$. It is impossible to store all data, and the task of reducing the number of events to be stored is performed by the CMS trigger

system. The system works in two steps:

- First, a system of programmable electronics is used to reduce the rate by a factor of about 400 to 100 kHz. This is called *Level-1 (L1) Trigger*.
- In a second step, a software system together with a huge number of processors are used to reduce the rate to about 100 Hz. This step is called *High-Level Trigger (HLT)*.

While the L1 Trigger uses coarsely segmented data from the muon detectors and the calorimeters, the HLT has access to the full high-resolution data and performs more complex calculations in order to find potentially interesting events. The L1 Trigger has local components, so called *Trigger Primitive Generators (TPG)* which are based on calorimeter deposits or hits in muon chambers. *Regional Triggers* combine the information to find trigger objects such as electron or muon candidates. The *Global Trigger* gets the information needed from the global calorimeter and global muon triggers to decide on whether or not to keep an event for evaluation by the HLT, see figure 3.18. The *Trigger Control System (TCS)* adds information on readiness of sub-detectors and the *data acquisition (DAQ)* to be taken into account by the global trigger. The L1 Trigger has to evaluate every bunch crossing and communicate the trigger decision via the *Timing, Trigger and Control (TTC)* system to the detector front-end electronics with a maximum latency of $3.2 \mu\text{s}$. After a positive L1 decision, the data are read into the event building network of the DAQ and sent to the event filter farm for HLT evaluation. For some detectors the data are zero suppressed, which means that only signals above a programmable threshold are read out. The HLT can either discard the event or save it to an online storage system. The event size is around 1 MB. The L1 Trigger electronics is partly located on the detectors and partly in the underground control room.

The goal of the *calorimeter trigger* is to identify photon, electron, jet and τ -jet candidates and to measure transverse energies of single objects as well as the sum and the missing transverse energy. In the calorimeters, the TPGs sum transverse energies in neighboring units to obtain trigger towers with an (η, ϕ) -coverage of 0.087×0.087 for $|\eta| < 1.74$ (for the rest of the calorimeter region the towers are larger). Each trigger tower contains 5×5 crystals in ECAL and one single readout tower in HCAL. The *Regional Calorimeter Trigger* determines electron and photon candidates in regions consisting of 4×4 trigger towers. Transverse energies from both calorimeters are summed. The *Global Calorimeter Trigger (GCT)* forms jet and electron objects by searching for patterns of energy depositions.

In the *muon trigger* system the rate of particles with low transverse momenta (4–50 GeV) needs to be reduced by a factor of about 10^3 . All muon detector types take part in the trigger decision. In the DTs and CSCs track segments are formed and passed to the *Regional Trigger* to reconstruct tracks and assign ϕ , η and p_T . The four highest quality muon candidates both from DTs and CSCs are forwarded to the *Global Muon Trigger (GMT)*. For the RPCs, the patterns of hits are directly compared to predefined patterns. Also for the RPCs the four highest p_T muons are sent to the GMT. In addition the GMT receives information about isolation and minimum ionization for every region in the calorimeters from the GCT. The GMT selects up to four muon candidates for each bunch crossing that are forwarded to the

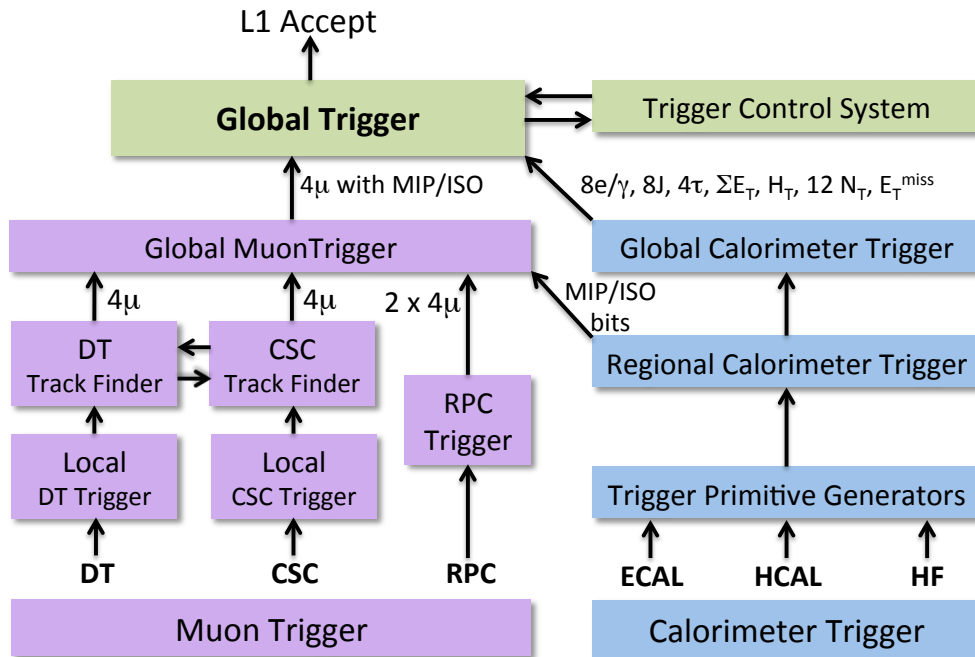


Figure 3.18: Architecture of the L1 trigger system [53].

Global L1 Trigger.

The Global L1 Trigger applies up to 128 algorithms using all input from muon detector and calorimeters. All algorithms have programmable thresholds in order to optimize trigger performance according to the luminosity.

The HLT is a pure software trigger, running on a computing farm (the *Event Filter Farm*). The HLT uses the same software modules as the offline reconstruction. The selection runs on one event at a time. The event selection allows to follow a diverse physics program. It must be monitored very carefully, since all discarded events are lost forever.

The trigger selections are implemented as trigger “paths”. Events that pass one (or even several) trigger paths are accepted, other events are rejected. Two types of modules make a trigger path: producers and filters. The first ones produce or reconstruct objects that are used as trigger primitives (i.e. for the trigger decision). Filters then apply selections exploiting the trigger primitives quantities. Apart from producers and filters there are also prescalers. They are necessary to reduce the output rate of trigger paths with high rates of selected events, in order to keep the rate within the allocated bandwidth. Prescalers simply apply a determined prescale factor, such that, when a trigger is prescaled by a factor N , only one out of N events is considered for processing by the trigger path. Prescale factors need to be changed when the luminosity changes.

The efficiency of the event selection needs to be measurable from data. Data of selected events are first saved to a large disk array located at the experiment. Later they are transferred to computing sites at CERN and worldwide.

3.11 Computing in CMS

Even after the HLT, a huge amount of potentially interesting data is left. The CMS offline computing system distributes and stores this data. In CMS different data formats are used to achieve more data reduction. The RAW format contains the full information from the detector and triggers. Based upon trigger signature, the RAW data is divided into several distinct *primary datasets*. An extension of the RAW data format is used to store the output of CMS MC simulation tools. The CMS simulation is based on GEANT4 [62]. It is run on HepMC [63] format files generated by MC programs to produce persistent hits in the CMS detectors. These are then used as input for the digitization step which produces digital hits in the same format as the CMS detector electronics. The same software algorithms can be used for real and simulated events.

On the RAW data, several algorithms defined in the *CMS Software Framework* (CMSSW) are run to go from detector level information to higher level physics objects, such as tracks, muons or electrons. These algorithms include detector-specific filtering, corrections of the digitized data, cluster finding, track reconstruction, primary and secondary vertex reconstruction, particle identification, and many algorithms using data from different sub-detectors. The reconstructed (RECO) data format contains these higher-level physics objects together with the reconstructed hits and clusters needed to produce them. There is a third data format containing only the higher-level physics objects. It is called *Analysis Object Data* (AOD) format. Figure 3.19 shows the different steps of event processing for data and MC events.

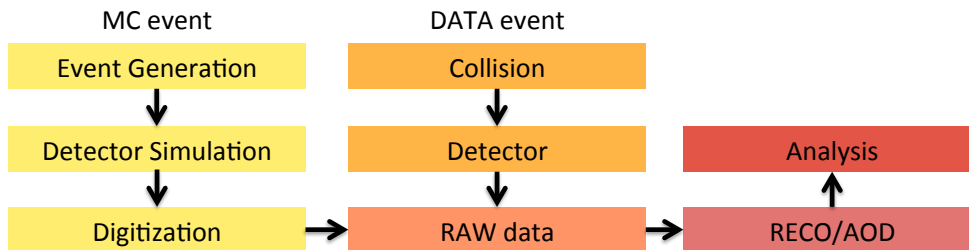


Figure 3.19: Steps in event processing for MC and real data events.

For data distribution and storage the Worldwide LHC Computing Grid (WLCG) was designed. Computing resources at a range of scales, provided by different institutes distributed all over the world, are connected. A hierarchical architecture of Tiered centers is defined. There is a single Tier-0 (T0) center at CERN, where all the RAW data from the online system is processed first. It is copied to permanent mass storage and the modules are run to produce RECO datasets. The system is powerful enough to keep pace with the rate of data coming from the online system. Both, the RAW and RECO datasets are copied to Tier-1

(T1) centers. Data is only considered safe once at least two copies exist at independent sites (one is the T0). There exist 7 T1 centers. At the T1s, the datasets are permanently stored and the reconstruction algorithms are run again using improved algorithms or calibrations. From the T1s, datasets are redistributed to Tier-2 (T2) centers. The T2s are designed to support analysis requiring frequent access of the same datasets. MC data is mostly produced at T2s, and then transferred to T1s for long-term storage. At the T2s, resources are divided between the local user community and the whole CMS collaboration. There exist also Tier-3 (T3) centers. Those usually provide storage for datasets frequently used and processors for running analysis software.

Chapter 4

Analysis Overview

A measurement of the angular correlations between beauty and anti-beauty hadrons ($B\bar{B}$) produced in proton-proton collisions at a center-of-mass energy of 7 TeV at the CERN LHC is presented [64]. The data have been recorded with the CMS detector during 2010. The region of small angular separation is probed for the first time at $\sqrt{s} = 7$ TeV. The study provides a test of pQCD and gives further insight into the dynamics of $b\bar{b}$ production. The measured distributions are compared to various theoretical predictions based on LO and NLO perturbative QCD calculations. The angle is measured between the flight directions of the B hadrons, where the flight direction is defined as the direction from the primary-interaction vertex to the B hadron decay point, given by a displaced secondary vertex. For secondary vertex reconstruction an *Inclusive Vertex Finder* (IVF) is used together with a B candidate identification technique. The IVF is described later in section 6.7 and the B candidate identification in section 6.8. The visible kinematic range for the measurement is defined by the B hadron kinematics. Both B hadrons are required to be produced in the central region $|\eta(B)| < 2.0$ and with transverse momentum $p_T(B) > 15$ GeV (see section 7.1).

In this chapter, an overview of the analysis is given. This includes trigger selection, the data samples studied, the event simulation and event selection. At the end of the chapter, information about the settings of the different MC event generators that provide theoretical predictions is given.

4.1 Trigger

The study is based on events triggered with single-jet triggers. Both on the hardware and on the software level jets are required. On the HLT level events with at least one jet with an uncorrected transverse calorimetric energy E_T^U above trigger threshold are selected. Three different thresholds are used in this analysis: 15 GeV, 30 GeV and 50 GeV. The corresponding L1 triggers have thresholds of 6 GeV, 20 GeV and 30 GeV. When the first collisions at $\sqrt{s} = 7$ TeV were recorded, none of these triggers was prescaled. But as the instantaneous luminosity grew, the trigger path with 15 GeV threshold needed to be prescaled first by a factor of 10 and then even higher. Later, also the other two jet triggers relevant for this analysis have been prescaled. The prescale factors were chosen to keep a constant rate, i.e. the

number of events triggered by the jet triggers per time unit stayed about the same. Hence, this analysis did not profit from the luminosity increase the way analyses looking for rare events could do.

The leading jet p_T spectra for the three jet triggers are shown in figure 4.1 (left plot). The jets are reconstructed with the anti- k_T algorithm (see section 5.1.1), which is applied on particle flow (PF) objects [65, 66]. All information of all sub-detectors is collected for each particle individually and the resulting PF objects are used as input for jet reconstruction. For the p_T of the leading jet corrected jet energies are used [67]. In the right plot the efficiency of triggering an event on the HLT as a function of the p_T of the leading jet is shown. The efficiency is determined using events with a lower E_T^U trigger.

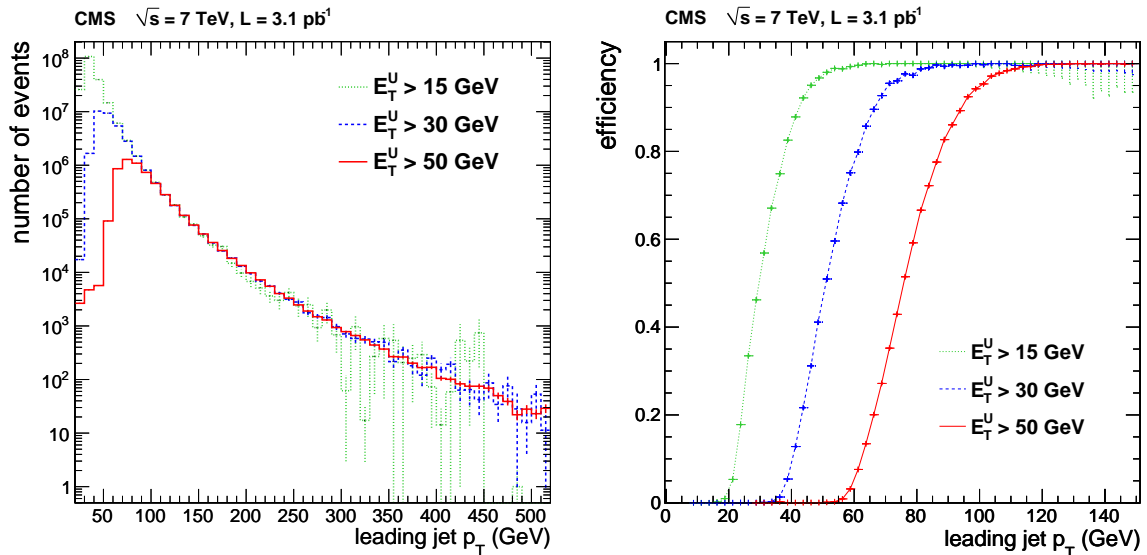


Figure 4.1: The measured transverse momentum distributions of the leading jet in the event (left) and the measured HLT efficiency as a function of jet p_T (right). Both are shown for the three jet trigger thresholds.

For every jet trigger, the p_T range where the trigger is more than 99% efficient is determined. The event sample is later divided into three energy bins corresponding to the three p_T ranges found. Table 4.1 contains a summary of the three triggers and the p_T ranges of the leading jet for the triggers to be > 99% efficient.

4.2 Data Samples

The data used for this study were collected by the CMS detector during 2010. The center-of-mass energy was $\sqrt{s} = 7 \text{ TeV}$ for the whole data taking period and the full sample corresponds to an integrated luminosity of $3.1 \pm 0.3 \text{ pb}^{-1}$. Only data for runs with all sub-detectors relevant for this study fully functional and when stable beam conditions were declared are used. If

Trigger	E_T^U cut at HLT (GeV)	E_T^U cut at L1 (GeV)	> 99 % efficiency range
HLT_Jet15U	15	6	$p_T > 56$ GeV
HLT_Jet30U	30	20	$p_T > 84$ GeV
HLT_Jet50U	50	30	$p_T > 120$ GeV

Table 4.1: Jet triggers used for the correlation measurement. For every trigger the E_T^U cuts at HLT and L1 are given as well as the p_T range of > 99 % efficiency. For the p_T of the leading jet corrected jet energies are used.

the stable beam flag is not set, the tracker and pixel detector high voltages are usually turned off for detector safety reasons. In order to reject events with no collision, a reconstructed primary interaction vertex with at least four well reconstructed tracks, $|z| < 24$ cm and $\rho = \sqrt{x^2 + y^2} < 2$ cm is required. For events with more than 10 tracks, a fraction of at least 25 % is required to be of high quality to reduce the background from beam-gas events. Events from beam-wall and beam halo interactions have been filtered out using timing criteria. The L1 technical trigger bits use information from the *Beam Scintillator Counter* (BSC) and the *Beam Pick-up Timing for Experiments* (BPTX) detector. The BSCs are located at 10.9 and 14.4 m distance to the CMS center on both sides. The BPTX detectors are located at ± 175 m from the CMS center and they are used to measure the beam timing. Comparison of information from opposite sides gives an accurate measurement of the vertex z coordinate and bunch timing relative to the CMS clock. The rejection of beam-wall and beam halo events is done by requiring

- BPTX signal for both beams
- at least one hit in BSC on both sides
- none of the four BSC halo trigger bits fired
- BSC splash trigger bit fired for both sides or no side.

Events faking high energy deposits in the calorimeters are filtered out based on pulse shape and hit multiplicity criteria.

In the beginning of the $\sqrt{s} = 7$ TeV data taking period, all data were collected in a single *Primary Dataset* (PD). With increasing luminosity the data were split into different PDs, each containing events from a number of HLT trigger paths performing similar selection. More information on the commissioning of the CMS HLT trigger is found in [68]. The PD used for this analysis is the JetMETTau dataset. It contains the data collected with different jet triggers (for one, two or four jets), triggers for missing transverse energy, tau triggers and triggers used for b-tagging. Later, this PD is split into two datasets, the JetMET and the BTau PDs. The first one is used for this analysis. The dataset is split into three energy bins using the jet triggers with three different E_T^U thresholds and the p_T requirement on the leading jet (for > 99 % trigger efficiency). The datasets used for the different run periods are summarized in table 4.2. The luminosity for the different triggers is given in the table. The

instantaneous luminosity in the CMS detector is measured using signals in the HF calorimeters. The luminosity information is logged by a dedicated data acquisition system and the integrated luminosity is computed using this information [69]. The effective integrated luminosity for the combined dataset, taking into account prescale factors, corresponds to 0.031, 0.313 and 3.069 pb⁻¹ for the three leading jet p_T bins (above 56, 84 and 120 GeV), including some overlap.

Dataset	Run range	Events (total)	Integrated luminosity (nb ⁻¹)		
			> 56 GeV	> 84 GeV	> 120 GeV
MinimumBias	132596 – 135735	1312861	7.875	7.875	7.875
JetMETTau	136080 – 137028	718879	4.924	4.924	4.924
JetMETTau	137437 – 139558	2745616	4.261	61.262	61.262
JetMETTau	139779 – 140160	2991560	2.872	35.501	117.168
JetMETTau	140160 – 140338	1431211	1.082	10.821	63.807
JetMETTau	140399 – 141882	935077	0.758	7.582	41.099
JetMET	141950 – 143731	11192914	6.800	136.005	1430.000
JetMET	143732 – 144114	3983871	2.459	49.181	1342.896
TOTAL	132596 – 144114	25311989	31.031	313.151	3069.031

Table 4.2: Datasets used for different run periods. The run range, the total number of events in the set and the integrated luminosity for the three leading jet p_T bins used for the analysis are given for every dataset.

4.3 Event Simulation

The basic MC program used for tuning and optimizing the vertex reconstruction with the IVF and the B candidate identification and for determining the selection efficiencies is the LO PYTHIA program (see section 2.3.1). It was used with standard settings and the CTEQ6L1 PDFs. For modeling the underlying event the D6T tune [40] is applied. The b quark mass is set to 4.8 GeV. The CMS detector response is simulated in detail for all generated events. The simulation is based on GEANT4 [62]. For event generation, detector simulation and reconstruction the standard CMS Software Framework has been used (version CMSSW_3.5.6). The analysis has been done in CMSSW_3.7.0_patch2. The same reconstruction algorithms and trigger and event selection were applied on simulated events and on measured data.

The PYTHIA samples used are QCD samples. High p_T QCD events are generated for hadron-hadron collisions (by setting the PYTHIA parameter MSEL = 1). The samples have been produced centrally in the CMS Spring10 production. The PYTHIA parameter describing the transverse momentum of the outgoing partons of the hard subprocess in the center of mass frame of the colliding partons is \hat{p}_T . Samples with different minimum \hat{p}_T have been used, see table 4.3. For comparison between PYTHIA predictions and measured data distributions, the different PYTHIA samples have been combined. This has been done by assigning weights to the PYTHIA samples to scale each sample to the total integrated luminosity \mathcal{L}_{data} of the data

sample. The weight w_i for sample i is computed using the cross section σ_i and the number of events n_i of the sample as

$$w_i = \frac{\sigma_i}{n_i} \cdot \mathcal{L}_{data}. \quad (4.1)$$

To avoid overlap between the weighted MC samples, an upper \hat{p}_T cut has been applied. The relative weights of the different samples can also be seen in table 4.3. In figure 4.2 the number of events as function of \hat{p}_T is shown for the different samples, scaled with the factors given in the table. It is found that adding the scaled samples gives a continuous distribution, as one should expect. The PYTHIA prediction for the cross section for having two B hadrons in events with $\hat{p}_T > 15$ GeV is 41 μb .

Dataset	min. \hat{p}_T (GeV)	max. \hat{p}_T (GeV)	Events	σ (pb)	\mathcal{L} (pb^{-1})	Factor (1 pb^{-1})
/QCD_Pt15	15	30	6090500	876215000	0.006951	143.9
/QCD_Pt30	30	80	4989664	60411000	0.08260	12.10
/QCD_Pt80	80	170	2971800	923821	3.217	0.3109
/QCD_Pt170	170	300	3091950	25474.9	121.4	0.008239
/QCD_Pt300	300	—	2852665	1256	2271	0.0004403
/InclusiveBB_Pt30	30	—	1017541	4140000	0.246	—

Table 4.3: PYTHIA samples used in this analysis (Spring10 production). For every dataset the minimum and maximum \hat{p}_T is given. The maximum \hat{p}_T requirement is only applied if the samples are combined. The number of events, production cross section σ , and integrated luminosity \mathcal{L} is given as well as the scaling factor to be applied for scaling the sample to an integrated luminosity of 1 pb^{-1} . The last line contains information on an “InclusiveBB” sample that is only used for efficiency and purity determination.

For efficiency and purity determination an additional file, an “InclusiveBB” sample, is used to improve the MC statistics. The only difference to the QCD files is that a b quark filter was applied (at least one b or \bar{b} in the event). The file contains also gluon splitting events, since no b or \bar{b} is required to participate in the hard interaction (the b filter is applied on all generated particles). The procedure to weigh the samples when this additional file is included is described later.

4.4 Event Selection

The event selection is based on the three jet triggers at both HLT and L1 as discussed above. At least one reconstructed primary vertex and at least one reconstructed jet are required in the offline event selection. For primary vertex reconstruction, tracks with low impact parameter with respect to the nominal interaction region are used. In events with more than one interaction (pile-up events) several primary vertices can be reconstructed. In these cases the vertex with the largest squared track transverse momentum sum $S_T = \sum p_{T_i}^2$ is taken as the primary collision vertex. The sum runs over all tracks that are associated to the vertex. Residual effects from pile-up events are found to be negligible. The reconstructed

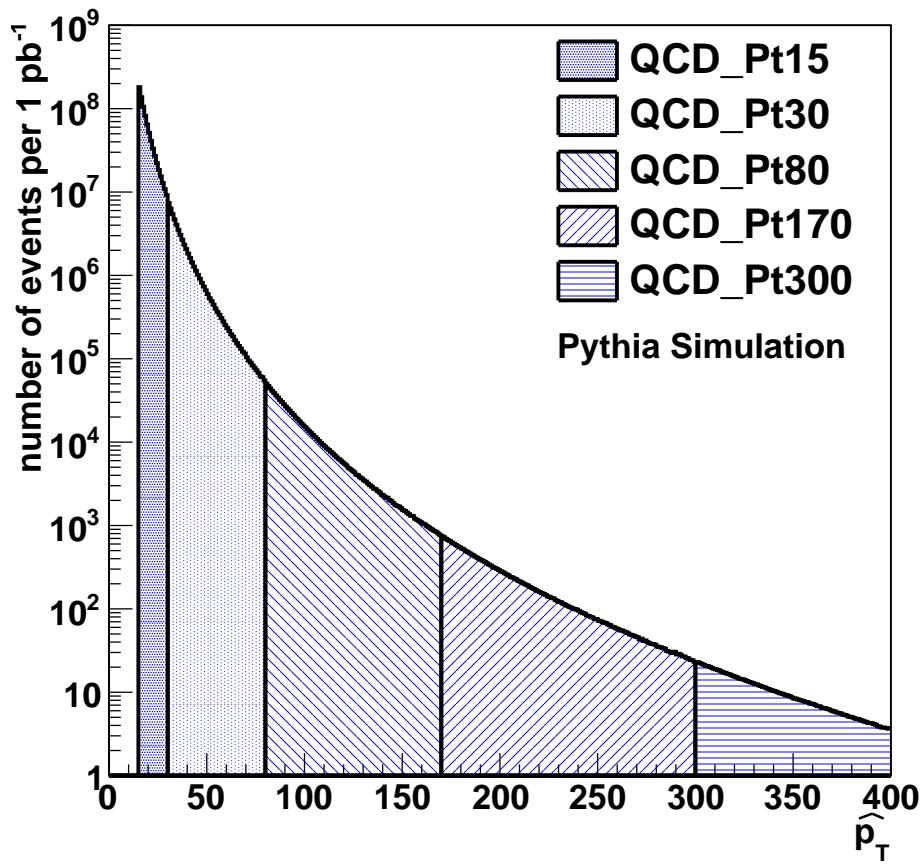


Figure 4.2: Generated events as function of \hat{p}_T for the different QCD samples. An upper \hat{p}_T cut is applied to avoid overlap between the samples and all distributions are scaled to an integrated luminosity of 1 pb^{-1} .

jet is required to be within $|\eta(\text{jet})| < 3.0$ and have a minimum corrected p_T such that the trigger is more than 99% efficient. For offline jet reconstruction the anti- k_T algorithm (see section 5.1.1) is applied on particle flow objects with a distance parameter $R_{k_T} = 0.5$. Furthermore, at least two reconstructed secondary vertices (SVs) are required. The IVF is used for vertex reconstruction with parameters and settings as described in section 6.7.4. The vertex finding and fitting are completely independent of any jet direction. The B candidate identification as described later in section 6.8 is applied, and both vertices are required to produce a B candidate with the following properties:

- 3D flight distance significance $S_{3D} > 5$
- pseudorapidity of the vertex flight direction in the range $|\eta(\text{SV})| < 2.0$
- transverse momentum $p_T(\text{SV}) > 8 \text{ GeV}$
- vertex mass $m_{\text{sv}} > 1.4 \text{ GeV}$.

These B candidates are referred to as “selected” B candidates. The B candidate four-momentum vector p_{sv} is calculated as the sum of all track four momenta (using pion mass hypothesis) of all vertices contributing to the B candidate. For $B \rightarrow D \rightarrow X$ decay chains, two or more vertices are merged into one B candidate.

Events with exactly two selected B candidates with a scalar sum of the B candidate masses $m_1 + m_2 > 4.5 \text{ GeV}$ are retained. A total of 160, 380 and 1038 events pass all these requirements for the three leading jet p_T regions with cuts at 56, 84 and 120 GeV. The contribution from events with three or more B candidates is measured to be less than 1% and they are not considered in the analysis.

4.5 Monte Carlo Event Generators

For comparison between the measured distributions and QCD predictions, several MC event generators are used: PYTHIA, MC@NLO, MadGraph/MadEvent and CASCADE. They are briefly described in section 2.3, including a description of some parameter settings used for this study. A summary of the most important settings is given in table 4.4 for convenience. Apart from the events simulated with PYTHIA, there is no full detector simulation done. For the other predictions, the anti- k_T jet algorithm is applied on generated particle level. These jets are subject to the same cuts in η and p_T as the reconstructed jets in data and PYTHIA ($|\eta(\text{jet})| < 3.0$ for the leading jet and minimum p_T above 56, 84 or 120 GeV for the three samples).

For MC@NLO, the factorization and renormalization scales are set equal to the transverse b mass ($\sqrt{m_b^2 + p_T^2}$). For MadGraph, the scales are not fixed, they change with the sum of the p_T of the partons. For CASCADE, the factorization scale is set by the angular ordering constraint. It is equal to $\mu^2 = \hat{s} + Q_T^2$, where Q_T is the vectorial sum of the transverse momenta of both incoming partons.

Generator	Version	PDF	m_b (GeV)	Showering	Detector Simulation
PYTHIA	6.422	CTEQ6L1	4.8	PYTHIA	yes
MC@NLO	3.4	CTEQ6M	4.75	Herwig 6.510	no
MadGraph	4	CTEQ6L1	0 / 4.75	PYTHIA	no
CASCADE	2.204	CCFM set A	4.75	PYTHIA	no

Table 4.4: Parameter settings for the Monte Carlo event generators used in this correlation study.

Chapter 5

B-tagging

The ability to identify jets containing B hadrons (b-jets) is important for many of the physics analyses at the LHC. Examples include measurements of top or bottom pair production, Higgs boson searches and also tests of new physics scenarios. The identification of jets originating from a b quark or \bar{b} antiquark is called b-tagging. Several algorithms are implemented in CMS [70]. They exploit different B hadron properties, such as the hard fragmentation, the high B mass, the long lifetime and semileptonic decay modes. The algorithms use jet properties to calculate a *discriminator* d associated to each jet. The discriminator can be a simple physical quantity for some taggers, or a more complex variable like the output of a neural network for others. The probability density distribution of d for b quarks is aimed to be as different as possible to that of light and c quarks and gluons. B-jets are then identified by choosing a threshold value of the discriminator. The dependence of the algorithm efficiency and purity on the threshold has been studied in detail [70].

B-tagging is not used for the correlation measurement presented herein. The angle is measured between flight directions of reconstructed secondary vertices and not between b-tagged jets. In the kinematic region where the two B hadrons are well separated, the SV based analysis is compared to a jet based analysis: the angle between two b-tagged jets is measured and the distribution is compared to the measured angular distribution obtained using the reconstructed SVs (see section 9).

In this chapter, an overview on the input objects for b-tagging is given and the different b-tagging algorithms implemented in CMS are discussed. A few performance studies, obtained with the first CMS data collected at $\sqrt{s} = 7$ TeV are shown and the special case of two nearly collinear b quarks is discussed.

5.1 Input for B-tagging

5.1.1 Jets

Jets are the most important input for b-tagging. There exist several jet algorithms meeting different requirements: from an experimental point of view jet reconstruction should be fast

(e.g. for triggering), from a theoretical point of view jet algorithms should be collinear and infrared safe. A jet algorithm is said to be infrared safe, if infrared singularities do not appear in the perturbative calculations and if it finds jets that are insensitive to any soft radiation in the event. Similar, an algorithm is collinear safe, if no collinear singularities appear and jets are insensitive to collinear radiation. Every jet algorithm needs input objects, a distance measurement and a recombination scheme [71]. The energy and momentum of a jet is defined as the sum of energies and momenta of its constituents. Often, calorimetric information is used as input for jet algorithms. Energy deposits in the ECAL and HCAL are summed. Instead of calorimeter towers, other objects such as tracks are suited as input for jet reconstruction. *Jet-plus-track* algorithms improve the energy measurement of the calorimeter jets exploiting the kinematics of tracks that are associated to the jets. In addition, there are PF jets. For those, the reconstruction and calibration of each particle is done individually, combining the information of all sub-detectors prior to formation of jets.

Different jet reconstruction algorithms are implemented in CMS, some based on *cones*, others are *clustering* algorithms. Only a brief description of some of the algorithms implemented in CMS is given here, more information is found in [72] and references therein.

Cone based algorithms

From an experimental point of view, the simplest jet algorithm is the *Iterative Cone* (IC) algorithm that is used e.g. by the CMS HLT. IC jets have a fixed cone size and all objects within the cone are counted to the same jet. For seeding, the first object in a p_T ordered list is chosen. All objects within a cone of radius R (meaning all objects with ΔR between object and seed direction smaller than R) are collected and the jet axis is recalculated. This is repeated until the axis is stable. The collection is then called a jet and the constituents are removed from the p_T ordered list. To save computing time and reduce noise, a threshold is applied on the input list objects. The IC algorithm is neither collinear nor infrared safe. Improvements of the IC are the *Midpoint Cone* and the *Seedless Infrared-Safe Cone* (SIS cone) algorithm. While the first one is at least infrared safe at NLO, the SIS cone algorithm is collinear and infrared safe [73, 74].

Clustering algorithms

Jets calculated with sequential clustering algorithms do not have a fixed cone size. One example of such an algorithm is the k_T algorithm [75]. For every input object i a “distance to the beam line” d_i and the “distances to other particles” d_{ij} are calculated (for all particles $j \neq i$):

$$d_i = E_{T,i}^2 \cdot D^2 \quad \text{and} \quad d_{ij} = \min(E_{T,i}^2, E_{T,j}^2) \cdot R_{ij}^2, \quad (5.1)$$

where R_{ij} corresponds to the ΔR between the directions of particles i and j and the parameter D plays the role of a cone size. By construction every pair of jets is guaranteed to be separated by $\Delta R > D$. For every i the smallest d_{ij} is compared to d_i and if $d_i > d_{ij}$ the object i is called a jet. Otherwise, objects i and j are merged. The k_T algorithm is relatively slow. A fast implementation exists [76].

The *anti- k_T* algorithm is a modification of the k_T algorithm. The distances are defined

slightly different: the exponent of $E_{T,i}$ gets a negative sign both in the definition of d_i and d_{ij} . The key feature of this algorithm is that soft particles do not modify the jet shape, while hard particles do. For pairs involving a hard and a soft particle the distance is small. Hence soft particles are combined with hard particles before recombining among themselves. That is similar to a cone algorithm and the anti- k_T algorithm is often seen as an infrared and collinear safe replacement of a cone algorithm.

For b-tagging in CMS calorimetric jets are used. Jet energy corrections and a p_T threshold of 20 GeV are applied. The cone size for jets used in b-tagging algorithms is $\Delta R = 0.5$.

5.1.2 Tracks

Apart from jets, tracks are an important ingredient for b-tagging. Track reconstruction is described later in section 6.1. One set of tracks is assigned to every jet and this set is used to compute the discriminators for algorithms based on secondary vertices or impact parameters. Since tracks from B hadron decays should be separated from tracks originating from the primary interaction vertex, it is important to have a precise measurement of the track parameters close to the interaction point. Hence, hits in the pixel detector play an important role. The following requirements reduce the number of poorly measured tracks:

- total number of silicon hits (pixel + strips) ≥ 8
- total number of pixel hits ≥ 2
- transverse impact parameter $IP_{xy} < 0.2$ cm
- longitudinal impact parameter $IP_z < 17$ cm
- transverse momentum $p_T > 1.0$ GeV
- χ^2 of the track fit divided by number of degrees of freedom < 5.0
- distance (ΔR) to the jet axis < 0.5 .

5.1.3 Primary Vertex

The primary (collision) vertex is also used as b-tagging input. It is reconstructed using all tracks in the event satisfying the above requirements. For the vertex fit the Adaptive Vertex Fitter (see section 6.2) is used. If there are several vertices found by the fitter, the one with the highest $\sum p_T^2$ is selected (the sum runs over all tracks of a vertex).

5.1.4 Leptons

Some b-tagging algorithms use lepton (muon) information. The muons used are called *global muons* [77] since information from the muon chambers is combined with tracker information in order to find the muon parameters.

5.2 Impact Parameter and Impact Parameter Significance

For a single track the *impact parameter* (IP) is defined as the distance between the vertex and the linearized track, where the track is linearized in the point of closest approach to the jet axis, see figure 5.1 [78]. Since the z resolution provided by the pixel detector is comparable to the resolution in the transverse plane, the IP can be calculated in three dimensions. The IP calculated in the transverse plane does also have some power to discriminate between b - and light or gluon jets. The IP uncertainty σ_{IP} might be of the same order as the IP magnitude IP , such that the track may or may not be originating from the primary vertex even if the IP is large. Hence, the impact parameter significance $s_{IP} = IP/\sigma_{IP}$ is more suited for b -tagging.

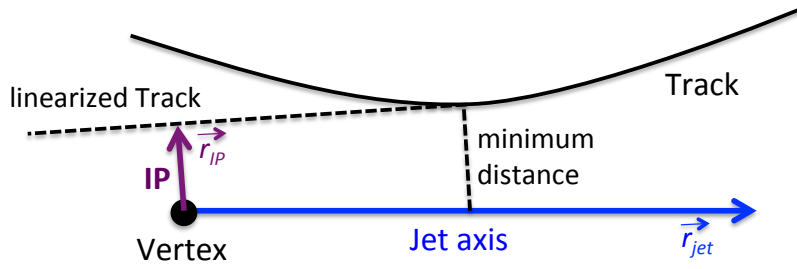


Figure 5.1: Definition of the impact parameter: distance between linearized track and vertex. The track is linearized in the point of closest approach to the jet axis. The sign of the impact parameter is the same as the sign of the scalar product between \vec{r}_{IP} (purple) and the jet direction \vec{r}_{jet} (blue).

To increase the discriminating power, a sign is assigned to the IP. It is equal to the sign of the scalar product between the jet direction \vec{r}_{jet} and the IP vector \vec{r}_{IP} as shown in figure 5.1.

$$\text{sgn}(IP) = \text{sgn}(\vec{r}_{IP} \cdot \vec{r}_{jet}) \quad (5.2)$$

For tracks coming from the primary vertex, the IP is distributed symmetrically around zero. For tracks originating from B hadron decays or other secondary decay vertices the sign is mostly positive, see figure 5.2. The IP significance is used to define probability to come from the primary vertex for each track. For this purpose all tracks with $IP < 0$ are taken to compute a probability density function R for a track to originate at the primary vertex. Based on this function, a probability P_{tr} is assigned to each track as follows [78]:

$$P_{tr}(s_{IP}) = \text{sgn}(s_{IP}) \cdot \int_{|s_{IP}|}^{\infty} R(x) dx. \quad (5.3)$$

To assure the track probability is always positive, it is redefined as

$$\tilde{P}_{tr} = \begin{cases} P_{tr}/2 & \text{for } P_{tr} > 0 \\ 1 + P_{tr}/2 & \text{otherwise.} \end{cases} \quad (5.4)$$

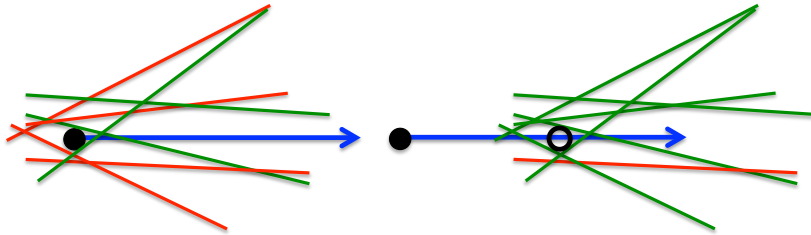


Figure 5.2: Sign of impact parameter: For tracks with origin close to the primary vertex positive IP signs (green) and negative IP signs (red) appear equally often (left). If the tracks originate from a vertex at some distance to the primary vertex tracks with positive IP dominate (right).

5.3 B-tagging Algorithms used in CMS

Track Counting algorithm

This is a very simple algorithm exploiting the long lifetime of the B hadrons. The signed impact parameter significance of all good tracks is calculated and ordered by decreasing significance. If there are at least N entries larger than a threshold d_{thr} the jet is identified as b-jet. The N th entry in the list is taken as continuous discriminator. In CMS this algorithm is used with two different settings: $N = 2$ for identifying b-jets with high efficiency and $N = 3$ for high b-jet purity.

Jet Probability algorithm

This algorithm is an extension of the previous one. For each track, the track probability P_{tr} to originate from the primary vertex is calculated and the information for all selected tracks is combined. Two different discriminators are provided. The first one is called “jet probability” P_{jet} . It provides the probability that all tracks in a jet come from the primary vertex and it is defined as

$$P_{jet} = \Pi \cdot \sum_{j=0}^{N-1} \frac{(-\ln \Pi)^j}{j!} \quad \text{with} \quad \Pi = \prod_{i=1}^N \tilde{P}_{tr}(i). \quad (5.5)$$

The second is called “jet B probability” and it calculates the probability giving the four most displaced tracks more weight in the calculation. The reason for considering four tracks is that the average charged tracks multiplicity of a B hadron is around 5, and the average track reconstruction efficiency is around 80% for tracks in jets.

Soft Lepton taggers

These algorithms search for an electron or muon from a semi-leptonic B decay, which has large momentum relative to the jet axis (p_T^{rel}). In the “soft muon by p_T^{rel} ” algorithm this variable is used as discriminator. There is also a “soft muon by IP significance” algorithm where s_{IP} of the muon is used instead, but only when found to be positive. It is also possible to combine the two variables. Similar taggers exist also for electrons. For jets with more

than one muon the one with the highest discriminator is taken.

Simple Secondary Vertex (SSV) algorithm

Secondary vertices are used to tag b-jets with high purity. An Adaptive Vertex Fitter is used to reconstruct the decay vertex (see section 6.2). Vertices sharing at least 65 % of their tracks with the primary vertex are removed from the list. If at least one secondary vertex is reconstructed within a jet the 3D flight distance significance is used as a discriminator for the SSV tagger ($d = -1$ if no vertex is reconstructed). The maximum efficiency is therefore limited by the probability of finding a vertex for a weakly decaying B hadron. It is around 60–70 %. The SSV tagger has been found to be more robust to tracker misalignment than the other lifetime-based taggers listed here. It is best suited for b-tagging with early LHC data. Two standard settings for the SSV tagger exist: one for high efficiency and one for high purity. The high-purity one uses a cut on the track multiplicity at the reconstructed secondary vertex.

Combined Secondary Vertex (CSV) algorithm

In a more complex approach, secondary vertices are combined with other lifetime-based information like IP significance of the tracks. Combining all available information allows to compute a discriminator when no secondary vertex is reconstructed. In some cases tracks with $s_{IP} > 2$ are combined to a "pseudo-vertex" (without applying a vertex fit) and this one is used to calculate a subset of secondary vertex based quantities. If even that is not possible the discriminator is calculated similarly as in the jet probability algorithm. The list of variables used in the CSV tagger is:

- the vertex category (real, pseudo, no vertex)
- 2D flight distance significance
- vertex mass
- number of tracks at the vertex
- fraction of energy carried by tracks at vertex with respect to all tracks in the jet
- 2D IP significance of the first track that raises the invariant mass above the charm threshold of 1.5 GeV when subsequently summing up tracks ordered by decreasing s_{IP} .
- number of tracks in the jet
- 3D signed IP significances of all tracks in the jet.

All these variables are used twice as input for a Likelihood Ratio. First to discriminate between b and c quarks, second for distinguishing between b and light jets. The two variables are added with weights 0.75 and 0.25 to calculate the final discriminator.

The performance of the different algorithms is studied in [70] in simulation and in [79] for the first LHC data collected with the CMS detector at $\sqrt{s} = 7$ TeV during spring 2010. The second performance study focuses on the TC and SSV algorithms. For the observables used for b-tagging, a good agreement between MC predictions and data has been found. Figure 5.3

shows the quantities directly related to the vertex reconstruction and figure 5.4 shows the SSV discriminators.

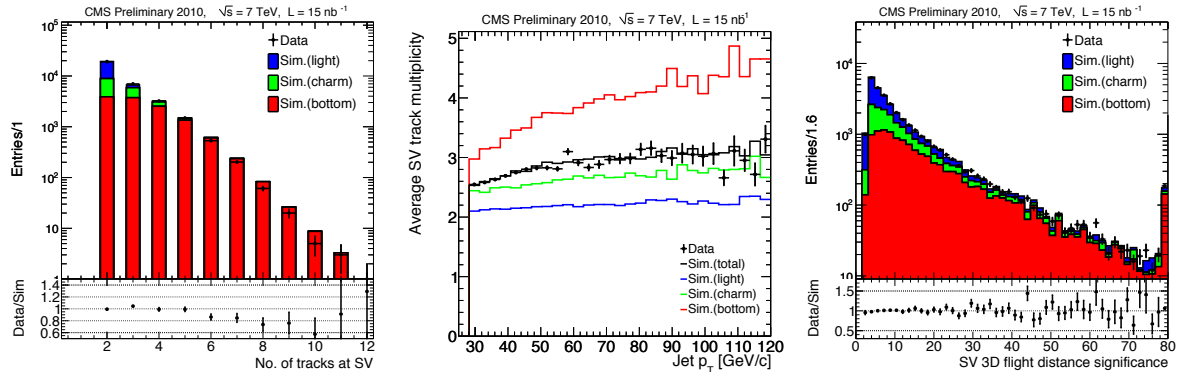


Figure 5.3: Secondary vertex properties: number of tracks (left), average number of tracks versus jet p_T (middle) and flight distance significance (right) [79].

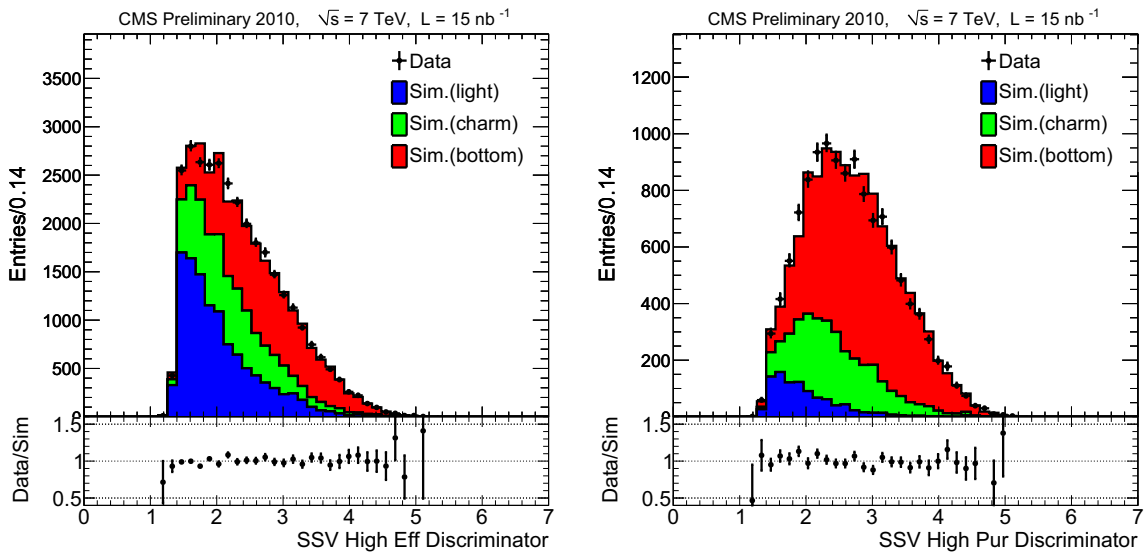


Figure 5.4: Comparison of MC prediction with data for SSV discriminators: high efficiency (left) and high purity (right) [79].

5.4 Small Opening Angles between Two B Hadrons

In principle, b-tagging algorithms compute how likely a jet is originating from a b quark, or, in other words, they compute a number, which indicates how likely a jet contains a B hadron. Depending on the tagger used, some more information about this B hadron or its decay is provided. The vertex based algorithms estimate the B hadron decay point, while the lepton

based algorithms tell that the B hadron decayed semileptonically. One interesting question is what happens if more than one B hadron is contained in a single jet. Especially for fixed cone size jets it is clear that if the opening angle between two b quarks is small enough the corresponding B hadrons are merged into one single jet, see figure 5.5.

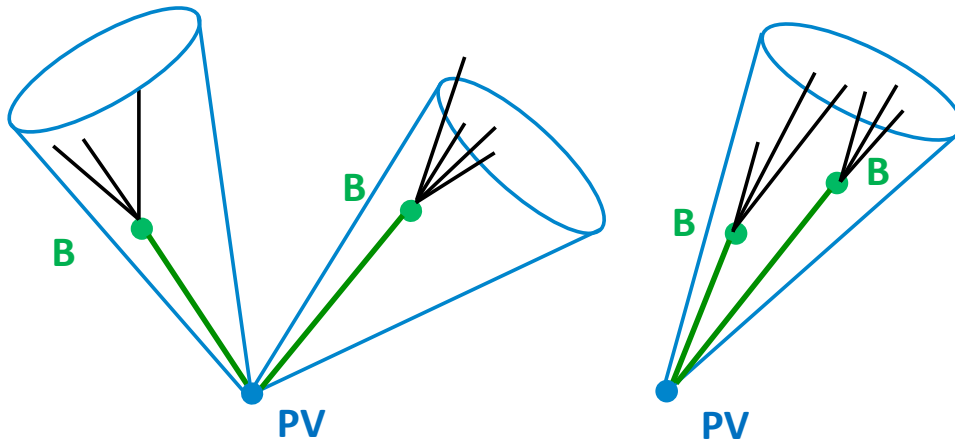


Figure 5.5: For small opening angles between two b quarks, two B hadrons are merged into a single jet.

This happens for example in a gluon jet, when the gluon splits into a $b\bar{b}$ pair. Due to the gluon mass being zero, the opening angle between the $b\bar{b}$ pairs is usually small and the corresponding B hadrons will often be contained in the same jet. On one hand, one can argue that since such a jet is initiated by a gluon and not by a b quark from the hard scattering process, it should not be called a b-jet. On the other hand, it will contain one or two B hadrons with their decay points and tracks not originating from the primary vertex and it might very well be tagged as b-jet. For inclusive b cross section measurements or for studying LO versus NLO $b\bar{b}$ production, one might want to include also those jets. For other studies, e.g. for a measurement of the angular correlations between B hadrons, it is important to know not only whether a jet might contain a B hadron or not, but also *how many* B hadrons it contains.

Chapter 6

Track and Vertex Reconstruction

Having a good estimate for the primary decay vertex position and its uncertainty is crucial for many physics analyses. Furthermore, the precise reconstruction of secondary vertices is important for B hadron or τ reconstruction. Tracks are the input for primary and secondary vertex reconstruction. Vertex reconstruction is done in two steps: vertex *finding* and vertex *fitting*. The first step involves grouping tracks that are compatible to be produced in a common point to form vertex candidates. Vertex fitting is the task to determine the best estimate of the vertex parameters like position, covariance matrix and eventually track parameters constrained by the vertex position for a given set of tracks.

Vertex fitting techniques are also used in the CMS trigger. Pixel standalone track and vertex reconstruction is fast enough to be used at HLT. Standard tracking with regional reconstruction is also used at HLT for a small fraction of events. The offline primary vertex reconstruction yields ultimate vertex position resolution, as well as the best possible estimation of the primary vertex position error matrix. It is part of the default sequence of modules run for every event. Since tracks play an important role for vertex finding, this chapter starts with a description of track reconstruction. Afterwards, methods for vertex finding and vertex fitting are presented. For b-tagging, the vertex finding is performed by a module called *Adaptive Vertex Reconstructor* (AVR). The AVR is capable to find and fit both primary and secondary vertices by calling an *Adaptive Vertex Fitter* (AVF) iteratively. Both, the AVF and the AVR are presented in this chapter. The Simple Secondary Vertex b-tagging algorithm is reviewed and its performance for the special case of jets containing two B hadrons is studied. The IVF that reconstructs vertices independent of any jet direction is presented and its performance is discussed. The concept of *B Candidates* is introduced in order to deal with events with several reconstructed secondary vertices possibly representing a $B \rightarrow D \rightarrow X$ decay chain. In the last section, the resolution of the ΔR reconstruction is discussed.

6.1 Track Reconstruction

Neglecting material effects, the trajectory of a charged particle in a magnetic field is described by a helix. In CMS the perigee parametrization is used to describe the helix. The track parameters are defined at the *Point of Closest Approach* (PCA) in the transverse plane with

respect to the beam line. Five parameters are needed:

- $\kappa = -qB_z/p_T$: signed transverse curvature
- θ : polar angle of the momentum vector
- ϕ_0 : azimuthal angle of the momentum vector at the PCA
- d_0 : signed transverse distance of the PCA
- d_z : longitudinal distance of the PCA.

Passive material present in the tracker volume leads to energy loss of the charged particles and to multiple scattering, and it has to be taken into account for reconstruction. The tracker material budget in units of radiation length is shown in figure 6.1. For track reconstruction, the detailed model used for simulation is simplified and replaced by an attribution of material to the measurement layers. The advantage is that the energy loss and the effect of multiple scattering are estimated at the tracking detector layers, without requiring additional propagation steps.

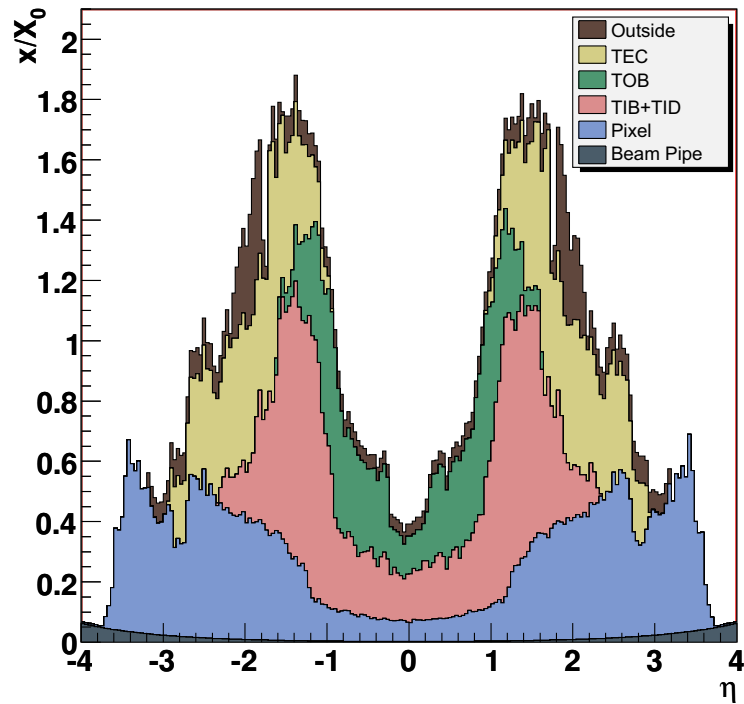


Figure 6.1: Tracker material budget in units of radiation length as a function of pseudorapidity for different sub-detectors [53].

The digitized hits in the tracker are transferred into local reconstructed hit positions in two steps: neighboring pixels or strips with a signal above threshold are clustered and the

reconstructed hit positions and errors are computed. Starting from the reconstructed hit positions, tracks are reconstructed as follows [80]:

- Seed finding
- Pattern recognition (trajectory building)
- Ambiguity resolution
- Final track fitting.

The default pattern recognition algorithm in CMS is the *Combinatorial Track Finder* (CTF) [80]. The CTF uses both the pixel and the strip detector for seed finding. The good resolution in three dimensions and the small occupancy in the pixel detector make tracking from the inside out the most efficient approach. In addition, the proximity to the beam line allows to use the transverse beam spot as constraint to reduce the combinatorial background. Pixel hit pairs and pixel triplets are used as seeds. There is also pixel-less seeding (e.g. for tracks coming from nuclear interactions). Pattern recognition is based on a combinatorial Kalman filter method. Starting from an initial trajectory seed, the CTF algorithm grows a tree of possible trajectories. In an iterative process layer by layer is processed from inside-out, and multiple scattering and energy loss are taken into account. At each layer compatible reconstructed hits are added to the trajectory based on a χ^2 measurement. If several compatible hits are found, several trajectory candidates are created. One trajectory candidate with no hit in the particular layer is also created. After adding a new hit to a trajectory it is updated according to the Kalman filter formalism, and then propagated to the next layer. At the end, based on the percentage of shared hits, trajectory duplicates are removed and the trajectories are refitted using a least-squares approach. The fit is performed using a Kalman filter and the list of hits is processed in an iterative way. In the smoothing step the track is fitted from the outside to the inside, which yields optimal estimates for the track parameters. The CTF is a robust algorithm and it can be optimized to reconstruct tracks with high efficiency (for offline reconstruction) or to be fast (for HLT).

In order to optimize tracking efficiency and purity an iterative tracking approach is used in CMS. The CTF algorithm including seeding, pattern recognition, final fit and cleaning is run several times. Each iteration is called a *step* of the CMS tracking. After each step the hits associated to high quality tracks are removed from the list of hits and in the next iteration the algorithm is run with different seeding and/or looser algorithmic requirements. Currently there are 6 iterations labeled from 0 to 5. In iteration 0 and 2 pixel triplets are used for seeding, in iterations 1 and 3 pixel pairs. The triplet seeding is run first because it is faster and has a lower fake rate. Algorithmic cuts in steps 2 and 3 are optimized to find lower momentum tracks. Steps 4 and 5 use only measurements in the strip detector for seeding and are optimized to find tracks that are significantly displaced from the beam line or tracks with missing pixel hits.

The tracking performance has been studied both in MC and in collision data. In figure 6.2 the global tracking efficiency for muons and pions is shown. The efficiency obtained for muons is high (around 99% for muons with $p_T = 100$ GeV) over a large η range. For pions the efficiency

is lower because of nuclear interactions in the tracker material. The tracking performance has been studied in early LHC operation using collision data at center-of-mass energies 0.9 and 2.36 TeV [81]. Some results are shown in figure 6.3. On average, more tracks per event are found in measured than in simulated data. This result can be used to tune the PYTHIA model. Except for the track multiplicity there is very good agreement between measured and simulated data. In [82] the performance of the track, vertex and beam line reconstruction in the first proton-proton collisions at 7 TeV is reported. The detector performance and the understanding of the CMS tracking detectors is found to be very good.

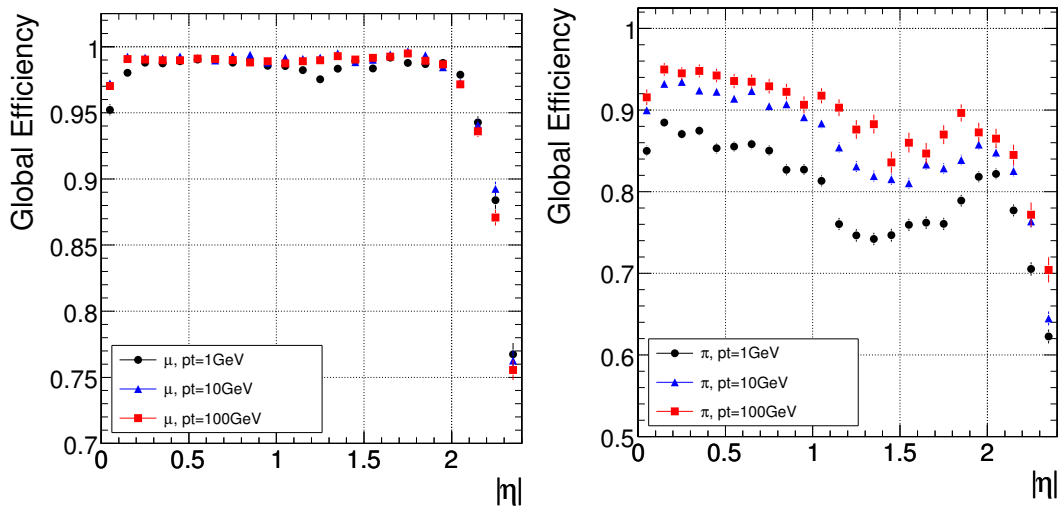


Figure 6.2: Track reconstruction efficiency for muons (left) and pions (right) with transverse momenta of 1, 10 and 100 GeV [80].

6.2 Adaptive Vertex Fitter

A vertex fitting algorithm computes the best estimates of vertex parameters, such as position and covariance matrix, from a given set of tracks. In addition, the track parameters can be recalculated and constrained to the vertex. The quality of the vertex is estimated by the total χ^2 of the fit or the number of degrees of freedom. Fitting algorithms can be divided into linear (least-squares) and non-linear algorithms. In linear algorithms all tracks have equal weight, while in non-linear algorithms tracks can be down-weighted or discarded (weight = 0) if they are not compatible with the vertex. In this section, the AVF is presented [83]. More information on vertex reconstruction in CMS can be found in [84].

The AVF is a non-linear fitting algorithm developed at CMS. It relies on the Kalman filter, which is based on the least-squares method. The sum of the squared standardized distances of all tracks from the vertex position

$$\frac{1}{2} \sum_{i=1}^n \frac{d_i^2(\vec{v})}{\sigma_i^2}, \quad (6.1)$$

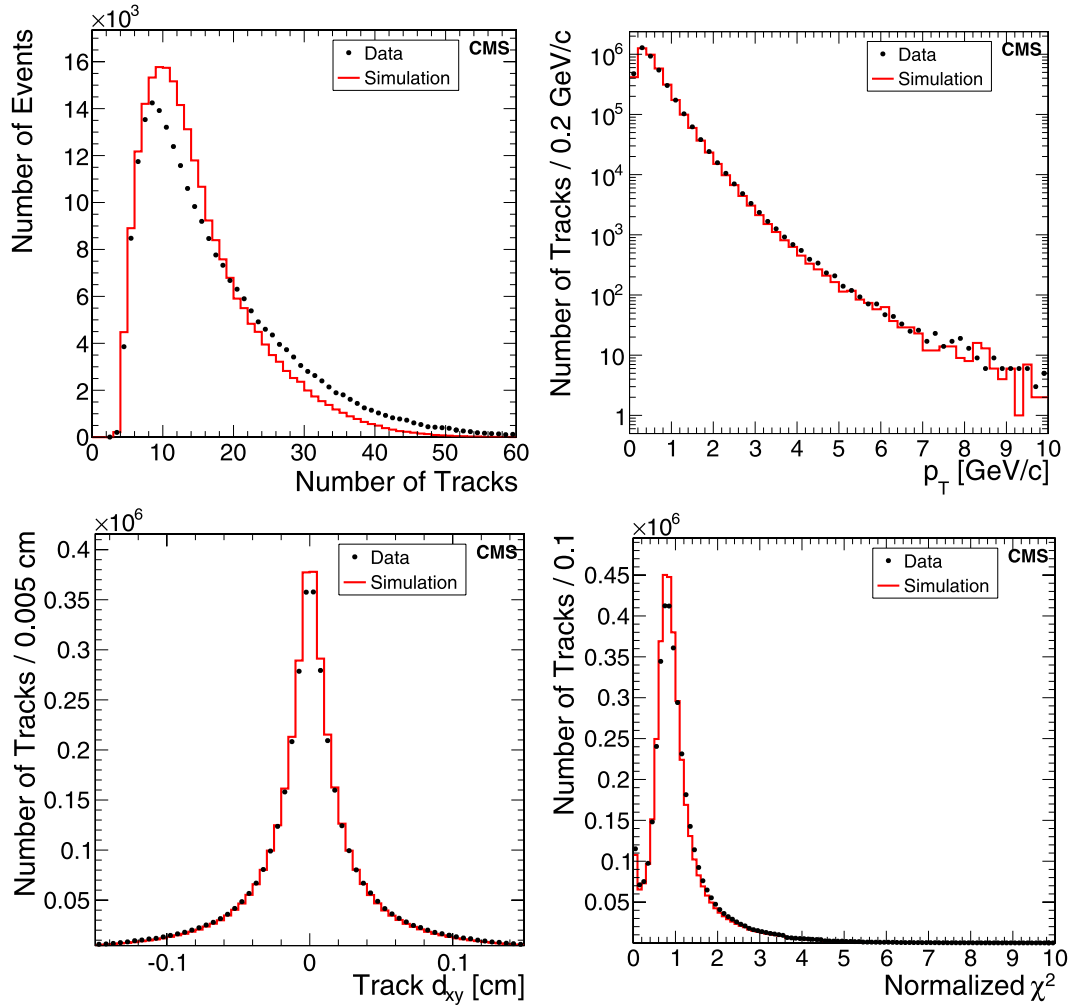


Figure 6.3: Comparison of measured (points) and simulated (solid line) distributions of tracking parameters: number of tracks per event (top left), transverse momentum p_T (top right), transverse impact parameter d_{xy} with respect to the primary vertex (bottom left) and normalized χ^2 (bottom right). Shown are tracks with $\sigma_{p_T}/p_T < 0.1$ and $|d_z| < 10\sigma_z$, where d_z is the longitudinal impact parameter with respect to the primary vertex and σ_z is the combined track and primary vertex uncertainty in z . The simulated distributions are normalized to the number of measured events (top left) or the number of reconstructed tracks in measured data (others) [81].

where \vec{v} is the estimated vertex position, is minimized. The distance is approximated using a first order Taylor expansion. The equation for finding the best vertex position becomes linear, and it is solved iteratively with the Kalman filter.

To avoid problems with mis-measured tracks or tracks not belonging to the fitted vertex, outlying tracks are down-weighted in the AVF with a weight w_i . The weight function depends on the distances between the tracks and the vertex, measured by χ^2 , and is given by the sigmoidal function

$$w_i(\chi_i^2) = \frac{1}{1 + e^{-\frac{\chi_c^2 - \chi_i^2}{2T}}}. \quad (6.2)$$

The parameter χ_c^2 is a cut off parameter for which the weight function crosses 0.5. For values of χ_i^2 exceeding χ_c^2 , a track is considered to be more likely an outlier. The “temperature” T controls the shape of the weight function, see figure 6.4. Including the weight functions the equation to solve is

$$\sum_{i=1}^n w_i(\chi_i^2(\vec{v})) \chi_i(\vec{v}) \frac{\partial \chi_i}{\partial \vec{v}} = 0. \quad (6.3)$$

Since the weights depend on the vertex position, an iterative procedure is applied to numerically solve the equation. An initial vertex position is needed to compute the weights. The vertex is then fitted with the weights obtained in the previous step and this is repeated until convergence. A geometric annealing scheme helps to avoid local minima. Starting from a pre-defined value, the temperature is lowered at each iteration according to an annealing schedule, see [83]. At each temperature, a Kalman filter is used to fit the vertex with the weights computed in the previous iteration. A geometric annealing is used, where the temperature is successively multiplied by a factor smaller than 1 until the temperature is 1. The factor is called annealing ratio.

Finding a good initial estimate for the vertex location (a seed) is very crucial for a good vertex fit, because it is not only used for computing the track weights for the first iteration, but also as linearization point for the tracks. The method for finding an initial vertex seed is called *Fraction-of Sample Mode with Weights* (FSMW) [83]. The method is based on *crossing points* of tracks. The coordinates of a crossing point are the algebraic mean of the coordinates of two points of closest approach of two tracks. A weight based on the inverse distance d between the two tracks is assigned to the crossing point. The default weight used is $w = (d + 10 \mu\text{m})^{-0.5}$. The FSMW finds the *mode* (point of highest density) of the crossing points in the three coordinates. Finding the mode is done by searching the shortest interval containing points with a sum of weights exceeding a fixed fraction (0.4 by default) of the sum of all weights. The procedure is repeated on the previous interval, until at most two points remain. The mode is then the average of the coordinates of the remaining points.

The performance of the AVF has been studied in [83] and [84] and has been found to improve the estimate of position and error of the reconstructed vertex with respect to the Kalman filter. It is the default algorithm used in CMS b-tagging.

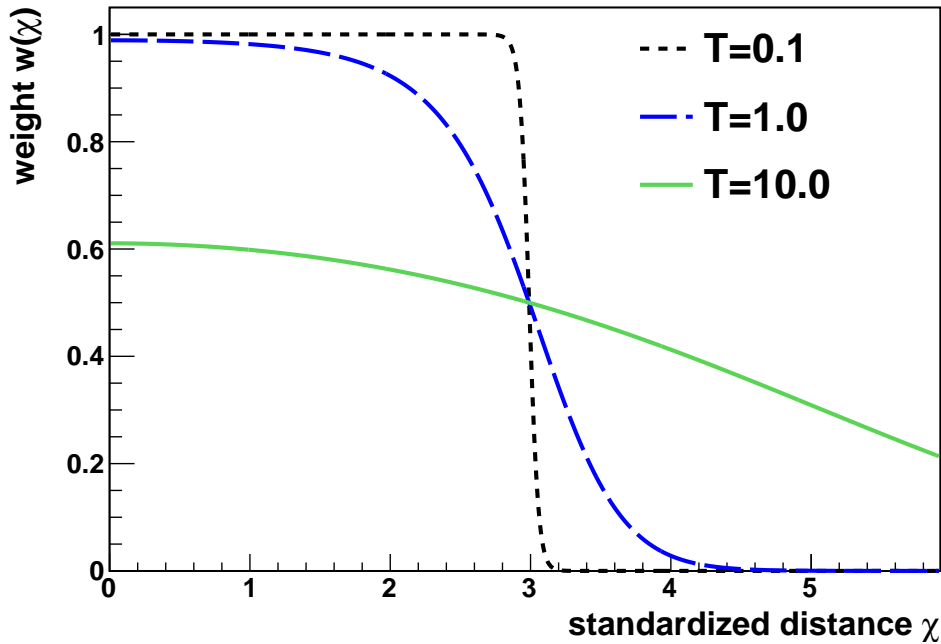


Figure 6.4: AVF weight function $w_i(\chi)$ for $\chi_c = 3$ and different temperatures T .

6.3 Adaptive Vertex Reconstructor

The AVR [85] finds and fits both primary and secondary vertices by means of calling the AVF iteratively. Numerical values for the χ_c^2 parameter, the initial temperature T_{ini} , and for the annealing ratio r are specified.

To find vertices within a specific jet, the AVR uses two sets of tracks: one set of tracks of the specific jet (or in general tracks that should be used for fitting secondary vertices) and one set of tracks from all other jets (all tracks, including those to fit the primary vertex). Vertices are fitted as follows:

- In the first iteration, the primary vertex is fitted using the sum of both sets. All tracks associated to the primary vertex are removed from the first set of tracks.
- The tracks remaining in the first set are used to fit secondary vertices iteratively. After every iteration the tracks remaining un-associated are passed again to the AVF as new input track set.
- This is repeated until less than two tracks are left or no further vertices are found.

Two different sets of parameters, one for the first and one for the other iterations, can be defined. The cut off parameter χ_c for the first iteration is tighter than for the other iterations, such that less tracks are assigned to the primary vertex and more tracks are available to find

secondary vertices with maximum efficiency. The vertices found by the AVR can be used for track refitting (smoothing). More details about the AVR are found in [85].

6.4 Secondary Vertex Definitions

The *flight direction* \vec{d}_{sv} of a secondary vertex (SV) is defined as the three dimensional vector from the primary vertex (PV) position to the SV position, see figure 6.5. The flight direction between two vertices is denoted by ΔR_{VV} , where $\Delta R = \sqrt{\Delta\phi^2 + \Delta\eta^2}$.

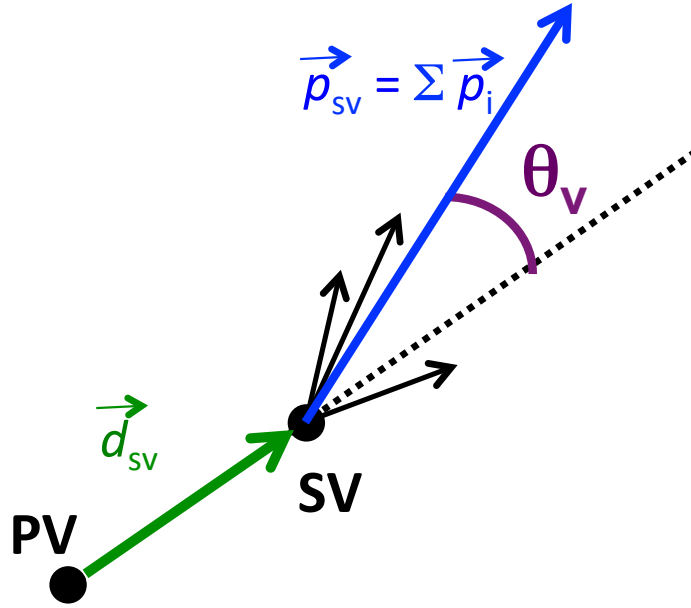


Figure 6.5: Definition of the vertex flight direction \vec{d}_{sv} (direction from the PV to the SV position), the vertex momentum \vec{p}_{sv} (sum of the track momenta). The angle between the flight direction and the momentum is θ_v .

The *flight distance* d_{3D} is computed as distance between PV and SV and the 2D flight distance d_{2D} is the projection onto the xy plane. The *flight distance significance* is $S_{3D} = d_{3D}/\sigma(d_{3D})$ in 3D and $S_{2D} = d_{2D}/\sigma(d_{2D})$ in 2D. The errors $\sigma(d_{3D})$ and $\sigma(d_{2D})$ are calculated using the covariance matrix of the secondary vertex.

The four-momentum of the vertex $p_{sv} = (E_{sv}, \vec{p}_{sv})$ is calculated as the sum of the four-momenta of all tracks i with weight $w_i > 0.5$ for the vertex (the vertex momentum is shown in figure 6.5). To obtain the track energy the pion mass hypothesis is used. The vertex mass is then calculated as $m_{sv} = \sqrt{E_{sv}^2 - \vec{p}_{sv}^2}$.

The angle between the vertex momentum \vec{p}_{sv} and the flight direction \vec{d}_{sv} is θ_v and ΔR_v is ΔR between those two directions.

The quality of the vertex is estimated by the total χ^2 of the fit or the normalized χ^2 , which is defined as χ^2 divided by the *number of degrees of freedom* (ndof). For unconstrained vertex fits, ndof is defined as

$$\text{ndof} = 2 \cdot \sum_i w_i - 3, \quad (6.4)$$

where the sum runs over all tracks used for the vertex fit.

When calculating the efficiency and purity of reconstructing B hadron decay points, the reconstructed SV is compared to the generated B hadron. How likely a reconstructed vertex is a B hadron decay point is estimated using the angles ΔR_{BV} between the vertex flight direction and the flight directions of the generated B hadrons. If not stated differently, the vertex is considered to be a B hadron decay point if the minimum $\Delta R_{BV} < 0.1$. If several vertices are reconstructed, a one-to-one matching between vertices and generated B hadrons is applied, see figure 6.6. A D vertex is a non-B vertex with at least one D hadron found in a cone of $\Delta R < 0.1$ around the vertex flight direction. All other vertices are denoted as light vertices (the light vertices include also fake vertices).

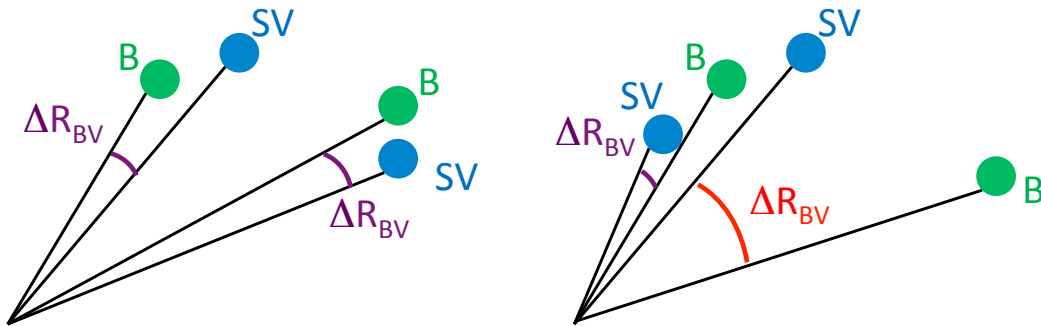


Figure 6.6: Definition of the angle ΔR_{BV} between reconstructed vertices and generated B hadrons. Left: Both vertices are reconstructed with $\Delta R_{BV} < 0.1$ for different B hadrons, i.e. both hadrons are considered a B hadron decay point. Right: Both vertices are reconstructed close to the same B hadron and because of the one-to-one matching applied one vertex is not considered a B hadron decay point.

6.5 Simple Secondary Vertex Algorithm

The SSV algorithm uses the AVR with one track set per jet. By default all of the high purity tracks within a cone of $\Delta R_c = 0.3$ around the jet axis are input to the AVR if they pass the following additional requirements: total number of hits ≥ 8 , number of pixel hits ≥ 2 , the minimum distance between the track and the jet axis is smaller than 0.2 cm and $p_T > 1$ GeV. The standard parameters used with the AVR in the SSV are shown in table 6.1.

Some checks are made on the compatibility of the secondary with the primary vertex, and some other cuts are applied to the vertices found:

	first iteration	other iterations
Cut off χ_c	1.8	6.0
Initial temperature T_{ini}	256	256
Annealing ratio r	0.25	0.25

Table 6.1: Standard parameters used with the AVR for b-tagging.

- Not more than 65 % of the tracks shared with the primary vertex
- $0.01 \text{ cm} < d_{2D} < 2.5 \text{ cm}$
- $S_{2D} > 3$
- $m_{sv} < 6.5 \text{ GeV}$
- ΔR_v between vertex flight direction and vertex momentum axis < 0.5
- invariant mass window around K_s rejected for vertices with two tracks (0.05 GeV).

The flight distance measurement is used as a discriminator as stated above. There is a choice between flight distance in 2D or 3D and between flight distance or flight distance significance. The default setting is to use the 3D flight distance significance S_{3D} . If no reconstructed secondary vertex is found, the value of the discriminator is set to -1 . Two variants based on the minimum number of tracks N_{trk} attached to the vertex are considered: $N_{trk} \geq 2$ yields the “high efficiency” version (SSVHE) and $N_{trk} \geq 3$ yields the “high purity” version (SSVHP). The algorithm is very robust compared to the other b-tagging algorithms, however its efficiency is limited to the efficiency of reconstructing at least one secondary vertex.

6.6 Two B Hadrons in a Single Jet

The angular correlations between B hadrons are measured either in 3D (ΔR) or in the transverse plane ($\Delta\phi$). One possibility to approximate the angle between two B hadrons is to measure the angle between two b-tagged jets, see figure 6.7.

When measuring angles between jets, events with both B hadrons inside a single jet will be lost for the correlation analysis. How often two B hadrons are predicted to be in the same jet is shown in figure 6.8 for one of the CMS samples produced with the PYTHIA event generator in summer 2008 with ideal detector conditions and a lower \hat{p}_T cut at 80 GeV. The jets are iterative cone jets with a cone of $\Delta R = 0.5$. The left plot shows the ΔR between the two generated B hadrons. It is found that the contribution in the small opening angle region is large for the given event energy scale. Only for three out of four events the B hadrons appear in different jets, while the amount of events with B hadrons centrally produced and in one single jet is 14 %. In the right plot the difference in azimuthal angle $\Delta\phi$ between two B hadrons and between the two jets containing the B hadrons is shown. In the low $\Delta\phi$ region many events are lost for correlation studies. The events at $\Delta\phi < 0.5$ are due to large separation in η , i.e. in 3D.

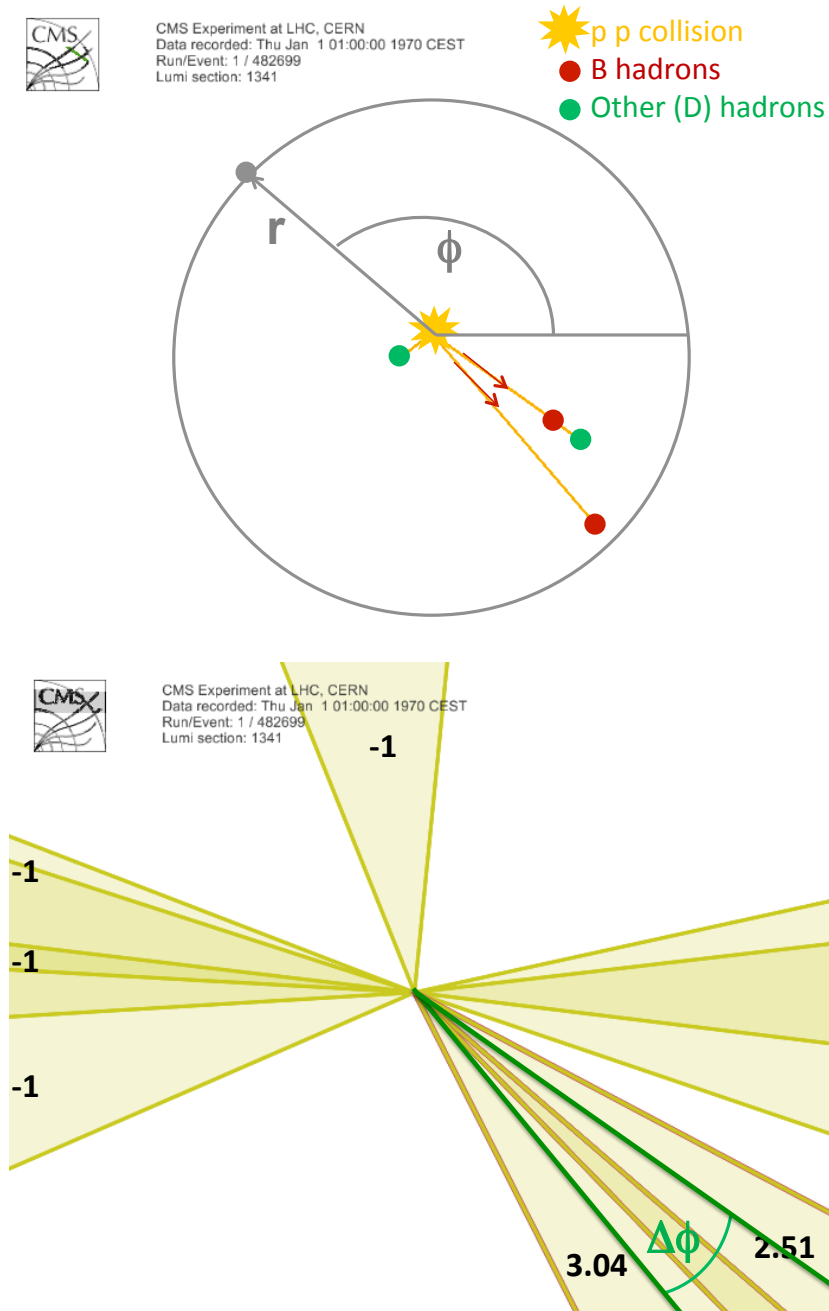


Figure 6.7: B-tagged jets are used to measure the angle between two B hadrons as shown in these two event displays. They show the $r\phi$ view of a MC event with two generated B hadrons and two D hadrons. In the top display the red points mark the generated B hadron decay points (and the green points mark the D hadrons). In the bottom display the jets reconstructed in this particular event are shown together with the SSV b-tag discriminator values (-1 if no vertex is found). The two jets containing the B hadrons are correctly tagged and the angle $\Delta\phi$ between the jets gives an accurate estimate of the angle between the B hadrons.

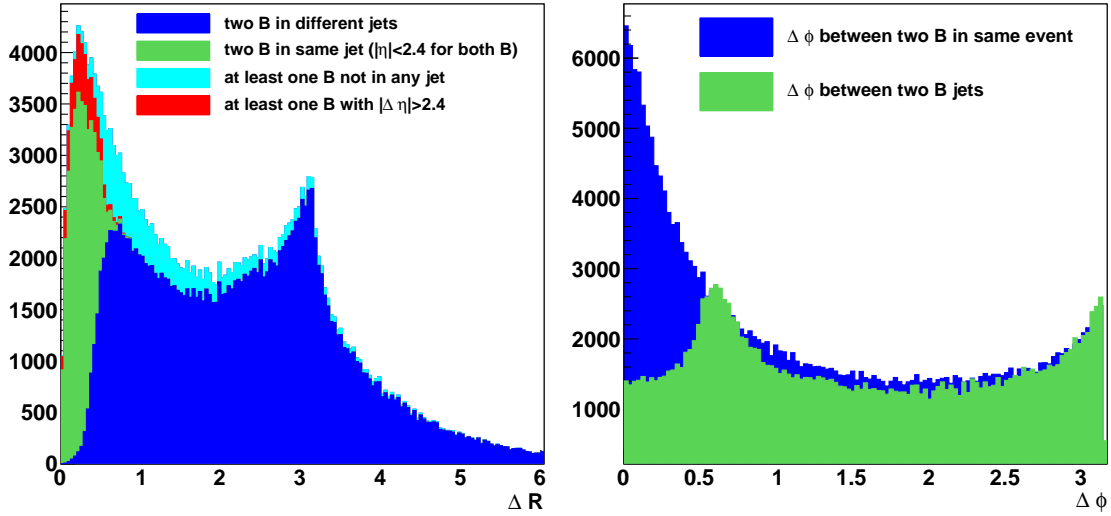


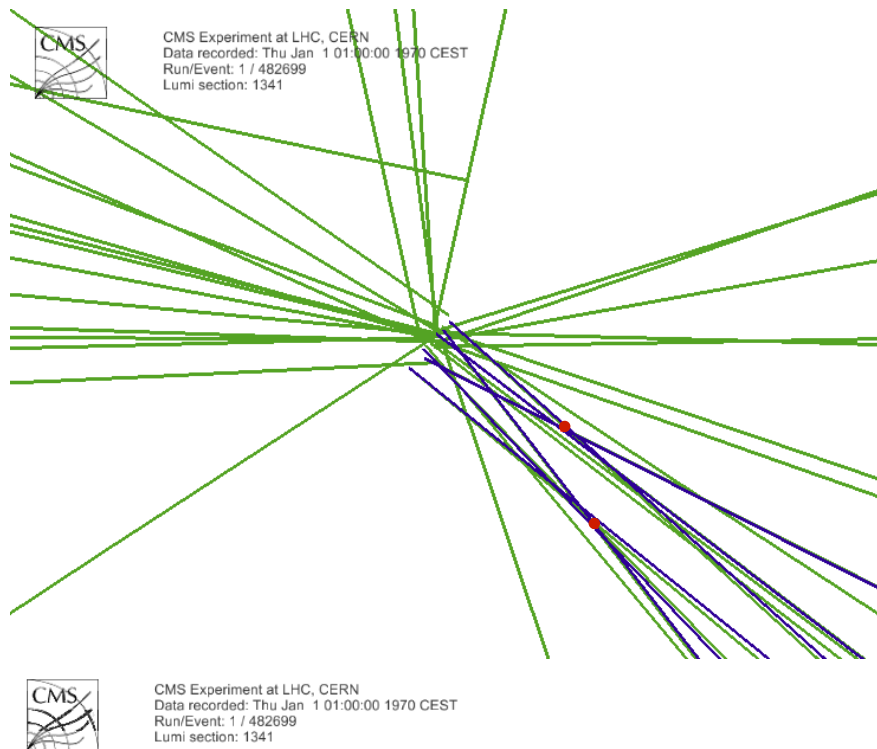
Figure 6.8: Left: angle ΔR between two B hadrons in different jets (blue), in the same jet and both B with $|\eta| < 2.4$ (green), at least one B not in any jet (cyan) and at least one B with $|\eta| > 2.4$ (red). Right: $\Delta\phi$ between B hadrons (blue) and between jets containing the B hadrons (green).

The inefficiency in the small angular region due to two B hadrons being in one single jet is reduced when using secondary vertex flight directions to measure the angle, see figure 6.9. Using vertices reconstructed by the SSV b-tagging algorithm instead of jets, the green events in figure 6.8 can partly be recovered.

Using secondary vertex information from the AVR with standard settings for measuring the angle between two B hadrons is efficient if there is at most one B in every jet: the flight direction of the B hadron and the jet direction are likely to be parallel and most tracks of the B hadron decay are close to the jet axis and selected as input for the AVR (the default cone size is $\Delta R_c < 0.3$). For small opening angles between b and \bar{b} the situation is different: by taking only tracks in a small cone around the jet axis some tracks of the decaying hadrons are lost and the reconstruction of one (or both) B hadrons might fail, see figure 6.10 (middle). Therefore, in the small angular region the efficiency ϵ_{BB} of reconstructing both B hadrons is significantly lower than the expected squared efficiency ϵ_B of reconstructing one B hadron inside a jet ($\epsilon_{BB} < \epsilon_B \cdot \epsilon_B$). One attempt to avoid losing tracks is to enlarge the track acceptance cone size and to rerun the b-tagging algorithm (or the AVR, respectively), see figure 6.10 (right).

Unfortunately, enlarging the cone size does not solve the problem of inefficiency in the low opening angle region. In figure 6.11 the angle between two generated B hadrons, ΔR_{BB} , is compared to the angle between two reconstructed SVs, ΔR_{VV} ¹. Only B hadrons pairs

¹for a spring 2010 PYTHIA CMS MC sample with startup detector conditions and $\hat{p}_T > 80$ GeV.



angle between B hadrons
measured angle between vertices
measured angle between jets

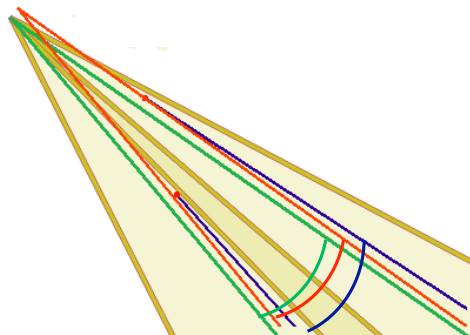


Figure 6.9: The angle between B hadrons is measured using the flight directions of two reconstructed secondary vertices (top). The event displays shown are the same event as in figure 6.7. The red dots mark the secondary vertex position. The tracks used for secondary vertex reconstruction are marked purple. The bottom plot shows the difference between the true angle measured between the generated B hadrons (red) and the angles measured with jets (green) and secondary vertices (blue) for the particular event.

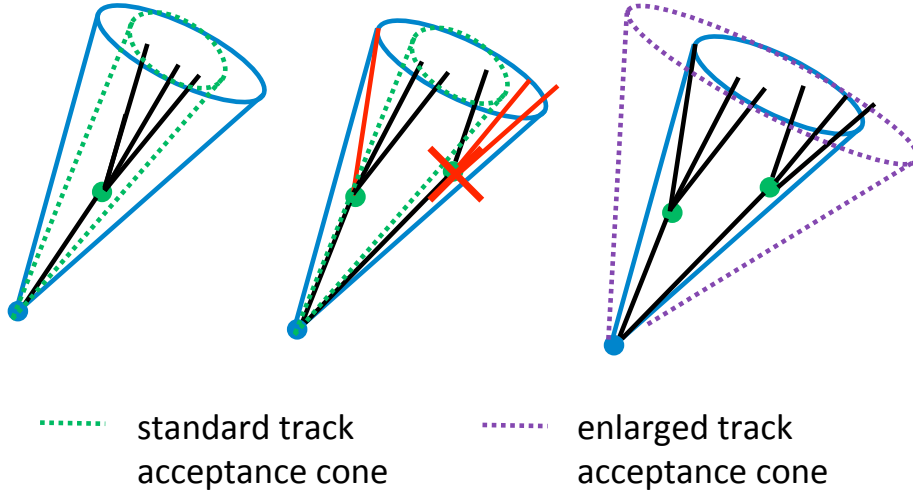


Figure 6.10: Left: One B hadron in a jet. All tracks are selected as input for the AVR and the vertex is reconstructed. Middle: Two B inside a single jet. Some tracks are outside the track acceptance cone (red) and are discarded. One vertex can still be reconstructed, the other one not. Right: The track acceptance cone was enlarged (even beyond the jet cone size), all tracks are inside the cone and both B hadrons are reconstructed.

with $p_T(B) > 15 \text{ GeV}$ and $|\eta(B)| < 2$ for both B and only SVs with mass above $> 1.4 \text{ GeV}$, $p_T(\text{SV}) > 8 \text{ GeV}$, $|\eta(\text{SV})| < 2$ and $S_{3D}(\text{SV}) > 5$ are considered. The top left plot shows ΔR_{BB} between two B hadrons, the top right plot shows ΔR_{VV} for events with two generated B hadrons, exactly two SVs sharing not more than 40% of the tracks (with respect to the vertex with lower number of tracks) and with difference $|\Delta R_{BB} - \Delta R_{VV}| < 0.1$. Different settings for the track acceptance cone size ΔR_c are plotted: standard (0.3), 0.8 and 1.0. It is found that especially in the low angle region more vertex pairs are reconstructed when the acceptance is increased to 0.8. The reconstruction efficiency is slightly higher, while the purity is very low in the small ΔR region for the larger cone sizes due to reconstruction of similar vertices from partially identical sets of tracks (see figure 6.11). The average efficiency and purity numbers are given in table 6.2. The performance for $\Delta R_c < 1.0$ is worse than for $\Delta R_c < 0.8$.

If the cone size is too large, more tracks are assigned to the primary vertex by the AVF and no “new” SVs are reconstructed. Clearly the purity can be increased when cutting harder on the quality of the vertex pairs, but the efficiency will suffer especially in the low ΔR region. Hence, the reconstruction efficiency for low opening angle cannot be improved by enlarging the track acceptance cone size around the jet axis.

A possible solution to the problem of low efficiency ϵ_{BB} in the small opening region is a vertex finder that is independent of any jet direction and uses track collections different from the ones of the AVR. Such an algorithm is presented in the next section.

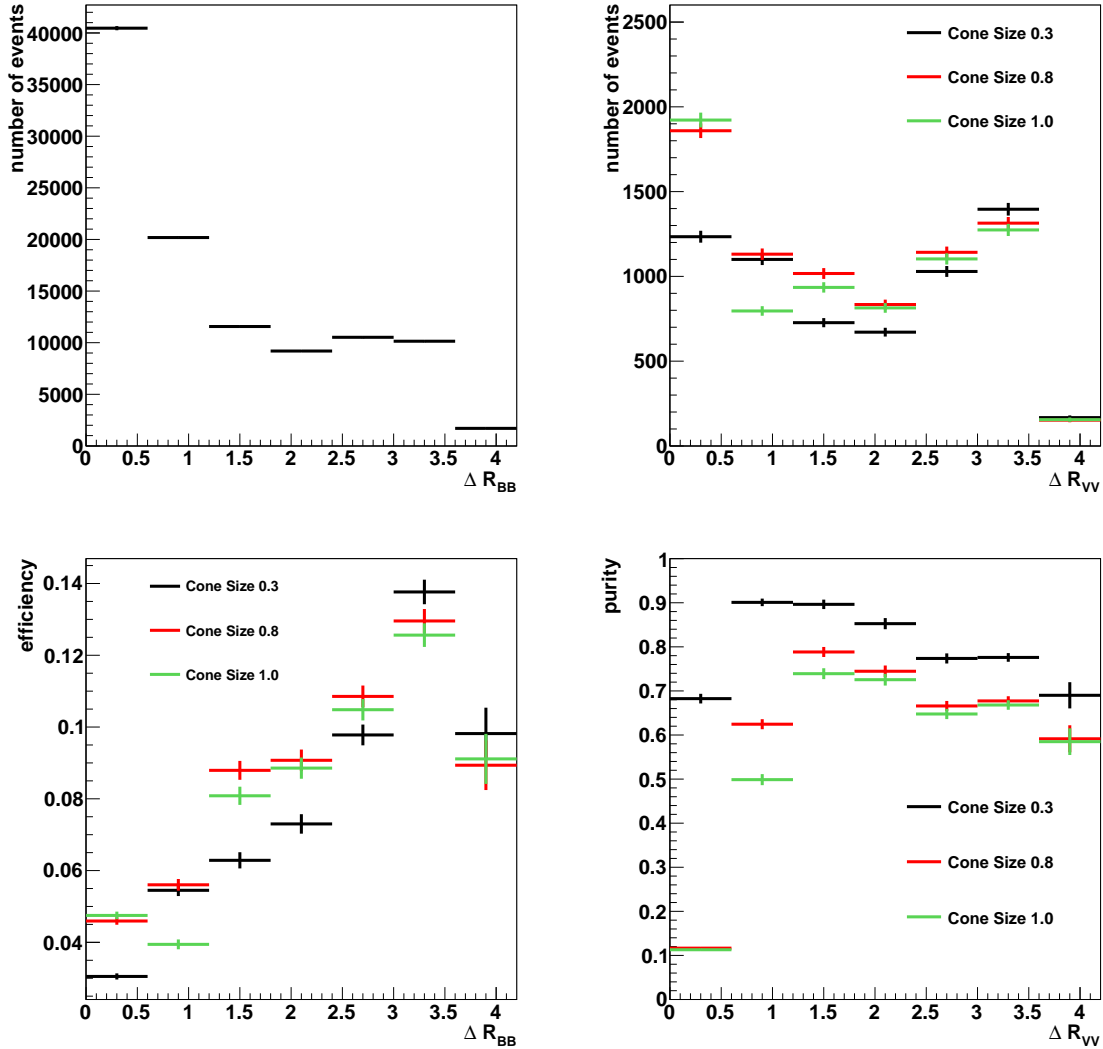


Figure 6.11: Top left: ΔR_{BB} between two B hadrons with $p_T(B) > 15 \text{ GeV}$ and $|\eta(B)| < 2.0$. Top right: ΔR_{VV} for events with two generated B and two reconstructed SVs with mass $> 1.4 \text{ GeV}$, $p_T(SV) > 8 \text{ GeV}$, $|\eta(SV)| < 2$ and $S_{3D}(SV) > 5$, sharing less than 40% of their tracks, and $|\Delta R_{BB} - \Delta R_{VV}| < 0.1$. Bottom left: Efficiency as a function of ΔR_{BB} defined as ratio between top right and top left plot. Bottom right: Purity as function of ΔR_{VV} (top right plot divided by number of events with two SVs as function of ΔR_{VV}). The different colors show different track acceptance cone size settings in the AVR: $\Delta R_c < 0.3$ (standard setting, black), $\Delta R_c < 0.8$ (red) and $\Delta R_c < 1.0$ (green).

Cone size	efficiency (%)	purity (%)
$\Delta R_c < 0.3$	6.1	79
$\Delta R_c < 0.8$	7.1	31
$\Delta R_c < 1.0$	6.7	28

Table 6.2: Comparison of average efficiency and purity for different track acceptance cone sizes used in the AVR.

6.7 Inclusive Vertex Finder

The IVF is designed to be completely independent of any jet direction. Figure 6.12 illustrates the basic concept. Track clusters are built using seed tracks with high 3D impact parameter value IP and significance s_{IP} . Herein, all tracks with 8 or more hits and $p_T > 0.8$ GeV are considered and the ones with impact parameter value $IP \geq 0.005$ cm and $s_{IP} \geq 1.5$ are taken as seeds.

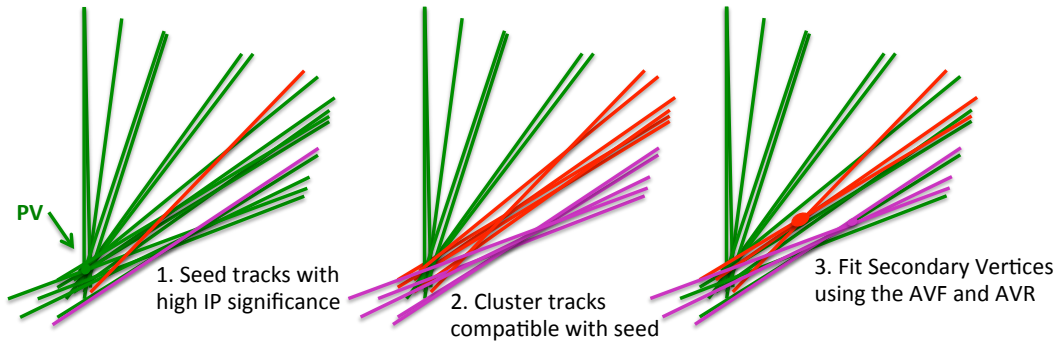


Figure 6.12: IVF: For seeding, tracks with high IP significance are used (left). For every seed, tracks compatible to originate from the same vertex as the seed track are clustered (middle). The different track clusters found are fitted using the AVR and the AVF (right).

6.7.1 Track Clustering

The tracks are clustered based on their compatibility to originate from the same secondary vertex as the seed track. This compatibility is computed using

- separation distance in three dimensions
- separation distance significance
- different angular separation variables.

To describe the clustering in more detail some variables need to be introduced. The distance between the two *points of closest approach* (PCA) of a track and a seed-track is $d_{s,t}$ and its significance is $s_{s,t}$. Angles used in the clustering procedure are illustrated in figure 6.13: an

angle θ_t (θ_s) between the vector from the primary vertex (PV) to PCA (seed/track) on the track (seed) and the direction of the track (seed) at the impact point. The angle θ_{ts} is the angle between the 2D track direction and the 2D seed direction (computed at the impact points of the track/seed). A track is added to a cluster if:

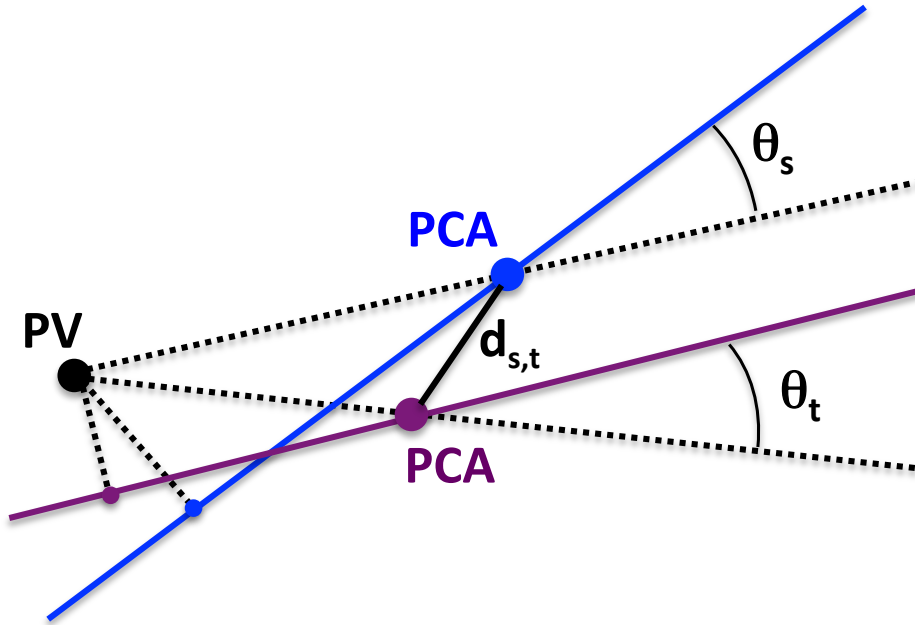


Figure 6.13: Definitions of variables used for track clustering. Shown is a seed track (blue) and one other track (purple). Both tracks are drawn linearized for simplicity. The PCA mark the two points of closest approach in 3D (the two tracks have in general no common point). Shown are the distance between seed and track $d_{s,t}$ and the angles between the vectors from the PV to the PCA and the track directions (θ_s , θ_t).

- $d_{s,t} < 500 \mu\text{m}$
- $s_{s,t} < 3.0$
- $\cos \theta_t > 0.5$, $\cos \theta_s > 0.5$ and $\cos \theta_{ts} > 0.5$
- $d_{s,t} \cdot \lambda_c < f_{density} \cdot d_{PV,seed}$,

where $d_{PV,seed}$ denotes the distance from the PV to the PCA (seed/track) on the seed, $\lambda_c = 1.0$ is a cluster scale factor and $f_{density}$ is an estimate of the track density at some distance. It is set to $f_{density} = 0.05$ for this study. An upper cut on the number of tracks in a cluster is applied: a cluster is not used if it contains more than 30 tracks. Such a set of tracks probably originates from the primary vertex.

Configurable parameters for the seeding are (default values in brackets): maximum cluster distance (500 μm) and distance significance (3.0), minimum cosine of angles defined above (0.5), the cluster scale factor (1.0) and the threshold for the maximum number of cluster tracks (30).

The performance of the IVF depends only weakly on these parameters. Changing the parameters for track clustering (by a factor 2 or $\frac{1}{2}$) has no major effect on the performance, as shown in section 6.7.5.

6.7.2 Vertex Fitting

Both a direct fit with the AVF and an iterative AVR procedure are attempted on the clustered tracks. The cutoff parameter χ_c for the first iteration in the AVR is set to 1.0, for the other iterations (and for standalone usage of the AVF) 3.0 is used. Vertex smoothing is applied. The following quality cuts are applied on the vertices:

- $S_{3D} > 0.5$
- $S_{2D} > 2.5$
- normalized $\chi^2 < 10$
- $\cos \theta_v > 0.98$.

6.7.3 Vertex Merging and Track Arbitration

Several clusters can have identical tracks, if for one seed a track is added to the cluster which itself is a seed track. Since the seeding depends both on the quantities of the seed track and of the other tracks, it is possible to have different clusters containing partly identical tracks. Those result in identical or similar reconstructed secondary vertices. These duplicates are cleaned up in the next step. All vertices that are compatible within their uncertainties (distance significance < 2.0) and that are sharing more than 70 % of their tracks are merged, the vertex with more tracks is kept. After this cleaning step, all secondary vertex tracks with a minimum of one hit in the pixel detector, a minimum of four tracker layers with measurements, and $p_T > 0.4 \text{ GeV}$ are tested for compatibility with the primary and secondary vertex and assigned to one of them. This is done on the basis of the 3D impact parameter with respect to the secondary vertex (IP_{sv}), the one with respect to the primary vertex (IP_{pv}), and their significances s_{sv} and s_{pv} . All vertices found in the previous step are refitted with all tracks that belong to one of the two following groups:

- $s_{sv} < 5$, $IP_{sv} < 0.01 \text{ cm}$, $IP_{sv} < IP_{pv}$, $\Delta R < 0.4$ between track and flight direction of vertex and $IP_{sv} < 0.333$ times the flight distance (decay length) of the vertex
- weight $w_i > 0.5$ in the previous vertex fit, $IP_{sv} < IP_{pv}$ and $\Delta R < 0.4$ (between flight and track direction).

6.7.4 Vertices for Correlation Measurement

The vertices produced in the steps described above are further processed. First, the vertex merging step is run for a second time with tighter cuts, vertex pairs are merged if they share more than 20% of their tracks and if the distance significance is smaller than 10. A filter is applied to increase the amount of vertices from B hadron decays and discard light vertices, D hadron vertices and primary vertices from pile-up events. The cuts are similar to the ones used in the b-tagging sequence. The values are listed in table 6.3.

Max. fraction of tracks shared with PV	0.65
Min. 2D flight distance	0.1 cm
Max. 2D flight distance	2.5 cm
Max. ΔR_v (flight direction, momentum)	0.1
K_s mass window width	0.05 GeV
Min. 2D flight distance significance	3
Min. number of tracks	3
Max. vertex mass	6.5 GeV

Table 6.3: Filter applied on vertices produced in IVF.

6.7.5 Performance

The IVF has been written by Andrea Rizzi² and it has been optimized for the $b\bar{b}$ correlation study presented in this thesis. Nevertheless, the vertices produced with the IVF are of general nature and can be used for any other study using secondary vertices. The IVF vertices are also suitable for the vertex based b-tagging algorithms. Performance studies and comparisons to other vertex finders have been done by Pierluigi Bortignon³. The performance of the IVF is similar to the standard b-tagging algorithms in most cases.

Since there are various possible use cases there is no study in terms of absolute efficiency or purity in this section. Instead it is shown how the efficiency and purity change with the parameters used for the seeding, clustering and the vertex fitting step. This has also been studied by Pierluigi Bortignon. The following seven parameters are adjustable in the different steps:

- Seeding: The minimum track IP and the minimum s_{IP} for tracks to be taken as seeds.
- Clustering: The cut on the distance between seed and track $d_{s,t}$ and on its significance $s_{s,t}$, the cluster scale λ_c and the minimum cosine of the three angles $\cos \theta_c$ (just one angle θ_c is specified for all three cuts).
- Vertexing: The minimum $\cos \theta_v$ and the minimum S_{2D} and S_{3D} .

²Postdoc at ETH.

³PhD student at ETH.

The dependence of the efficiency and purity on these parameters has been studied on a CMS PYTHIA $t\bar{t}$ sample. The IVF has been run several times with all parameters fixed to the standard setting except the parameter under investigation. All parameter settings are given in table 6.4.

	IP	s_{IP}	$d_{s,t}$	$s_{s,t}$	λ_c	$\cos \theta_c$	$\cos \theta_v$	s_v^{2D}	s_v^{3D}
default	50 μm	1.5	500 μm	3	1	0.5	0.98	2.5	0.5
$\times 2$	100 μm	3.0	1000 μm	6	2	0.8	0.2	5	1
$\times \frac{1}{2}$	25 μm	0.75	250 μm	1.5	0.5	0.25	0.49	1.25	0.25

Table 6.4: Seeding, clustering and vertexing parameter settings taken for studying the dependence of the IVF performance on these parameters. The value of the parameter has been multiplied by factors of 2 and 1/2. For the angles, the parameters have been varied differently.

The change in the reconstruction efficiency for a B hadron with $p_T > 15 \text{ GeV}$ and $|\eta| < 2.4$ is illustrated in figure 6.14. Reconstructing a B hadron means in this context to reconstruct a secondary vertex within a cone of $\Delta R_{BV} < 0.1$ around the B hadron direction. The purity is defined as the number of correctly reconstructed B vertices divided by the total number of reconstructed secondary vertices. The dependence of the purity on the parameters is shown in figure 6.15. It is found that both, efficiency and purity depend only weakly on the exact parameter setting. The maximum change in efficiency is slightly more than 2%, the maximum purity change is around 1.3%. In general, it is found that for most changes the efficiency decreases slightly, while the purity can be increased. The time for vertex reconstruction per event was also studied and the result is shown in figure 6.16. The largest influence on the IVF reconstruction time per event is found to be due to variations of the minimum s_{IP} of the seed tracks. A higher cut value leads to less seed tracks and therefore the time is shorter (order of 75% if s_{IP} is doubled). Neither the efficiency nor the purity change significantly. s_{IP} is thus well suited for improving the IVF performance. The IVF is found to be stable in terms of efficiency, purity and timing.

In order to motivate the different steps in the IVF reconstruction a posteriori, the different steps of the IVF are illustrated in the following. For the correlation study five vertex collections are produced:

- by the IVF
- in the first merging step
- in the arbitration step (where all tracks are assigned either to the PV or a SV)
- in the second merging step
- after the filtering.

For the following comparison, a CMS QCD sample produced with PYTHIA in spring 2010 with 80 GeV \hat{p}_T cut (3221800 events, 9% of them with two B hadrons) is used. One MC event

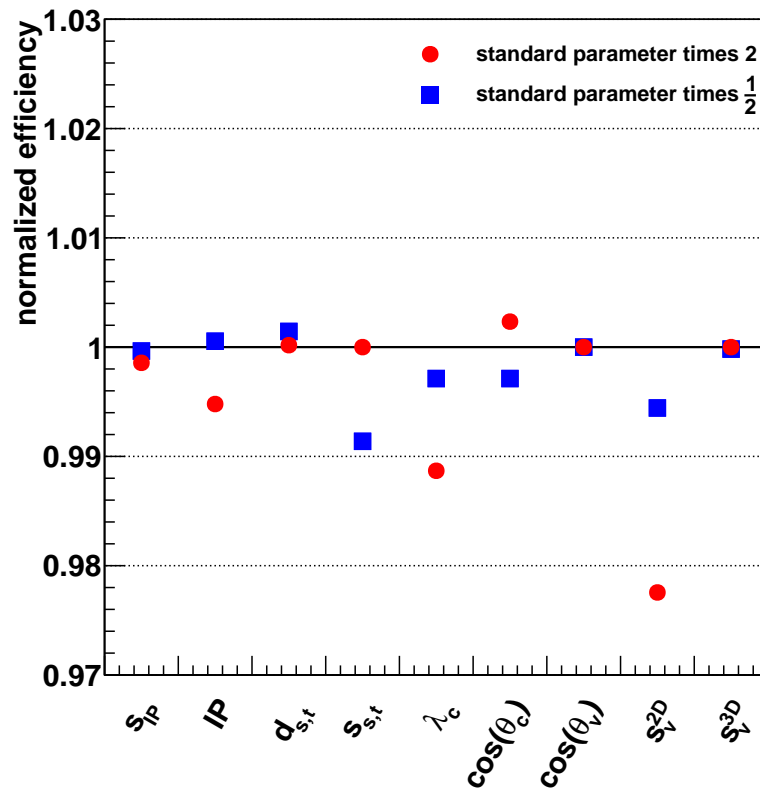


Figure 6.14: Dependence of the efficiency on the IVF parameters. The efficiency is drawn normalized to the efficiency with standard settings. The efficiency of reconstructing a B hadron ($p_T > 15$ GeV, $|\eta| < 2.4$) is defined as number of B hadrons with at least one SV in a cone ($\Delta R < 0.1$) around its flight direction divided by the total number of B hadrons.

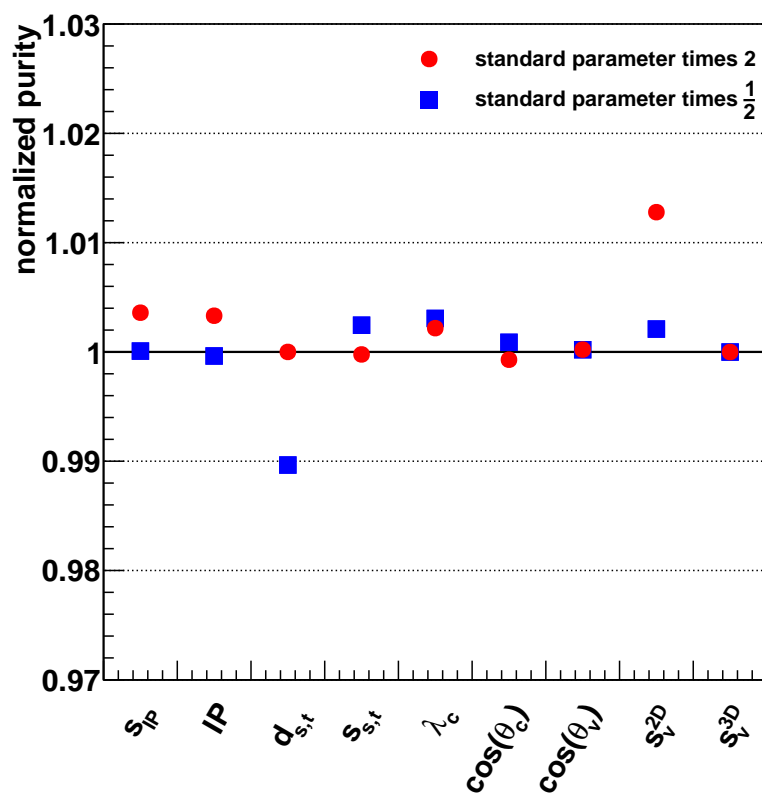


Figure 6.15: Dependence of the B vertex purity on the IVF parameters. The purity is drawn normalized to the purity with standard settings. It is defined as number of reconstructed vertices in a cone of $\Delta R < 0.1$ around a B hadron divided by the total number of reconstructed secondary vertices.

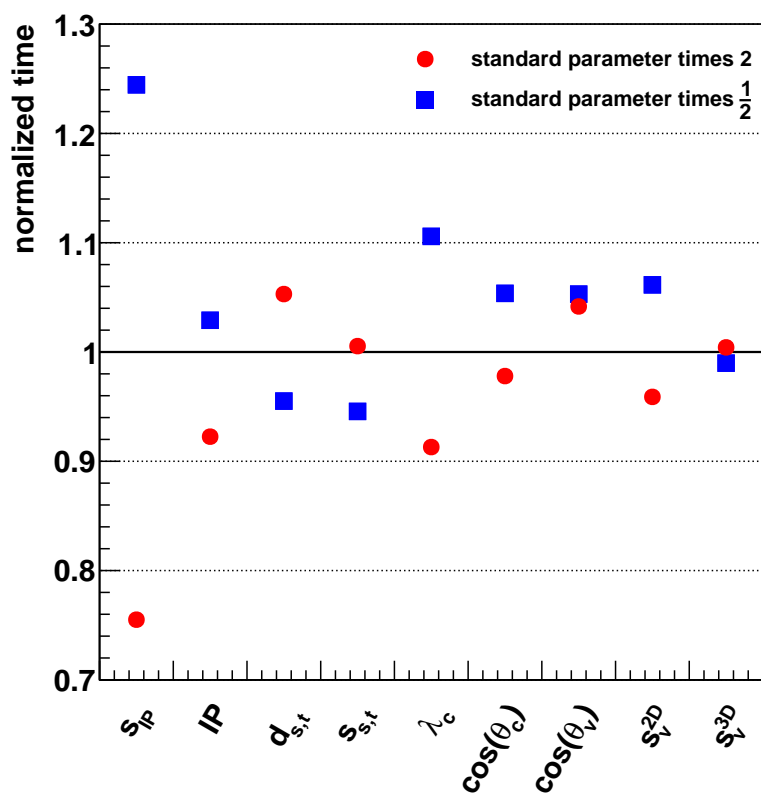


Figure 6.16: Dependence of the time needed for vertex reconstruction steps on the choice of the seeding, clustering and vertexing parameters. The time is drawn normalized to the time with standard settings.

with two B hadrons ($\Delta R_{BB} = 0.499$) is chosen to explicitly show the different steps. In the first step of the IVF, 22 seed tracks are found for this particular event. In the clustering step, 12 clusters are built out of those. For the rest of the seed tracks, no other tracks compatible for building a vertex with the seed are found. Some of the clusters are identical. An example of two different clusters containing partly identical tracks is a seed track a that is found to be compatible with a track b and forms a cluster of two tracks (ab), while b itself is a seed track and found to be compatible with track a and a third track c to form a cluster of three tracks (abc). The tracks used in the different clusters and the number of vertices reconstructed for each cluster are indicated in table 6.5. Because the AVF and the AVR are both used for finding/fitting secondary vertices, the same vertex appears often twice in the first collection. Only in the vertex merging step the duplicates are removed, and in the subsequent steps the number of vertices is further reduced more and more in order to keep only good quality vertices.

Tracks	1,5,6 10,38 78	1,5 36 38	8,9 10	8,9 10	1,6 8,9 10	21 26	21 26 30	26,28 29,30 76	1,5 36 38	69 76	28,29 30,76	1 78
Vertices	3	2	2	2	3	2	2	3	2	2	3	2
Cuts	3	2	2	2	2	2	0	1	2	2	1	2

Table 6.5: Track clusters for a sample MC event. The numbers indicate the numbers of the tracks in the track collections. The second row gives the number of vertices that are fit from the cluster and the third row the number surviving the cuts applied for IVF vertices.

Details about the vertices in the five collections are listed in table 6.6 and shown in figure 6.17. The table shows the position coordinates with their uncertainty as well as the number of tracks (ntr), the χ^2 and the number of degrees of freedom (ndof). The 22 vertices produced in the first step are grouped in 9 groups of almost identical vertices. The reasons are that similar track clusters are obtained by different seed tracks and that the AVF and the AVR are both used to fit vertices. One vertex per group is left after the merging step. In the arbitration step, the number of vertices is reduced from 9 to 5. Vertices are lost if just one track is left, because either part of the tracks of a vertex from the merger step are more compatible to originate from the PV or they do not pass the quality cuts applied in the arbitration step. After the second vertex merging with tighter settings four vertices are left, and finally two of them are selected in the vertex filter.

Four event displays for the selected two B event are shown in figure 6.18. In the top left event display all the vertices left after the first merging step are shown. To give a length scale the pixel barrel detector is drawn. Five vertices are located close together in the center of the detector, while there are four displaced vertices. A zoomed version of the event is shown in the top right plot. Apart from the two B hadrons there are four D hadrons generated in this event, two of them at the B hadron decay points. The decay points of the generated B and D hadrons are drawn in red and bright red. The other colors show the vertices after the different steps. Because the vertices are refitted only after the arbitration step the vertices produced in the later steps hide the ones of the previous steps. This means that e.g. a “selected” vertex

collection	x	σ_x	y	σ_y	z	σ_z	ntr	χ^2	ndof
Finder	0.055	0.006	-0.074	0.013	-4.112	0.027	3	0.614	2.89
Finder	1.557	0.096	-7.3	0.421	11.844	0.937	2	0.136	0.939
Finder	1.288	0.069	-8.286	0.487	15.118	1.145	6	0.568	0.926
Finder	0.08	0.006	-0.52	0.035	-3.196	0.077	3	1.657	2.866
Finder	0.08	0.006	-0.52	0.035	-3.196	0.078	4	1.622	2.867
Finder	0.29	0.015	-0.405	0.026	-3.347	0.058	3	1.235	2.869
Finder	0.29	0.015	-0.405	0.026	-3.347	0.058	3	1.244	2.869
Finder	0.29	0.015	-0.405	0.026	-3.347	0.058	3	1.235	2.869
Finder	0.29	0.015	-0.405	0.026	-3.347	0.058	3	1.28	2.867
Finder	0.056	0.006	-0.071	0.013	-4.118	0.027	4	4.73	4.678
Finder	0.056	0.006	-0.071	0.013	-4.118	0.027	5	4.721	4.678
Finder	-0.643	0.02	0.605	0.017	-2.901	0.04	2	0.495	0.928
Finder	-0.643	0.02	0.605	0.017	-2.901	0.04	2	0.495	0.928
Finder	0.041	0.005	0.166	0.032	-3.444	0.159	5	3.1	4.775
Finder	0.08	0.006	-0.52	0.035	-3.196	0.077	3	1.657	2.866
Finder	0.08	0.006	-0.52	0.035	-3.196	0.078	4	1.622	2.867
Finder	-11.513	0.177	10.695	0.164	20.521	0.396	2	0.289	0.935
Finder	-11.513	0.177	10.695	0.164	20.521	0.396	2	0.289	0.935
Finder	0.041	0.005	0.164	0.032	-3.45	0.157	5	3.263	4.715
Finder	0.394	0.009	-13.009	0.608	22.44	1.246	2	0	0.943
Finder	0.394	0.009	-13.009	0.608	22.44	1.246	2	0	0.943
Merger (loose)	1.557	0.096	-7.3	0.421	11.844	0.937	2	0.136	0.939
Merger (loose)	1.288	0.069	-8.286	0.487	15.118	1.145	6	0.568	0.926
Merger (loose)	0.29	0.015	-0.405	0.026	-3.347	0.058	3	1.28	2.867
Merger (loose)	0.056	0.006	-0.071	0.013	-4.118	0.027	5	4.721	4.678
Merger (loose)	-0.643	0.02	0.605	0.017	-2.901	0.04	2	0.495	0.928
Merger (loose)	0.08	0.006	-0.52	0.035	-3.196	0.078	4	1.622	2.867
Merger (loose)	-11.513	0.177	10.695	0.164	20.521	0.396	2	0.289	0.935
Merger (loose)	0.041	0.005	0.164	0.032	-3.45	0.157	5	3.263	4.715
Merger (loose)	0.394	0.009	-13.009	0.608	22.44	1.246	2	0	0.943
Arbitration	1.568	0.037	-7.343	0.16	11.94	0.361	2	0.195	0.938
Arbitration	0.286	0.014	-0.397	0.024	-3.365	0.055	4	2.129	4.818
Arbitration	0.052	0.007	-0.101	0.068	-4.045	0.139	3	4.873	2.401
Arbitration	-0.643	0.02	0.605	0.017	-2.901	0.04	2	0.494	0.928
Arbitration	0.079	0.004	-0.524	0.029	-3.182	0.061	4	3.158	4.801
Merger (tight)	1.568	0.037	-7.343	0.16	11.94	0.361	2	0.195	0.938
Merger (tight)	0.286	0.014	-0.397	0.024	-3.365	0.055	4	2.129	4.818
Merger (tight)	-0.643	0.02	0.605	0.017	-2.901	0.04	2	0.494	0.928
Merger (tight)	0.079	0.004	-0.524	0.029	-3.182	0.061	4	3.158	4.801
Selected	0.286	0.014	-0.397	0.024	-3.365	0.055	4	2.129	4.818
Selected	0.079	0.004	-0.524	0.029	-3.182	0.061	4	3.158	4.801

Table 6.6: Vertex properties for the vertices produced in the different steps: position and position uncertainty ($x, \sigma_x, y, \sigma_y, z, \sigma_z$) given in nm, number of tracks (ntr), χ^2 and number of degrees of freedom (ndof).

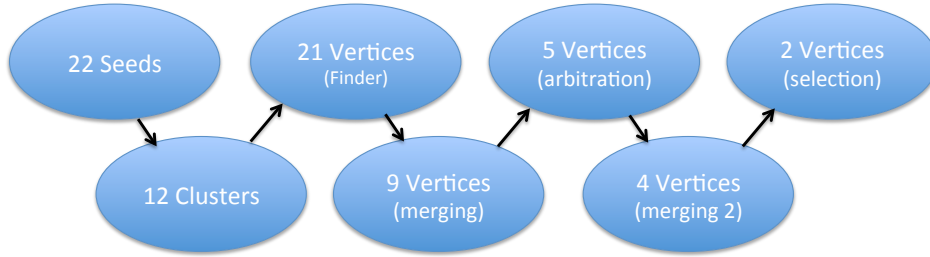


Figure 6.17: Number of objects after different steps of the IVF for the sample MC event.

is also a “merger 2” vertex (but not vice versa). In the arbitrator step, one vertex that is not close to any B or D hadron decay point is lost. In the second merger step, the vertex between the two B hadron flight directions is lost, and in the filter the vertex at the decay point of one D hadron that is not originating from a B hadron is not selected, such that the two selected vertices are indeed the two vertices corresponding to the B hadron decay. The third figure shows the positions and tracks of the merger vertices, and in the last subfigure the two selected vertices are shown.

The number of vertices that are produced in the different steps for the full PYTHIA QCD sample are shown in figure 6.19. The number of vertices per event is shown for all events, for events with exactly two B hadrons and for events with no generated B hadrons. The number of vertices per B hadron ($\Delta R_{BV} < 0.1$) is also shown in figure 6.19. For the finder step, the number of vertices per event is mostly even because of simultaneous use of the AVR and AVF. In table 6.7 the mean number of vertices for the four different plots are indicated. As shown in the figure, up to more than 40 vertices are produced in the finder step. In average there are 6.3 vertices per event. This number is already reduced to 2.5 in the merger step and then it is 1.4 after the arbitration step. In the filter step, the average number of vertices is reduced to 0.10. In events with two B hadrons there are in average 3.9 vertices after the first merging step, 1.6 times more than in events without B hadrons. This factor is increased to 15.1 for the selected vertices (0.65 in average per event with two B hadrons). The mean number of vertices per B hadron is reduced from 0.84 after the first merging step to 0.29 after filtering. Clearly one vertex per B hadron would be desirable. However it is also important to reduce the number of vertices originating from D and light hadron decays and in this reduction step also some B hadron vertices are lost.

The normalized χ^2 of the vertex fit and the number of tracks assigned to a vertex are shown in figure 6.20 for the vertex collections produced in the different steps. Both distributions are normalized to one. The normalized χ^2 distribution looks very similar for all steps apart from the selected vertices. The number of tracks distribution does not change much in the first four steps, but it is found that in the arbitration step some tracks are lost mainly for vertices with a large number of tracks.

The invariant mass, the 3D flight distance, the 3D flight distance significance and the ΔR between the vertex flight direction and the B hadron direction of the closest B hadron (for

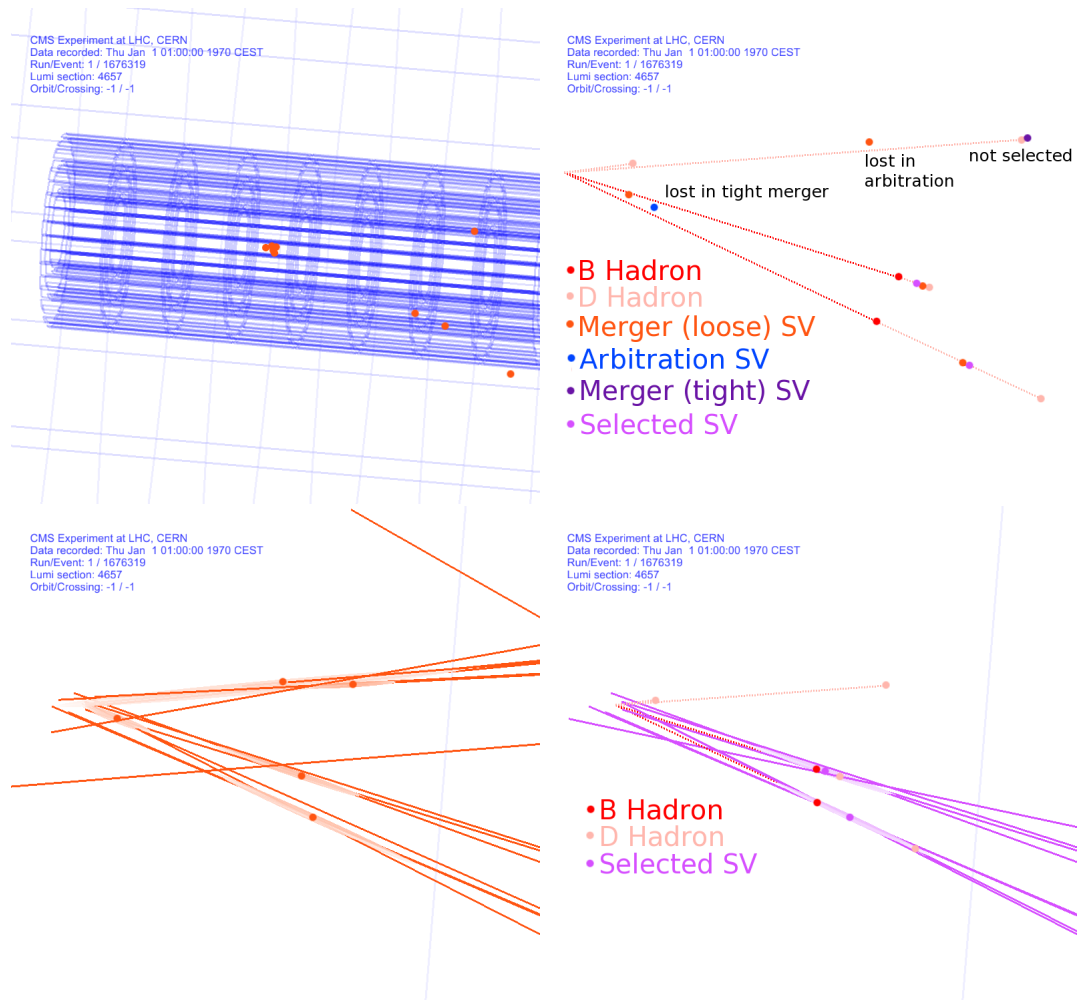


Figure 6.18: Event displays for a sample PYTHIA MC event. Top left: After the merging step there are nine vertices (orange). To give a length scale the pixel barrel detector is schematically drawn (blue). Top right: Zoom to the central region of the event. The B (red) and D (bright red) hadron decay points are shown as well as the vertices left after different IVF steps. Bottom left: The position and tracks of the (central) vertices produced in the merging step. Bottom right: The selected vertices with their tracks.

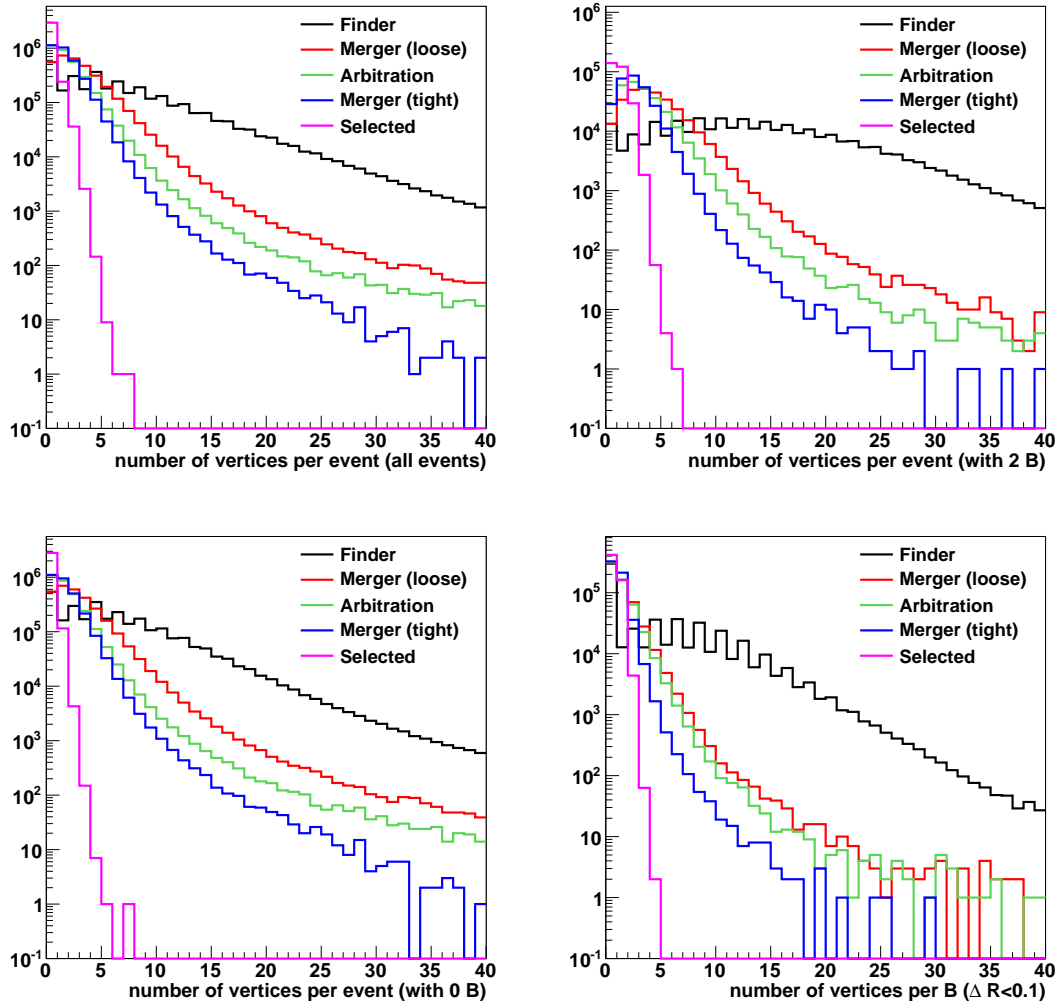


Figure 6.19: Number of vertices produced in the different steps per event for all events (top left), for events with exactly two generated B hadrons (top right), and for events with no generated B (bottom left), and the number of vertices per B hadron ($\Delta R_{BV} < 0.1$). The colors show vertices after the finder (black), after the first merging step (red), after all tracks are assigned to the PV or a SV (green), after the second merger step (blue) and after the filter (purple).

	Finder	Merger (loose)	Arbitration	Merger (tight)	Selection
Per event	6.3	2.5	1.4	1.2	0.10
Per 2 B hadron event (*)	13.0	3.9	2.7	2.2	0.65
Per 0 B hadron event (**)	5.6	2.4	1.3	1.1	0.043
(*) divided by (**)	2.3	1.6	2.1	2.0	15.1
Vertices per B hadron	3.8	0.84	0.74	0.54	0.29

Table 6.7: Mean number of vertices after the five reconstruction steps. The mean number of vertices per event, per 2 B hadron event, per 0 B hadron event and the mean number of vertices per B hadron ($\Delta R_{BV} < 0.1$) are shown. The mean number of SV per 2 B event divided by the mean number per 0 B event is also indicated. As expected, this number is significantly higher after the selection step.

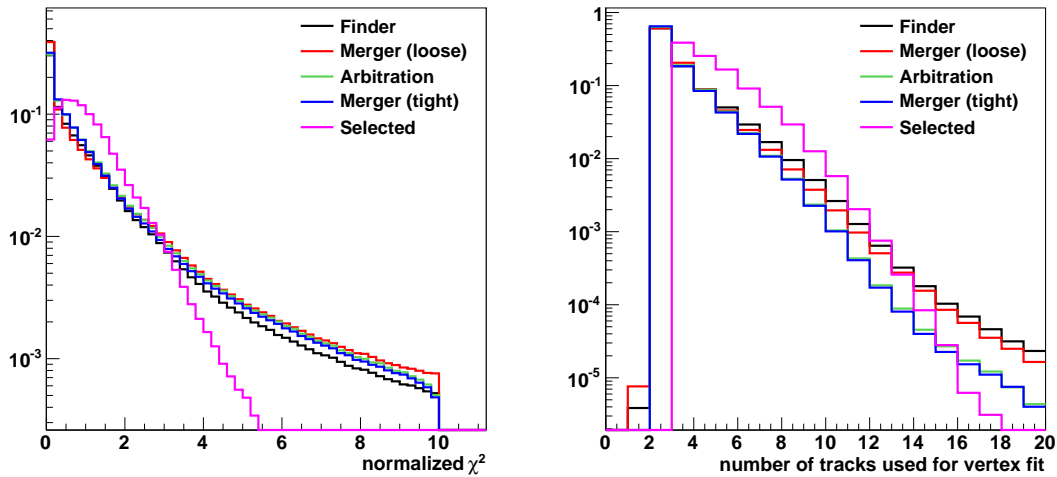


Figure 6.20: Comparison of vertices produced in the different steps (colors are the same as in figure 6.19). Left: Normalized χ^2 . Right: Number of tracks used for the vertex fit. All distributions are normalized to one.

events with two B hadrons) are shown in figure 6.21. All distributions are normalized to one. The invariant mass distribution for the vertices from finder and after merging look very similar. The shape changes after the arbitration step due to lost tracks. The second merger does not change the shape, but it changes when selecting vertices that are most likely B hadron decay vertices. The 3D flight distance distribution is very similar for the first four steps and only different after the filter. The true B hadron flight distance distribution is comparable to the shape of the selected vertices. The 3D flight distance significance changes shape only after the filter. The same is also true for the ΔR_{BV} between vertex and closest B flight direction. While for the first four steps the mean ΔR_{BV} (counting only the vertices in events with two B hadrons) is around 1 it is around 0.17 for the selected vertices.

6.8 B Candidate Identification

B hadrons decay mostly via weak interaction into final states containing a D hadron. D hadrons are lighter than B hadrons, and their decay length $c\tau$ is shorter. They mostly decay into Kaons (strange mesons). Mass, life time and decay length of D^\pm and D^0 hadrons are listed in table 6.8. The decay length of D hadrons is of the same order as the decay length of the B hadrons. This makes the discrimination of D and B hadrons experimentally difficult. Since long lived D hadrons decay at some distance to the primary vertex, their decay vertices are reconstructed as secondary vertices.

	quark content	mass (MeV)	lifetime τ (ps)	decay length $c\tau$ (μm)
D^\pm	$c\bar{d}, \bar{c}d$	1869.60 ± 0.16	1.040 ± 0.007	311.8
D^0	$c\bar{u}$	1864.83 ± 0.14	0.4101 ± 0.0015	122.9

Table 6.8: Properties of D hadrons: quark content, mass, mean life time τ and decay length $c\tau$.

If secondary vertices are used for tagging events or jets containing a B hadron, the successive decay of D hadrons produced at the B hadron decay vertex may be helpful. Since both hadrons decay, more displaced tracks exist in events with $B \rightarrow D \rightarrow X$ decay chains. Hence, the chance to reconstruct one (or even two) high quality secondary vertices is higher than in events with B hadrons not decaying into D hadrons. Whether the vertices refer to the B or the D hadron decays or whether they are “merged” vertices containing tracks from both hadron decays is irrelevant for tagging the jet or the event.

For topological studies the reconstructed vertices corresponding to a B hadron decay have to be distinguished from those corresponding to the decay of a D hadron. The D hadron decay vertices can either be separated from the B decay vertices by adding suitable requirements on the vertex kinematics, or—for $B \rightarrow D \rightarrow X$ decay chains—they can be “merged” with the corresponding B hadron decay vertices.

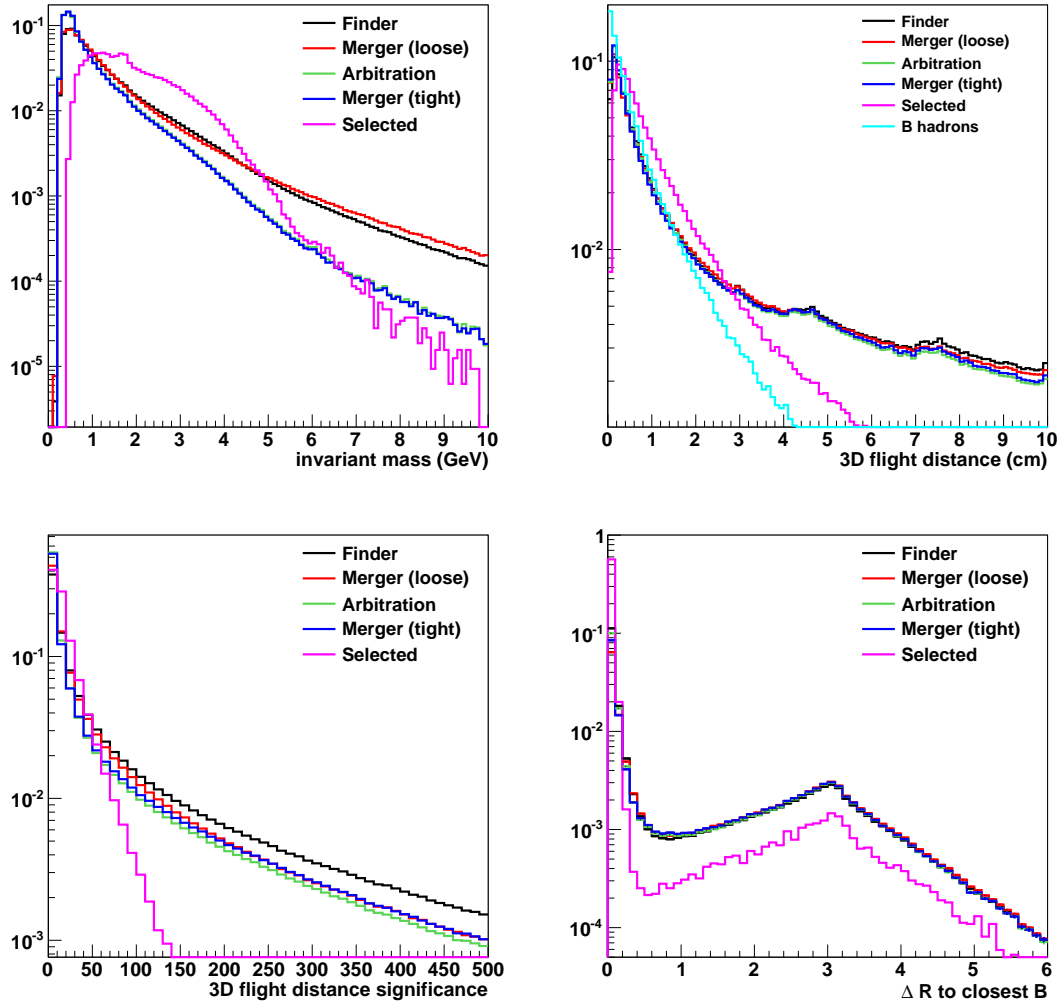


Figure 6.21: Comparison of vertices produced in the different steps (colors are the same as in figure 6.19). Top left: Invariant vertex mass distribution. Top right: 3D flight distance. The generated B hadron flight distance (for B with $p_T > 15$ and $|\eta| < 2.0$) is also shown (bright blue). Bottom left: 3D flight distance significance. Bottom right: ΔR_{BV} between vertex flight direction and the closest B hadron (for events with two B hadrons). All distributions are normalized to one.

For D hadrons produced in B hadron decays the angle between the flight direction of the B and D hadrons (assuming that both are produced at the PV) tends to be small, and the two hadron decay points are located relatively close in space. Since the IVF was designed to reconstruct hadron decay vertices even if the distance between those is relatively small, often both, the B and D hadron decay points are reconstructed as secondary vertices. An example is shown in figure 6.22. Both vertices in this event are selected vertices.

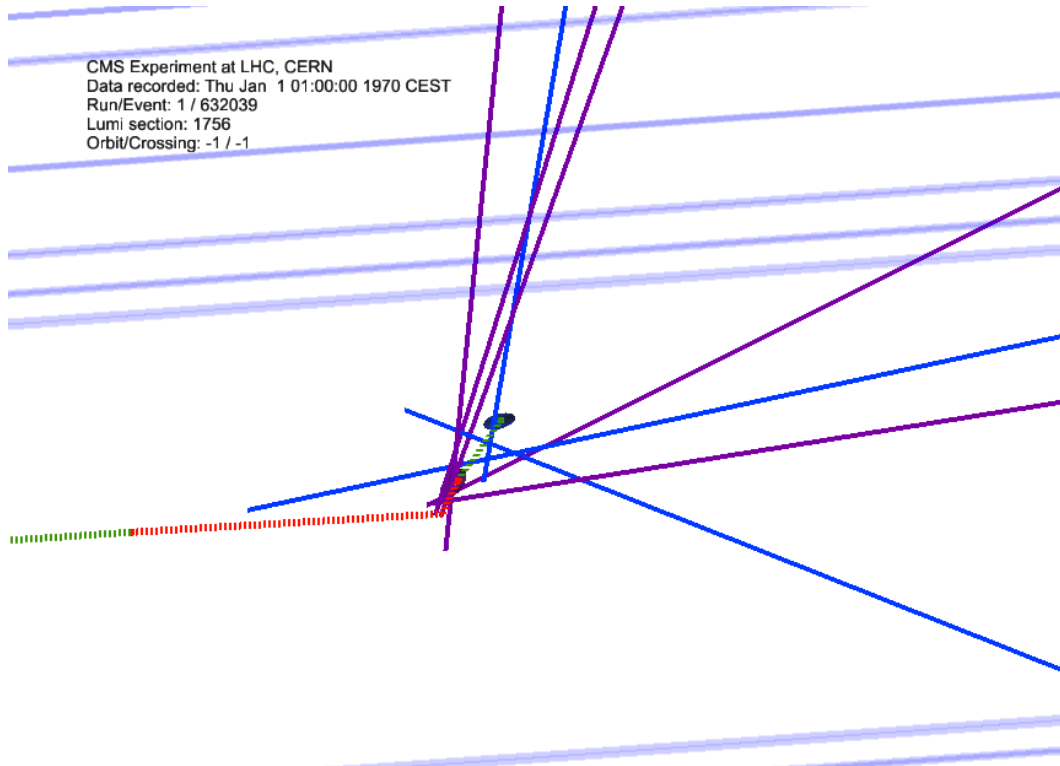


Figure 6.22: Simulated event with two $B \rightarrow D \rightarrow X$ decay chains. The B hadron flight paths are shown in red, the D hadron flight paths in green. For the right decay chain, both, the B and D hadron decay vertex are reconstructed. The two vertices are both selected in the filtering step. Position errors and tracks attached to the vertices are shown (purple for the B hadron and blue for the D hadron decay).

In order to merge vertices from a $B \rightarrow D \rightarrow X$ decay chain, while still keeping both vertices in events with quasi-collinear B hadrons, an iterative merging procedure is applied to vertex pairs with an angle $\Delta R_{VV} < 0.4$ between their flight directions. The goal is to yield a single *B candidate* associated with a $B \rightarrow D \rightarrow X$ decay chain, while still retaining both vertices (i.e. creating two B candidates) in events where two B are emitted nearly collinear. The procedure applied is the following:

All vertices with three or more tracks are ordered by the invariant mass (from heavy to light). Next, all remaining vertices are ordered by the invariant mass. Any pair of two SVs

is checked for $B \rightarrow D \rightarrow X$ decay. For the first SV in the ordered list, other SV with mass $m_{sv} < 1.5 \text{ GeV}$ are tested first in order to merge low mass with high mass SV first. Then, all the remaining vertices with $m_{sv} > 1.5 \text{ GeV}$ are tested. Two vertices are considered to be part of the same B decay if

- $\Delta R_{VV} < 0.4$
- the pair invariant mass is lower than 5.5 GeV
- the cosine of the angle θ between the vector from the position of the SV that is closer to the PV to the position of the other SV and the three momentum of the vertex with larger decay length is larger than 0.99.

The last point is true if the vertex with larger decay length is more likely to be reconstructed from particles that are produced at the closer SV than from particles originating from the PV, see figure 6.23.

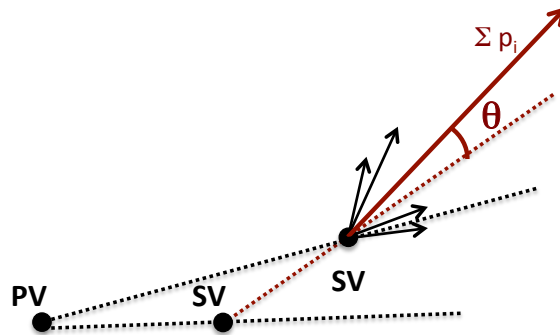


Figure 6.23: Angle θ between direction from vertex with smaller decay length to other vertex and sum of track momenta of vertex with larger decay length.

If two vertices are considered to be $B \rightarrow D$ decay positions they are combined. The lighter vertex is removed and for the heavier one a *B candidate* is created. The B candidate four-momentum is computed as the sum of the momenta of all tracks of both vertices. Shared tracks are taken only once and the pion mass hypothesis is applied to the tracks. This B candidate is used to compute the vertex mass and its momentum. For the event shown in figure 6.22 this procedure works and only the correct vertex is kept, see figure 6.24. The same procedure is applicable for three or more SV cases.

The effect of the $B \rightarrow D \rightarrow X$ cleaning procedure for the correlation analysis is estimated in simulation and illustrated in figure 6.25. Shown is the ΔR_{VV} between two B candidate vertices. The colors show the contribution from different sources: events where both vertices belong to a B hadron ($\Delta R_{BV} < 0.1$ for one-to-one matched B hadron) are shown in green. Those are the signal events. All other colors are events where at least one vertex corresponds to a D hadron (non-B vertex with at least one D hadron in a $\Delta R < 0.1$ cone around the vertex) or a light hadron (all other than B and D vertices, including fake vertices). The largest background contribution comes from events with one B and one D vertex (bright

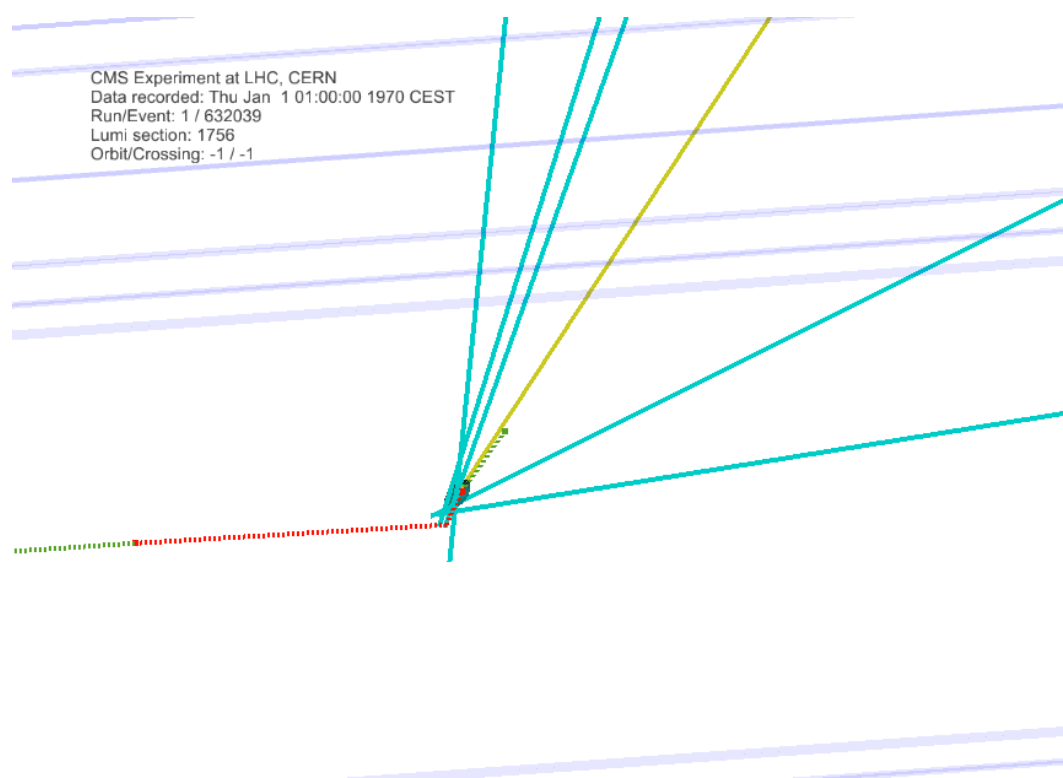


Figure 6.24: Same simulated event as in figure 6.22. The two selected vertices have been combined and a B candidate has been created. The B candidate vertex is shown in blue and the momentum of the B candidate in yellow. It is computed using the five tracks of the B candidate vertex and the three tracks of the other original vertex (see figure 6.22).

blue), all other contributions are negligible. The left plot shows the distribution without $B \rightarrow D \rightarrow X$ cleaning, while in the right plot the cleaning procedure is applied. The one B one D background is reduced by a factor of two from 159 to 78 events, while the number of signal events is even increased from 2962 to 3106. The signal over background ratio is increased from 13.5 to 23.2. If in events with three or more selected vertices some of them are combined, such that the number of selected vertices left in the event is two, previously unselected events are selected and the number of signal events increases. The largest difference between the two plots is found in the first bin, where the events with two vertices from $B \rightarrow D$ chains are removed.

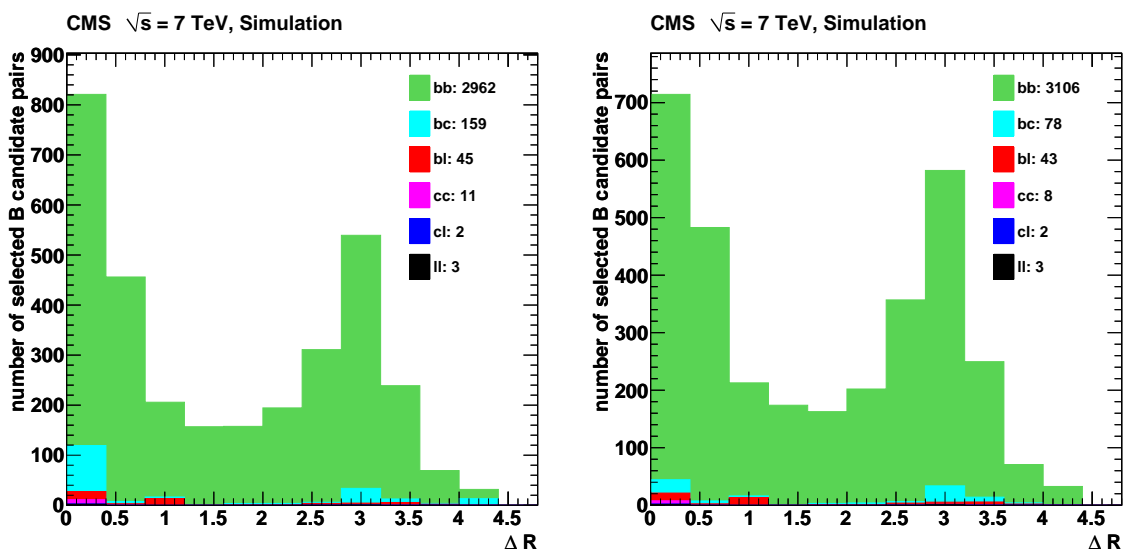


Figure 6.25: ΔR_{VV} between two B candidate vertices without (left) and with (right) $B \rightarrow D \rightarrow X$ cleaning procedure applied. The colors show the contribution from different sources: events where both vertices belong to a B hadron are signal events (green). The background events include events with one B and one D vertex (bright blue), one B and one light vertex (red), two D vertices (pink), one D and one light vertex (blue) and two light vertices (black).

6.9 Resolution of the ΔR Reconstruction

A good angular resolution and the ability to resolve small opening angles are necessary for measuring the $B\bar{B}$ angular separation in the full range. The resolution is determined using MC events generated with PYTHIA. The different PYTHIA QCD samples (see section 4.3) are combined using upper \hat{p}_T cuts to avoid overlap and with the proper weights. The angular separation between the two generated B hadrons (ΔR_{BB}) is compared to the angular separation between the flight directions of the two reconstructed B candidates (ΔR_{VV}). This is done for triggered events (in the $> 99\%$ efficiency range) with exactly two B hadrons and exactly

two selected B candidates with mass sum above 4.5 GeV. The result for the three leading jet p_T bins is shown in figures 6.26 to 6.28. The left plots are 2D plots, where ΔR_{BB} is plotted against ΔR_{VV} . The bin size is 0.4 for both angles. For the three jet p_T bins most entries are located on the diagonal, which means that the angle has been reconstructed correctly. Most of the off-diagonal contributions lie in the regions where the angle between the B hadrons is very small (collinear B hadrons), while the angle between the reconstructed B candidates is large (around π). These are typically events with a gluon splitting into a $b\bar{b}$ pair, where one B hadron is correctly reconstructed and the other one is lost. The second B candidate is a vertex reconstructed in the recoiling (light) jet, which does not contain any b or \bar{b} . The largest effect on a single bin is around 10% (number events off the diagonal divided by the number of events on the diagonal). This impurity due to bin migration is corrected for (see chapter 7) and its uncertainty is taken into account in the systematic uncertainties (see chapter 9).

The difference $\Delta R_{VV} - \Delta R_{BB}$, is also shown in the figures. The core of the distributions are observed to be significantly smaller than the bin size in the left plots ($\Delta R = 0.4$). To quantify the resolution, the width of the distribution is determined by a gaussian fit to the core, see figure 6.29 (leading jet $p_T > 84$ GeV). The fit yields $\sigma = 0.013 \pm 0.0003$, which is more than thirty times smaller than the bin width. For the fits in the $p_T > 56$ GeV and $p_T > 120$ GeV samples, $\sigma = 0.017 \pm 0.00011$ and $\sigma = 0.0096 \pm 0.00019$ is extracted. The number of entries off the diagonal in the tail (with $|\Delta R_{VV} - \Delta R_{BB}| > 0.2$) is found to be below 4% in all leading jet p_T samples (1.9%, 3.0% and 4.0% for $p_T > 56$, 84 and 120 GeV).

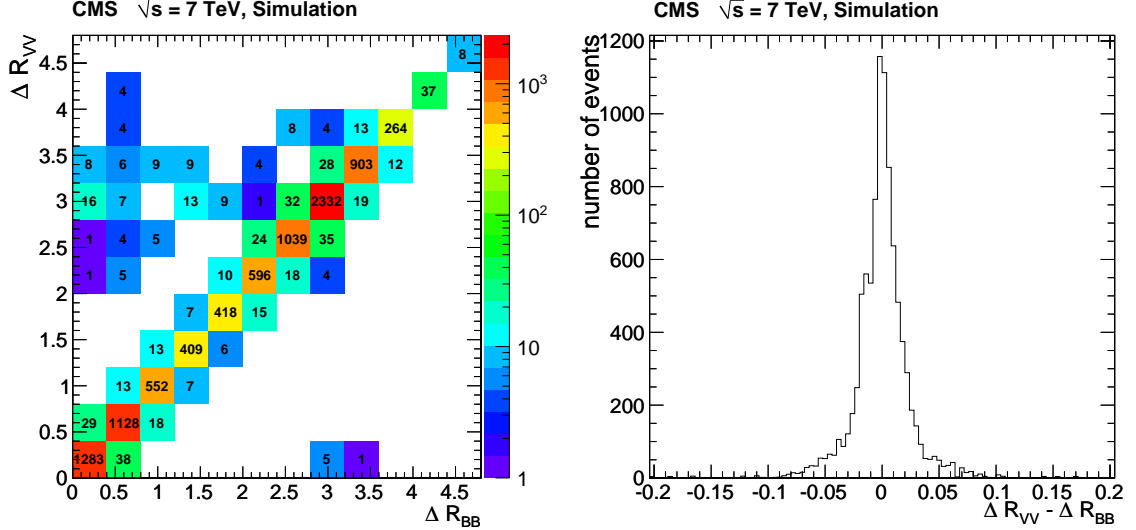


Figure 6.26: Resolution of the ΔR reconstruction, obtained using simulation for the leading jet $p_T > 56$ GeV sample. Left: ΔR values between the flight directions of two selected B candidates ΔR_{VV} versus the values between the generated B hadrons ΔR_{BB} in bins of 0.4. The numbers in the boxes represent the number of events in the particular bin. The color range starts at one. Right: Projection onto the diagonal, $\Delta R_{VV} - \Delta R_{BB}$.

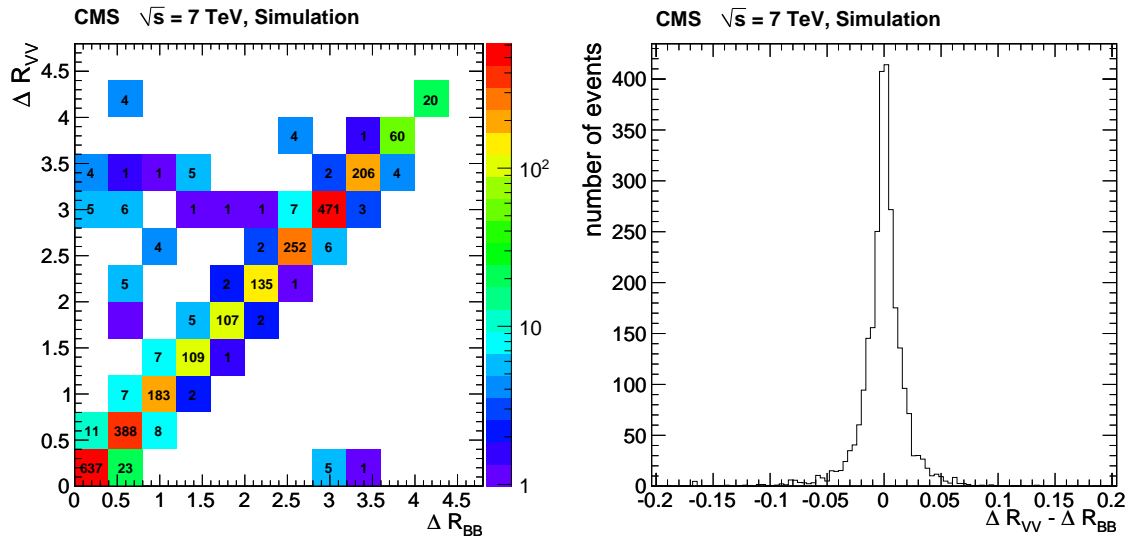


Figure 6.27: Resolution of the ΔR reconstruction for the leading jet $p_T > 84$ GeV bin (see figure 6.26 for details).

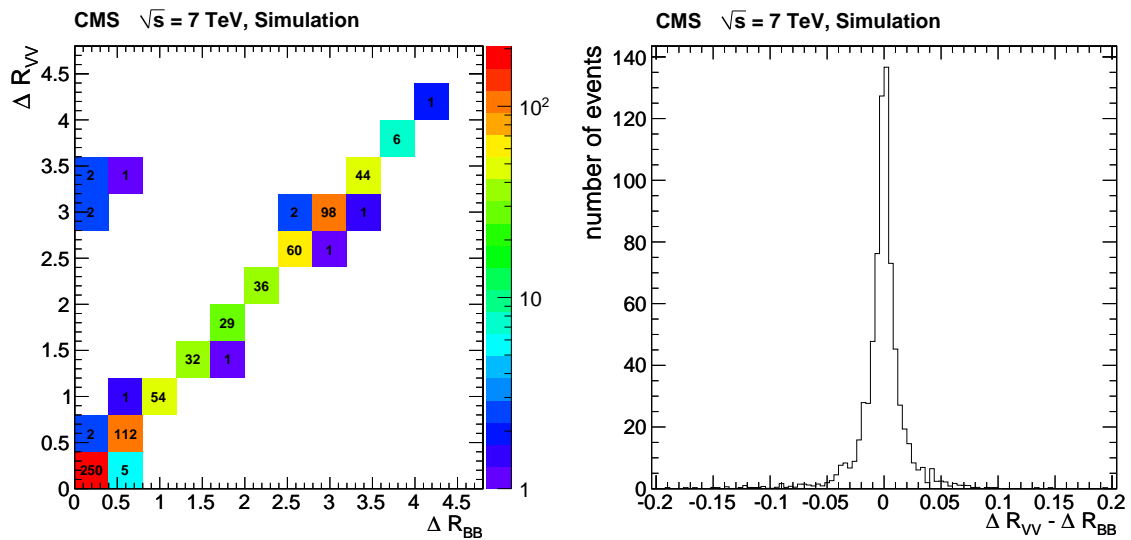


Figure 6.28: Resolution of the ΔR reconstruction for the leading jet $p_T > 120$ GeV bin (see figure 6.26 for details).

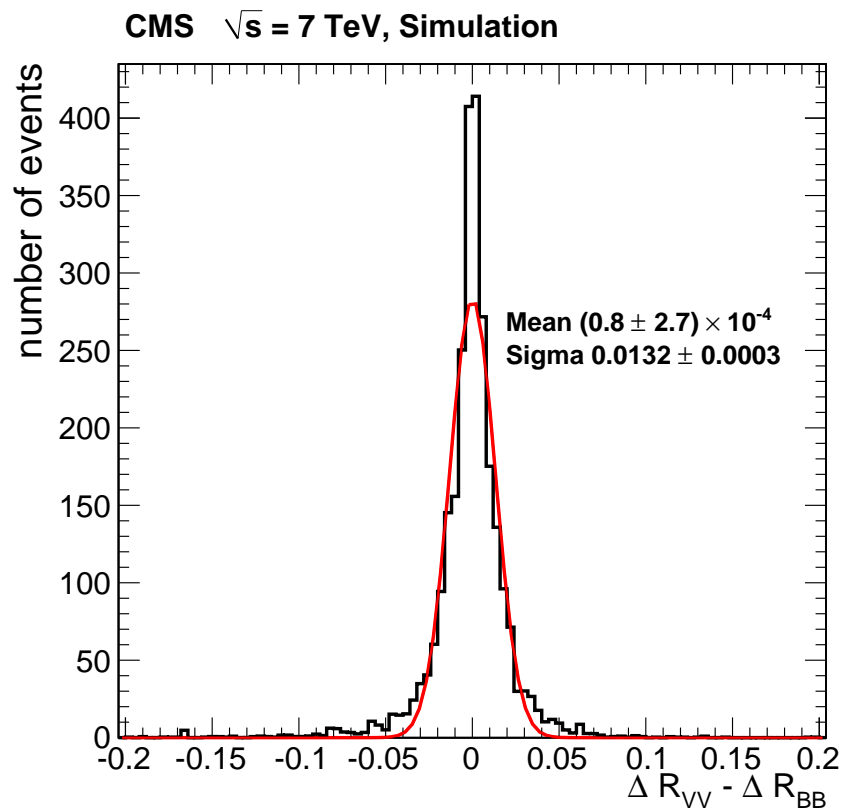


Figure 6.29: Resolution of the ΔR reconstruction (leading jet $p_T > 84$ GeV, see figure 6.27). The core of the distribution, $|\Delta R_{VV} - \Delta R_{BB}| < 0.2$, is fit with a gaussian function. The fit parameters are indicated in the figure.

Chapter 7

Efficiency and Purity Correction

To study the vertex reconstruction efficiency and the purity the PYTHIA samples have been processed with full detector simulation. The efficiency of correctly identifying events with two B hadrons, while correctly measuring the angle between those, and the purity of the selected events, are determined from MC. An extrapolation from the measured angular distribution ΔR_{VV} to the prediction of the angular distribution ΔR_{BB} (angle between B hadrons) is determined using the event selection efficiency and purity (see section 7.2).

Because the efficiency and the purity are taken from MC, it is crucial to study the acceptance and the proper description of the event kinematics in MC (see section 7.1). B hadrons decaying outside the detector acceptance region or too soft hadrons can not be reconstructed. A “fiducial” phase space of B hadrons with a minimum p_T that decay within the detector is defined.

7.1 Kinematics of Events with Two B Hadrons

The η , ϕ and p_T distributions of B hadron pairs is shown in figure 7.1 for the weighted combination of events simulated with PYTHIA for the leading jet $p_T > 56$ GeV bin. The PYTHIA cross section for events with two B hadrons with $\hat{p}_T > 15$ GeV is $41 \mu\text{b}$. Requiring leading jet $p_T > 56$ GeV the cross section is reduced to $0.5 \mu\text{b}$. As expected from the production dynamics, the pseudorapidities η of the two B hadrons are similar in most events. The difference of the azimuthal angles ϕ_1 and ϕ_2 of the two hadrons is mostly close to zero (small opening angle) or around π (back-to-back topology). For most events, both B hadrons are very soft ($p_T < 10$ GeV).

For the LO PYTHIA MC event generator, $b\bar{b}$ production is divided into the three production mechanisms (FCR, FEX and GSP, see section 2.2.5) using the status information of the generated particles. All events with at least one generated b and at least one \bar{b} particle taking part in the hard interaction (i.e. with PYTHIA status equal to 3), are denoted as flavor creation. The events with either at least one generated b or at least one \bar{b} in the hard interaction are flavor excitation and all other $b\bar{b}$ events are gluon splitting events (no b or \bar{b} with PYTHIA status equal to 3). The different kinematics of these three process types become apparent in

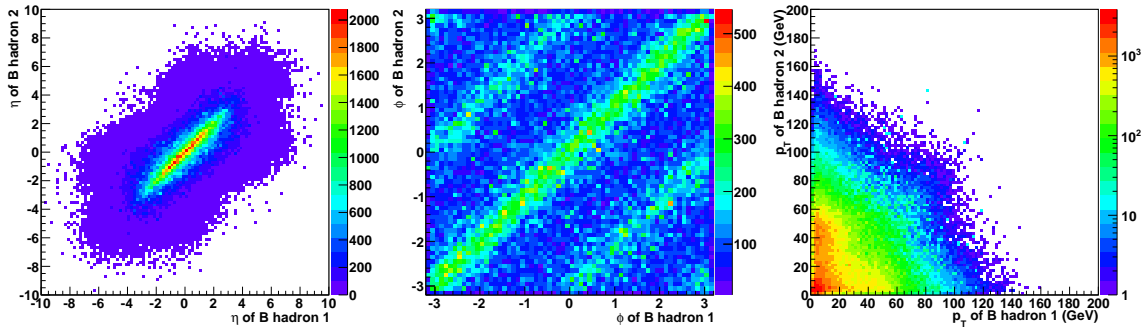


Figure 7.1: Properties of B hadrons in events with exactly two B hadrons (leading jet $p_T > 56$ GeV region): η correlation (left), ϕ correlation (middle) and p_T correlation (in logarithmic scale, right).

figure 7.2, which shows the same η , ϕ and p_T distributions as figure 7.1, but separately for FCR, FEX and GSP. For the event energy scale defined by the leading jet $p_T > 56$ GeV cut, the relative amount of FCR is 5.9% in the combined PYTHIA sample, the one of FEX is 35.3% and the largest contribution (58.8%) comes from GSP. Events with symmetric η are mainly GSP events and many FEX events are produced with one B produced centrally and one with large $|\eta|$. This is expected because GSP pairs are produced with small opening angle in η and ϕ and in FEX events one b or \bar{b} taking part in the hard process while the other (anti-) quark stays in the remnant. The ϕ distributions show that in the FCR events the two B are produced back-to-back in azimuthal angle, as expected from pure momentum conservation in a 2-2 process. The p_T plot shows that the contribution with small p_T for both B hadrons comes mainly from GSP events and that the p_T is distributed asymmetrically in FEX events.

The plots in figures 7.1 and 7.2 show the full B hadron phase space for the leading jet $p_T > 56$ GeV region. The fiducial kinematic range for this measurement is defined such that the B hadron decays can be reconstructed using secondary vertexing with reasonable efficiency. In order to take into account the fact that tracks are used for secondary vertex finding, a cut on the absolute pseudorapidity is taken. The CMS silicon tracker covers the region $|\eta| < 2.5$. Since the tracks of a decaying B hadron are spread around the flight direction of the hadron the region where secondary vertex finding is efficient is smaller. For this analysis the pseudorapidity cut is set at $|\eta(B)| < 2.0$. Furthermore, events with soft B might fail the reconstruction. The p_T distributions for the softer and harder B hadrons in events with two B are shown in figure 7.3. The softer B transverse momenta range from a few GeV up to around hundred GeV, with an average of 15.7 GeV and a maximum probability at around 8 GeV. The harder B in the event has an average p_T of 38 GeV. In figure 7.4 the efficiencies of reconstructing two selected B candidates in events with two B hadrons as a function of the p_T of the softer B and of the harder B in the event are shown. The efficiency is defined as ratio between number of events with two selected B candidate vertices and two B hadrons with $|\eta| < 2.0$ and the number of events with two B hadrons in $|\eta| < 2.0$ (for every bin). For this efficiency plot, a p_T cut is applied neither on the B hadrons nor on

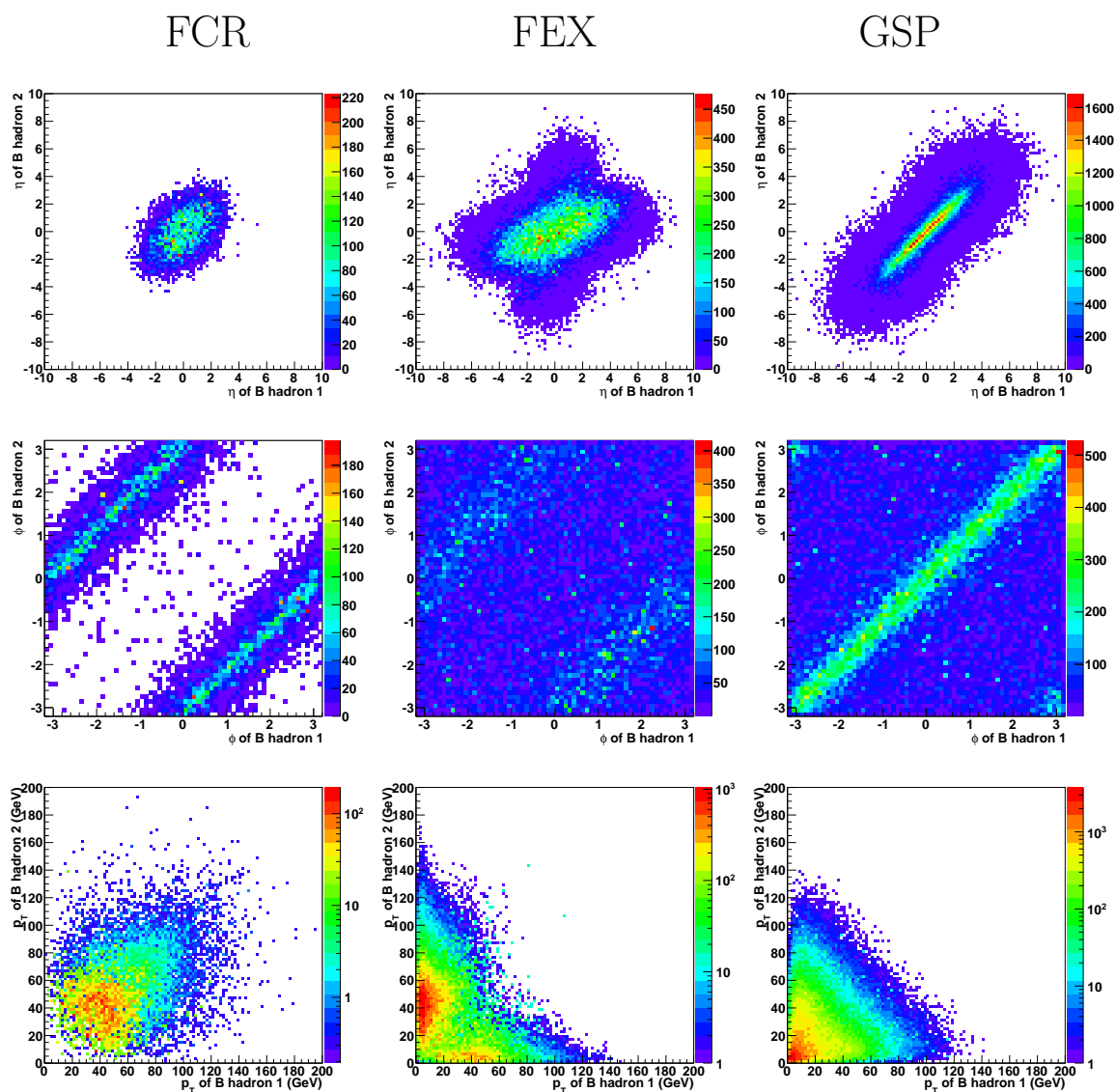


Figure 7.2: η , ϕ and p_T correlation as in figure 7.1, shown separately for the three production mechanisms: flavor creation (left), flavor excitation (middle) and gluon splitting (right).

the B candidate vertices. The efficiency as function of the softer B p_T is almost zero up to around 12 GeV and it grows until it reaches a plateau at 40 GeV. The efficiency as function of the harder B behaves similarly. The fiducial phase space for this analysis is defined as $p_T(B) > 15$ GeV for both B hadrons.

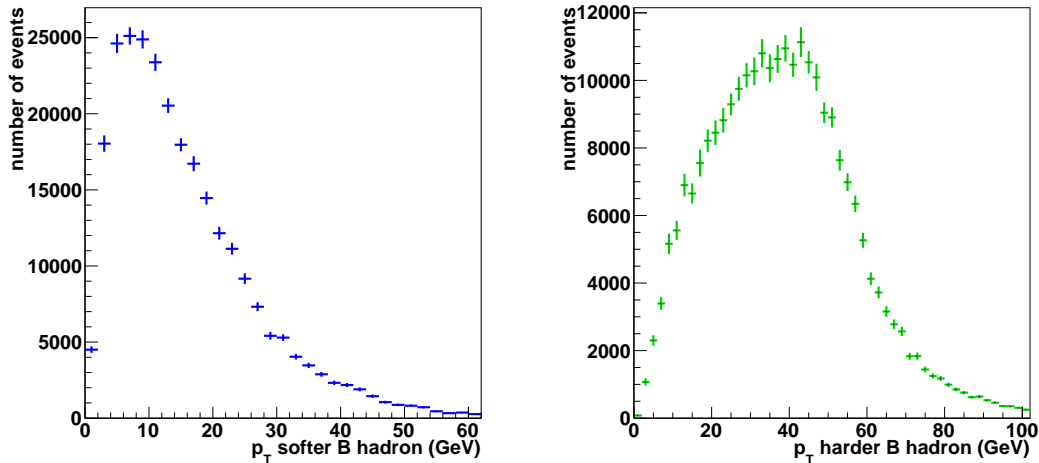


Figure 7.3: The p_T distribution of B hadrons in events with two B (leading jet $p_T > 56$ GeV region). Left: the p_T of the softer B hadron. Right: p_T of the harder B hadron in the event.

The transverse momentum of the softer B hadron determines the efficiency cut off. If one B is too soft ($p_T < 15$ GeV) the event will not be selected because one B vertex will be missing. Events with soft B hadrons are mainly GSP events. Those events are the ones with small opening angles between b and \bar{b} . In figure 7.5 the dependence of the p_T of the B hadron on the opening angle ΔR_{BB} between the B hadrons is shown in the leading jet $p_T > 56$ GeV region. The left plot shows the dependency for all events with two B with $|\eta(B)| < 2.0$. The right plots show the mean p_T as a function of the opening angle for events in the fiducial phase space. For the right plot the p_T cut on the B hadrons is applied (only events with two B with $p_T > 15$ GeV have been considered). The ΔR_{BB} and the p_T are strongly correlated both for the softer and the harder B hadron. Larger opening angle means higher average p_T and therefore better B hadron reconstruction efficiency. The event selection efficiency will suffer in the low opening angle region.

Since a p_T cut of 15 GeV is applied on the B hadrons, a p_T cut should also be applied on the B candidates. Otherwise, events with two selected B candidates and two B hadrons which are not (both) selected due to the p_T cut on the hadrons decrease the purity. The correlation between the p_T of the simulated B hadrons and the p_T of the reconstructed vertices is shown in figure 7.6. In the profile the mean p_T of the vertex for every bin of the p_T of the simulated hadron is shown and the relation between both is found to be linear above $p_T = 15$ GeV. For a fit with a straight line $y = mx + q$ (purple) the fit parameters determined are $m = 0.554 \pm 0.003$ and $q = 3.15 \pm 0.09$. In average about half of the p_T of a B

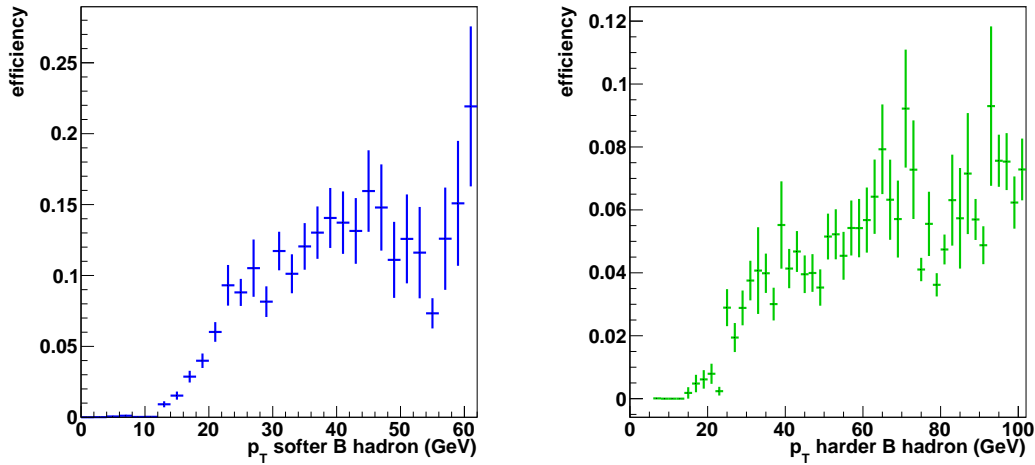


Figure 7.4: Efficiency of reconstructing two selected B candidates in events with two B hadrons ($|\eta| < 2.0$, no p_T cut). On the B candidates, all selection criteria apart from the p_T cut are applied. The efficiency is shown as a function of the p_T of the B hadron (softer B left, harder B right) for events in the leading jet $p_T > 56$ GeV bin.

hadron is reconstructed. Therefore, all vertices with $p_T > 8$ GeV are selected for the analysis.

Given the cuts on the B hadron pseudorapidity and transverse momentum the fiducial phase space is defined by $|\eta(B)| < 2.0$ and $p_T(B) > 15$ GeV. About 22% of the leading jet $p_T > 56$ GeV bin events with two generated B hadrons are in the fiducial phase space. The PYTHIA cross section prediction is 116 nb, 28 nb and 7 nb for the leading jet p_T above 56, 84 and 120 GeV bins, respectively. Figure 7.7 shows the ΔR_{BB} between B hadrons in events with exactly two B hadrons in the fiducial phase space. The colors show the production mechanism. It is found that the contribution from GSP events is large (54%). Figure 7.8 shows the opening angle Ψ_{BB} between the flight directions of the two B hadrons for the same events as the previous figure. Again, the contributions from different production mechanisms are shown in different colors. Comparing the two variables, it is observed that for the GSP, small ΔR_{BB} also means small opening angles Ψ_{BB} , while the back-to-back peak in ΔR_{BB} from FCR and FEX events is more flat in Ψ_{BB} . The FEX contributions goes down to very small angles Ψ_{BB} . For the FCR events, the angle is never smaller than about 0.5. The correlation between the two variables is shown in figure 7.9. The FCR events are mostly at $\Delta R_{BB} \approx \pi$ but spread over a large range of Ψ_{BB} (from around 0.5 to π). In this analysis the variable ΔR_{BB} is used as 3D angle instead of the 3D opening angle Ψ_{BB} .

7.2 Efficiency and Purity Determination

Since the event selection efficiency depends on the p_T of the B hadrons, and therefore on the opening angle, the measured angular distributions need to be corrected as a function of ΔR .

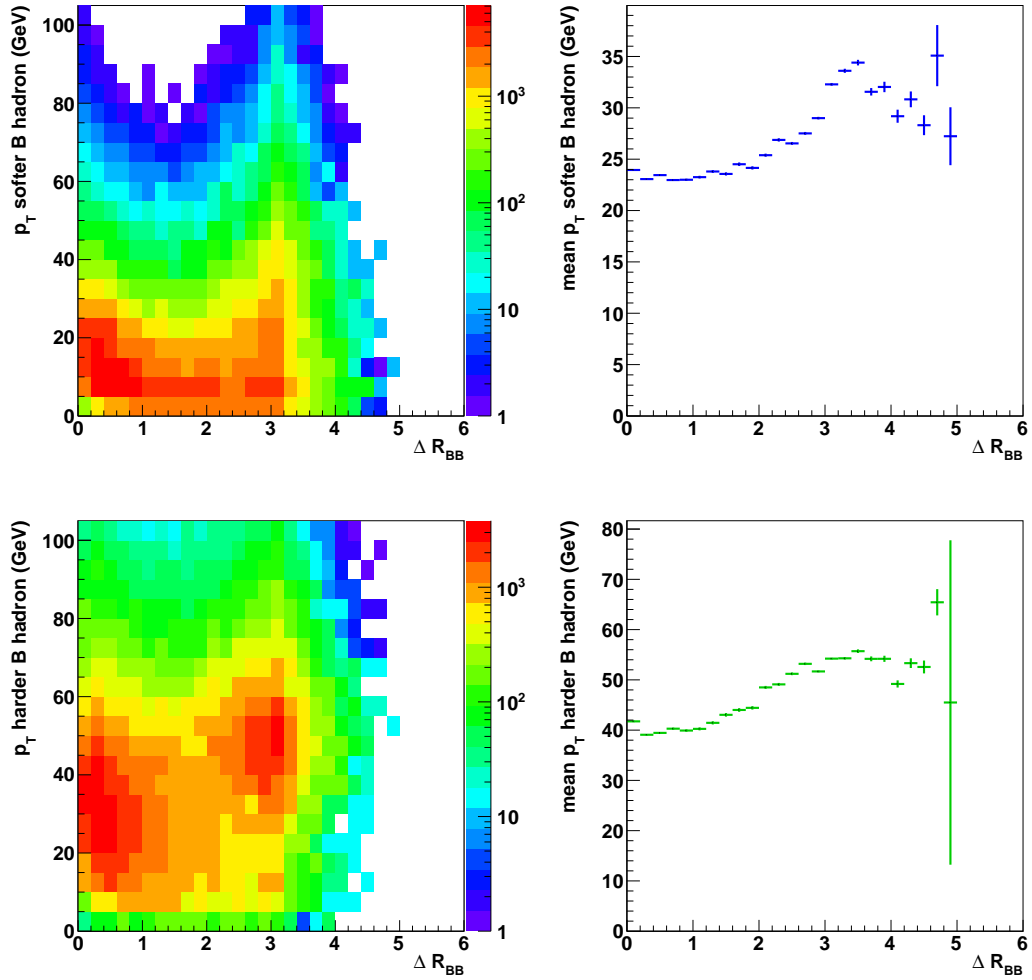


Figure 7.5: Correlation between ΔR_{BB} and the p_T of the softer (top) and harder (bottom) B hadron (leading jet $p_T > 56$ GeV region). Left: two dimensional correlation. Right: mean p_T of softer (top) and harder (bottom) B hadron as a function of the opening angle ΔR_{BB} between the two B hadrons. For calculating the mean only the fiducial phase space is considered ($p_T(B) > 15$ GeV).

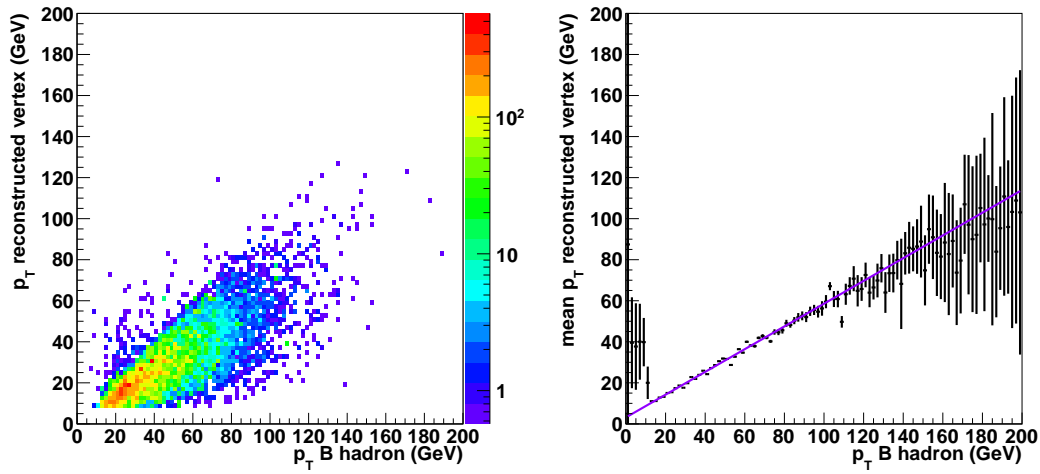


Figure 7.6: Left: correlation between the p_T of the reconstructed vertex and the p_T of the generated B hadron in events with two B hadrons and two selected B candidate vertices (leading jet $p_T > 56$ GeV). Only events where for both B hadrons are correctly reconstructed ($\Delta R_{BV} < 0.1$) are shown. Right: the mean p_T of reconstructed vertex for every generated B hadron p_T bin, with linear fit (purple).

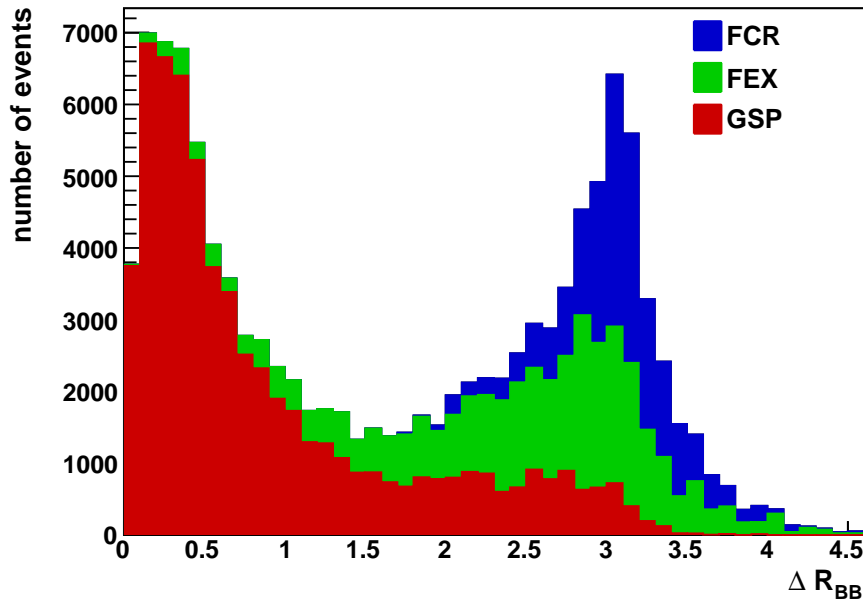


Figure 7.7: ΔR_{BB} for events with two B hadrons (with $|\eta(B)| < 2.0$, $p_T(B) > 15$ GeV, leading jet $p_T > 56$ GeV region). The colors show the contributions from FCR (17.8%, blue), FEX (28.2%, green) and GSP (54.0%, red) events.

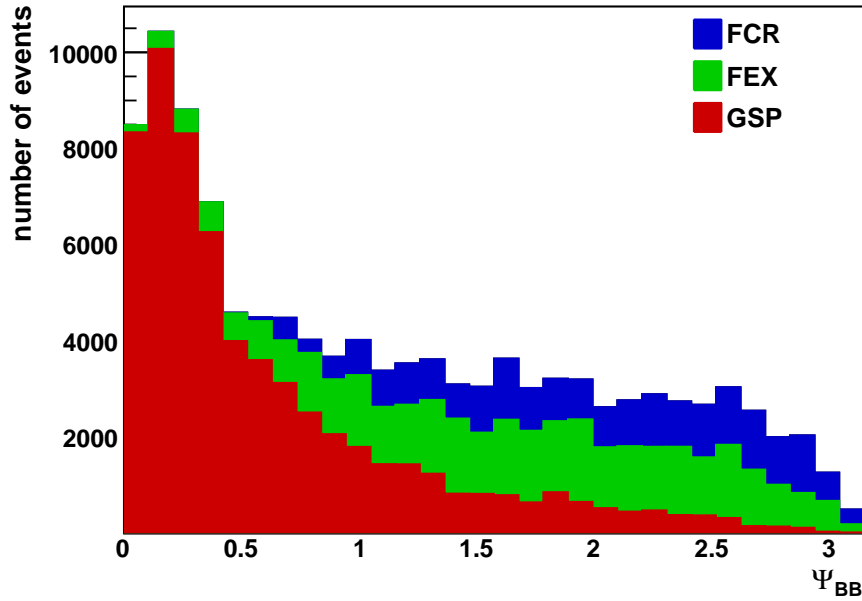


Figure 7.8: Angle Ψ_{BB} between the flight directions of the B hadrons for events with two B hadrons (with $|\eta(B)| < 2.0$, $p_T(B) > 15$ GeV, leading jet $p_T > 56$ GeV region). The colors show the contributions from FCR (17.8 %, blue), FEX (28.2 %, green) and GSP (54.0 %, red) events.

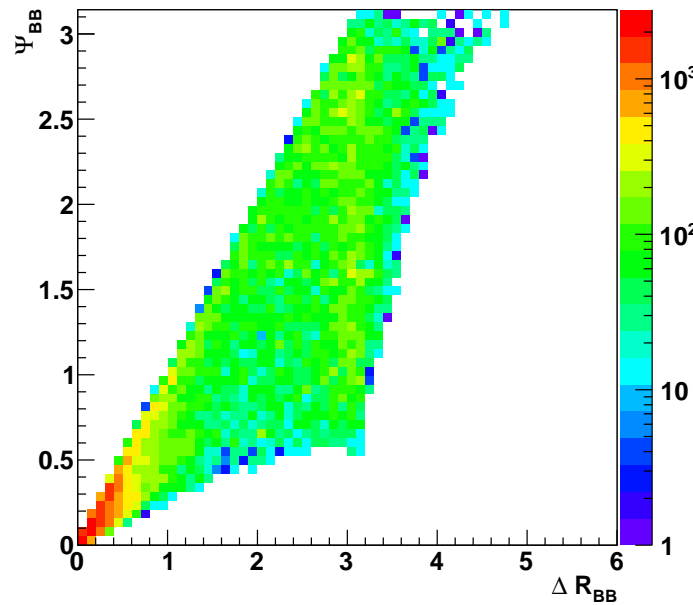


Figure 7.9: Angle Ψ_{BB} versus ΔR_{BB} for events with two B hadrons in the fiducial phase space ($|\eta(B)| < 2.0$, $p_T(B) > 15$ GeV, leading jet $p_T > 56$ GeV region).

The resolution for ΔR is of the order of 0.02 (obtained from MC, see section 6.9). The angular binning chosen for the analysis is 0.4. This choice is motivated by the limited statistics available in data and also in the simulation. The binning is much larger than the resolution. No unfolding is applied for correction of resolution effects. Since angular distributions are measured in this analysis, efficiency and purity corrections as a function of the ΔR_{VV} between the two selected B candidate vertices are applied to minimize possible distortions. Separate efficiency and purity correction factors are derived for the three leading jet p_T samples to extrapolate from the measured vertex momenta to the fiducial phase space of true B hadrons.

The efficiency is defined as

$$\epsilon = \frac{\# \text{ events with 2 selected B hadrons and a selected B candidate pair}}{\# \text{ events with 2 selected B hadrons}}, \quad (7.1)$$

where selected B hadrons means $p_T(B) > 15 \text{ GeV}$ and $|\eta(B)| < 2.0$ and in the numerator B candidate pair means that the sum of the two vertex masses has to be above 4.5 GeV. This number is calculated for every ΔR_{BB} bin.

The average event selection efficiencies for the three leading jet p_T bins are 7.4%, 9.3% and 10.7% (p_T above 56, 84 and 120 GeV). The ΔR_{BB} dependency of the efficiency is shown in figure 7.10. The bin size varies from 0.2 to 1.2 depending on the number of simulated events available in the given ΔR_{BB} region.

The purity as a function of ΔR_{VV} is defined as

$$p = \frac{\# \text{ events with 2 selected B hadrons and a selected B candidate pair}}{\# \text{ events with a selected B candidate pair}}. \quad (7.2)$$

While the numerator is calculated for every ΔR_{BB} bin, the denominator is a function of ΔR_{VV} . The purity correction takes into account the bin migration in the resolution plot. The purity as a function of ΔR_{VV} is shown in figure 7.11 for the three different leading jet p_T bins. The average $B\bar{B}$ purity is found to be between 83% and 85% for the three samples and the variations are within $\pm 10\%$.

The overall multiplicative correction factor cf as function of ΔR_{VV} is given by

$$cf = \frac{p}{\epsilon}, \quad (7.3)$$

and is shown in figure 7.12 for the three bins. Both, the PYTHIA QCD sample (combination of the different \hat{p}_T samples) and the Inclusive BB sample are used for the efficiency and purity calculation (see section 4.3). The Inclusive BB sample is added in order to improve the statistics. The samples are added as follows: the bin contents $N_i(X)$, where X stands for either of the two samples, are weighted with

$$w_i(X) = \begin{cases} 0 & \text{if no entry in bin } i \\ 1/\sigma_i^2(X) & \text{otherwise,} \end{cases} \quad (7.4)$$

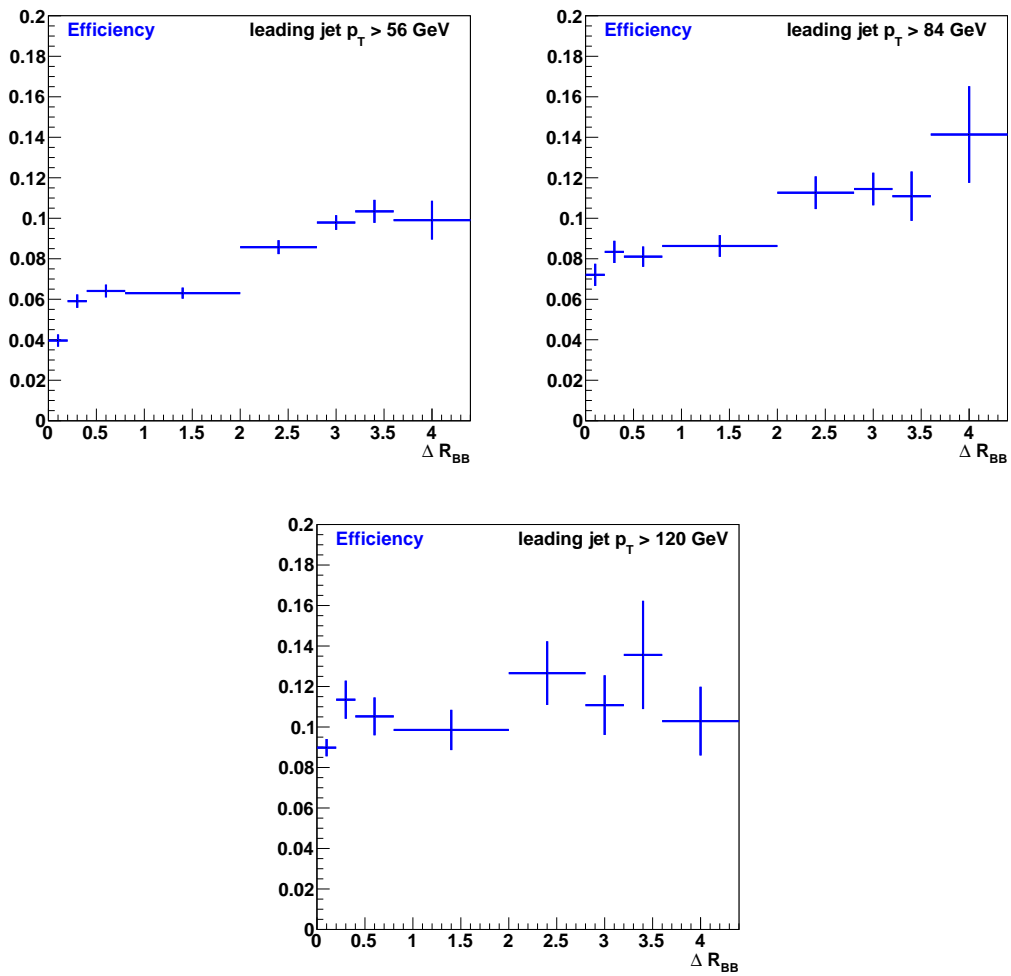


Figure 7.10: Efficiency as function of ΔR_{BB} for the three leading jet p_T bins.

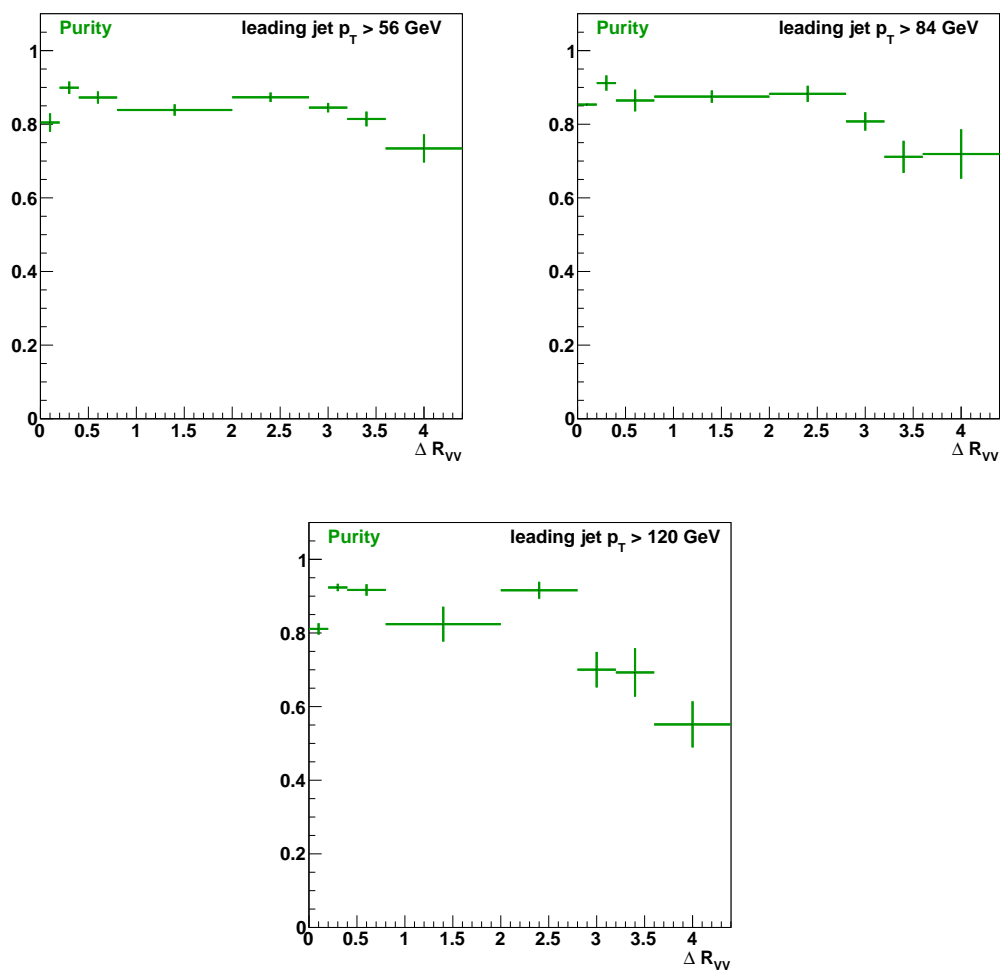


Figure 7.11: Purity as function of ΔR_{VV} for the three leading jet p_T bins.

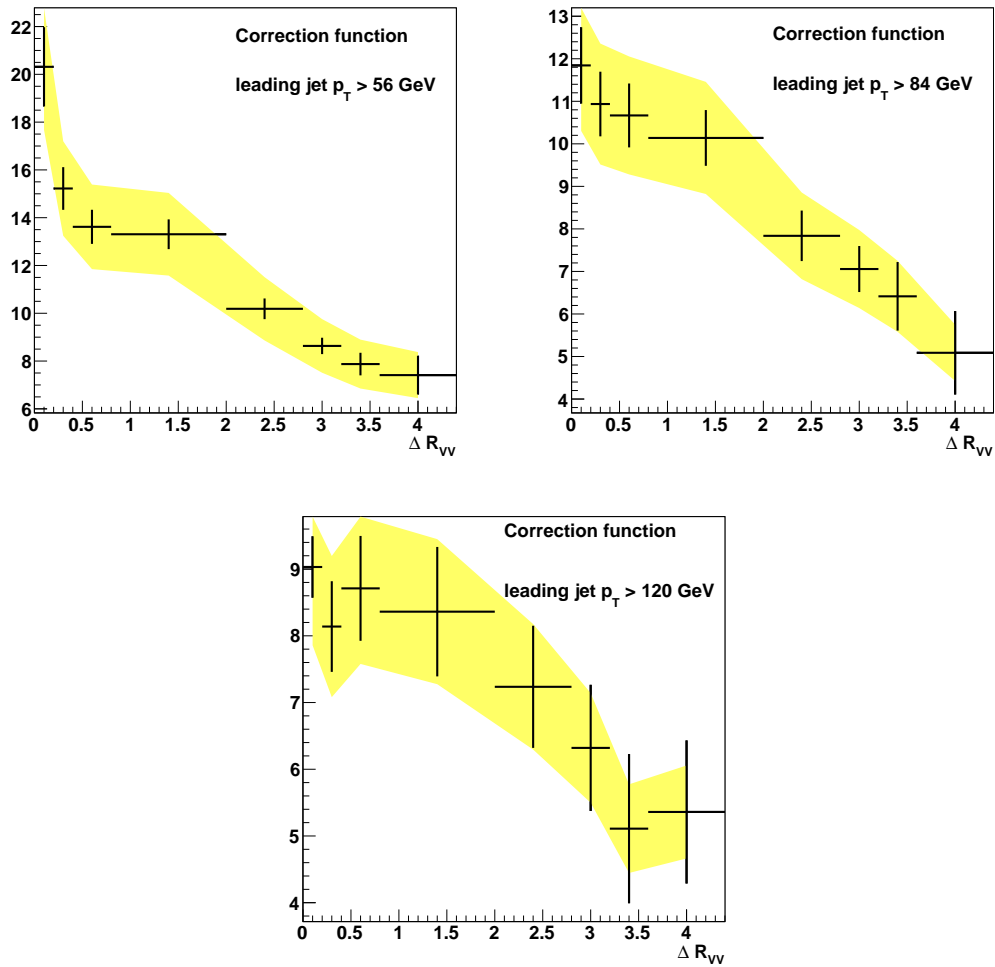


Figure 7.12: Overall correction factor as function of ΔR_{VV} for the three leading jet p_T bins. The yellow band shows a systematic uncertainty of 13 GeV (see chapter 9).

where $\sigma_i(X)$ are the bin errors. The new bin contents N_i and bin errors σ_i are computed as

$$N_i = \frac{N_i(\text{QCD}) \cdot w_i(\text{QCD}) + N_i(\text{BB}) \cdot w_i(\text{BB})}{w_i(\text{QCD}) + w_i(\text{BB})} \quad (7.5)$$

$$\sigma_i = \begin{cases} 0 & \text{if } w_i(\text{QCD}) = w_i(\text{BB}) = 0 \\ (w_i(\text{QCD}) + w_i(\text{BB}))^{-\frac{1}{2}} & \text{otherwise.} \end{cases} \quad (7.6)$$

The calculation of bin contents N_i is done separately for the efficiency and purity numerator and the efficiency denominator. For the purity denominator, the procedure had to be slightly changed since in the Inclusive BB sample there are no non-B events. The denominator of the QCD sample is divided into events containing two B and events without B. The events with two B are added as described above to the events of the Inclusive BB sample. To the combined value, the non-B events are added. In figure 7.13 the efficiency and the correction function for the Inclusive BB and the combined QCD sample are shown together with the combined function. The plot shows the functions for the leading jet $p_T > 56$ GeV bin. The efficiency, purity and correction factor numbers for every ΔR bin can be found in appendix A.

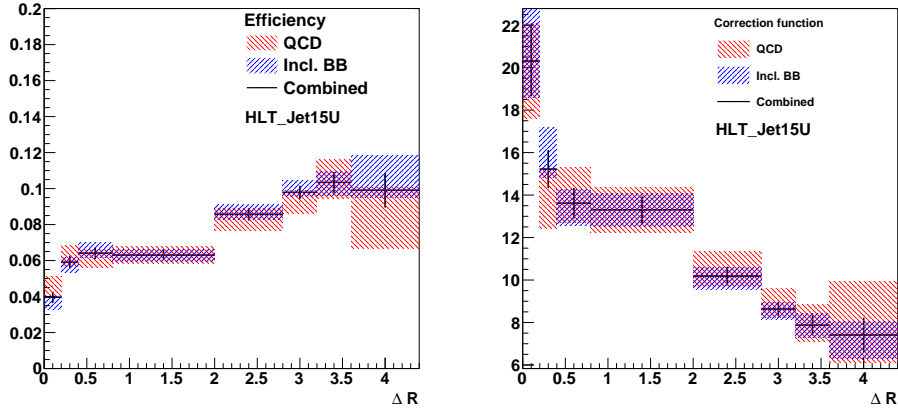


Figure 7.13: Efficiency (left) and correction function (right) for the QCD sample, the Inclusive BB sample and the combined function for leading jet $p_T > 56$ GeV.

A data driven method based on event mixing is used to check the validity of the ΔR_{VV} dependence (the shape) of the efficiency correction functions obtained from simulation. The method is described in the chapter about systematic uncertainties. The ΔR_{VV} dependence is found to be well described by the simulation.

Chapter 8

Measured Properties of Reconstructed B Candidates

In this chapter the properties of the previously defined B candidates are studied. The properties of the selected B candidates measured from data are compared to the PYTHIA MC predictions. The data samples listed in section 4.2 and the combined PYTHIA MC sample are used. All plots in this chapter are shown for the leading jet $p_T > 84 \text{ GeV}$ bin. The distributions for the other bins are provided in appendix B. The simulated data is decomposed into the different sources, beauty, charm and light vertices according to MC truth (see section 6.4 for the definition of B, D and light vertices). The PYTHIA prediction on the relative amount of B, D and light selected B candidate vertices (all cuts applied) are listed in table 8.1 for the three different leading jet p_T bins.

leading jet p_T	B (%)	D (%)	light (%)
$> 56 \text{ GeV}$	80.8	16.3	2.9
$> 84 \text{ GeV}$	78.6	16.2	5.3
$> 120 \text{ GeV}$	76.1	15.9	8.0

Table 8.1: PYTHIA prediction on the relative amount of selected B candidate vertices from B, D and light hadron decays for the three leading jet p_T bins.

The data are shown in the figures by solid black points. The simulated distributions are normalized to the total number of data events. If the MC distributions are normalized to the data luminosity the amount of MC B candidates corresponds to 99.3 % of the total number of B candidates found in data. For the leading jet $p_T > 56 \text{ GeV}$ and 120 GeV bins this number is 109.7 % and 101.9 %, respectively. For the different plots all selection cuts apart from those on the shown quantities are applied.

The η and ϕ distributions are shown in figure 8.1. The pseudorapidity distribution is symmetric with its maximum around zero. The contribution from light vertices is small in the central region and grows towards large absolute pseudorapidity. The cut for the selected vertices is $|\eta| < 2.0$. As expected, the B candidates azimuthal angle distribution is flat. Both data distributions are very well described by PYTHIA.

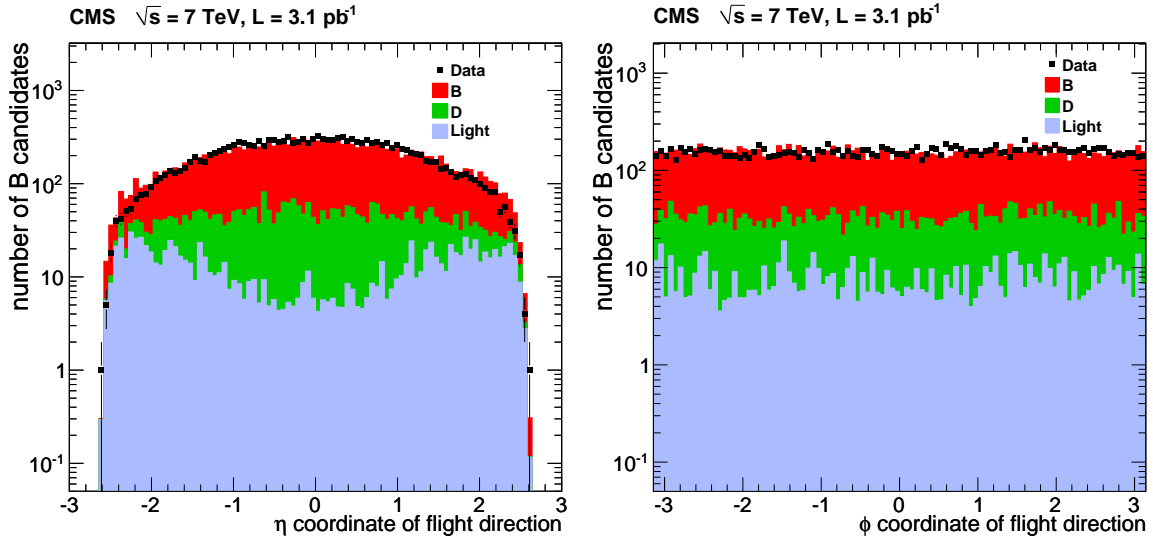


Figure 8.1: Properties of reconstructed B candidate vertices: η (left) and ϕ (right) distribution. The data are shown by solid points. The PYTHIA simulation is decomposed in B, D and light vertices. The simulated distribution is normalized to the number of data events. All selection cuts apart from those on the shown quantities are applied.

The vertex mass and the p_T distribution for the selected B candidate vertices are shown in figure 8.2. The mean vertex mass is very similar for D (1.45 GeV) and light (1.44 GeV), while it is significantly higher for B vertices (2.36 GeV). A cut at 1.4 GeV is applied for the selected B candidates. There are only a few vertices with $p_T < 8$ GeV. The mean p_T is similar for B, D and light vertices. The agreement between data and PYTHIA is good. A small excess in the data mass distribution is observed just below 2 GeV, in the leading jet $p_T > 84$ GeV and $p_T > 120$ GeV bins. About 16% more events are measured compared to the PYTHIA prediction at 1.7 GeV. This is exactly where the contribution from D vertices has its maximum. Hence, the reason for the excess could be larger contribution from charm vertices in the measured data.

The 3D flight distance and 3D flight distance significance distributions are shown in figure 8.3. The mean flight distance significance (after all other cuts are applied) is significantly different for the three vertex categories. It is 27.1, 13.1 and 7.1 for B, D and light vertices, respectively. With a cut at 5, mainly D and light vertices are removed. The inset shows a zoom into the small flight distance significance region in linear scale. Both the flight distance and the flight distance significance data distributions are well described by the PYTHIA MC simulation. In the flight distance there is a small excess in data for small values, there are 13% more events measured than predicted by PYTHIA in the region < 0.5 cm for leading jet $p_T > 84$ GeV. A similar excess is observed in the leading jet $p_T > 56$ GeV bin, but not in the $p_T > 120$ GeV region.

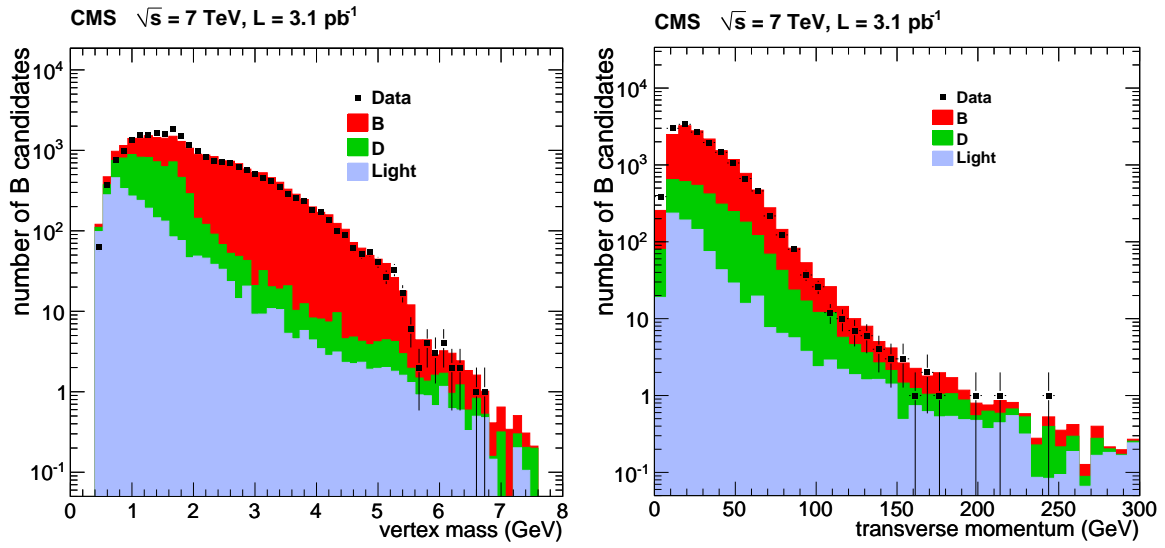


Figure 8.2: Properties of reconstructed B candidate vertices: vertex mass (left) and vertex p_T (right) distribution. The data are shown by solid points. The PYTHIA simulation is decomposed in B, D and light vertices. The simulated distribution is normalized to the number of data events. All selection cuts apart from those on the shown quantities are applied.

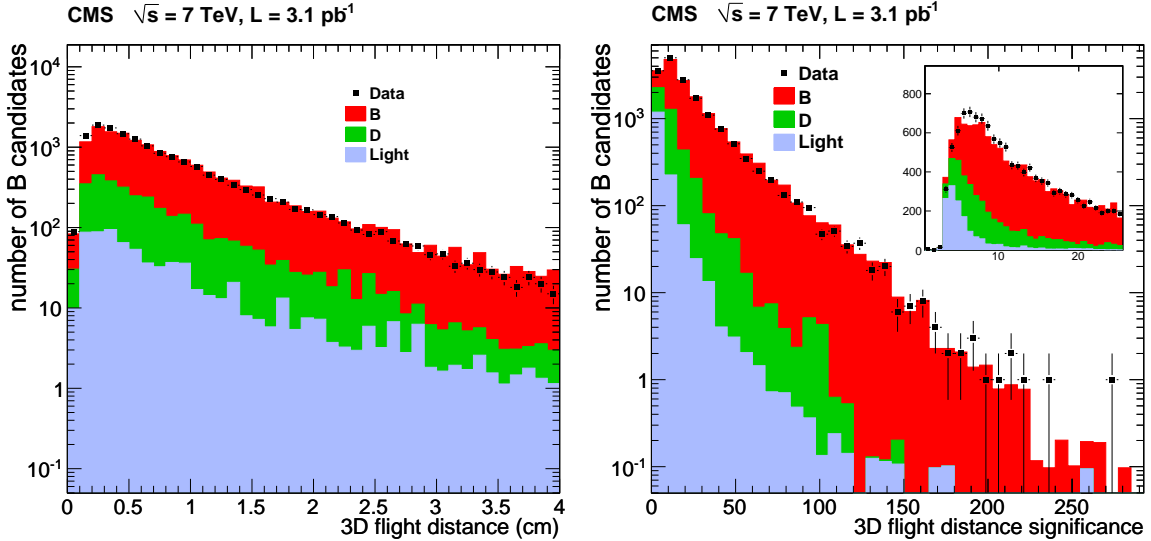


Figure 8.3: Properties of reconstructed B candidate vertices: 3D flight distance (left) and 3D flight distance significance (right) distribution. The data are shown by solid points. The PYTHIA simulation is decomposed in B, D and light vertices. The simulated distribution is normalized to the number of data events. All selection cuts apart from those on the shown quantities are applied. The inset in the right plot shows a zoom of the flight distance significance distribution with narrower bins and linear scale.

The total number of tracks associated with at least one selected B candidate vertex with weight $w_i > 0.5$ per event is shown in figure 8.4. The mean number of tracks is slightly different for the B and other categories: 5.2, 3.9 and 3.9 for B, D and light vertices, respectively. Again, charm and light vertices are similar. The mean value of the data distribution is 4.6. When comparing the shape of the MC and data distribution the agreement is very good. For data there are in average slightly less tracks than predicted by the PYTHIA simulation (the mean number for the combination of B, D and light vertices is 4.9).

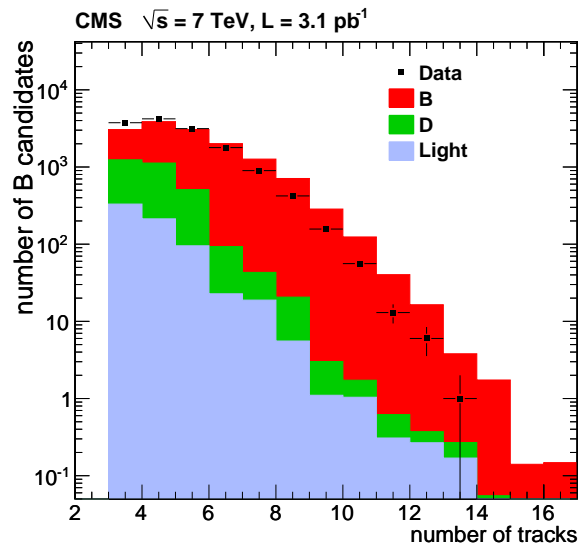


Figure 8.4: Number of tracks in the reconstructed B candidate vertices. The data are shown by solid points. The PYTHIA simulation is decomposed in B, D and light vertices. The simulated distribution is normalized to the number of data events.

Chapter 9

Systematic Uncertainties

The systematic uncertainties relevant for the differential distributions shown in the next chapter are divided into two categories, which are treated separately: uncertainties relevant to the *shape* of the distributions and uncertainties related to the *absolute normalization*. The uncertainties affecting the shape of the distribution are described in section 9.1. The uncertainties on the absolute normalization are described in section 9.2. The uncertainties relevant for absolute normalization are much larger than those on the shape. They sum up to almost 50%. The dominant contribution originates from the uncertainty on the efficiency of reconstructing two B hadrons. This analysis focuses on measuring the shape of the differential cross section as function of ΔR and $\Delta\phi$. The shape dependent uncertainties are discussed for the ΔR distributions. Very similar systematic uncertainties arise for the $\Delta\phi$ distributions. They are not quoted separately. All systematic uncertainties are calculated bin-wise, and are also included bin-wise in the distributions shown in the results chapter. The statistical uncertainty σ_{stat} and the systematic uncertainties on the shape $\sigma_{sys,shape}$ and on the absolute normalization $\sigma_{sys,abs}$ are added in quadrature. The total uncertainty σ_{tot} is defined as

$$\sigma_{tot} = \sqrt{\sigma_{stat}^2 + \sigma_{sys,shape}^2 + \sigma_{sys,abs}^2}. \quad (9.1)$$

Two kinematic regions are used for comparisons or normalizations of the simulation:

$$\Delta R < 0.8 \quad \text{and} \quad \Delta R > 2.4. \quad (9.2)$$

This choice is inspired by the fact that at low ΔR values, the gluon splitting process is the significant contribution, whereas at high ΔR values flavor creation prevails. The cross sections integrated over the two regions are denoted as $\sigma_{\Delta R < 0.8}$ and $\sigma_{\Delta R > 2.4}$ and the ratio as $\rho_{\Delta R} = \sigma_{\Delta R < 0.8} / \sigma_{\Delta R > 2.4}$. Measuring the two cross sections and the ratio $\rho_{\Delta R}$ provides information about the $b\bar{b}$ production mechanism. Uncertainties relevant to the shape are quoted in terms of the relative change of the integrated cross section ratio $\rho_{\Delta R}$.

9.1 Shape Dependent Systematic Uncertainties

9.1.1 Algorithmic Effects (data mixing)

One source of systematic uncertainty is related to the ΔR dependence of the vertex reconstruction efficiency. An algorithmic efficiency loss is observed at small ΔR , and the correc-

tions applied for $\Delta R < 0.5$ are quite large. An event mixing technique is applied on data and simulation, to verify whether this loss is well modeled in PYTHIA. First, events with at least one selected reconstructed B candidate are selected. Then pairs of such events are mixed by properly summing the output of single readout channels if their 3D primary vertex positions are compatible within the primary vertex resolution ($20 \mu\text{m}$). The mixed event is re-reconstructed, i.e. tracking, vertex finding and fitting as well as B candidate cleaning are performed. This is done both for a fraction of the data and for two CMS PYTHIA MC samples, one with a minimum \hat{p}_T cut at 30 GeV and one with $50 \text{ GeV} < \hat{p}_T < 80 \text{ GeV}$. Finally, a relative efficiency $\alpha(\Delta R)$ is defined as the fraction of mixed events where the two B candidates from the two original events are re-reconstructed. The shape of the relative efficiency for data and MC are compared to estimate a systematic uncertainty. In figure 9.1 the relative efficiency $\alpha(\Delta R)$ is shown for data and for the two MC samples. The two MC curves are similar, the efficiency in data is smaller than in MC. The ratio between data and MC is shown in the right plot for shape comparison (for the $\hat{p}_T > 30 \text{ GeV}$ sample). The variation of the ratio for different ΔR bins is small and the systematic uncertainty due to algorithmic effects is estimated to be 2%.

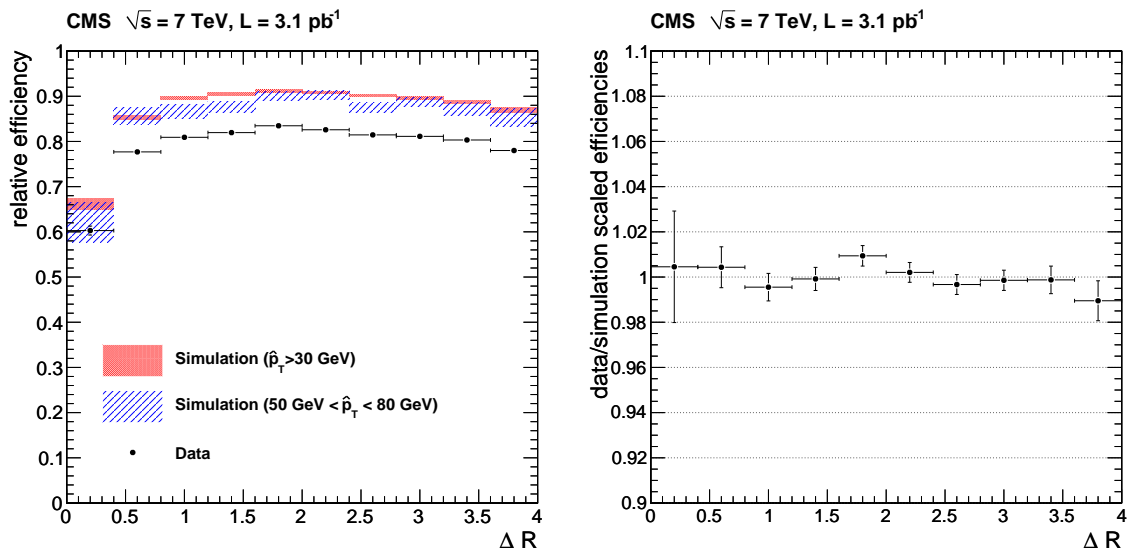


Figure 9.1: Study of the vertex reconstruction efficiency as function of ΔR by the event mixing method. Left: relative vertex reconstruction efficiency $\alpha(\Delta R)$. The simulation is shown for two energy scales, characterized by the PYTHIA \hat{p}_T (red: $\hat{p}_T > 30 \text{ GeV}$, blue: $50 \text{ GeV} < \hat{p}_T < 80 \text{ GeV}$). Right: ratio between the quantities $\alpha(\Delta R)$ determined from the data and from the simulation ($\hat{p}_T > 30 \text{ GeV}$ sample). To estimate the accuracy of the simulated shape the ratio has been rescaled to unity.

9.1.2 B Hadron Kinematics

A second source of systematic uncertainty is related to the modeling of the B hadron kinematics. The p_T of the B hadrons and the opening angle are strongly correlated as discussed in section 7.1. The mean reconstruction efficiency for an observed ΔR value strongly depends on the properties of the B hadron pair, especially on the p_T of the softer B hadron. Because all efficiency corrections are taken from MC simulation, it is important to verify that the kinematic behavior of the $B\bar{B}$ pairs are properly described by the simulation, otherwise the correction factors are wrong. Confidence in the modeling is provided by comparing the p_T distributions of the reconstructed B candidates derived from data and MC simulation. Figure 9.2 shows distributions characterizing the p_T behavior of the soft and the hard B hadron. Data and PYTHIA simulation are compared for the leading jet $p_T > 84$ GeV bin. The plots for the other two leading jet p_T bins are shown in appendix C.

In order to estimate the systematic uncertainty due to modeling of the B hadrons kinematics, the ΔR dependence of the average p_T of the softer B hadron is studied (see figure 9.3). The differences between data and simulation, convoluted with the p_T dependent efficiency, are found to have an effect of about 8%, 7% and 4% on the final result and these values are used as estimation for the systematic uncertainties.

9.1.3 Jet Energy Scale

The relative amount of GSP versus FCR events changes with the leading jet p_T (see chapter 10). Hence, an uncertainty on the absolute Jet Energy Scale (JES) translates into an uncertainty on the shape of the angular distributions between two B hadrons and on $\rho_{\Delta R} = \sigma_{\Delta R < 0.8} / \sigma_{\Delta R > 2.4}$. The JES uncertainty in CMS has been estimated in [67]. For the p_T range of the (leading) jets used herein to define the three bins for this study (56 to about 200 GeV) the uncertainty is below 3% (see figure 9.4). In addition, an uncertainty of 5% is added to take into account the differences for the jet energy corrections between b and light jets. This number is estimated comparing PYTHIA and Herwig simulation in [2]. The combined uncertainty of 6% on the leading jet p_T results in 6% systematic uncertainty on the ratio $\rho_{\Delta R}$.

9.1.4 Phase Space Correction

The efficiency and purity correction is defined such that it corrects the distributions measured using the B candidates to the visible phase space of the B hadrons defined by $|\eta(B)| < 2.0$ and $p_T(B) > 15$ GeV. B candidates are selected if $|\eta(SV)| < 2.0$ and $p_T(SV) > 8$ GeV. To estimate the uncertainty arising from the choice of the p_T cut, the analysis has been repeated with a cut on the reconstructed vertex p_T at 10 GeV instead of 8 GeV. The efficiency and purity corrections have been recalculated and the final measurement has been repeated. A comparison of the differential distributions determines the systematic uncertainty, see table 9.1. The distributions and their ratio are shown in figure 9.5 for the three leading jet p_T bins. The largest effect on $\rho_{\Delta R}$ is 2.8% and it is taken for all bins.

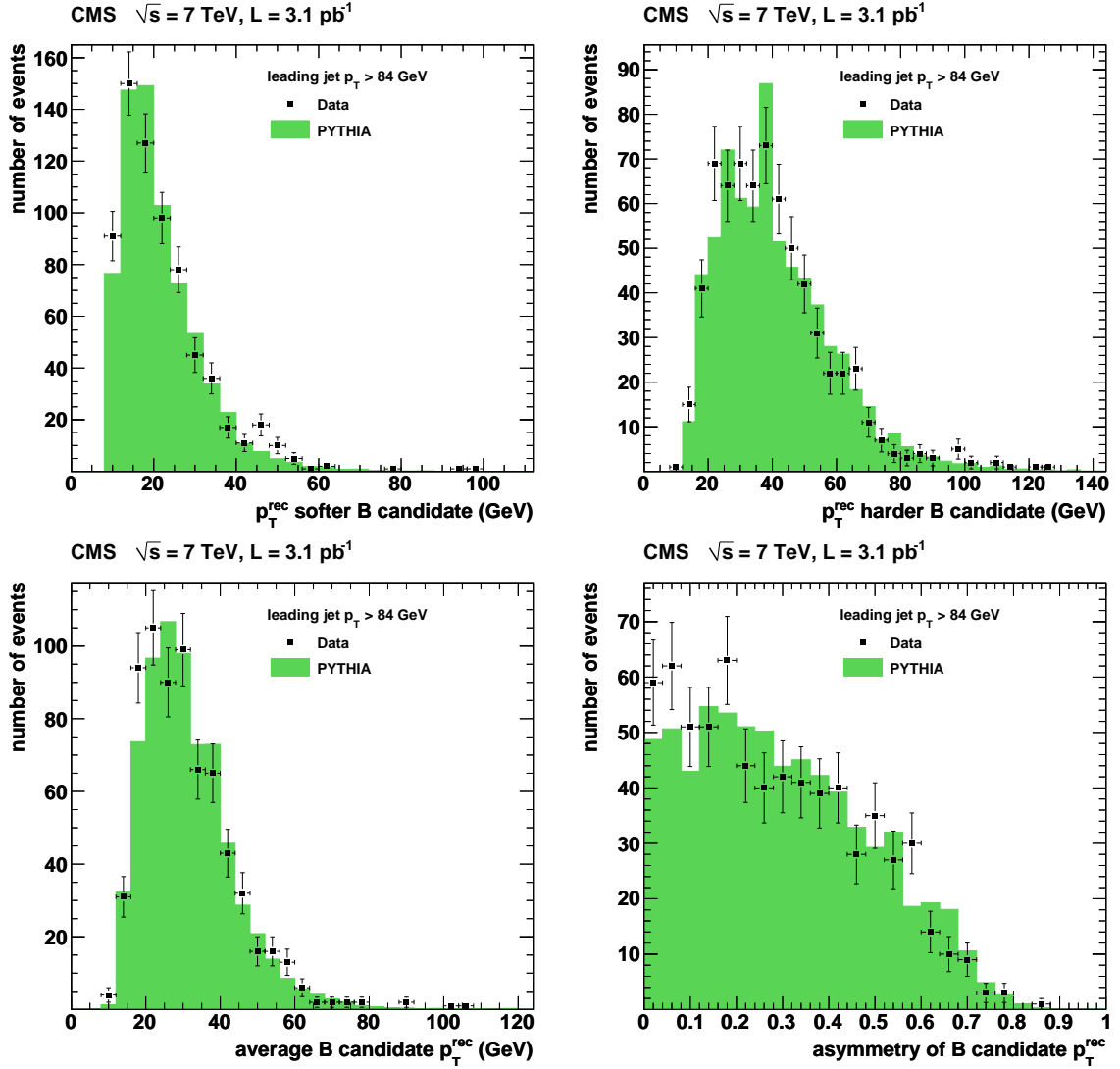


Figure 9.2: Comparison between data (solid dots) and PYTHIA simulation (green bars) for distributions of the reconstructed p_T of the two B hadrons: p_T of the softer B hadron (top left); p_T of the harder B hadron (top right); average p_T of the two B hadrons (bottom left); asymmetry of the p_T of the harder and the softer B hadron (bottom right). All plots are shown for the leading jet $p_T > 84$ GeV bin.

leading jet p_T	$p_T > 56$ GeV	$p_T > 84$, GeV	$p_T > 120$ GeV
$\rho_{\Delta R}(10 \text{ GeV})/\rho_{\Delta R}(8 \text{ GeV})$	0.985	0.972	0.986

Table 9.1: Relative change of $\rho_{\Delta R} = \sigma_{\Delta R < 0.8} / \sigma_{\Delta R > 2.4}$ when changing the p_T cut on the reconstructed vertices from 8 to 10 GeV.

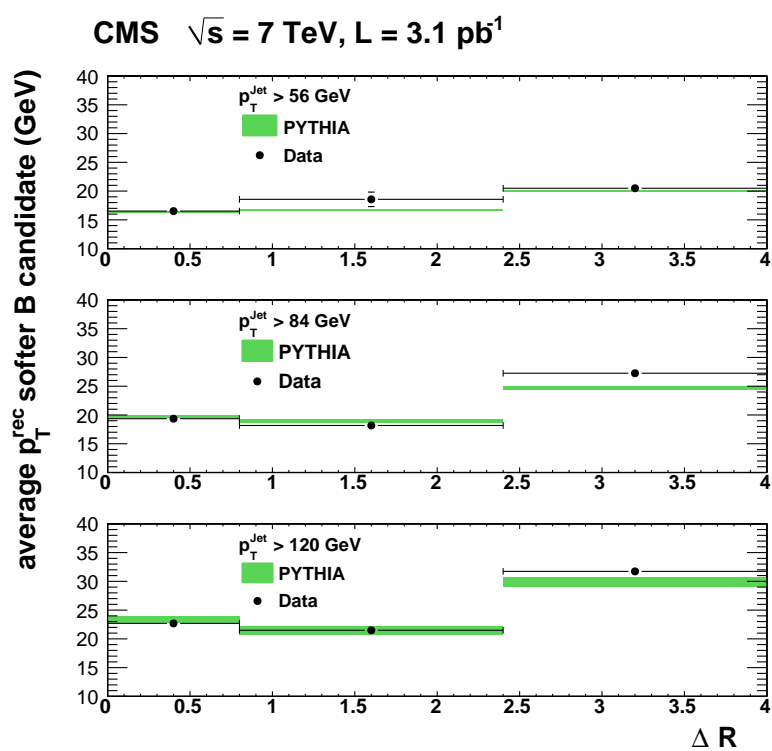


Figure 9.3: Average p_T of the softer B hadron as a function of ΔR for data (solid points) and simulation (green bars) for the three leading jet p_T regions.

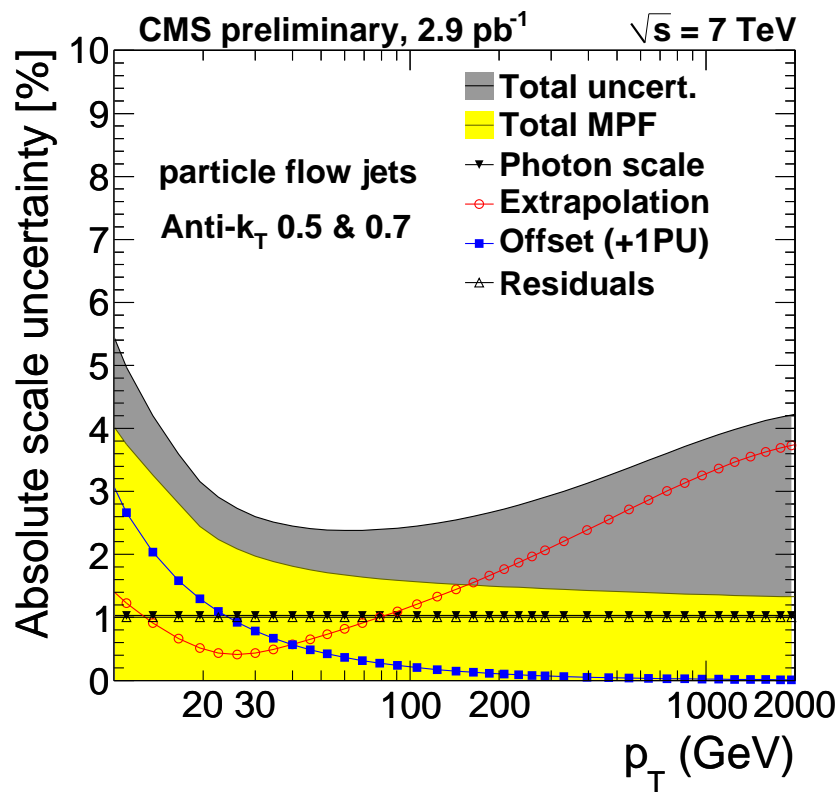


Figure 9.4: Overall uncertainty on the absolute JES for particle flow jets [67].

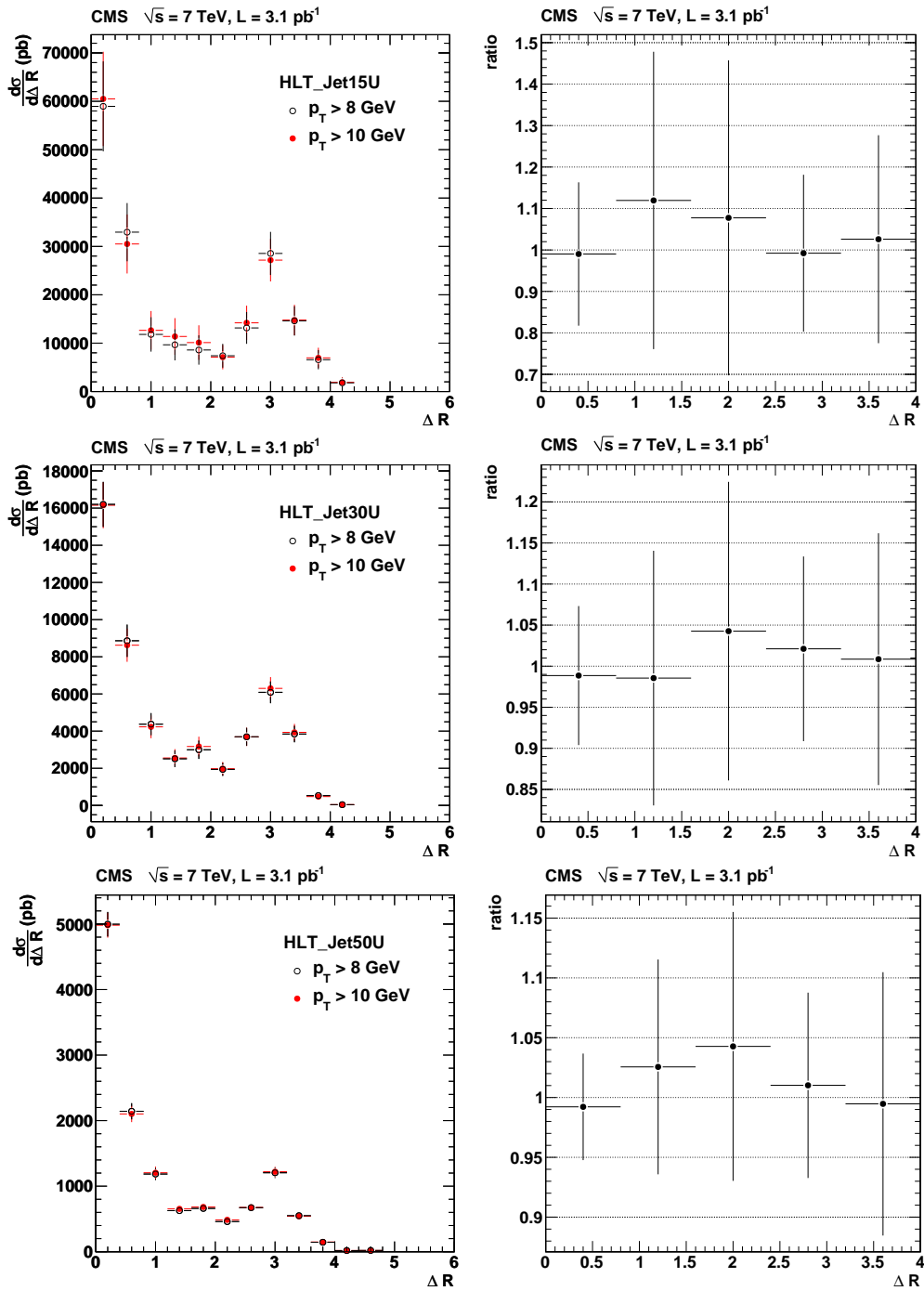


Figure 9.5: Left: Comparison of the differential $B\bar{B}$ production cross section as a function of ΔR for two choices of reconstructed p_T cut on the B candidates: 8 GeV (black) and 10 GeV (red). Right: ratio between the two (red curve divided by black curve). All plots are shown for the three leading jet p_T bins. The variations are taken as systematic uncertainty.

9.1.5 Bin Migration from Resolution

The bin-to-bin migration is an additional source of systematic uncertainty. The vertex resolution in ΔR is shown to be around 0.02, much smaller than the bin width in the ΔR distributions (0.4). Therefore, the uncertainty from bin migration is small. Migrations are taken into account through the efficiency corrections and the off-diagonal contributions are subtracted on a bin-to-bin basis. The largest amount of off-diagonal events comes at $\Delta R_{VV} \approx \pi$ (gluon splitting with one B vertex and one non-B vertex in the recoiling jet). The largest migration into one single bin is determined to be below 9%. The migration from the $\Delta R < 0.8$ to the $\Delta R > 2.4$ region is 1.2%, 2.6% and 4.2% for the three leading jet p_T regions, respectively. When increasing by 50% the small angle $\Delta R < 0.8$ contribution, 0.6%, 1.3% and 2.1% are obtained for the uncertainties on the purity correction in the different bins.

9.1.6 Monte Carlo Statistics Uncertainty

The MC statistics available to compute efficiency and purity correction functions is limited and this results in an additional bin-to-bin systematic uncertainty. The maximum value of either the statistical uncertainty of the simulation or half of the largest bin-to-bin fluctuation observed in the correction function between any of the ΔR bins, is taken as systematic uncertainty. It is found to be 13% and is reduced when integrating over multiple bins (as it is done for example when showing the $\rho_{\Delta R}$ ratio).

9.1.7 Total Systematic Uncertainties

The systematic uncertainties relevant for the shape are summarized in table 9.2.

Source of uncertainty in shape	Change in $\rho_{\Delta R} = \sigma_{\Delta R < 0.8} / \sigma_{\Delta R > 2.4}$ (%)		
	Leading jet p_T region		
	> 56 GeV	> 84 GeV	> 120 GeV
Algorithmic effects (data mixing)	2.0	2.0	2.0
B hadron kinematics (p_T of softer B)	8.0	7.0	4.0
Jet energy scale	6.0	6.0	6.0
Phase space correction	2.8	2.8	2.8
Bin migration from resolution	0.6	1.3	2.1
Subtotal shape uncertainty	10.6	9.9	8.3
MC statistical uncertainty	13.0	13.0	13.0
Total shape uncertainty	16.8	16.4	15.4

Table 9.2: Systematic uncertainties affecting the shape of the differential cross section as a function of ΔR , for the three different leading jet p_T regions. The values are quoted in terms of percentage changes of the integrated cross section ratio $\rho_{\Delta R}$. In the figures, these values are included for each bin. Similar systematic uncertainties are assumed for the $\Delta\phi$ distributions.

9.2 Systematic Uncertainties Affecting the Absolute Normalization

Albeit the main message of the analysis lies in the shape of the $\Delta R/\Delta\phi$ dependence, the cross sections are also measured in absolute normalized numbers. The systematic uncertainties for the absolute measurement are discussed in this section. The largest contribution is due to the uncertainty on the average IVF efficiency of correctly reconstructing a B hadron decay vertex. This uncertainty is estimated using standard b-tagging efficiency studies (see below). A possible way to reduce this uncertainty is to match the *SV based* analysis to a *jet based* analysis in the region where the two B are well separated and are reconstructed in two jets. The angle between two b-tagged jets with $p_T > 30$ GeV is measured, and the shape of the angular distribution is compared to the distribution of the angle measured between two vertices reconstructed with the IVF. The known b-tagging uncertainty is lower than the SV efficiency uncertainty, but additional sources of uncertainties for this jet matching method need to be evaluated. Uncertainties relevant for both methods are discussed first.

All distributions shown in the next chapter are obtained applying the ΔR dependent efficiency and purity corrections derived from simulation (without jet matching). Consequently, the total systematic error calculated with the method using the b-tagging efficiency studies is shown.

9.2.1 Uncertainties for Both Methods

Jet Energy Scale

Because of the falling jet p_T spectrum, the uncertainty on the (leading) jet p_T of 5 % due to JES translates into a variation of 10 % in the total number of events. This number is identical for all leading jet p_T regions.

Luminosity

The overall systematic uncertainty due to the luminosity is measured by the CMS luminosity group. For the run period taken in this analysis it is 11 % [69].

Trigger Efficiency

The systematic uncertainty due to uncertainty in the trigger turn-on curves yields 1 %.

Event Modeling

Uncertainties in the modeling of the b quark, the b hadronization and the B hadron decays, as implemented in the simulation, are expected to have a minor effect on the efficiency. The systematic uncertainty due to the applied jet algorithm is neglected.

9.2.2 Uncertainties for IVF Efficiency Correction

Phase space correction:

The uncertainty due to the normalization to the visible phase space is determined as described above for the shape dependent uncertainty and found to be ± 5 %.

Average IVF efficiency:

The uncertainty on the IVF absolute efficiency is estimated starting from standard b-tagging efficiency studies. The same level of data/MC agreement is observed for the IVF as in [79]. Therefore the uncertainty of reconstructing one B is estimated to be 20%. This results in an uncertainty of 40% for reconstructing two B hadrons. This is the dominant uncertainty for the absolute cross section measurement. It can be avoided if using the jet matching method instead of the correction functions derived from simulation.

9.2.3 Uncertainties for B-Jet Matching Method

The absolute normalization of the SV reconstruction is probed by performing an independent analysis based on tagged b-jets in events with two well separated B hadrons. The standard CMS b-tag procedure with the SSVHP discriminator [70, 79, 86] was applied to identify events with two tagged b-jets and measure the angle between two jets with $p_T > 30$ GeV and $|\eta| < 2.0$. The measurement is corrected to the phase space with a B hadron with $p_T > 15$ GeV. The ΔR distribution determined with the vertex based method is compared with the one obtained with tagged b-jets. Both methods agree in the region $\Delta R > 1.0$, as proven in figure 9.6. This data driven test complements the mixing method because consistency is provided not only in terms of shape and structure, but also in terms of absolute normalization.

The deviations between the SV and b-tagging method are used to determine the systematic uncertainty on the absolute normalization. There are three contributions:

Average b-tagging efficiency:

The average b-jet tagging efficiency uncertainty, taken from the CMS b-tagging group, is about 10% for a single b-jet [79]. This results in 20% uncertainty for double b-tag.

Jet phase space correction:

The b-tag analysis requires a jet of $p_T > 30$ GeV. This phase space is corrected to the phase space with a B hadron with $p_T > 15$ GeV, using simulation. The uncertainty on this is estimated based on the variations of different MC samples with respect to PYTHIA mean. The maximum variation of 20% is taken as systematic uncertainty.

Jet matching uncertainty:

The influence of the choice of the region in ΔR where the two methods are compared is estimated by varying the cut between $\Delta R > 1.0$ and $\Delta R > 2.4$. It is 5%.

9.2.4 Total Systematic Uncertainties

Systematic uncertainties relevant for the normalization are summarized in table 9.3.

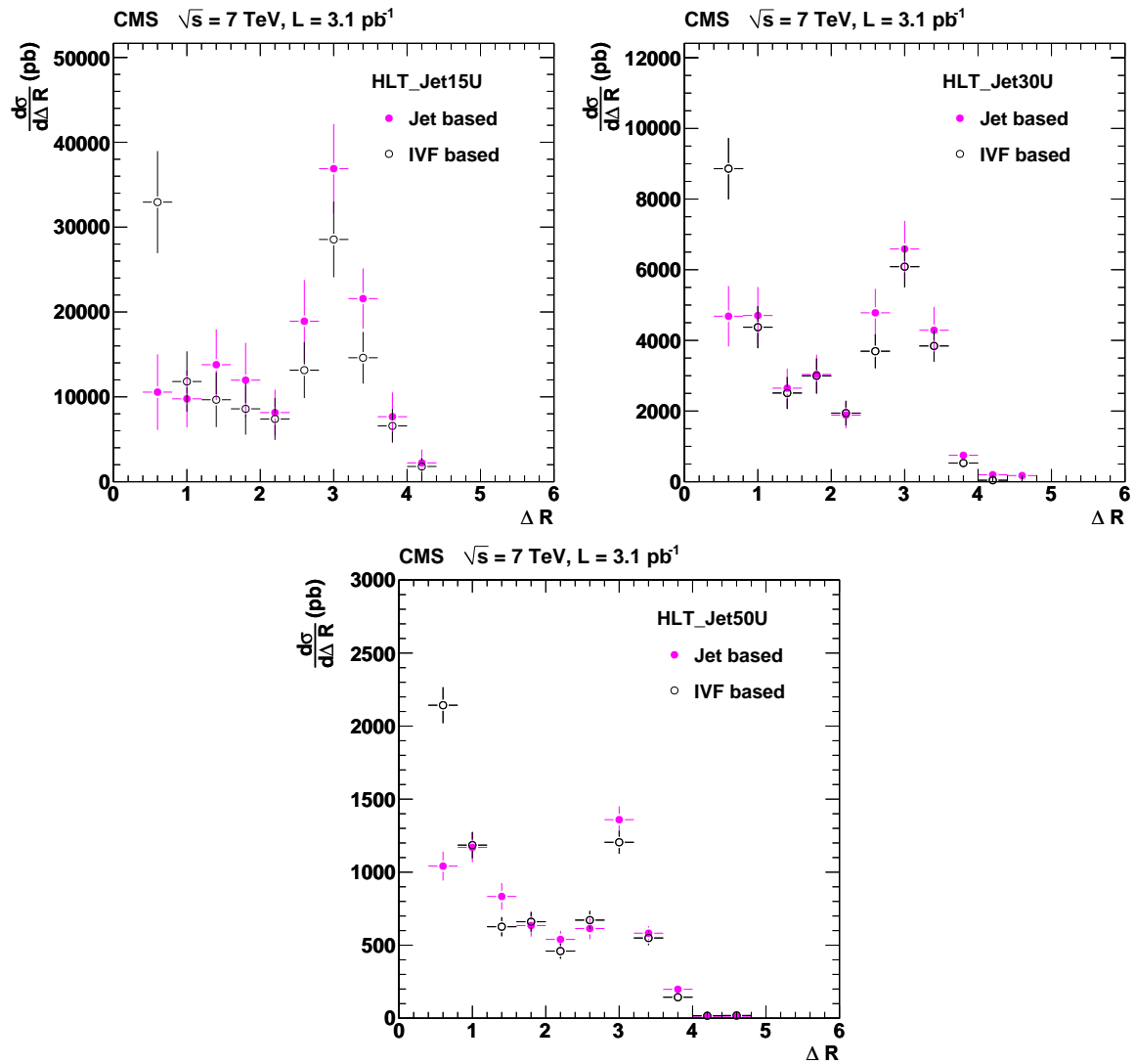


Figure 9.6: Comparison of the differential $B\bar{B}$ production cross section as a function of ΔR obtained with the IVF based method (black) and with the method based on b-tagging (pink) for the three leading jet p_T regions. The first bin is suppressed.

Source of uncertainty in normalization	relative uncertainty (%)
Jet energy scale	10
Luminosity	11
Trigger efficiency	1
Phase space correction	5
Average IVF efficiency	40
Average b-tagging efficiency	20
Jet phase space correction	20
Jet matching uncertainty	5
Total (IVF efficiency correction)	43
Total (b-jet matching method)	32

Table 9.3: Systematic uncertainties affecting the normalization of differential cross section values. Maximum values are typically reached at low ΔR values.

Chapter 10

Results

Angular correlations between pairs of beauty hadrons are measured at $\sqrt{s} = 7$ TeV for the first time. The differential $B\bar{B}$ cross sections are measured in the full angular region down to small opening angles using a data sample collected by CMS during the 2010 data taking period. The sample corresponds to an integrated luminosity of 3.1 pb^{-1} .

First, measurements of $B\bar{B}$ production are presented differentially as a function of the opening angles ΔR and $\Delta\phi$ between the two B hadrons. The measurements are done for three different event scales, defined by the transverse momentum of the leading jet. An extrapolation from hadron (B) to parton (b quark) level is not done here as it would introduce additional uncertainty due to modeling of the heavy quark fragmentation and hadronization. All results are given for the visible kinematic phase space defined by $|\eta(B)| < 2.0$ and $p_T(B) > 15$ GeV for both B hadrons.

Second, the measurements are compared with the theoretical predictions obtained with various MC event generator programs, based on LO and NLO perturbative QCD calculations.

10.1 Differential Cross Section Distributions in ΔR and $\Delta\phi$

The differential cross sections are determined independently for the three different jet p_T regions. The determinations are done according to

$$\left(\frac{d\sigma_{\text{visible}}(pp \rightarrow B\bar{B} X)}{dA} \right)_i = \frac{N_i(\text{data}) \cdot p_i}{\Delta A_i \cdot \mathcal{L} \cdot \epsilon_i} \quad (10.1)$$

for the three leading jet p_T regions. The conventions used are the following:

- i is the bin number,
- $N_i(\text{data})$ denotes the number of measured selected $B\bar{B}$ events in bin i ,
- \mathcal{L} is the integrated luminosity,

ϵ_i is the total efficiency in the given bin,
 p_i is the purity for bin i ,
 ΔA_i is the bin width of bin in variable A , with A being ΔR or $\Delta\phi$.

Due to prescales, the integrated luminosity is 0.031, 0.313 and 3.069 pb⁻¹ for the leading jet p_T regions (above 56, 84 and 120 GeV, respectively). The efficiency, the purity and the combined correction factor $cf_i = p_i/\epsilon_i$, are discussed in chapter 7. The distributions obtained for data are compared to MC simulation (PYTHIA). The measured differential cross section is always calculated using equation 10.1 with the measured integrated luminosity. For the MC distributions, three different normalization procedures are applied:

- (i) *Absolute normalization*: the MC distributions are scaled to the same integrated luminosity as the data distributions. Systematic uncertainties on efficiency and purity corrections and on the data luminosity are relevant for comparison of the measured total cross section with the predicted cross section, and those are large (see chapter 9).
- (ii) *Relative normalization in the back-to-back region*: the MC distribution is normalized using the cross section integrated over the region $\Delta R > 2.4$ (or $\Delta\phi > \frac{3}{4}\pi$). In this region, the theory calculations are expected to be most reliable, since the cross section is anticipated to be dominated by leading order diagrams (FCR). The uncertainty on the absolute normalization is then not shown in the figure and only the shape dependent systematic uncertainties are shown. Those are significantly smaller than the uncertainties relevant for the absolute normalization (between 15.4% and 16.8% compared to 43%).
- (iii) *Relative normalization to the measured cross section*: The MC distribution is normalized to the cross section integrated over the visible range. Again, only shape dependent systematic uncertainties are shown.

The measured cross sections as a function of ΔR and $\Delta\phi$ are shown in figure 10.1 for the three leading jet p_T regions. The inner error bars show statistical uncertainty, the outer bars combined statistical and shape dependent systematic uncertainties added in quadrature. The systematic error of 43% for the absolute normalization is added in quadrature on top of the other uncertainties and shown as a yellow band.

It is observed that the contributions at low values of ΔR and $\Delta\phi$ are substantial and exceed those at large angles, where the two B hadrons are emitted back-to-back. PYTHIA overestimates the differential $B\bar{B}$ production cross section for ΔR and $\Delta\phi$ around π (back-to-back topology). In the collinear region, the PYTHIA prediction is rather accurate. The ratio between the data distribution and the PYTHIA prediction is shown in figure 10.2 for the three leading jet p_T bins.

Because errors on the absolute normalization are large, only the shape comparison is shown in [64]. The measured distributions are the same as in figure 10.1, and the simulated distributions are normalized to the region $\Delta R > 2.4$ ($\Delta\phi > \frac{3\pi}{4}$) (see figure 10.3).

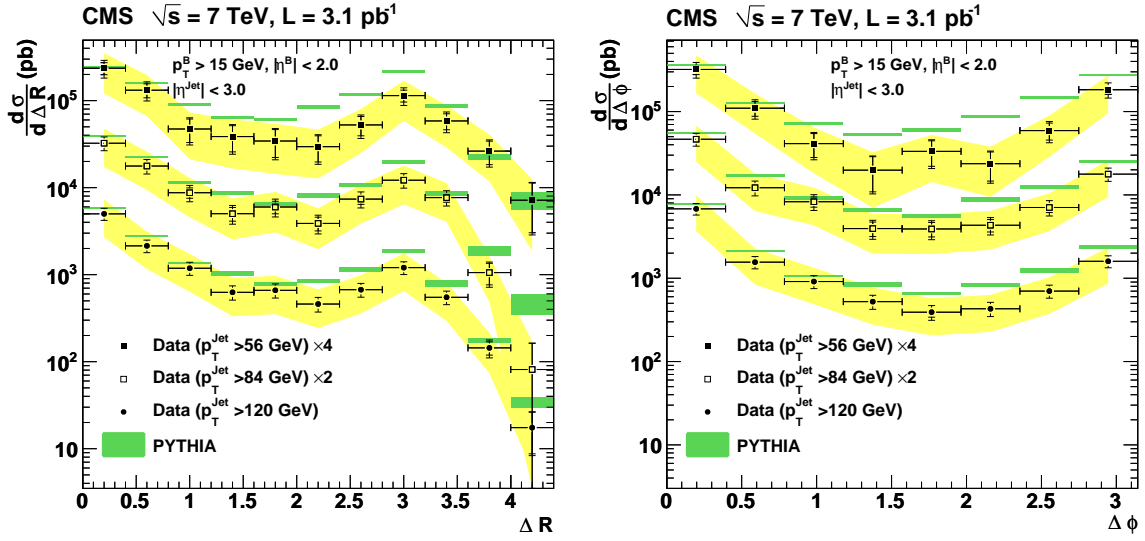


Figure 10.1: Differential $B\bar{B}$ production cross sections as a function of ΔR (left) and $\Delta\phi$ (right) for the three leading jet p_T regions. For clarity, the $p_T > 56$ and $p_T > 84$ GeV bins, the $p_T > 56$ and $p_T > 84$ GeV bins, are offset by a factor 4 and 2, respectively. For the data points, the error bars show the statistical uncertainties (inner bars) and statistical and shape dependent systematic uncertainties added in quadrature (outer bars). The yellow bands show the total uncertainties including the systematic uncertainty on the absolute normalization. The symbols denote the values averaged over the bins and are plotted at the bin centers. The PYTHIA simulation (shaded bars) is normalized to the measured integrated luminosity. The widths of the shaded bands indicate the statistical uncertainties of the predictions.

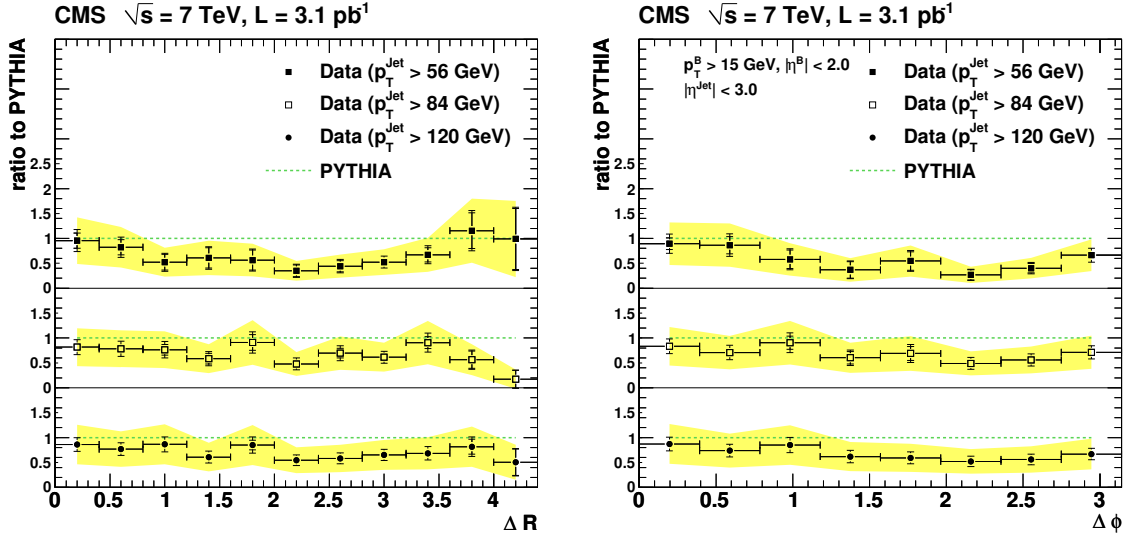


Figure 10.2: Ratio of the differential $B\bar{B}$ production cross sections: data with respect to PYTHIA predictions, as function of ΔR (left) and $\Delta\phi$ (right), for the three leading jet p_T regions. The simulation is normalized to the measured luminosity. The statistical errors (inner error bars), the statistical and shape dependent systematic uncertainties added in quadrature (outer error bars) and the total systematic uncertainties including the uncertainty on the absolute normalizations (yellow band) are shown.

Finally, the data and simulation are compared by scaling the MC distribution to the integrated cross section in the visible range in figure 10.4.

The numerical values of the measurements are listed in tables 10.1 and 10.2. A more detailed table with the statistical and different systematic uncertainties listed separately is given in appendix C. The total measured cross sections are

$$\sigma_{\text{visible}}(pp \rightarrow B\bar{B} X) = 78 \pm 35 \text{ nb} \quad (\text{leading jet } p_T > 56 \text{ GeV}), \quad (10.2)$$

$$\sigma_{\text{visible}}(pp \rightarrow B\bar{B} X) = 20 \pm 9 \text{ nb} \quad (\text{leading jet } p_T > 84 \text{ GeV}), \quad (10.3)$$

$$\sigma_{\text{visible}}(pp \rightarrow B\bar{B} X) = 5.1 \pm 2.2 \text{ nb} \quad (\text{leading jet } p_T > 120 \text{ GeV}). \quad (10.4)$$

The ΔR shape is measured to be different for the three leading jet p_T regions, because the relative amount of FCR, FEX and GSP changes. The jet energy scale dependence is shown in figure 10.5. The ratio $\rho_{\Delta R}$ is shown as a function of the leading jet p_T , which is an indication of the scale of the hard interaction. The symbols are plotted at the mean leading jet p_T of the bins. The asymmetry between the small angle and the back-to-back contribution is characterized by the variable $(\sigma_{\Delta R < 0.8} - \sigma_{\Delta R > 2.4}) / (\sigma_{\Delta R < 0.8} + \sigma_{\Delta R > 2.4})$. The measurement clearly indicates that the relative contributions of $\sigma_{\Delta R < 0.8}$ significantly exceed those at $\sigma_{\Delta R > 2.4}$. The ratio and the asymmetry strongly depend on the event energy scale. Higher values are measured for increasing event energy. Identical behavior is also observed for the azimuthal angle difference $\Delta\phi$, the contributions of $\sigma_{\Delta\phi < \frac{\pi}{4}}$ are significantly exceeding those at $\sigma_{\Delta\phi > \frac{3\pi}{4}}$.

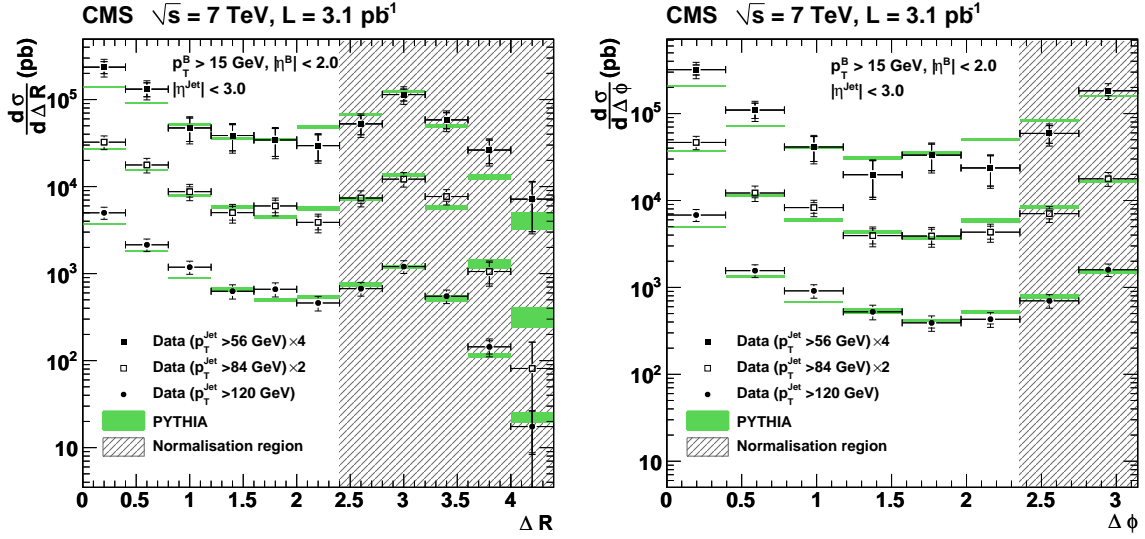


Figure 10.3: Differential $B\bar{B}$ production cross sections as a function of ΔR (left) and $\Delta\phi$ (right) for the three leading jet p_T regions. For clarity, the $p_T > 56$ and $p_T > 84$ GeV bins are offset by a factor 4 and 2, respectively. For the data points, the error bars show the statistical (inner bars) and the total (outer bars) uncertainties. A common uncertainty of 43% due to the absolute normalization on the data points is not included. The symbols denote the values averaged over the bins and are plotted at the bin centers. The PYTHIA simulation (shaded bars) is normalized to the region $\Delta R > 2.4$ or $\Delta\phi > \frac{3}{4}\pi$, as indicated by the shaded normalization regions. The widths of the shaded bands indicate the statistical uncertainties of the predictions.

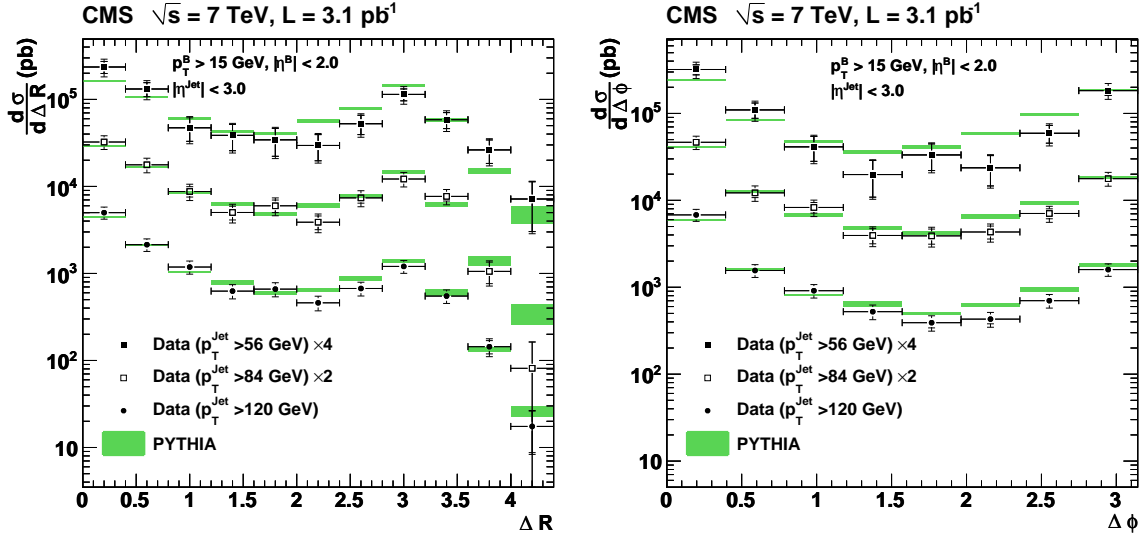


Figure 10.4: Differential $B\bar{B}$ production cross sections as a function of ΔR (left) and $\Delta\phi$ (right) for the three leading jet p_T regions. The data points (including the error bars) are identical to the ones in figure 10.3. The PYTHIA simulation (shaded bars) is normalized to the integrated cross section in the visible range.

Bin center	Jet $p_T > 56$ GeV		Jet $p_T > 84$ GeV		Jet $p_T > 120$ GeV	
	σ	σ_{err}	σ	σ_{err}	σ	σ_{err}
0.2	23582	11502.7	6480.29	3020.1	1998.81	916.168
0.6	13178.3	6541.12	3544.48	1667.1	857.191	394.68
1	4721.75	2603.16	1749.14	839.075	474.087	219.536
1.4	3863.25	2199.5	1004.13	495.863	250.666	117.455
1.8	3434	1996.56	1198.48	585.454	264.29	123.68
2.2	2957.44	1683.79	776.203	383.305	183.898	86.5513
2.6	5257.67	2759.83	1477.29	706.247	268.774	125.337
3	11418.2	5563.68	2434.87	1144.29	481.878	222.376
3.4	5841.64	2958.63	1537.08	728.996	219.77	102.202
3.8	2629.87	1449.88	211.291	113.494	57.6338	28.1753
> 4.0	717.237	530.158	16.2532	17.8903	14.5924	7.33119

Table 10.1: Cross sections σ and the total uncertainties on the cross sections σ_{err} for the different ΔR bins and the three leading jet p_T bins. All values are given in pb. The statistical and the systematic uncertainties on shape and absolute normalization are added in quadrature. The bin width is 0.4.

Bin center	Jet $p_T > 56$ GeV		Jet $p_T > 84$ GeV		Jet $p_T > 120$ GeV	
	σ	σ_{err}	σ	σ_{err}	σ	σ_{err}
$\pi/16$	31448.9	15098.9	9144.79	4244.94	2670.68	1223.1
$3\pi/16$	10781.0	5424.19	2394.63	1137.22	612.063	282.638
$5\pi/16$	4051.12	2272.57	1626.42	781.679	358.348	166.616
$7\pi/16$	1944.96	1254.84	774.268	387.737	205.673	96.8207
$9\pi/16$	3270.5	1872.1	766.157	383.598	153.579	72.8887
$11\pi/16$	2326.26	1393.38	849.127	416.422	168.855	79.6396
$13\pi/16$	5804.27	2994.87	1386.7	663.18	275.216	128.119
$15\pi/16$	17974.4	8578.78	3487.42	1627.44	627.171	288.603

Table 10.2: Cross sections σ and the errors on the cross sections σ_{err} for the different $\Delta\phi$ bins and the three leading jet p_T bins. All values are given in pb. The statistical and the systematic uncertainties on shape and absolute normalization are added in quadrature. The bin width is $\pi/8$.

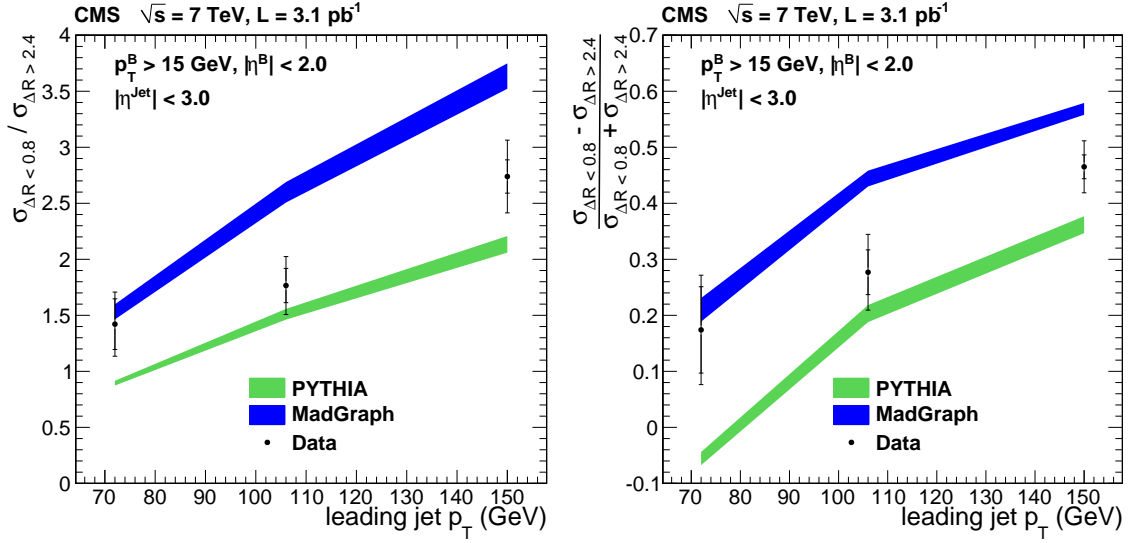


Figure 10.5: Left: Ratio between the $B\bar{B}$ production cross sections in $\Delta R < 0.8$ and $\Delta R > 2.4$, $\rho_{\Delta R} = \sigma_{\Delta R < 0.8} / \sigma_{\Delta R > 2.4}$, as a function of the leading jet p_T . Right: asymmetry between the two regions, $(\sigma_{\Delta R < 0.8} - \sigma_{\Delta R > 2.4}) / (\sigma_{\Delta R < 0.8} + \sigma_{\Delta R > 2.4})$. The symbols denote the data averaged over the bins and are plotted at the mean leading jet p_T of the bins. For the data points, the error bars show the statistical (inner bars) and the total (outer bars) uncertainties. Also shown are the predictions from the PYTHIA and MadGraph simulations. The widths of the bands indicate the uncertainties arising from the limited number of simulated events.

The numerical values of the measurement are listed in table 10.3. For data the error given in the table consists of the statistical error and the systematic error due to limited MC statistics added in quadrature. The other systematic uncertainties on shape and on absolute normalization cancel when computing the ratio $\rho_{\Delta R}$, because they are fully correlated for all bins. When summing the contributing bins to determine the total cross sections for the two ΔR regions, both the statistical and the systematic errors per bin are added quadratically since the errors for the different bins are uncorrelated. Finally, the relative errors on $\sigma_{\Delta R < 0.8}$ and on $\sigma_{\Delta R > 2.4}$ are added quadratically to get the relative uncertainty on the ratio. For the MC ratios only the statistical errors are given.

The ratio $\rho_{\Delta R}$ increases from 1.42 ± 0.28 at the lowest event energy scale bin by almost a factor of two to 2.74 ± 0.37 at the highest energy scale bin. A similar change is also observed for the change of the ratio $\rho_{\Delta\phi}$. While PYTHIA overestimates the contribution in the back-to-back region (both for ΔR and $\Delta\phi$) the ratios $\rho_{\Delta R}$ and $\rho_{\Delta\phi}$ are overestimated in MadGraph.

The Ratio $\rho_{\Delta R}$ for different data taking periods

The data used herein are based on the first proton-proton collisions produced at a center-of-mass energy $\sqrt{s} = 7$ TeV. The instantaneous luminosity was increased by orders of magnitudes during the 2010 data taking period and trigger prescales changed from time to time.

Jet p_T						$\rho_{\Delta R} = \sigma_{\Delta R < 0.8} / \sigma_{\Delta R > 2.4}$		
Cut (GeV)	$\langle p_T \rangle$ (GeV)	$\sigma_{\Delta R < 0.8}$ (nb)	$\sigma_{\Delta R > 2.4}$ (nb)	$\langle \epsilon \rangle$ (%)	$\langle p \rangle$ (%)	Data (stat+sys)	PYTHIA (stat)	MadGraph (stat)
> 56	72	37 ± 18	26 ± 13	7.4	84.9	1.42 ± 0.28	0.90 ± 0.02	1.53 ± 0.07
> 84	106	10 ± 4.7	5.7 ± 2.7	9.3	84.6	1.77 ± 0.26	1.51 ± 0.05	2.60 ± 0.09
> 210	150	2.9 ± 1.3	1.0 ± 0.5	10.7	83.2	2.74 ± 0.37	2.14 ± 0.07	3.64 ± 0.11

Jet p_T						$\rho_{\Delta\phi} = \sigma_{\Delta\phi < \frac{\pi}{4}} / \sigma_{\Delta\phi > \frac{3\pi}{4}}$		
Cut (GeV)	$\langle p_T \rangle$ (GeV)	$\sigma_{\Delta\phi < \frac{\pi}{4}}$ (nb)	$\sigma_{\Delta\phi > \frac{3\pi}{4}}$ (nb)	$\langle \epsilon \rangle$ (%)	$\langle p \rangle$ (%)	Data (stat+sys)	PYTHIA (stat)	MadGraph (stat)
> 56	72	42 ± 20	24 ± 12	7.4	84.9	1.78 ± 0.38	1.15 ± 0.03	2.07 ± 0.09
> 84	106	11.5 ± 5.4	4.9 ± 2.3	9.3	84.6	2.37 ± 0.40	1.95 ± 0.06	3.41 ± 0.12
> 210	150	3.3 ± 1.5	0.9 ± 0.4	10.7	83.2	3.64 ± 0.57	2.73 ± 0.10	4.79 ± 0.15

Table 10.3: Input values used to calculate the $B\bar{B}$ production cross section ratio $\rho_{\Delta R}$, as shown in figure 10.5, and the corresponding ratio $\rho_{\Delta\phi}$. Listed are the p_T cut of the leading jet, average jet p_T , cross sections in the two ΔR and $\Delta\phi$ regions (including the 43% uncertainty on the absolute normalization), average efficiency, average purity, and cross section ratio for the data, as well as for the PYTHIA and MadGraph simulations. Statistical and systematic uncertainties are included for the data, while for the simulations only the statistical uncertainties are given.

As an important consistency check to ensure that the result $\rho_{\Delta R}$ remains invariant over the data taking time, the data was split into three ranges of run numbers N_{run} :

- $N_{run} < 141950$
- $141950 < N_{run} < 143731$
- $143731 < N_{run}$

It is observed that the results for the three data taking periods are consistent (see figure 10.6). It is interesting to compare the errors for the three periods: for runs taken early (blue), the error grows with the leading jet p_T cut. In this period the instantaneous luminosity was low and the prescale factors were close to unity. Therefore more data were available in the lower leading jet p_T bins. Towards the end of the data taking period (green), the instantaneous luminosity was higher, the lower jet triggers were prescaled and most data were available in the highest leading jet p_T bin. Hence, the error in the lowest bin is largest.

10.2 Detailed Comparison with Theoretical Predictions

The measured distributions shown in the previous figures are compared with various theoretical predictions, based on both LO and NLO perturbative QCD calculations. Within pQCD, $B\bar{B}$ pairs are at LO expected to be produced in back-to-back topology (i.e. with large values of both ΔR and $\Delta\phi$). The region of phase space with small opening angles provides strong sensitivity to collinear emission processes. Higher-order processes, such as gluon radiation

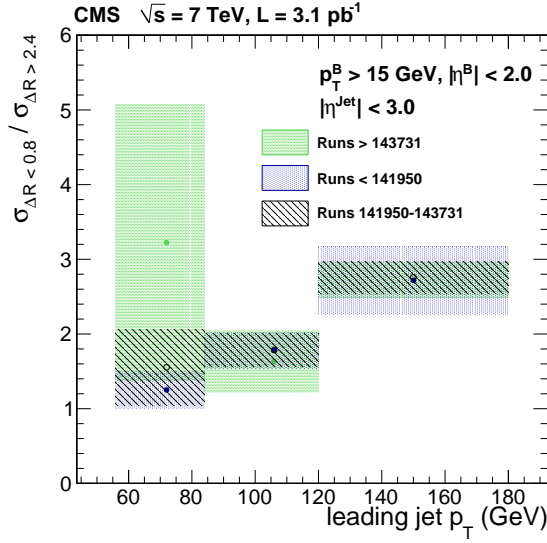


Figure 10.6: Ratio between the $B\bar{B}$ production cross section in $\Delta R < 0.8$ and $\Delta R > 2.4$, $\rho_{\Delta R} = \sigma_{\Delta R < 0.8} / \sigma_{\Delta R > 2.4}$, as a function of the leading jet p_T for three different data taking periods.

which splits into $b\bar{b}$ pairs, are anticipated to have a small angular separation between the b quarks.

The measurements show that the $B\bar{B}$ production cross section ratio $\rho_{\Delta R}$ increases with the event energy scale (see figure 10.5). Larger p_T values lead to more gluon radiation and, hence, are expected to produce more gluon splitting into $B\bar{B}$ pairs. This general trend is described by the theoretical calculations.

For comparison between data and theoretical predictions the PYTHIA, MadGraph, MC@NLO and CASCADE models are considered. The ratios between the predictions for the different MC models and for data with respect to PYTHIA are shown in figure 10.7 as function of ΔR and $\Delta\phi$ for the three leading jet p_T bins. The values for the predictions are normalized in the FCR region ($\Delta R > 2.4$ or $\Delta\phi > \frac{3\pi}{4}$). The widths of the theory bands indicate the statistical uncertainties of the simulation.

It is observed that none of the models matches the data distribution over the full ΔR or $\Delta\phi$ range. When normalizing to the back-to-back region, the data distribution lies between the PYTHIA and MadGraph predictions for small angles. CASCADE and MC@NLO underestimate the cross section in particular at small ΔR . While for CASCADE this is also true for the $\Delta\phi$ distribution, the MC@NLO prediction for $\Delta\phi$ is pretty accurate. Because the MC@NLO implementation is based on hard processes, it cannot account for all contributions generated with FEX and GSP. Some diagrams contributing to the almost collinear $b\bar{b}$ pair production are not included in MC@NLO, e.g. diagrams in which a gluon emits another gluon before splitting [33].

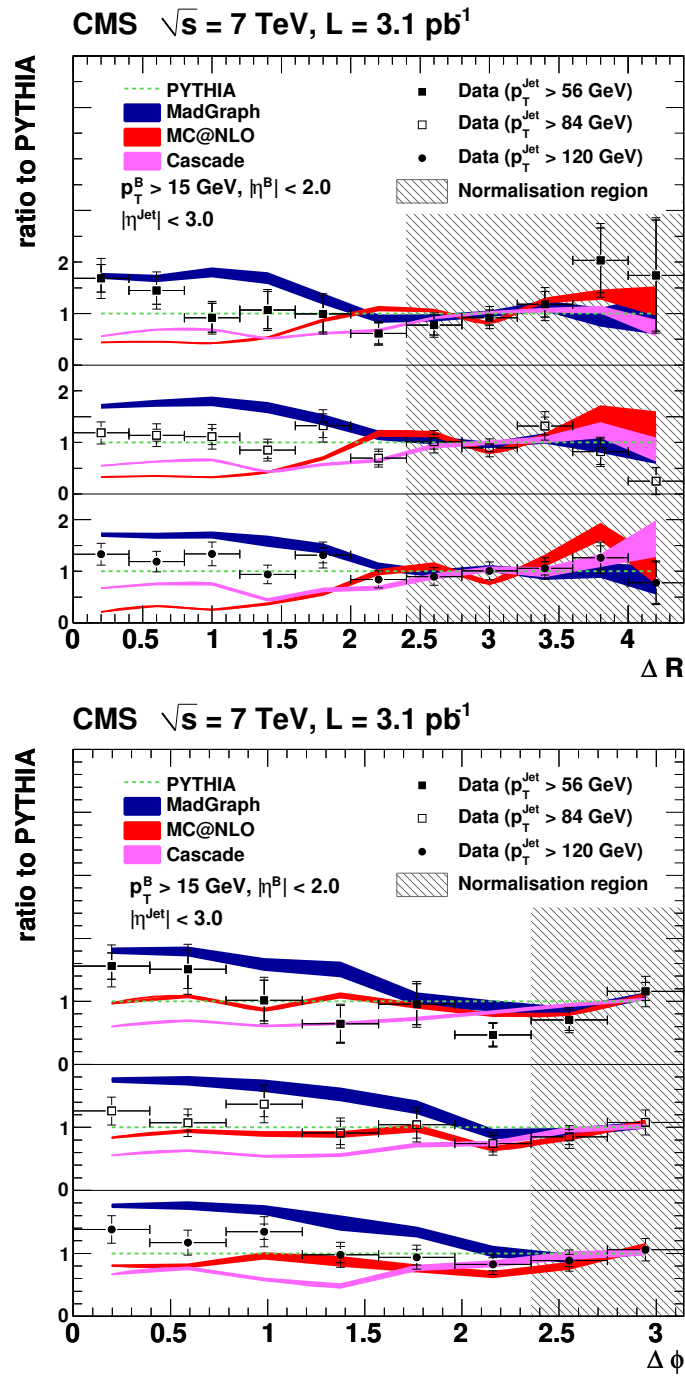


Figure 10.7: Ratio of the differential $B\bar{B}$ production cross sections, as a function of ΔR (top) and $\Delta\phi$ (bottom), for data, MadGraph, MC@NLO and CASCADE, with respect to the PYTHIA predictions, for the three different leading jet p_T regions. The simulation is normalized to the region $\Delta R > 2.4$ and $\Delta\phi > \frac{3\pi}{4}$ (FCR region), as indicated by the shaded normalization region. The widths of the theory bands indicate the statistical uncertainties of the simulation.

Chapter 11

Conclusions and Outlook

Detailed b quark production studies provide substantial information about the dynamics of the underlying hard scattering subprocesses within perturbative Quantum Chromodynamics. At the Large Hadron Collider (LHC), beauty quarks play a central role in some physics analyses as in top physics or low mass Higgs searches, and, on the other hand, $b\bar{b}$ pairs are one of the main backgrounds for many new physics searches. Hence, studying b quark production in detail and measuring the properties of the b quarks is of fundamental importance. The high b quark cross section at LHC center-of-mass energies made it possible to use a small amount of data collected in 2010 for the first beauty physics studies.

In this thesis, the B hadron pair production and the angular correlations between B hadron pairs have been studied. It is the first measurement of angular correlations at a center-of-mass energy of 7 TeV. The NLO contribution to the $b\bar{b}$ production cross section is expected to be significant. In particular, the contribution from events with a final state gluon splitting into a $b\bar{b}$ pair is presumed to be non-negligible. Because the two B hadrons from gluon splitting are produced almost collinear, the angle has been measured with a high-resolution technique using the flight direction of the B hadrons instead of b-jet directions. The flight direction was approximated as the vector from the reconstructed primary collision vertex to the B hadron decay vertex. The decay vertex has been fitted using an Adaptive Vertex Fitter. The standard vertex finder that builds clusters of tracks for the vertex fitter, has been replaced by a new Inclusive Vertex Finder. The striking feature of this inclusive finder is that it is independent of any jet direction. The standard finder—suited for identifying and tagging b-jets—builds clusters from tracks in a cone around the jet axis. Using the jet direction as an estimation of the B flight direction is inefficient if two B hadrons, produced with small opening angle, are merged into one single jet. For those jets the jet direction is not a good estimate of any of the two B hadron flight directions. The Inclusive Vertex Finder is described in this thesis and its performance has been studied and validated. The efficiency of reconstructing two almost collinear B hadrons is found to be better than using the standard finder and for b-tagging the performance of the two is comparable. With the Inclusive Vertex Finder it is possible for the first time to measure the angular correlations between B hadrons in the very small ΔR region.

The measurements are based on data corresponding to an integrated luminosity of $3.1 \pm 0.3 \text{ pb}^{-1}$ recorded by the CMS experiment during 2010. The measurements have been performed in three regions of phase space, characterized by the transverse momentum p_T of the leading jet in the event, which is a measure for the event energy scale. The results are given in terms of differential production cross sections as functions of the two angular separation variables ΔR and $\Delta\phi$ between the two B hadrons. Different normalizations are used for the simulated distributions to be compared to the measurements. First, the simulation is normalized to the measured integrated luminosity. The total systematic uncertainties on the *absolute* normalization are of the order of 43%. Most of this uncertainty comes from the uncertainty on the average Inclusive Vertex Finder efficiency of correctly reconstructing two B hadrons. This uncertainty can be reduced when using standard b-tagging techniques to measure the angular distributions in the region where the two B hadrons are well separated ($\Delta R > 1.0$) and to compare this jet based measurement to the vertex based measurement. The systematic uncertainty due to this method is estimated to be 32%. In order to avoid any uncertainties on the absolute normalization, a *relative* normalization was also chosen as alternative. The simulated distributions are normalized to the number of data events with back-to-back topology ($\Delta R > 2.4$, $\Delta\phi > \frac{3}{4}$). For this measurement, only systematic uncertainties on the shape of the differential cross section distributions are relevant. Those are estimated to be between 15.4% and 16.8% for the three leading jet p_T regions.

The data exhibit a substantial enhancement of the cross section in the collinear region. The values measured at small opening angles exceed those at large ΔR and $\Delta\phi$. The ratio of the cross section in the small opening angle region ($\Delta R < 0.8$) with respect to the back-to-back topology region ($\Delta R > 2.4$) is increasing with the event energy scale. Increasing the mean leading jet p_T from 72 GeV to 150 GeV the ratio changes by a factor of about two from 1.42 ± 0.28 to 2.74 ± 0.37 . The increase of the ratio with the event energy scale is well modeled both in PYTHIA and in MadGraph. The value of the ratio is underestimated by PYTHIA (0.90 ± 0.02 at mean leading jet $p_T = 72$ GeV) and overestimated by MadGraph (1.53 ± 0.07).

The measurements are compared to a number of theoretical predictions, based on LO and NLO perturbative QCD calculations. The relative normalization to the cross section in the flavor creation region is used. It is found that the data lie, for small opening angles, in between the PYTHIA and the MadGraph predictions, where the latter predicts more gluon splitting contributions. CASCADE and MC@NLO clearly underestimate the contributions at small values of ΔR . For CASCADE the same is true for the $\Delta\phi$ distribution, while the MC@NLO prediction for $\Delta\phi$ is comparable to PYTHIA and more accurate also for small opening angles. Overall it is observed that for this relative normalization to the flavor creation region the collinear region, where the gluon splitting processes are expected to be large, is not adequately described by any of the predictions.

The measurements presented herein can be used for tuning MC event generators, such that they predict the $b\bar{b}$ cross section as a function of the angle between the two B hadrons more accurately. The Inclusive Vertex Finder developed for the correlation measurement is well suited for any kind of study using secondary vertices, especially if a good spatial vertex resolution is required.

Appendix A

Numerical Values for Efficiency and Purity Correction

Low edge	High edge	HLT_Jet15			HLT_Jet30			HLT_Jet50		
		ϵ	p	cf	ϵ	p	cf	ϵ	p	cf
0	0.2	0.0396	0.805	20.3	0.0721	0.853	11.8	0.0898	0.811	9.03
0.2	0.4	0.0591	0.899	15.2	0.0834	0.912	10.9	0.113	0.924	8.14
0.4	0.8	0.0641	0.873	13.6	0.081	0.865	10.7	0.105	0.917	8.71
0.8	2	0.063	0.839	13.3	0.0863	0.875	10.1	0.0985	0.824	8.36
2	2.8	0.0857	0.873	10.2	0.113	0.883	7.84	0.127	0.916	7.24
2.8	3.2	0.0979	0.845	8.63	0.114	0.808	7.06	0.111	0.7	6.32
3.2	3.6	0.103	0.814	7.87	0.111	0.711	6.41	0.136	0.693	5.11
3.6	4.4	0.0991	0.734	7.41	0.141	0.719	5.09	0.103	0.552	5.36

Table A.1: Efficiency, purity and correction factor applied for the different ΔR bins. The values are listed for the three leading jet p_T regions.

Appendix B

Reconstructed B Candidate Properties: Additional Plots

Leading Jet $p_T > 56 \text{ GeV}$ region

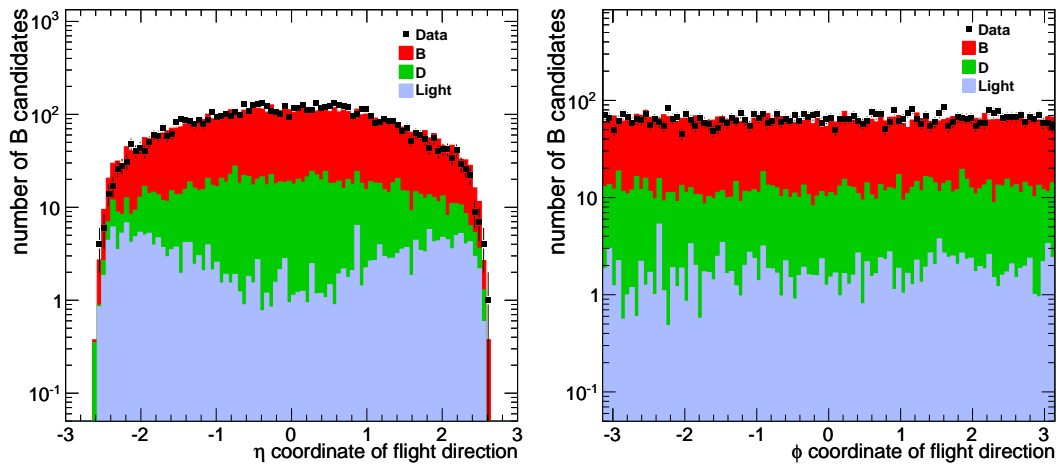


Figure B.1: Properties of reconstructed B candidate vertices: η (left) and ϕ (right) distribution. The data are shown by solid points. The PYTHIA simulation is decomposed in B, D and light vertices. The simulated distribution is normalized to the number of data events. All selection cuts apart from those on the shown quantities are applied.

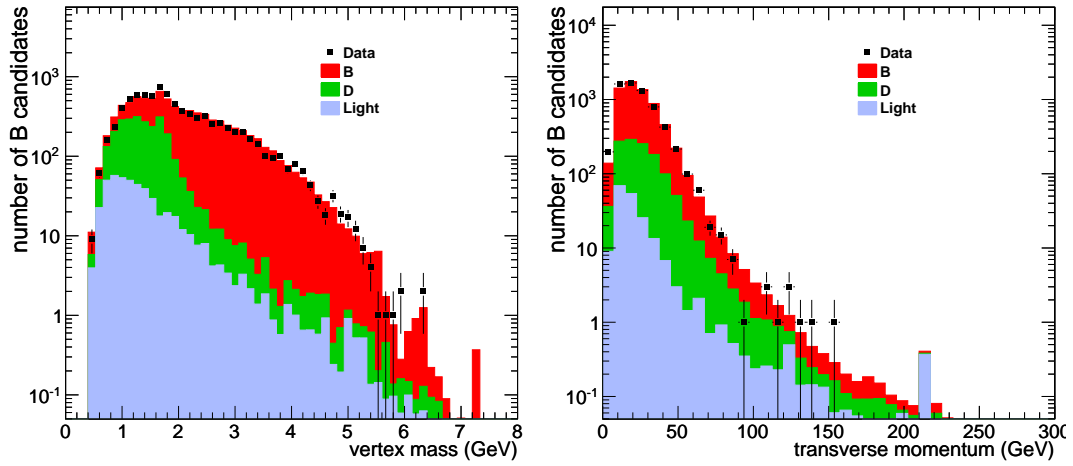


Figure B.2: Properties of reconstructed B candidate vertices: vertex mass (left) and vertex p_T (right) distribution (see figure B.1 for details).

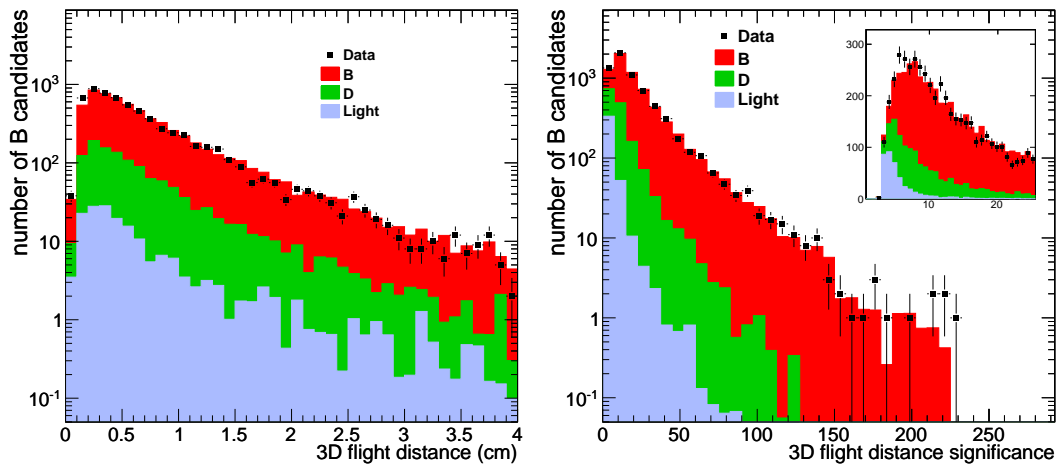


Figure B.3: Properties of reconstructed B candidate vertices: 3D flight distance (left) and 3D flight distance significance (right) distribution (see figure B.1 for details). The inset in the right plot shows a zoom of the flight distance significance distribution with narrower bins and linear scale.

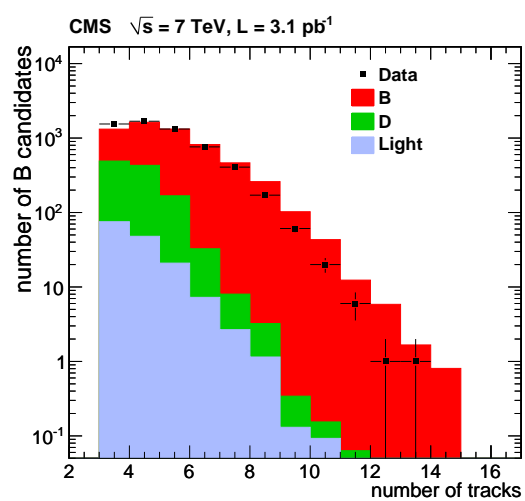


Figure B.4: Number of tracks attached to reconstructed B candidate vertices (see figure B.1 for details).

Leading Jet $p_T > 120$ GeV region

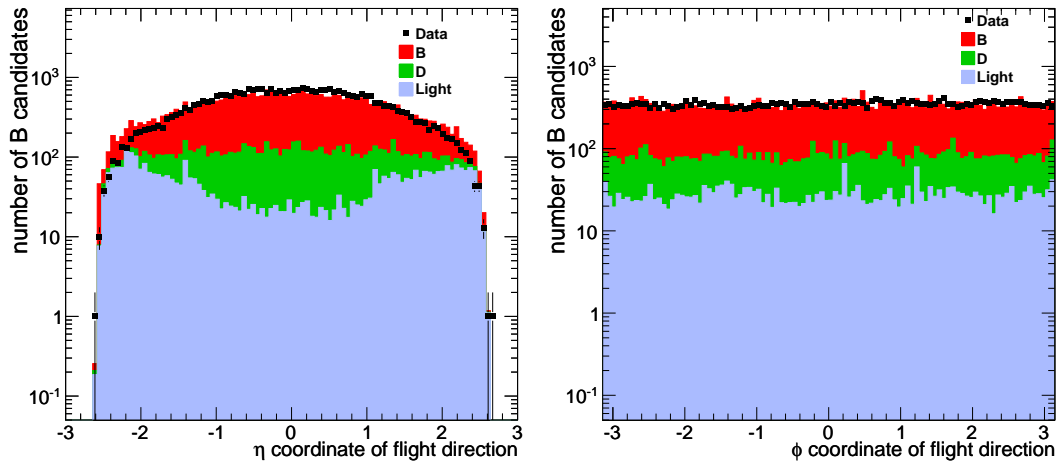


Figure B.5: Properties of reconstructed B candidate vertices: η (left) and ϕ (right) distribution (see figure B.1 for details).

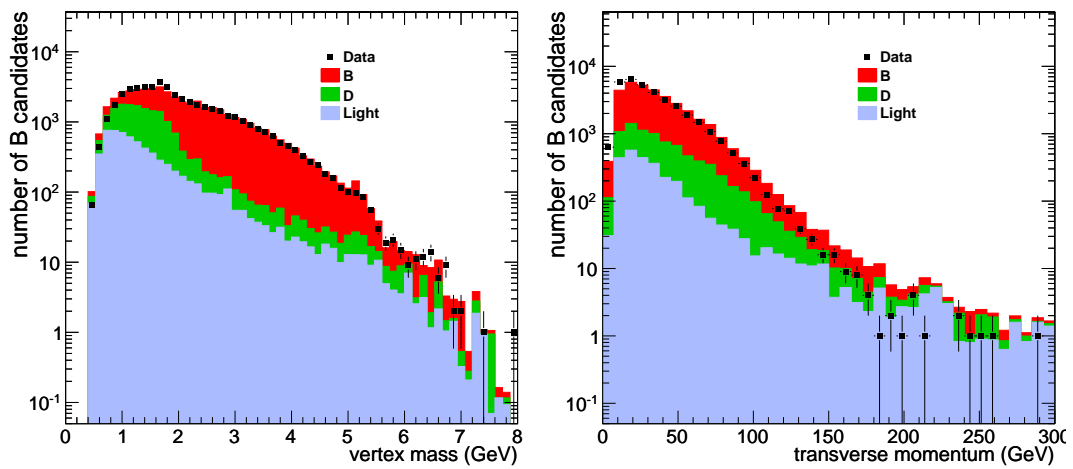


Figure B.6: Properties of reconstructed B candidate vertices: vertex mass (left) and vertex p_T (right) distribution (see figure B.1 for details).

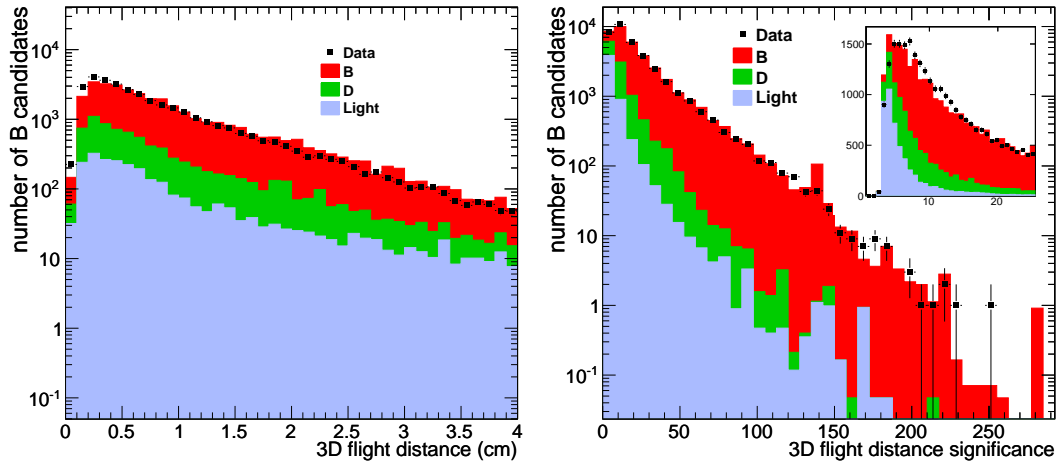


Figure B.7: Properties of reconstructed B candidate vertices: 3D flight distance (left) and 3D flight distance significance (right) distribution (see figure B.1 for details). The inset in the right plot shows a zoom of the flight distance significance distribution with narrower bins and linear scale.

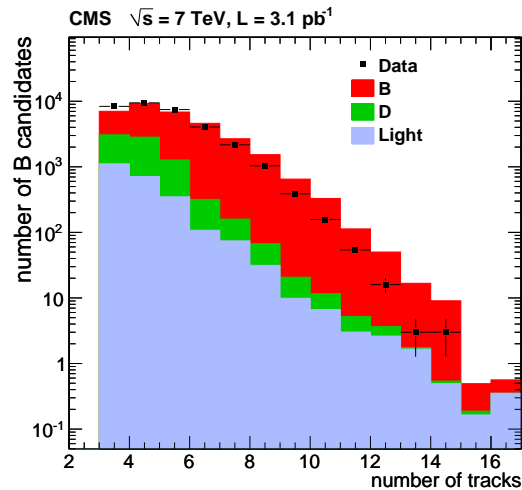


Figure B.8: Number of tracks attached to reconstructed B candidate vertices (see figure B.1 for details).

Appendix C

Systematic Uncertainties and Results: Additional Information

C.1 Systematic Uncertainties

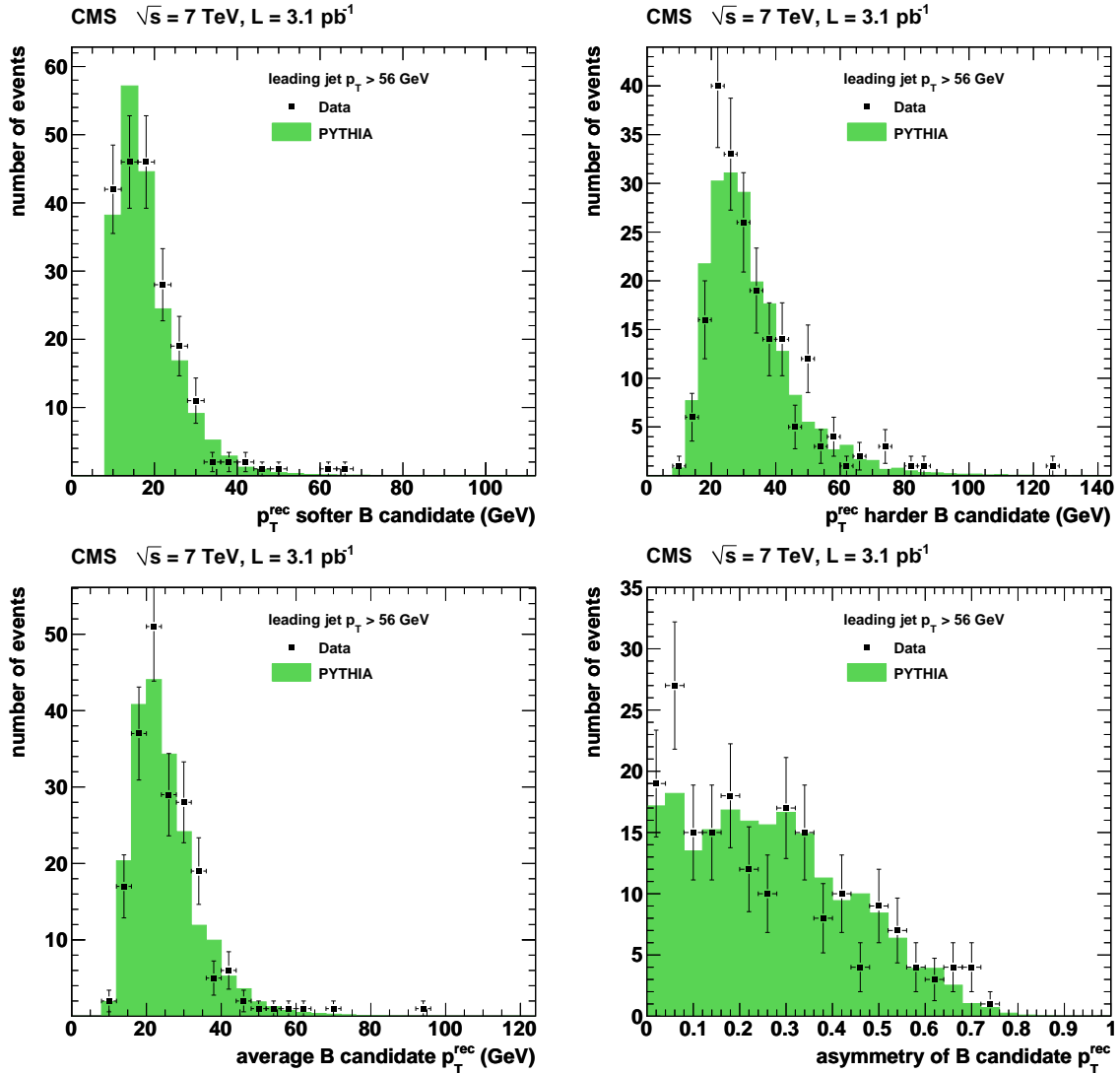


Figure C.1: Comparison between data (solid dots) and PYTHIA simulation (green bars) for distributions of the reconstructed p_T of the two B hadrons: p_T of the softer B hadron (top left); p_T of the harder B hadron (top right); average p_T of the two B hadrons (bottom left); asymmetry of the p_T of the harder and the softer B hadron (bottom right). All plots are shown for the leading jet $p_T > 56$ GeV bin.

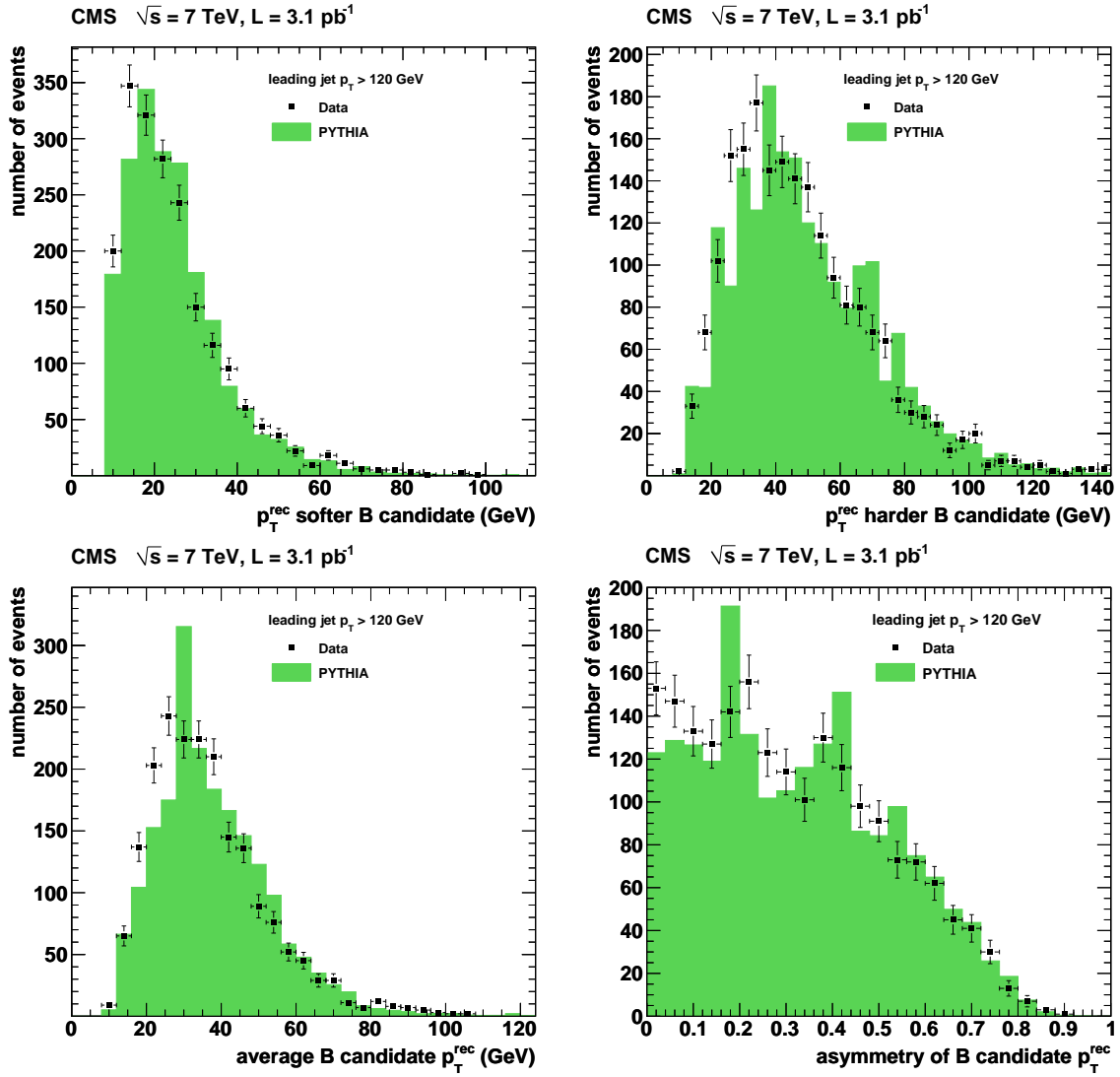


Figure C.2: Comparison between data (solid dots) and PYTHIA simulation (green bars) for distributions of the reconstructed p_T of the two B hadrons: p_T of the softer B hadron (top left); p_T of the harder B hadron (top right); average p_T of the two B hadrons (bottom left); asymmetry of the p_T of the harder and the softer B hadron (bottom right). All plots are shown for the leading jet $p_T > 120$ GeV bin.

C.2 Results

ΔR Bin	σ (pb)	stat (pb)	syst1 (pb)	syst2 (pb)	syst3 (pb)
0.0 – 0.4	23582	3720.22	3065.66	2499.69	10140.3
0.4 – 0.8	13178.3	2406.01	1713.18	1396.9	5666.66
0.8 – 1.2	4721.75	1423.66	613.828	500.506	2030.35
1.2 – 1.6	3863.25	1287.75	502.223	409.505	1661.2
1.6 – 2.0	3434	1214.1	446.42	364.004	1476.62
2.0 – 2.4	2957.44	985.813	384.467	313.488	1271.7
2.4 – 2.8	5257.67	1314.42	683.497	557.313	2260.8
2.8 – 3.2	11418.2	1783.22	1484.37	1210.33	4909.83
3.2 – 3.6	5841.64	1218.07	759.413	619.214	2511.9
3.6 – 4.0	2629.87	792.935	341.883	278.766	1130.84
> 4.0	717.237	414.097	93.2408	76.0271	308.412

Table C.1: Cross sections σ and its statistical uncertainty (stat), the systematic uncertainty due to limited MC statistics (syst1), the systematic uncertainty on the shape (syst2) and on the absolute normalization (syst3) for the different ΔR bins (leading jet $p_T > 56$ GeV).

ΔR Bin	σ (pb)	stat (pb)	syst1 (pb)	syst2 (pb)	syst3 (pb)
0.0 – 0.4	6480.29	484.742	842.438	641.549	2786.53
0.4 – 0.8	3544.48	347.565	460.782	350.903	1524.13
0.8 – 1.2	1749.14	238.027	227.388	173.165	752.129
1.2 – 1.6	1004.13	180.348	130.537	99.4093	431.778
1.6 – 2.0	1198.48	197.029	155.803	118.65	515.348
2.0 – 2.4	776.203	139.41	100.906	76.8441	333.767
2.4 – 2.8	1477.29	192.327	192.048	146.252	635.235
2.8 – 3.2	2434.87	234.295	316.533	241.052	1046.99
3.2 – 3.6	1537.08	177.487	199.821	152.171	660.945
3.6 – 4.0	211.291	58.6016	27.4678	20.9178	90.8552
> 4.0	16.2532	16.2532	2.11291	1.60906	6.98886

Table C.2: Cross sections σ and its statistical uncertainty (stat), the systematic uncertainty due to limited MC statistics (syst1), the systematic uncertainty on the shape (syst2) and on the absolute normalization (syst3) for the different ΔR bins (leading jet $p_T > 84$ GeV).

ΔR Bin	σ (pb)	stat (pb)	syst1 (pb)	syst2 (pb)	syst3 (pb)
0.0 – 0.4	1998.81	74.8522	259.845	165.901	859.487
0.4 – 0.8	857.191	49.3258	111.435	71.1468	368.592
0.8 – 1.2	474.087	35.9404	61.6313	39.3492	203.857
1.2 – 1.6	250.666	26.1338	32.5866	20.8053	107.787
1.6 – 2.0	264.29	26.8345	34.3577	21.936	113.645
2.0 – 2.4	183.898	20.8224	23.9068	15.2636	79.0762
2.4 – 2.8	268.774	25.173	34.9407	22.3083	115.573
2.8 – 3.2	481.878	31.5013	62.6441	39.9959	207.207
3.2 – 3.6	219.77	19.1285	28.5701	18.2409	94.5011
3.6 – 4.0	57.6338	10.0328	7.49239	4.78361	24.7825
> 4.0	14.5924	5.61134	1.34261	1.211173	6.27475

Table C.3: Cross sections σ and its statistical uncertainty (stat), the systematic uncertainty due to limited MC statistics (syst1), the systematic uncertainty on the shape (syst2) and on the absolute normalization (syst3) for the different ΔR bins (leading jet $p_T > 120$ GeV).

$\Delta\phi$ Bin	σ (pb)	stat (pb)	syst1 (pb)	syst2 (pb)	syst3 (pb)
0 – $\pi/8$	31448.9	4156.75	4088.35	3333.58	13523
$\pi/8$ – $\pi/4$	10781	2158.87	1401.53	1142.79	4635.83
$\pi/4$ – $3\pi/8$	4051.12	1291.62	526.646	429.419	1741.98
$3\pi/8$ – $\pi/2$	1944.96	876.772	252.845	206.166	836.332
$\pi/2$ – $5\pi/8$	3270.5	1107.3	425.165	346.673	1406.31
$5\pi/8$ – $3\pi/4$	2326.26	888.069	302.413	246.583	1000.29
$3\pi/4$ – $7\pi/8$	5804.27	1338.72	754.555	615.253	2495.84
$7\pi/8$ – π	17974.4	2183.61	2336.67	1905.28	7728.98

Table C.4: Cross sections σ and its statistical uncertainty (stat), the systematic uncertainty due to limited MC statistics (syst1), the systematic uncertainty on the shape (syst2) and on the absolute normalization (syst3) for the different $\Delta\phi$ bins (leading jet $p_T > 56$ GeV).

$\Delta\phi$ Bin	σ (pb)	stat (pb)	syst1 (pb)	syst2 (pb)	syst3 (pb)
0 – $\pi/8$	9144.79	569.13	1188.82	905.334	3932.26
$\pi/8$ – $\pi/4$	2394.63	282.654	311.302	237.068	1029.69
$\pi/4$ – $3\pi/8$	1626.42	226.465	211.435	161.016	699.361
$3\pi/8$ – $\pi/2$	774.268	153.256	100.655	76.6525	332.935
$\pi/2$ – $5\pi/8$	766.157	151.453	99.6004	75.8496	329.448
$5\pi/8$ – $3\pi/4$	849.127	144.359	110.386	84.0635	365.124
$3\pi/4$ – $7\pi/8$	1386.7	181.412	180.271	137.284	596.283
$7\pi/8$ – π	3487.42	273.924	453.365	345.255	1499.59

Table C.5: Cross sections σ and its statistical uncertainty (stat), the systematic uncertainty due to limited MC statistics (syst1), the systematic uncertainty on the shape (syst2) and on the absolute normalization (syst3) for the different $\Delta\phi$ bins (leading jet $p_T > 84$ GeV).

$\Delta\phi$ Bin	σ (pb)	stat (pb)	syst1 (pb)	syst2 (pb)	syst3 (pb)
$0 - \pi/8$	2670.68	86.4792	347.189	221.667	1148.39
$\pi/8 - \pi/4$	612.063	41.2931	79.5682	50.8012	263.187
$\pi/4 - 3\pi/8$	358.348	31.0212	46.5853	29.7429	154.09
$3\pi/8 - \pi/2$	205.673	23.376	26.7375	17.0708	88.4393
$\pi/2 - 5\pi/8$	153.579	19.7623	19.9652	12.747	66.0388
$5\pi/8 - 3\pi/4$	168.855	19.8079	21.9511	14.0149	72.6075
$3\pi/4 - 7\pi/8$	275.216	24.6509	35.778	22.8429	118.343
$7\pi/8 - \pi$	627.171	34.7162	81.5322	52.0552	269.683

Table C.6: Cross sections σ and its statistical uncertainty (stat), the systematic uncertainty due to limited MC statistics (syst1), the systematic uncertainty on the shape (syst2) and on the absolute normalization (syst3) for the different $\Delta\phi$ bins (leading jet $p_T > 120$ GeV).

List of Figures

2.1	Gluon self-interaction.	16
2.2	Measurements of the strong coupling constant α_s	17
2.3	Schematic view of hard collision process $p_1 p_2 \rightarrow Q_1 Q_2$	19
2.4	Scaling violation.	20
2.5	Leading order Altarelli-Parisi splitting functions.	21
2.6	PDFs from HERAPDF1.0.	22
2.7	Leading order Flavor Creation diagrams.	25
2.8	Flavor Excitation and Gluon Splitting diagrams.	26
2.9	MC event generation in several steps.	28
3.1	LHC injector chain.	33
3.2	Center-of-mass energies of accelerator facilities as function of starting year.	36
3.3	Schematic view of the CMS detector.	37
3.4	One of the first collisions at $\sqrt{s} = 7$ TeV recorded with the CMS detector.	38
3.5	Charge sharing among pixels due to Lorentz drift.	43
3.6	Schematic view of the CMS pixel detector.	44
3.7	Pixel detector layout.	45
3.8	Design of a pixel barrel module.	46
3.9	Design of the Read Out Chip.	47
3.10	The layout of the CMS tracker.	48
3.11	Schematic layout of the ECAL detector.	50
3.12	A schematic view of the HCAL readout.	52
3.13	A schematic view of the HCAL layout.	53
3.14	Ratio of energy stored in a magnet divided by the cold mass.	54
3.15	Material thickness in units of interaction lengths.	55
3.16	Layout of the CMS muon system.	56
3.17	Drift tube chamber layout.	57
3.18	Architecture of the L1 trigger system.	59
3.19	Steps in event processing for MC and real data events.	60
4.1	Leading jet transverse momentum and HLT efficiency as function of jet p_T	64
4.2	Generated events as function of PYTHIA \hat{p}_T	68
5.1	Definition of the impact parameter.	74
5.2	Sign of impact parameter.	75

5.3	Secondary vertex properties.	77
5.4	Comparison of MC prediction with data for SSV discriminators.	77
5.5	Merging of two B hadrons into one single jet.	78
6.1	Tracker material budget in units of radiation length.	80
6.2	Track reconstruction efficiency for muons and pions.	82
6.3	Comparison of measured and simulated distributions of tracking parameters.	83
6.4	AVF weight function $w_i(\chi)$ for $\chi_c = 3$ and different temperatures T	85
6.5	Definition of the vertex flight direction.	86
6.6	Definition of the angle ΔR_{BV} between vertices and B hadrons.	87
6.7	Event displays: angle measurement between B hadrons using b-tagged jets.	89
6.8	ΔR and $\Delta\phi$ between B hadrons or b-jets.	90
6.9	Event displays: angle measurement between B hadrons using secondary vertices.	91
6.10	Difference track acceptance cone vertex reconstruction with the AVR.	92
6.11	AVR performance for different track acceptance cone sizes.	93
6.12	Vertex reconstruction with the IVF.	94
6.13	Definitions of variables used for track clustering.	95
6.14	Dependence of the efficiency on the IVF parameters.	99
6.15	Dependence of the B vertex purity on the IVF parameters.	100
6.16	Dependence of vertex reconstruction time on the choice of IVF parameters.	101
6.17	Number of objects after different steps of the IVF for the sample MC event.	104
6.18	Event displays: IVF vertices in a sample MC event	105
6.19	Number of vertices produced in the different steps per event.	106
6.20	Comparison of vertices produced in the different IVF steps.	107
6.21	Comparison of vertices produced in different IVF steps.	109
6.22	Simulated event with a $B \rightarrow D \rightarrow X$ decay chain.	110
6.23	Definition of angle θ	111
6.24	Simulated event with a $B \rightarrow D \rightarrow X$ decay chain ($B \rightarrow D \rightarrow X$ cleaning applied).	112
6.25	ΔR_{VV} between B candidates with/without $B \rightarrow D \rightarrow X$ cleaning applied.	113
6.26	Resolution of ΔR reconstruction (leading jet $p_T > 56$ GeV).	114
6.27	Resolution of ΔR reconstruction (leading jet $p_T > 84$ GeV).	115
6.28	Resolution of ΔR reconstruction (leading jet $p_T > 120$ GeV).	115
6.29	Resolution of ΔR reconstruction (leading jet $p_T > 84$ GeV) with gaussian fit.	116
7.1	Properties of B hadrons in events with exactly two B hadrons.	118
7.2	Properties of B hadrons shown for FCR/FEX/GSP events.	119
7.3	The p_T distribution of B hadrons in events with two B.	120
7.4	B hadron reconstruction efficiency as a function of p_T	121
7.5	Correlation between ΔR_{BB} and the p_T of the B hadron.	122
7.6	Correlation between p_T of reconstructed vertex and p_T of generated B hadron.	123
7.7	ΔR_{BB} for events with two B hadrons.	123
7.8	Angle Ψ_{BB} for events with two B hadrons.	124
7.9	Angle Ψ_{BB} versus ΔR_{BB} for events with two B hadrons.	124
7.10	Efficiency as function of ΔR_{BB} for the three leading jet p_T bins.	126
7.11	Purity as function of ΔR_{VV} for the three leading jet p_T bins.	127

7.12	Overall correction factor as function of ΔR_{VV} for the three leading jet p_T bins.	128
7.13	Correction functions for QCD and Inclusive BB samples.	129
8.1	Reconstructed B candidates: η and ϕ distribution.	132
8.2	Reconstructed B candidates: mass and p_T distribution.	133
8.3	Reconstructed B candidates: 3D flight distance and significance distribution.	133
8.4	Number of tracks in the reconstructed B candidate vertices.	134
9.1	Event mixing method: study of vertex reconstruction efficiency.	136
9.2	Reconstructed p_T of B hadrons for simulation and measurement.	138
9.3	Average p_T of the softer B hadron as a function of ΔR	139
9.4	Overall uncertainty on the absolute JES for PF jets.	140
9.5	Differential $B\bar{B}$ production cross section for $p_T(SV)$ above 8 and 10 GeV. . .	141
9.6	Differential $B\bar{B}$ cross section: comparison of vertex and jet based method. . .	145
10.1	Differential $B\bar{B}$ cross sections as a function of ΔR and $\Delta\phi$	149
10.2	Ratio of the differential $B\bar{B}$ production cross sections.	150
10.3	Differential $B\bar{B}$ cross sections as a function of ΔR and $\Delta\phi$	151
10.4	Differential $B\bar{B}$ cross sections as a function of ΔR and $\Delta\phi$	151
10.5	Ratio $\rho_{\Delta R}$ and asymmetry $(\sigma_{\Delta R < 0.8} - \sigma_{\Delta R > 2.4}) / (\sigma_{\Delta R < 0.8} + \sigma_{\Delta R > 2.4})$	153
10.6	Ratio $\rho_{\Delta R} = \sigma_{\Delta R < 0.8} / \sigma_{\Delta R > 2.4}$ for three data taking periods.	155
10.7	Comparison of differential cross section measurement and theoretical predictions.	156
B.1	Reconstructed B candidates: η and ϕ distribution.	161
B.2	Reconstructed B candidates: mass and p_T distribution.	162
B.3	Reconstructed B candidates: 3D flight distance and significance distribution.	162
B.4	Number of tracks attached to reconstructed B candidate vertices.	163
B.5	Reconstructed B candidates: η and ϕ distribution.	164
B.6	Reconstructed B candidates: mass and p_T distribution.	164
B.7	Reconstructed B candidates: 3D flight distance and significance distribution.	165
B.8	Number of tracks attached to reconstructed B candidate vertices.	165
C.1	Reconstructed p_T of B hadrons for simulation and measurement.	168
C.2	Reconstructed p_T of B hadrons for simulation and measurement.	169

List of Tables

2.1	Properties of B hadrons.	26
3.1	Number of detector units in the pixel detector.	44
3.2	Properties of lead tungstate relevant for the CMS ECAL.	49
3.3	Properties of the C26000/cartridge brass.	51
4.1	Jet triggers used for the correlation measurement.	65
4.2	Datasets used for different run periods.	66
4.3	PYTHIA samples used in this analysis.	67
4.4	Parameter settings for the Monte Carlo event generators.	70
6.1	Standard parameters used with the AVR for b-tagging.	88
6.2	AVR efficiency and purity for different track acceptance cone sizes.	94
6.3	Filter applied on vertices produced in IVF.	97
6.4	IVF parameter settings for performance studies.	98
6.5	Track clusters for a sample MC event.	102
6.6	Vertex properties for the vertices produced in different IVF steps.	103
6.7	Mean number of vertices after the five reconstruction steps.	107
6.8	Properties of D hadrons.	108
8.1	PYTHIA prediction on relative amount B candidates from B, D and light.	131
9.1	Change of $\rho_{\Delta R}$ when changing p_T cut on vertices from 8 to 10 GeV.	138
9.2	Systematic uncertainties affecting the shape.	142
9.3	Systematic uncertainties affecting the normalization.	146
10.1	Cross sections and uncertainties per ΔR bin.	152
10.2	Cross sections and uncertainties per $\Delta\phi$ bin.	152
10.3	Input values used to calculate the $B\bar{B}$ production cross section ratio $\rho_{\Delta R}$	154
A.1	Efficiency, purity and correction factor applied for the different ΔR bins.	159
C.1	Cross sections and uncertainties per ΔR bin.	170
C.2	Cross sections and uncertainties per ΔR bin.	170
C.3	Cross sections and uncertainties per ΔR bin.	171
C.4	Cross sections and uncertainties per $\Delta\phi$ bin.	171

C.5	Cross sections and uncertainties per $\Delta\phi$ bin.	171
C.6	Cross sections and uncertainties per $\Delta\phi$ bin.	172

List of Abbreviations

ALICE	A Large Ion Collider Experiment
AOD	Analysis Object Data format
APD	Avalanche Photodiodes
ATLAS	A large Toroidal LHC ApparatuS
AVF	Adaptive Vertex Fitter
AVR	Adaptive Vertex Reconstructor
BPTX	Beam Pick-up Timing for Experiments
BSC	Beam Scintillator Counter
CERN	European Organization for Nuclear Research
CKM	Cabibbo-Kobayashi-Maskawa (matrix)
CMS	Compact Muon Solenoid
CMSSW	CMS Software Framework
CSC	Cathode Strip Chambers
CSV	Combined Secondary Vertex (algorithm)
CTF	Combinatorial Track Finder
DAC	Digital-to-Analog Converter
DAQ	Data Acquisition
DGLAP	Dokshitzer - Gribov - Lipatov - Altarelli - Parisi (equation)
DT	Drift Tube
EB	ECAL Barrel
ECAL	Electromagnetic Calorimeter

EE	ECAL Endcap
FCR	Flavor Creation
FEX	Flavor Excitation
FSMW	Fraction-of Sample Mode with Weights
GCT	Global Calorimeter Trigger
GMT	Global Muon Trigger
GSP	Gluon Splitting
HB	HCAL Barrel
HCAL	Hadronic Calorimeter
HE	HCAL Endcap
HF	Hadronic Very Forward Calorimeter
HLT	High-Level Trigger
HO	Hadronic Outer Calorimeter
HPD	Hybrid Photodiode
IC	Iterative Cone
IP	Impact Parameter
IR	Infrared
IVF	Inclusive Vertex Finder
JES	Jet Energy Scale
L1	Level-1 Trigger
LEP	Large Electron-Positron Collider
LHC	Large Hadron Collider
LHCb	Large Hadron Collider beauty experiment
LL	Leading-Logarithmic
LO	Leading-Order
MC	Monte Carlo
MET	Missing Transverse Energy

MSGC	Microstrip Gas Chambers
NLO	Next-to-Leading-Order
ndof	number of degrees of freedom
nr	number of tracks
PCA	Point of Closest Approach
PD	Primary Dataset
PDF	Parton Density Function
PDG	Particle Data Group
PF	Particle Flow
pQCD	perturbative QCD
PS	Proton Synchrotron
PV	Primary Vertex
QCD	Quantum Chromodynamics
QED	Quantum Electrodynamics
RECO	Reconstructed (data format)
RF	Radio Frequency
RGE	Renormalization Group Equation
ROC	Readout Chip
RPC	Resistive Plate Chambers
SL	Superlayer
SM	Standard Model of particle physics
SIS	Seedless Infrared-Safe (Cone algorithm)
SPS	Super Proton Synchrotron
SSV	Simple Secondary Vertex (algorithm)
SUSY	Supersymmetry
SV	Secondary Vertex
TBM	Token Bit Manager

TCS	Trigger Control System
TEC	Tracker Endcap
TIB	Tracker Inner Barrel
TID	Tracker Inner Disk
TOB	Tracker Outer Barrel
TPG	Trigger Primitive Generators
TTC	Timing, Trigger and Control
WLCG	Worldwide Computing Grid

Bibliography

- [1] CMS Collaboration, “Inclusive b-hadron production cross section with muons in pp collisions at $\sqrt{s} = 7$ TeV”, *JHEP* **03** (2011) 090, [arXiv:1101.3512](#).
[doi:10.1007/JHEP03\(2011\)090](#).
- [2] CMS Collaboration, “Inclusive b-jet production in pp collisions at $\sqrt{s} = 7$ TeV”, *CMS-PAS-BPH-10-009* (2010).
- [3] LHCb Collaboration, “Measurement of $\sigma(pp \rightarrow b\bar{b}X)$ at $\sqrt{s} = 7$ TeV in the forward region”, *Phys. Lett.* **B694** (2010) 209–216, [arXiv:1009.2731](#).
[doi:10.1016/j.physletb.2010.10.010](#).
- [4] CDF Collaboration, “Measurements of bottom-antibottom azimuthal production correlations in proton-antiproton collisions at $s = 1.8$ TeV”, *Phys. Rev. D* **71** (May, 2005) 092001. [doi:10.1103/PhysRevD.71.092001](#).
- [5] CDF Collaboration, “Measurement of correlated $b\bar{b}$ production in $p\bar{p}$ collisions at $s = 1960$ GeV”, *Phys. Rev. D* **77** (Apr, 2008) 072004.
[doi:10.1103/PhysRevD.77.072004](#).
- [6] D. J. Gross and F. Wilczek, “Ultraviolet Behavior of Non-Abelian Gauge Theories”, *Phys. Rev. Lett.* **30** (Jun, 1973) 1343–1346. [doi:10.1103/PhysRevLett.30.1343](#).
- [7] H. D. Politzer, “Reliable Perturbative Results for Strong Interactions?”, *Phys. Rev. Lett.* **30** (Jun, 1973) 1346–1349. [doi:10.1103/PhysRevLett.30.1346](#).
- [8] D. J. Gross and F. Wilczek, “Asymptotically Free Gauge Theories. I”, *Phys. Rev. D* **8** (Nov, 1973) 3633–3652. [doi:10.1103/PhysRevD.8.3633](#).
- [9] D. J. Gross and F. Wilczek, “Asymptotically free gauge theories. II”, *Phys. Rev. D* **9** (Feb, 1974) 980–993. [doi:10.1103/PhysRevD.9.980](#).
- [10] G. Dissertori, I. Knowles, and M. Schmelling, “Quantum Chromodynamics: High Energy Experiments and Theory”. International series of monographs on physics. Oxford Science Publications, Great Clarendon Street, Oxford OX2 6DP, 2003.
- [11] M. E. Peskin and D. V. Schroeder, “An Introduction To Quantum Field Theory (Frontiers in Physics)”. Westview Press, 1995.

- [12] K. Nakamura and P. D. Group, “Review of Particle Physics”, *J. Phys. G: Nucl. Part. Phys.* **37** (2010), no. 7A, 075021. doi:10.1088/0954-3899/37/7A/075021.
- [13] S. Bethke, “The 2009 world average of α_s ”, *EPJ C - Particles and Fields* **64** (2009) 689–703. doi:10.1140/epjc/s10052-009-1173-1.
- [14] J. C. Collins, D. E. Soper, and G. Sterman, “Factorization of Hard Processes in QCD”, *arXiv: hep-ph/0409313v1* (2004) arXiv:hep-ph/0409313v1.
- [15] Y. L. Dokshitzer, “Calculation of the Structure Functions for Deep Inelastic Scattering and e^+e^- Annihilation by Perturbation Theory in Quantum Chromodynamics”, *Sov. Phys. JETP* **46** (1977) 641–653.
- [16] V. Gribov and L. Lipatov, “Deep inelastic $e p$ scattering in perturbation theory”, *Sov.J.Nucl.Phys.* **15** (1972) 438–450.
- [17] G. Altarelli and G. Parisi, “Asymptotic Freedom in Parton Language”, *Nucl. Phys.* **B126** (1977) 298. doi:10.1016/0550-3213(77)90384-4.
- [18] The H1 and Zeus collaborations, “Combined measurement and QCD analysis of the inclusive $e^\pm p$ scattering cross sections at HERA”, *JHEP* **2010** (2010) 1–63. doi:10.1007/JHEP01(2010)109.
- [19] C. Peterson, D. Schlatter, I. Schmitt et al., “Scaling violations in inclusive e^+e^- annihilation spectra”, *Phys. Rev. D* **27** (Jan, 1983) 105–111. doi:10.1103/PhysRevD.27.105.
- [20] B. Andersson, G. Gustafson, G. Ingelman et al., “Parton fragmentation and string dynamics”, *Physics Reports* **97** (1983), no. 2-3, 31 – 145. doi:10.1016/0370-1573(83)90080-7.
- [21] T. Sjostrand, S. Mrenna, and P. Skands, “PYTHIA 6.4 Physics and Manual”, *arxiv: hep-ph/0603175* (2006) arXiv:hep-ph/0603175v2.
- [22] B. R. Webber, “A QCD model for jet fragmentation including soft gluon interference”, *Nuclear Physics B* **238** (1984), no. 3, 492 – 528. doi:10.1016/0550-3213(84)90333-X.
- [23] B. Andersson, G. Gustafson, and T. Sjöstrand, “A model for baryon production in quark and gluon jets”, *Nuclear Physics B* **197** (1982), no. 1, 45 – 54. doi:10.1016/0550-3213(82)90153-5.
- [24] T. Meyer, “A Monte Carlo model to produce baryons in e^+e^- annihilation”, *Zeit. Phys.* **C12** (1982) 77. doi:10.1007/BF01475734.
- [25] B. Andersson, G. Gustafson, and T. Sjöstrand, “Baryon Production in Jet Fragmentation and γ -Decay”, *Phys. Scripta* **32** (December, 1985) 574–580. doi:10.1088/0031-8949/32/6/003.

- [26] M. Mangano, “Two lectures on heavy quark production in hadronic collisions”, *CERN-TH/97-328* (1997) [arXiv:hep-ph/9711337](#).
- [27] P. Nason, S. Dawson, and R. K. Ellis, “The total cross section for the production of heavy quarks in hadronic collisions”, *Nuclear Physics B* **303** (1988), no. 4, 607 – 633. [doi:10.1016/0550-3213\(88\)90422-1](#).
- [28] W. Beenakker, “QCD corrections to heavy-quark production in $p\bar{p}$ collisions”, *Phys. Rev. D; Physical Review D* **40** (1989), no. 1, 54–82. [doi:10.1103/PhysRevD.40.54](#).
- [29] R. Field, “Sources of b quarks at the Fermilab Tevatron and their correlations”, *Phys. Rev. D; Physical Review D* **65** (2002), no. 9. [doi:10.1103/PhysRevD.65.094006](#).
- [30] CMS Collaboration, “Measurement of the Underlying Event Activity at the LHC with $\sqrt{s} = 7$ TeV and Comparison with $\sqrt{s} = 0.9$ TeV”, [arXiv:1107.0330v1](#).
- [31] S. Catani, M. Dittmar, D. Soper et al., “QCD”, *arxiv: hep-ph/0005025* (2000) [arXiv:hep-ph/0005025v1](#).
- [32] S. Frixione and B. R. Webber, “Matching NLO QCD computations and parton shower simulations”, *JHEP* **2002** (2002), no. 06, 029. [doi:10.1088/1126-6708/2002/06/029](#).
- [33] S. Frixione, P. Nason, and B. R. Webber, “Matching NLO QCD and parton showers in heavy flavour production”, *JHEP* **2003** (2003), no. 08, 007. [doi:10.1088/1126-6708/2003/08/007](#).
- [34] S. Frixione and B. R. Webber, “The MC@NLO 3.4 Event Generator”, *arxiv: hep-ph/0812.0770* (12, 2008) [arXiv:0812.0770v1](#).
- [35] G. Corcella, I. G. Knowles, G. Marchesini et al., “HERWIG 6: an event generator for hadron emission reactions with interfering gluons (including supersymmetric processes)”, *JHEP* **2001** (2001), no. 01, 010. [doi:10.1088/1126-6708/2001/01/010](#).
- [36] F. Maltoni and T. Stelzer, “MadEvent: automatic event generation with MadGraph”, *JHEP* **2003** (2003), no. 02, 027. [doi:10.1088/1126-6708/2003/02/027](#).
- [37] J. Alwall, P. Demin, S. de Visscher et al., “MadGraph/MadEvent v4: the new web generation”, *JHEP* **2007** (2007), no. 09, 028. [doi:10.1088/1126-6708/2007/09/028](#).
- [38] H. Jung and G. Salam, “Hadronic final state predictions from CCFM: the hadron-level Monte Carlo generator CASCADE”, *The European Physical Journal C - Particles and Fields* **19** (2001) 351–360. [doi:10.1007/s100520100604](#).
- [39] J. Pumplin, D. R. Stump, J. Huston et al., “New Generation of Parton Distributions with Uncertainties from Global QCD Analysis”, *JHEP* **2002** (2002), no. 07, 012. [doi:10.1088/1126-6708/2002/07/012](#).

- [40] R. Bernhard, R. Field, R. Chierici et al., “Proceedings of the First International Workshop on Multiple Partonic Interactions at the LHC (MPI08)”, *arXiv: hep-ex/1003.4220v1* (03, 2010) [arXiv:1003.4220v1](https://arxiv.org/abs/1003.4220v1).
- [41] T. Stelzer and W. F. Long, “Automatic generation of tree level helicity amplitudes”, *Computer Physics Communications* **81** (1994), no. 3, 357 – 371. doi:10.1016/0010-4655(94)90084-1.
- [42] J. Alwall, S. de Visscher, and F. Maltoni, “QCD radiation in the production of heavy colored particles at the LHC”, *JHEP* **2009** (2009), no. 02, 017. doi:10.1088/1126-6708/2009/02/017.
- [43] J. M. Butterworth and J. R. Forshaw, “Photoproduction of multi-jet events at HERA: a Monte Carlo simulation”, *J. Phys. G: Nucl. Part. Phys.* **19** (1993), no. 10, 1657. doi:10.1088/0954-3899/19/10/026.
- [44] S. Catani, M. Ciafaloni, and F. Hautmann, “High energy factorization and small-x heavy flavour production”, *Nuclear Physics B* **366** (1991), no. 1, 135 – 188. doi:10.1016/0550-3213(91)90055-3.
- [45] H. Jung, S. Baranov, M. Deak et al., “The CCFM Monte Carlo generator CASCADE Version 2.2.03”, *The European Physical Journal C - Particles and Fields* **70** (2010) 1237–1249. doi:10.1140/epjc/s10052-010-1507-z.
- [46] M. Deak, F. Hautmann, H. Jung et al., “Forward jet production at the Large Hadron Collider”, *JHEP* **2009** (2009), no. 09, 121. doi:10.1088/1126-6708/2009/09/121.
- [47] O. S. Brüning, P. Collier, P. Lebrun et al., “LHC Design Report”. CERN, Geneva, 2004.
- [48] P. Cortese, C. W. Fabjan, L. Riccati et al., “ALICE physics performance: Technical Design Report”. Technical Design Report ALICE. CERN, Geneva, 2005. revised version submitted on 2006-05-29 15:15:40.
- [49] ATLAS Collaboration, “ATLAS detector and physics performance: Technical Design Report, 1”. Technical Design Report ATLAS. CERN, Geneva, 1999.
- [50] ATLAS Collaboration, “ATLAS detector and physics performance: Technical Design Report, 2”. Technical Design Report ATLAS. CERN, Geneva, 1999.
- [51] CMS Collaboration, “CMS Physics Technical Design Report Volume I: Detector Performance and Software”. Number CERN-LHCC-2006-001 in Technical Design Report CMS. CERN, Geneva, 2006. There is an error on cover due to a technical problem for some items.
- [52] CMS Collaboration, “CMS Physics Technical Design Report, Volume II: Physics Performance”, *J. Phys. G: Nucl. Part. Phys.* **34** (2007), no. 6, 995. doi:10.1088/0954-3899/34/6/S01.

- [53] CMS Collaboration, “The CMS experiment at the CERN LHC”, *JINST* **3** (2008), no. S08004,. doi:10.1088/1748-0221/3/08/S08004.
- [54] LHCb Collaboration, “LHCb : Technical Proposal”. CERN-LHCC-98-004. CERN, Geneva, 1998.
- [55] CDF Collaboration, “Observation of Top Quark Production in $\bar{p}p$ Collisions with the Collider Detector at Fermilab”, *Phys. Rev. Lett.* **74** (Apr, 1995) 2626–2631. doi:10.1103/PhysRevLett.74.2626.
- [56] D0 Collaboration, “Search for High Mass Top Quark Production in $p\bar{p}$ Collisions at $\sqrt{s} = 1.8$ TeV”, *Phys. Rev. Lett.* **74** (Mar, 1995) 2422–2426. doi:10.1103/PhysRevLett.74.2422.
- [57] D. Green, ed., “At the Leading Edge: the ATLAS and CMS LHC Experiments”. World Scientific, 2010.
- [58] F. Sauli, “Principles of operation of multiwire proportional and drift chambers”., CERN-77-09.
- [59] CMS Collaboration, “The Tracker Project”, *Technical Design Report, CERN/LHCC 98-6, CMS TDR 5* (15 April 1998).
- [60] CMS Collaboration, “Addendum to the CMS Tracker TDR”, *CERN/LHCC 2000-016, CMS TDR 5 Addendum 1* (21 February 2000).
- [61] K. Cankoçak, P. de Barbaro, D. Vishnevskiy et al., “CMS HCAL installation and commissioning”, *Journal of Physics: Conference Series* **160** (2009), no. 1, 012055. doi:10.1088/1742-6596/160/1/012055.
- [62] S. A. et al., “G4—a simulation toolkit”, *Nuclear Instruments and Methods in Physics Research Section A: Accelerators, Spectrometers, Detectors and Associated Equipment* **506** (2003), no. 3, 250 – 303. doi:10.1016/S0168-9002(03)01368-8.
- [63] M. Dobbs and J. B. Hansen, “The HepMC C++ Monte Carlo event record for High Energy Physics”, *Computer Physics Communications* **134** (2001), no. 1, 41 – 46. doi:10.1016/S0010-4655(00)00189-2.
- [64] CMS Collaboration, “Measurement of B anti-B Angular Correlations based on Secondary Vertex Reconstruction at sqrt(s)=7 TeV”, *JHEP* **03** (2011) 136, arXiv:1102.3194. doi:10.1007/JHEP03(2011)136.
- [65] CMS Collaboration, “Particle-Flow Event Reconstruction in CMS and Performance for Jets, Taus, and MET”, *CMS-PAS-PFT-09-001* (Apr, 2009).
- [66] CMS Collaboration, “Commissioning of the Particle-Flow reconstruction in Minimum-Bias and Jet Events from pp Collisions at 7 TeV”, *CMS-PAS-PFT-10-002* (2010).

- [67] CMS Collaboration, “Jet Energy Corrections determination at 7 TeV”, *CMS-PAS-JME-10-010* (2010).
- [68] L. Agostino, G. Bauer, B. Beccati et al., “Commissioning of the CMS High Level Trigger”, *Journal of Instrumentation* **4** (2009), no. 10, P10005. doi:10.1088/1748-0221/4/10/P10005.
- [69] CMS Collaboration, “Measurement of CMS Luminosity”, *CMS-PAS-EWK-10-004* (1900).
- [70] CMS Collaboration, “Algorithms for b Jet identification in CMS”, *CMS-PAS-BTV-09-001* (Jul, 2009).
- [71] M. Cacciari, J. Rojo, G. P. Salam et al., “Quantifying the performance of jet definitions for kinematic reconstruction at the LHC”, *JHEP* **2008** (2008), no. 12, 032. doi:10.1088/1126-6708/2008/12/032.
- [72] CMS Collaboration, “Performance of Jet Algorithms in CMS”, *CMS-PAS-JME-07-003* (2007).
- [73] G. C. Blazey, J. R. Dittmann, S. D. Ellis et al., “Run II Jet Physics: Proceedings of the Run II QCD and Weak Boson Physics Workshop”, *hep-ex/0005012* (2000) arXiv:hep-ex/0005012. Comment: These proceedings include a recommendation for a standard jet cone and a standard jet KT algorithm for Run II. The algorithms are suitable for both CDF and D0 jet reconstruction as well as theoretical calculations. 32 Pages, 38 Figures.
- [74] G. P. Salam and G. Soyez, “A Practical Seedless Infrared-Safe Cone jet algorithm”, *JHEP* **0705** (2007) 086, arXiv:0704.0292. doi:10.1088/1126-6708/2007/05/086.
- [75] S. Catani, Y. L. Dokshitzer, M. H. Seymour et al., “Longitudinally-invariant k_{\perp} -clustering algorithms for hadron-hadron collisions”, *Nucl. Phys. B* **406** (February, 1993) 187–224.
- [76] M. Cacciari and G. P. Salam, “Dispelling the N3 myth for the kt jet-finder”, *Physics Letters B* **641** (2006), no. 1, 57 – 61. doi:10.1016/j.physletb.2006.08.037.
- [77] E. James, Y. Maravin, M. Mulders et al., “Muon Identification in CMS”, Technical Report CERN-CMS-NOTE-2006-010, CERN, Geneva, Jan, 2006.
- [78] A. Rizzi, F. Palla, and G. Segneri, “Track impact parameter based b-tagging with CMS”, Technical Report CERN-CMS-NOTE-2006-019, CERN, Geneva, Jan, 2006.
- [79] CMS Collaboration, “Commissioning of b-jet identification with pp collisions at $\sqrt{s} = 7$ TeV”, *CMS-PAS-BTV-10-001* (2010).
- [80] W. Adam, B. Mangano, T. Speer et al., “Track Reconstruction in the CMS tracker”, Technical Report CERN-CMS-NOTE-2006-041, CERN, Geneva, Dec, 2006.

-
- [81] CMS Collaboration, “CMS tracking performance results from early LHC operation”, *The European Physical Journal C - Particles and Fields* **70** (2010) 1165–1192. doi:10.1140/epjc/s10052-010-1491-3.
- [82] CMS Collaboration, “Tracking and Primary Vertex Results in First 7 TeV Collisions”, *CMS-PAS-TRK-10-005* (2010).
- [83] R. Frühwirth, W. Waltenberger, and P. Vanlaer, “Adaptive Vertex Fitting”, Technical Report CERN-CMS-NOTE-2007-008, CERN, Geneva, Mar, 2007.
- [84] T. Speer, K. Prokofiev, R. Frühwirth et al., “Vertex Fitting in the CMS Tracker”, Technical Report CERN-CMS-NOTE-2006-032, CERN, Geneva, Feb, 2006.
- [85] W. Waltenberger, “Adaptive Vertex Reconstruction”, Technical Report CERN-CMS-NOTE-2008-033, CERN, Geneva, Jul, 2008.
- [86] CMS Collaboration, “Tracking and Vertexing Results from First Collisions”, *CMS-PAS-TRK-10-001* (2010).

Acknowledgment

Working at ETH and in the large international collaboration of the CMS experiment at CERN was very exciting and a unique experience. Many people have contributed to this thesis in one way or another and I am thankful to all of them.

I am deeply indebted to Günther Dissertori for having given me the possibility to write this thesis and I am grateful for everything he has taught me.

I am heartily thankful to Christoph Grab. I appreciated his guidance and support from the initial to the final level. And I owe my deepest gratitude to Andrea Rizzi. He has a remarkable knowledge of CMS and he taught me everything I needed to know for writing this thesis. I feel privileged to have had advisors with such expertise and insight in the field of particle physics. I would like to thank Pierluigi Bortignon, especially for his inclusive vertex finder performance studies.

I would like to thank Thomas Gehrman for reading this thesis and being my co-examiner.

Very special thanks go to Lea Caminada for reading this thesis carefully. Her suggestions improved it considerably.

I am indebted to Leonardo Sala for providing help with computing grid related issues and for running a lot of grid jobs.

I wish to express my thank to my colleagues of the Institute of Particle Physics at ETH and at the University of Zurich and the CMS collaboration. I enjoyed meeting interesting and talented people.

I would also like to sincerely thank my parents, my sisters and their families for supporting me and providing help whenever needed.

Finally, I owe my loving thanks to my wife Simone for supporting me in so many ways. And I am grateful to my daughter Anja for smiling at me right now.

Curriculum Vitae

Personal Data

Name: Lukas David Wehrli
Date of Birth: 04.03.1982
Place of Birth: Aarau (AG)
Nationality: Swiss
Citizen of: Küttigen (AG)
Marital Status: married, one daughter (9.2.2011)

Education

2008- 2011 Doctoral studies at ETH Zurich (*Institute for Particle Physics IPP*)
Research at the CMS experiment at the CERN LHC

2007 Dipl. Phys. ETH
Diploma thesis at PSI in the group of Prof. Roland Horisberger
Title: Study of time walk behaviour of CMS pixel modules
(*ETHZ-IPP Internal Report 2007-04*)

2002-2007 Studies of Physics at ETHZ
Area of study: experimental physics

2002 Military service

2002 Matura Typus C

1998-2002 Gymnasium (Alte Kantonsschule Aarau)